Julius-Maximilians-Universität Würzburg

Fakultät für Biologie

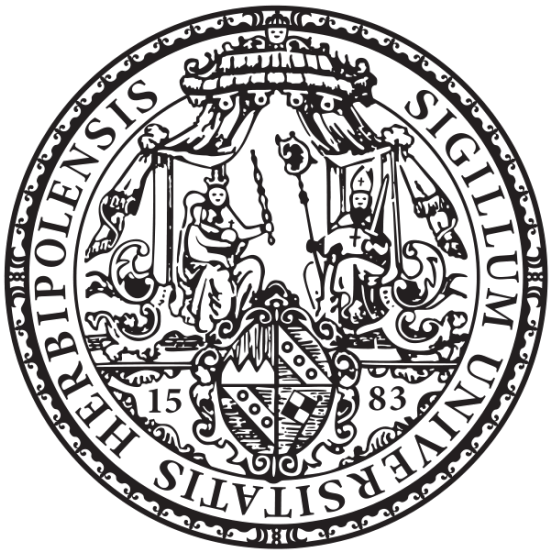

Vaccinia virus-encoded bacterial beta-glucuronidase as a diagnostic biomarker for oncolytic virotherapy

Dissertation

zur Erlangung des naturwissenschaftlichen Doktorgrades

der Julius-Maximilians-Universität Würzburg

vorgelegt von Michael Heß

aus Koblenz

Würzburg, 2013

Eingereicht am:

Mitglieder der Promotionskommission:

Vorsitzender: Prof. Dr. Rössler
1. Gutachter: Prof. Dr. Szalay
2. Gutachter: Prof. Dr. Krohne

Tag des Promotionskolloquiums:

Doktorurkunde ausgehändigt am:

Erklärung

Erklärung gemäß §4 Absatz 3 der Promotionsordnung der Fakultät für Biologie der Bayrischen Julius-Maximilians-Universität Würzburg vom 15. März 1999

1. Hiermit erkläre ich, dass ich die vorliegende Dissertation selbstständig angefertigt und keine anderen als die angegebenen Quellen und Hilfsmittel benutzt habe.

2. Ich erkläre, dass die vorliegende Dissertation weder in gleicher noch in ähnlicher Form bereits in einem anderen Prüfungsverfahren vorgelegt wurde.

3. Ich erkläre, dass ich außer den mit dem Zulassungsantrag urkundlich vorgelegten Graden keine weiteren akademischen Grade erworben oder zu erwerben versucht habe.

Würzburg, 2013

Michael Heß

Table of contents

1. Zusammenfassung

Onkolytische Viren stellen einen vielversprechenden Therapieansatz dar, der die Behandlung von Krebserkrankungen revolutionieren könnte. Intensive präklinische und klinische Studien zeigen sowohl die körperliche Verträglichkeit von onkolytischen Viren, als auch deren Wirksamkeit gegenüber soliden Tumoren. Die Entwicklung von therapiebegleitenden Diagnose- und Monitoringkonzepten sowie eine Optimierung der Antitumorwirkung onkolytischer Viren stellen Eckpunkte der aktuellen Forschung auf dem Gebiet der Virotherapie dar.

Im Rahmen dieser Arbeit wurde untersucht, welche diagnostischen und therapeutischen Möglichkeiten die virale Expression von beta-Glucuronidase durch den onkolytischen Vaccinia-Virus-Stamm GLV-1h68 eröffnet. In diesem Zusammenhang wurde ein, auf beta-Glucuronidase basierender, therapiebegleitender Biomarkertest entwickelt, dessen klinische Validierung derzeit stattfindet.

Mit Hilfe von fluorogenen Substraten konnte die Aktivität viral exprimierter beta-Glucuronidase detektiert und quantifiziert werden. Dies lies direkte Rückschlüsse auf das Replikationsverhalten von onkolytischen Viren im Tiermodell zu und ermöglichte zudem Aussagen über die Zelllyse Virus-infizierter Krebszellen. Diese Erkenntnisse führten letztendlich zur Ausarbeitung und Etablierung eines vielseitig anwendbaren Biomarker-Assays, der es ermöglicht anhand von Blutproben Aussagen über das Replikationsverhalten onkolytischer Viren in Mäusen zu machen. Neben retrospektiven Analysen erlaubt dieser Test auch ein therapiebegleitendes Monitoring der onkolytischen Virotherapie mit beta-Glucuronidase-exprimierenden Viren.

In weiteren präklinischen Untersuchungen diente der entwickelte Assay zudem als Ergänzung zum viralen Plaque Assays sowie als Referenz für Virus-exprimierte anti-angiogene Antikörper.

Eine fortführende Validierung dieses neuartigen Biomarkertests findet derzeit im Rahmen humaner Studien mit der klinischen Formulierung von GLV-1h68, GL-ONC1, statt und zeigte bereits erste positive Resultate.

Weiterhin konnte im Rahmen dieser Arbeit gezeigt werden, dass die Expression von beta-Glucuronidase durch onkolytische Viren in Verbindung mit fluoreszierenden Substraten eine optische Detektion von Karzinomen im präklinischen Tiermodell ermöglicht. Neben diagnostischen Zwecken, konnten Virus-kodierte Enzyme in Kombination mit Prodrugs genutzt werden, um den Therapieerfolg der onkolytischen Virotherapie zu verbessern.

In zusätzlichen Studien konnten zudem Methoden zur Visualisierung der Virus-induzierten Immunantwort sowie neuartige Konzepte zur Therapieverbesserung etabliert werden.

Zusammenfassend liefern die Ergebnisse der vorliegenden Arbeit wichtige Erkenntnisse über den Einfluss Virus-exprimierter beta-Glucuronidase auf unterschiedliche Diagnosekonzepte im Rahmen der onkolytischen Virotherapie. Daneben konnten entscheidende Erkenntnisse über den möglichen Einsatz neuer Monitoring- und Therapieansätze erzielt werden. Insbesondere durch die Entwicklung eines therapiebegleitenden Biomarkertests haben diese Resultate erheblichen Einfluss auf die weitere klinische Anwendung von onkolytischen Vaccinia-Viren.

2. Summary

Oncolytic virotherapy represents a promising approach to revolutionize cancer therapy. Several preclinical and clinical trials display the safety of oncolytic viruses as wells as their efficiency against solid tumors. The development of complementary diagnosis and monitoring concepts as well as the optimization of anti-tumor activity are key points of current virotherapy research.

Within the framework of this thesis, the diagnostic and therapeutic prospects of beta-glucuronidase expressed by the oncolytic vaccinia virus strain GLV-1h68 were evaluated. In this regard, a beta-glucuronidase-based, therapy-accompanying biomarker test was established which is currently under clinical validation.

By using fluorescent substrates, the activity of virally expressed beta-glucuronidase could be detected and quantified. Thereby conclusions about the replication kinetics of oncolytic viruses in animal models and virus-induced cancer cell lysis could be drawn. These findings finally led to the elaboration and establishment of a versatile biomarker assay which allows statements regarding the replication of oncolytic viruses in mice based on serum samples. Besides the analysis of retrospective conditions, this test is able to serve as therapy-accompanying monitoring tool for virotherapy approaches with beta-glucuronidase-expressing viruses.

The newly developed assay also served as complement to routinely used plaque assays as well as reference for virally expressed anti-angiogenic antibodies in additional preclinical studies. Further validation of this biomarker test is currently taking place in the context of clinical trials with GL-ONC1 (clinical grade GLV-1h68) and has already shown promising preliminary results.

It was furthermore demonstrated that fluorogenic substrates in combination with beta-glucuronidase expressed by oncolytic viruses facilitated the optical detection of solid tumors in preclinical models. In addition to diagnostic purposes, virus-encoded enzymes could also be combined with prodrugs resulting in an improved therapeutic outcome of oncolytic virotherapy. In further studies, the visualization of virus-induced immune reactions as well as the establishment of innovative concepts to improve the therapeutic outcome of oncolytic virotherapy could be accomplished.

In conclusion, the results of this thesis provide crucial findings about the influence of virally expressed beta-glucuronidase on various diagnostic concepts in the context of oncolytic virotherapy. In addition, innovative monitoring and therapeutic strategies could be established. Our preclinical findings have important clinical influence, particularly by the development of a therapy-associated biomarker assay which is currently used in different clinical trials.

3. Introduction

Cancer is the second most common cause of death in Germany (Fig. 1). According to the German Center of Cancer Register Data and the Robert Koch-Institute, 469.800 new cancer cases were recorded in 2008 [1]. Despite constantly improving screening and prevention methods, the prognosis indicates a growing number of cancer occurrences in the future. Therefore cancer remains one of the major health problems these days.

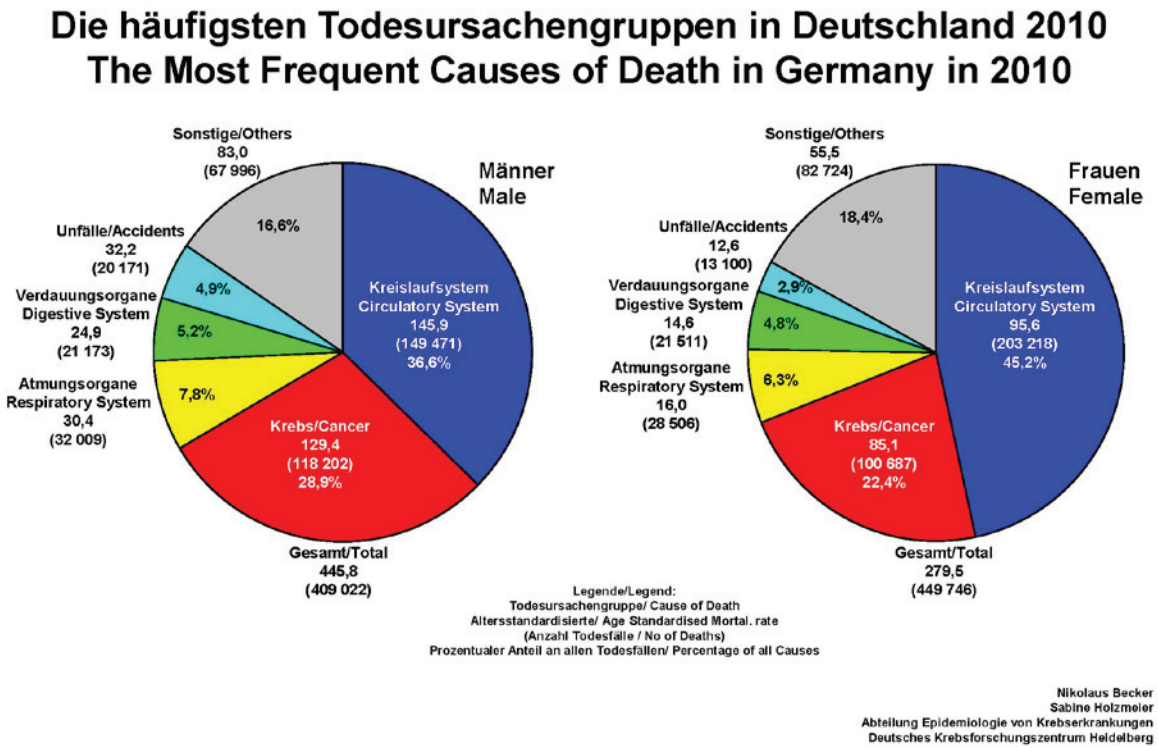

Fig. 1 **The most frequent causes of death in Germany 2010**
Source: DKFZ Heidelberg, Division of Cancer Epidemiology

3.1 The complexity of cancer

One of the major problems of cancer is its complexity. In contrast to other diseases which have defined causes, origins and progressions, cancer acts as an unpredictable ailment. Almost every organ of the human body can be origin of a cancer disease [2]. Although certain organs are more frequently affected than others, cancer cannot be described as a definable disease. Even men and women show fundamental differences in cancer causes. While women are affected by breast cancer in 30% of all cases, the most common kind in

men is prostate cancer. Beside those two types intestine, lung, stomach and pancreas are frequently affected by cancer (Fig. 2). The Robert Koch-Institute evaluates as much as 26 different origins of cancer, but overall about 100 cancer locations in the human body are known [1].

Fig. 2 **Incidences of cancer in Germany 2007/2008**

Source: DKFZ Heidelberg, Division of Cancer Epidemiology

Beside the different localizations of cancer origins, the progression of the disease causes problems for researchers and physicians. In addition to the primary tumor, almost every type of cancer is able to spread over the body by developing metastases [3]. Metastases are segregations of the primary tumor settling down in distant sites and transforming cancer from a localized to a systemic disease. But even the appearance of metastases is not a defined pattern. While some tumors show a high tendency to metastasize, this spread is completely lacking in other cases [3]. For that reason, it is not possible to apply a consistent treatment to all cancer cases.

The diversity of cancer can also be shown by the various causes of the disease. Initial assumptions about the reasons for malignant growth were made by Theodor Boveri in 1914 [4, 5]. His hypothesis of chromosomal changes is still valid today, as numeral and structural

aberrations of the chromosome content seem to be an important feature of many malignant cells [6]. Whether those aberrations are reason or consequence of unregulated cell divisions remains unknown [7, 8]. In recent years particularly molecular mechanisms of cancer pathogenesis were elucidated. It has become clear that not only changes in the whole chromosome content are characteristic for malignant cells but mutations in certain genes are able to cause cancer [9]. Of special significance are so called tumor suppressor genes and oncogenes. Tumor suppressor genes are usually involved in cell cycle control and initiation of apoptosis. With the appearance of specific mutations in those genes, deregulation of cell cycle and unhindered proliferation are a consequence. The most prominent example of a tumor suppressor is the transcription factor p53 which is involved in cell cycle control, apoptosis pathways and DNA repair [10]. Beside those suppressors, oncogenes are of critical importance in the development of cancer. This group of genes especially comprises transcription factors, chromatin remodelers, growth factors and signal transducers, which play a role in cell growth and proliferation [11]. A malfunction of those gene products often leads to defective cell divisions and increased proliferation. Out of the approximately 100 identified oncogenes, H-*ras* and *c-myc* are best characterized. But investigations have also shown that a single mutation in such an oncogene is insufficient in causing cancer. Cellular reparation and protection mechanisms are either able to repair those mutations or to trigger a programmed cell death. In case of an additional defect of a tumor suppressor, these mechanisms are deficient in special circumstances. In this case, malfunctions of an oncogene and a tumor suppressor interact and lead to uninhibited cell proliferation with lacking apoptosis mechanisms and finally to cancer. These observations led to the establishment of the so called multiple-hit theory by Knudson in 1971 [12], a hypothesis which is still discussed intensively at present [13]. Possible mutations in cancer related genes are attributed to different causes. Genetic predispositions are quite common in specific types of cancer and can be diagnosed with genetic tests. Definite mutations in the base sequence of *BRCA1* or *BRCA2* for example increase the risk of breast cancer up to 75% [14, 15] and can be detected with a well established routine test [16]. Diagnoses are more complicated when mutations are caused by exogenous influences. Certain chemicals, like polycyclic aromatic hydrocarbon or bromine for example, are known to act mutagenic. But also more common substances like nicotine [17] or alcohol [18] are associated with an increased cancer risk. In addition to this, unbalanced diet, obesity and physical inactivity are related to up to 30% of all cancer deaths [19, 20]. Beside these lifestyle habits, radiation is another frequent cause of malignancies. Ionizing as well as non-ionizing radiation is associated with increased cancer risk including skin cancer and leukemia [19, 21, 22]. These facts are causing a dangerous conflict in connection with cancer diagnosis methods: On the one hand, X-ray computed tomography is used to detect malignancies, on the other hand a single skull CT examination increases the risk to develop cancer by the factor 10.000 [23].

Additionally, disease triggering mechanisms like infective onco viruses [24], stem cells [25] or immune suppressive therapies [26] have been revealed in recent years. The described variety of cancer causing mechanisms underlines the heterogeneity of this disease.
Especially cancer with its complexity and heterogeneity is therefore a parade example for the need of personalized medicine based on customized diagnoses and therapy methods to maximize the treatment outcome [27].

3.2 Standard diagnostic and therapeutic procedures in cancer treatment

In consequence of the inhomogeneity of cancer, it is not possible to apply a consistent therapy. Beside the type of cancer, especially the time point of diagnosis plays a major role in making a decision which therapy is appropriate. The presence of metastases at the time of diagnosis for example reduces the chances of recovery many times over [28]. Therefore a preterm detection of cancer is of major importance. However, cancer is often only diagnosed with the occurrence of consistent symptoms. Reasons therefore are rarely applied diagnostic methods which are clinically established but simultaneously time and cost intensive. In particular magnetic resonance imaging and ultrasonography as well as techniques including high radiation exposure like computed tomography or positron emission tomography are used to show evidence of cancer [29]. Taking regard of these procedures, cancer cases are classified to compile a therapeutic regime. Classification is usually taking place using the TNM (tumor-nodes- metastases) system, giving information about state of the primary tumor, circumjacent lymph nodes and potential distant metastases [30]. The TNM system allows prognostic predictions and therefore determines the further therapy. First line therapy in treating putatively unmetastasized carcinomas is resection [31]. The surgical removal often includes the adjacent lymph nodes to prevent a potential spread of metastasizing cells. In cases where metastases already occurred, additional therapies are applied. These often include chemotherapy, which is used as adjuvant as well as standalone therapy. Chemotherapeutics intervene in various cancer mechanisms, but all aim at either killing malignant cells (cytotoxic effect) or at least stopping these cells from proliferating (cytostatic effect). In most cases, the DNA replication machinery of malignant cells is the point of attack. At systemic application, this machinery is impaired also in other fast proliferating cells in the human body leading to undesirable side effects like nausea, mucositis or blood count chances [31]. Alternatively or in combination with chemotherapeutics, irradiation is dosed to the affected tissue. Gamma rays are able to induce DNA damage leading to cell death in malignant tissues [32]. Crucial for the success of radiation therapy is a precise spatial and temporal application to achieve an optimal outcome without harming healthy cells [33].
Besides those decades-long used applications, especially molecular targeted therapies are

subject of intense research. A meanwhile routinely used agent is a monoclonal antibody called bevacizumab. It is currently approved for five advanced stage tumor types in Europe and is able to bind to the growth factor VEGF-A. Bevacizumab hinders VEGF-A from binding to its receptor and interrupts the angiogenetic cascade of tumor vasculature [34]. This interruption inhibits neoangiogenesis and prevents the nutrition and oxygen supply of tumors. Like most other cancer therapies, anti-angiogenic agents are often used in combination with chemotherapeutics to maximize treatment outcome [35].

Up to now, all mentioned therapy types cannot guarantee a complete recovery from cancer. The endeavor to optimize existing therapies and develop innovative technologies is of greatest importance to reduce cancer mortality rates.

3.3 Oncolytic viruses

Beside the improvement of existing technologies, biomedical research focuses on the development of new, groundbreaking therapy concepts. Breakthroughs are expected from immune therapies and gene therapy attempts, but also oncolytic virotherapy seems to be a promising approach in the fight against cancer.

For a closer insight into the history and development of oncolytic virotherapy, the reader is referred to the background section of the following review article drafted by the author of this thesis.

A prominent representative of an advanced oncolytic virus is GLV-1h68, engineered by Genelux Corporation, San Diego, USA. Based on the LIVP strain (Lister virus from the Institute of Viral Preparations, Moscow, Russia), site-targeted mutagenesis was used to develop an efficient oncolytic agent [36]. GLV-1h68 contains three foreign expression cassettes coding for a *Renilla* luciferase-*Aequorea* green fluorescent (RUC-GFP) fusion protein, beta-galactosidase (LacZ) and beta-glucuronidase (GusA). The reporter genes enable a monitoring of therapeutic progress making GLV-1h68 a promising theranostic agent [37].

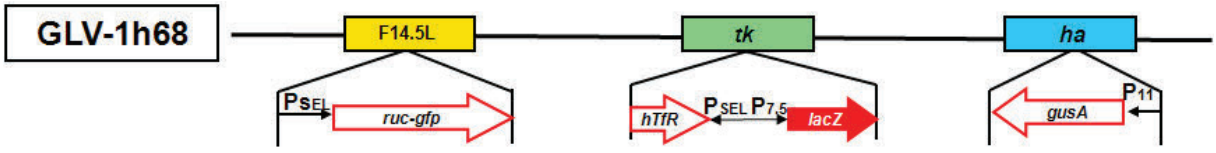

Fig. 3 **Oncolytic vaccinia virus GLV-1h68**

Schematic representation showing the genetic variances of GLV-1h68 in comparison to its parental strain LIVP.

3.4 Oncolytic viruses as theranostic agents

Therapy systems with combined diagnostic features represent a promising approach to optimize the treatment of cancer. Due to the fact that treatment is increasingly accompanied by diagnosis, an integrated diagnosis-therapy concept would allow an optimized patient care. A so called theranostic agent would enable a personalized therapy together with the possibility to monitor the therapeutic success on the basis of the same agent.

Clinically used systems enabling such approaches are specific radiopharmaceuticals like metaiodobenzylguanidine (MIBG). MIBG is a diagnostic radiotracer used in positron emission tomography but it can also be used for therapeutic approaches [38]. However these attempts are still uncommon and rarely used in the clinic.

Especially biological agents are predestinated for a use as theranostics. Molecular biological methods facilitate the insertion of reporter genes into therapeutically efficient microorganisms. Particularly oncolytic viruses have been studied extensively with regard to theranostic possibilities. The insertion of foreign DNA fragments into the genome of vaccinia virus allows a variety of imaging opportunities and will be discussed in the following chapter.

3.5 Visualization of oncolytic virotherapy

The possibilities to use oncolytic viruses to visualize tumors and tumor therapy success are shown in the following review manuscript drafted by the author of this thesis.

Manuscript Title

Imaging cancer with oncolytic vaccinia viruses

Authors

Michael Hess[1], Ulrike Donat[1], Jochen Stritzker[1, 2] and Aladar A. Szalay[1, 2, 3]

Affiliations

[1] Department of Biochemistry, Biocenter, University of Würzburg, Würzburg, Germany;

[2] Genelux Corporation, San Diego, CA, USA;

[3] Department of Radiation Oncology, Moores Cancer Center, University of California, San Diego, La Jolla, CA, USA

Correspondance

AAS - 3030 Bunker Hill St, Ste 310, San Diego, CA-92109, USA. phone: +1 858 483 0024, fax: +1 858 483 0026, email: aaszalay@genelux.com

Introduction

Due to the tremendous increase of cancer cases in the last decades the interest in new therapy strategies rises in research as well as in pharmaceutical industries. Beside innovative combination of already approved agents the search for new chemical and biological agents develops to a hot topic in research. As essential as the therapeutic effect of new cancer drugs is their ability to contribute to a successful diagnosis of the therapy. The perfect cancer drug would therefore facilitate both: therapy and diagnosis. Especially biological therapeutics show great promises in this so called theranostic direction. The valid usage of molecular biology methods enables an application of a variety of reporter genes especially in biological agents.

In this review we focus on oncolytic vaccinia viruses as cancer theranostics and their opportunities to promote highly diverse diagnosis technologies.

Background

The dream of using pathogens like viruses to treat cancer is older than the discovery of penicillin. Early virus-attempts were done in 1904 using replication competent rabies viruses [1] and revealed the enormous therapeutic potential of these applications. Even the observation that injection of viruses can lead to tumor regression in humans [2] did not lead to a breakthrough of oncolytic virus therapy. Major obstacles were prejudices against voluntary injection of live pathogens and the fact that cancer was not considered as that great threat it is nowadays. Thus the research as well as the interest of pharmaceutical industries in oncolytic virotherapy went down over many years. But in the last 15 years oncolytic viruses underwent a renaissance and developed to a so called hot topic in research. Hundreds of publications revealed the enormous potential of many kinds of viruses to act against different types of tumors. RNA viruses like reo- [3], polio- [4], measles [5] or vesicular stomatitis virus [6] were used as well as DNA viruses where most experiments were done with adeno- [7], herpes- [8] and vaccinia viruses [9]. These studies and the growing demand for new strategies to fight against cancer led to the implementation of several clinical trials all over the world (for a detailed register please see [10]).

The vigor of oncolytic viruses is highlighted by two major breakthroughs achieved in the past few years. One was the approval of the adenovirus H101 for treatment of head and neck cancer in china in 2005 [11] and the other one was the 1 billion deal between Amgen and BioVex regarding Biovex oncolytic herpes virus OncoVex [12].

This reveals the step of oncolytic viruses from bench to bedside. But bedside has two aspects nowadays: therapy on the one and monitoring on the other side. Monitoring a disease and especially monitoring its therapy became as import as the therapy itself in the last years. Clinicians are looking for techniques to monitor and thereby predict the possible success of a therapy. Biological agents like oncolytic viruses could be the perfect therapeutic

tool in the future edged with reporter genes for monitoring the therapy process.

The equipment of an oncolytic virus with reporter genes is limited by its natural capacity to carry foreign genes. Therefore vaccinia virus seems to be a perfect candidate as theranostic agent. Its capability to carry foreign DNA is about 25kBp [13] and allows researchers to insert diverse reporter (or therapeutic) genes into the vector genome. Even a combination of different reporters is possible due to the large DNA genome of vaccinia and could open a new field of multi-mechanistic diagnostic. Moreover vaccinia virus was used in over 200 million people during the eradication program against smallpox and showed an excellent safety profile [14]. Clinical studies with vaccinia viruses attested the oncolytic performance [15] and resulted in ongoing phases I to III [16].

In this review we want to give an overview about the capabilities of vaccinia virus to act as a theranostic tool by arming the vector with different kinds of reporter genes. Future directions will give a prospect in possible applications using vaccinia as an imaging agent even for metastases and circulating tumor cells.

Imaging modalities supported by reporter genes inserted into the genome of oncolytic viruses

Beside the therapeutic aspects of oncolytic virotherapy, monitoring gains more and more relevance. Reporter genes are a distinguished tool in connection with biological agents like viruses because modern cloning strategies facilitate the combination of both. As diverse the variety of oncolytic viruses is, the various is the number of different reporter genes. In the following the large number of examined reporter genes is clustered into their imaging modality context.

Bioluminescence

Bioluminescence as a special kind of chemiluminescence occurs upon the oxidation of luciferin catalyzed by a group of enzymes called luciferases resulting in the emission of light which can be detected with sensitive CCD cameras. Many kinds of marine luciferin-luciferase pairs have been characterized since about 40 years ago [17] and due to the discovery of other non-marine luciferases and molecular cloning methods new types of bioluminescence systems got entry into research [18]. Like every in vivo optical imaging method bioluminescence is dependent on the optical properties of tissues and body fluids [19]. Therefore the most commonly used luciferase in research is the firefly luciferase [20] but also Renilla and Gaussia luciferases are quite popular in laboratories' daily routine. Both substrates – D-luciferin for firefly and Gaussia as well as coelenterazine for Renilla luciferase – can be injected into live animals without any side effects and enable researchers whole body studies by tracking the luciferase reporters. These facets and the fact that bioluminescence imaging (BLI) can be performed relatively cheap compared to other whole-

body imaging techniques, led to an extensive use of BLI in many aspects of molecular biology. Since early achievements in 1967 [21] luciferase systems are used to detect contaminations in food and water [22]. First in vivo approaches in plants revealed the capabilities of this system [23] and gave rise to gene-expression studies in bacteria [24], zebrafish [25] and mammalian cells [26]. In context of cancer research bioluminescence was used to image tumors as well as tumor colonizing agents like bacteria and viruses [27]. Nearly all oncolytic viruses were tentatively equipped with luciferases to visualize viral routes and replication in vivo. Adenoviruses were one of the first examples for these investigations [28] followed by herpes simplex [29], vaccinia [9], measles [30] and vesicular stomatitis virus [31]. Even a comparatively small vector like parvovirus could be engineered with luciferase to investigate its capabilities as oncolytic agent [32]. Especially luciferase equipped vaccinia viruses were investigated extensively and revealed a plenty of new insights into virus-tumor interactions. Yu and collaborators could expose not only the location of the primary tumor but also of lung metastases by systemic administration of vaccinia viruses armed with a gfp-luc fusion gene and subsequent monitoring of the light emission [33]. Thorne et al. for example could load cytokine-induced killer cells with luc-expression vaccinia virus and achieved a enhanced delivery to and regression of xenografted tumors in mice [34]. The same virus was used to show the different spatial biodistribution of intravenous and intraperitoneal injected viruses [35]. Systemic injection of oncolytic viruses furthermore plays a role when not only a solid tumor is present but also metastases. However not only in vivo approaches were enabled by BLI but also the fact that tumor tissue can be infected ex vivo with oncolytic viruses could be discovered. Therefore tumors were excised from laboratory animals, treated with luciferase expressing vaccinia viruses and imaged afterwards to visualize the viral replication [36]. Taken together bioluminescence is one of the best evaluated imaging methods in coherence with oncolytic viruses. Newly discovered and genetically engineered luciferases like the secreted Gaussia luciferase could open a new field in bioluminescence research and influence the monitoring of oncolytic viruses [37]. On the other hand it has to be considered that bioluminescence is not used in the clinics up to now and therefore is limited to laboratory research. The way that has to be taken to get into patients could be too far to be walked. This is the major reason why other imaging modalities gain more and more recognition in association with oncolytic viruses especially when it comes to clinical trials.

Fluorescence

More common in medical centers is the imaging of fluorescence. It is defined as the spontaneous emission of light by a material after excitation and was first described by Stokes in 1852 [38]. Routinely fluorescence is applied in ophthalmology [39], perfusion diagnostics [40] and cancer diagnosis to detect sentinel lymph nodes [41]. Therefore fluorescence devices like endoscopes or cameras are routinely available in hospitals facilitating the fast

transition of new fluorescence applications from basic research to field testing. To combine oncolytic viruses with fluorescence imaging (FLI) chemical dyes like regularly used indocyanine green (ICG) are less suitable than biological coloring through permanent emitting proteins. The first fluorescent protein (FP) that was cloned was green fluorescent protein (GFP) from the jellyfish Aequorea victoria in 1992 [42] and finally led to the Nobel Prize for Shimomura, Chalfie and Tsien in 2008 [43]. Since then GFP is the most common fluorescent marker in molecular biology. It is especially used to visualize gene expression in vivo [44],as a fusion tag [45] and as an indicator for fluorescence resonance energy transfer (FRET) approaches [46]. In terms of in vivo imaging GFP is limited by the absorption of visible light by tissue, hemoglobin and melanin and therefore limited to imaging of surface near superficial tissues. Therefore fluorescent proteins were developed that emit light in the so called optical window between 600 and 1100nm [47] to avoid the massive absorption of photons. The first step to an improved FP was the discovery of red fluorescent protein (RFP) from Discosoma coral by Fradkov et al. in 2001 [48]. In the following years especially the group of Roger Tsien contributed to the improvement of fluorescent proteins for in vivo imaging for instance by directed mutagenesis of Discosoma RFP to create stable monomeric proteins [49]. The same group developed assays to test different FP's for their photostability and thereby opened the field of FP-improvement for a wide range of researchers [50]. A major step in FP progress was done in 2007 when Shcherbo and collaborators designed the RFP derivative katushka which is distinguished by a tremendous brightness, fast maturation and high pH- and photostability [51]. Katushka could be further improved to act as a flagship candidate for FP's used in vivo and especially as a imaging tool that could be used in somewhat deeper tissue [52, 53].

But as GFP still is the most common fluorescent marker, a wide range of oncolytic viruses were tagged with it. Parvo virus [54], vaccinia virus [55], vesicular stomatitis virus [56], rabies virus [57], herpes virus [58], measles virus [59] and adenovirus [60] are only a few of the investigated OVs equipped with GFP. Even comparative studies focusing on the cytotoxic effect of different OVs were promoted by GFP expression [61]. Beside the early experiments where GFP mainly worked as a tool to show the competence of OV's to replicate in tumor cells, current studies examinating more in-depth aspects of oncolytic virotherapy are supported by GFP expression of OVs. For example feasible combination therapies are investigated and show the capabilities of combining virotherapy with radiation [62]. Furthermore the mix of different FPs opened up a new era of tumor-OV interaction studies. By labeling PC-3 cells with RFP and challenging them with a GFP expressing OV, Donat et al. could show the preferential colonization of metastases in comparison to the solid tumor [63]. In in vivo experiments even the route of migrating tumor cells to the lymph nodes as well as the oncolytic vaccinia virus infecting them in lymph vessels could be visualized. Fundamental insights into vaccinia spreading mechanisms could be achieved by fusing

different FPs to vaccinias core protein A5 respectively actin and gave insights into the extremely fast spreading mechanisms of vaccinia virus [64]. In another approach Hiley and colleagues showed that it is not obligatory to express a FP by an oncolytic virus. They used an elegant way to label vaccinia viruses with an Alexa dye and could show the importance of VEGF-A in host cell entry by vaccinia [65].

Magnet resonance imaging

Magnet resonance (MR) is one the most commonly used imaging technologies in hospitals. It makes use of the property of nuclear magnetic resonance to image nuclei of atoms inside the body. Magnet resonance imaging benefits from the fact that it is not dependent on ionizing radiation and is therefore free of harmful emission. MR is routinely used and provides a good contrast especially between different soft tissues making it a standard method for imaging for example the brain, muscles or carcinomas. Like in most imaging modalities it is possible to enhance the MR contrast by applying different contrast media. Gadolinium based media like Dotarem are approved for different fields of application [66], but also iron oxide agents are proven for safety and efficiency [67]. On the other hand gene evoked reporters can offer great opportunities to improve MR contrasts.

One of the first reporter genes that could be imaged properly by MR was beta-galactosidase. Thomas Meade and his team designed a paramagnetic MR probe that could be activated by beta-galactosidase and let to an enhanced MR contrast allowing high resolution MR in vivo [68]. But not only enzyme based reporters showed success in this area of research. Another way of contrast enhancement was opened with the aid of ferritin gene reporters [69, 70]. This family of iron based system could be extended to different receptors and related iron-binding proteins to an entire research area [71]. Most approaches work with the overexpression of iron uptake/storage systems in stably transduced cell lines [72, 73], but the expression of ferritin genes was also used to track tumor colonizing microorganisms. Hill and colleagues for example could visualize tumor colonization by an E. coli Nissle strain through expression of a special kind of ferritin called bacterioferritin [74]. This specific kind of iron binding protein enhanced R2-relaxation leading to contrast improvement in MRI. The system was strengthened by combining it with an arabinose inducible system to temporarily switch on the transgene expression. Although magnet resonance imaging in context of oncolytic virotherapy is so far mainly applied without reporter genes and merely used to monitor effects like oncolysis [75, 76], gene evoked MRI reporter systems are conceivable. Enzymes like Galactosidase or Glucuronidase facilitating enzyme-based MRI reporter systems are integrated in many well characterized OVs [77-80] but also iron dependent platforms are under laboratory investigations.

The use of enzymes involved in the melanin synthesis as MR reporters has been shown to be a further promising approach improving contrast in magnet resonance imaging. Ralph

Weissleder et al. already showed in 1997 that melanin production by transfection of a tyrosinase gene led to an enhanced MR signal in cell culture experiments [81]. These experiences were taken by Stritzker et al to generate oncolytic vaccinia viruses equipped with different enzymes of the melanin synthesis pathway. In this regard the combination of tyrosinase and tyrosinase related protein 1 expressed by the OV resulted in an extensive production of melanin in xenografts in turn enabling an amended MR imaging [82].

Another starting point connecting MRI with oncolytic viruses is the imaging of inflammation caused by OVs. Two different systems are published up to now: the usage of contrast agents which directly label immune cells on the one hand and MR agents activated by inflammatory enzymes on the other hand. The latter was shown in a pioneering study by Kleijn and colleagues which used a gadolinium based agent activated by myeloperoxidase (MPO-Gd), an inflammatory enzyme present in myeloid cells which is secreted upon inflammation by activated subsets of these cells. With the aid of MPO-Gd Kleijn could report the temporal and spatial expansion of the inflammatory response to OV treatment in coherence with two different rodent glioma models [83]. The strategy of directly labeling immune cells was performed in our own laboratory. Based on approaches visualizing the center of bacterial inflammations with perfluorocarbon (PFC) nanoemulsions in combination with 19F MRI [84], Weibel and collaborators could illustrate the immune response to oncolytic vaccinia viruses in different xenografts. The MR signal provided by the PFC emulsion correlated with CD68-positive macrophages and reflected the grade of inflammation caused by the OV [85].

Beside this considerable number of different reporter and labeling systems to optimize MRI in context of the application of oncolytic viruses laboratory investigations lead to the emergence of totally new strategies to accomplish an excellent MR contrast. Innovative approaches like the use of nonmetallic, biodegradable, lysine rich-protein reporters [86] will be transferred to OV development likely leading to even more improved diagnostic capabilities.

PET Imaging

Besides MRI, positron emission tomography (PET) is the second state of the art imaging modality used in daily hospital routine. It is based on the detection of coinciding gamma rays emitted during the electron-positron annihilation after positron emission from radiotracers and allows three-dimensional image reconstruction. In contrast to magnet resonance imaging, PET is dependent on ionizing radiation and the administration of radioactive tracers making it highly sensitive on the one but critical in case of safety reasons on the other hand. By the administration of labeled tracers like 18-Fludeoxyglucose, PET is able to provide statements about degrees of metabolic activity and therefore serves as functional imaging method. This ability is utilized in cancer diagnosis and staging: Because of the enhanced metabolic activity of solid tumors, FDG-PET allows an accurate spatial localization of carcinomas and

metastases. For a deeper insight into clinical use of FDG-PET in context of cancer the reader is referred to two articles by Delbeke [87] and Gambhir [88]. Because of the fact that PET-imaging is often not able to display sufficient morphological information it is often used in combination with either computer tomography or MRI allowing a preciser interpretation of data [89].

Combining oncolytic viruses with PET could lead to even more sensible radiotracer detection by expression specific reporter genes published in the context of positron emission tomography. As we will focus on PET reporters expressed especially by OVs the reader is referred to an excellent review by Serganova and Blasberg to learn more about PET reports in general and its possible impact on therapies in particular [90].

A major group of PET reporter systems depends on the expression of foreign enzymes phosphorylating special radiotracers and thereby trapping them in the target cell. A well characterized model for this is the thymidine kinase (TK). Shortly after first studies showing the feasibility of this system [91, 92], the groups of Blasberg and Fong could image the distribution and replication of oncolytic herpes strains by using a 124I-labeled FIAU in combination with the viral TK [93, 94]. The same HSV thymidine kinase was also cloned into a Sindbis virus facilitating simultaneous gene-directed enzyme-prodrug therapy with ganciclovir and 18F-FEAU PET [95]. Although TK in combination with its corresponding tracers can visualize even micrometastases via PET [96], latest studies focus on another group of reporter genes. These genes are characterized by their function as transporters and operate by pumping ions into the cell. In some cases these transporters simultaneously bind the associated ions. By utilizing this system, radiolabeled tracers can be designed for specific transporters and operate as PET reporter systems. Studies with the human norepinephrine transporter (hNET) could reveal the functionality of hNET and its tracer 124I-MIBG as PET tool but accuracy and resolution in mouse studies seemed to be insufficient for further translational studies [97, 98]. Therefore the recent investigations are mainly focusing on another ion transporter system called human sodium iodine symporter (hNIS). hNIS uses an electrochemical gradient of sodium ions to transport molecules across a phospholipid membrane with the help of an a ATP-driven pump [99]. It is mainly found in the thyroid but hNIS activity can also be detected in the salivary glands and in gastric mucosa [100]. But due to its low or non detectable expression levels in every other tissue hNIS offers a great opportunity to function as PET-reporter. Measles virus was the first OV equipped with hNIS to support the imaging capabilities of the agent [101]. But also vesicular stomatitis virus [102], adeno [103] and vaccinia virus [104] were shown to be combinable with hNIS. Beside the fact that hNIS allows a continuous monitoring because tracer can be administrated repeatedly the symporter shows the advantage of allowing simultaneous therapy approaches by radiotherapy [105-108].

Multimodel imaging – achievements and prospects

Beside the improvement of the already mentioned reporter systems for different kinds of imaging modalities, another worthwhile goal is the development of so called multimodal reporters. These constructs consist of either different reporters which are fused to each other or of specific reporters which can be utilized for varying imaging systems. The major goal of such attempts is trying to combine the advantages of specialized imaging systems to gain a far reaching insight in OV-tumor interactions.

In coherence with oncolytic viruses, one of the first investigated multimodal reporters was a fusion protein composed of Renilla luciferase and GFP [33]. But as bioluminescence and fluorescence are both limited to the absorption of light by tissue the progress led to a triple fusion protein including a PET reporter [109]. Here Ray et al. fused an improved version of firefly luciferase to red fluorescent protein and a HSV-1 thymidine kinase. This construct showed excellent imaging abilities but to our knowledge it was not cloned into an OV up to now. Instead of that Kimball and colleagues encapsulated a dual-imaging reporter comprised again out of a red fluorescent protein and thymidine kinase into an oncolytic adenovirus and could show the therapeutic and diagnostic activity of this virus in ovarian cancer cell lines.

A different strategy was realized with the tyrosinase expressing vaccinia virus by Stritzker et al. mentioned in the MRI section above. It could be shown that beside MRI imaging a highly contemporary imaging method called multispectral optoacoustic tomography could be used to visualize tumors and metastases [82].

All this different approaches show the significance of the field of multimodal imaging in cancer therapy and will certainly be extended in near future.

Outlook

To fulfill the enormous requirements which are needed for an almost perfect reporter-imaging system in combination with oncolytic viruses, further steps have to be taken. On the one hand an improvement of established reporter systems is possible and certainly the easiest way to gain new insights in the complex interaction of tumors and OVs. On the other hand the development of new systems could open a wide field of capabilities. Innovative techniques like optoacoustic imaging show that new technologies can contribute to the improvement of sensitivity and resolution in cancer imaging. Therefore especially multimodal systems will be highly relevant.

Other groundbreaking challenges will be the detection of metastases or even circulating tumor cells with the help of OVs and new reporter systems. First studies were already done in this direction [110, 111] and show the applicability.

But due to the fact that cancer theranostic shows such a complexity a lot of further effort has to be expended to find a perfect OV-reporter system

References

1. Dock, G., Rabies virus vaccination in a patient with cervical carcinoma. American Journal of Medical Science, 1904. 127(563).
2. Southam, C.M. and A.E. Moore, Clinical studies of viruses as antineoplastic agents with particular reference to Egypt 101 virus. Cancer, 1952. 5(5): p. 1025-34.
3. Hirasawa, K., et al., Systemic reovirus therapy of metastatic cancer in immune-competent mice. Cancer Res, 2003. 63(2): p. 348-53.
4. Pond, A.R. and E.E. Manuelidis, Oncolytic Effect of Poliomyelitis Virus on Human Epidermoid Carcinoma (Hela Tumor) Heterologously Transplanted to Guinea Pigs. Am J Pathol, 1964. 45: p. 233-49.
5. Peng, K.W., et al., Systemic therapy of myeloma xenografts by an attenuated measles virus. Blood, 2001. 98(7): p. 2002-7.
6. Ebert, O., et al., Oncolytic vesicular stomatitis virus for treatment of orthotopic hepatocellular carcinoma in immune-competent rats. Cancer Res, 2003. 63(13): p. 3605-11.
7. Zhang, J.F., et al., Treatment of a human breast cancer xenograft with an adenovirus vector containing an interferon gene results in rapid regression due to viral oncolysis and gene therapy. Proc Natl Acad Sci U S A, 1996. 93(9): p. 4513-8.
8. Fu, X. and X. Zhang, Delivery of herpes simplex virus vectors through liposome formulation. Mol Ther, 2001. 4(5): p. 447-53.
9. Zhang, Q., et al., Eradication of solid human breast tumors in nude mice with an intravenously injected light-emitting oncolytic vaccinia virus. Cancer Res, 2007. 67(20): p. 10038-46.
10. Patel, M.R. and R.A. Kratzke, Oncolytic virus therapy for cancer: the first wave of translational clinical trials. Transl Res, 2013.
11. Garber, K., China approves world's first oncolytic virus therapy for cancer treatment. J Natl Cancer Inst, 2006. 98(5): p. 298-300.
12. Deal watch: Amgen buys oncolytic virus company. Nat Rev Drug Discov, 2011. 10(3): p. 166.
13. Smith, G.L. and B. Moss, Infectious poxvirus vectors have capacity for at least 25 000 base pairs of foreign DNA. Gene, 1983. 25(1): p. 21-8.
14. Ellner, P.D., Smallpox: gone but not forgotten. Infection, 1998. 26(5): p. 263-9.
15. Breitbach, C.J., et al., Intravenous delivery of a multi-mechanistic cancer-targeted oncolytic poxvirus in humans. Nature, 2011. 477(7362): p. 99-102.
16. Guse, K., V. Cerullo, and A. Hemminki, Oncolytic vaccinia virus for the treatment of cancer. Expert Opin Biol Ther, 2011. 11(5): p. 595-608.

17. McElroy, W.D., H.H. Seliger, and E.H. White, Mechanism of bioluminescence, chemiluminescence and enzyme function in the oxidation of firefly luciferin. Photochem Photobiol, 1969. 10(3): p. 153-70.
18. Close, D.M., et al., In vivo bioluminescent imaging (BLI): noninvasive visualization and interrogation of biological processes in living animals. Sensors (Basel), 2011. 11(1): p. 180-206.
19. Jobsis, F.F., Noninvasive, infrared monitoring of cerebral and myocardial oxygen sufficiency and circulatory parameters. Science, 1977. 198(4323): p. 1264-7.
20. Zhao, H., et al., Emission spectra of bioluminescent reporters and interaction with mammalian tissue determine the sensitivity of detection in vivo. J Biomed Opt, 2005. 10(4): p. 41210.
21. Levin, G.V., C.S. Chen, and G. Davis, Development of the firefly bioluminescent assay for the rapid, quantitative detection of microbial contamination of water. AMRL-TR-67-71. AMRL TR, 1967: p. 1-73.
22. Prosser, J.I., et al., Luminescence-based systems for detection of bacteria in the environment. Crit Rev Biotechnol, 1996. 16(2): p. 157-83.
23. Legocki, R.P., et al., Bioluminescence in soybean root nodules: Demonstration of a general approach to assay gene expression in vivo by using bacterial luciferase. Proc Natl Acad Sci U S A, 1986. 83(23): p. 9080-4.
24. Schauer, A., et al., Visualizing gene expression in time and space in the filamentous bacterium Streptomyces coelicolor. Science, 1988. 240(4853): p. 768-72.
25. Mayerhofer, R., K. Araki, and A.A. Szalay, Monitoring of spatial expression of firefly luciferase in transformed zebrafish. J Biolumin Chemilumin, 1995. 10(5): p. 271-5.
26. Lorenz, W.W., et al., Expression of the Renilla reniformis luciferase gene in mammalian cells. J Biolumin Chemilumin, 1996. 11(1): p. 31-7.
27. Yu, Y.A., et al., Optical imaging: bacteria, viruses, and mammalian cells encoding light-emitting proteins reveal the locations of primary tumors and metastases in animals. Anal Bioanal Chem, 2003. 377(6): p. 964-72.
28. Nanda, D., et al., Treatment of malignant gliomas with a replicating adenoviral vector expressing herpes simplex virus-thymidine kinase. Cancer Res, 2001. 61(24): p. 8743-50.
29. Yamamoto, S., et al., Imaging immediate-early and strict-late promoter activity during oncolytic herpes simplex virus type 1 infection and replication in tumors. Gene Ther, 2006. 13(24): p. 1731-6.
30. Msaouel, P., et al., Engineered measles virus as a novel oncolytic therapy against prostate cancer. Prostate, 2009. 69(1): p. 82-91.
31. Moussavi, M., et al., Oncolysis of prostate cancers induced by vesicular stomatitis virus in PTEN knockout mice. Cancer Res, 2010. 70(4): p. 1367-76.

32. Maxwell, I.H., et al., Expansion of tropism of a feline parvovirus to target a human tumor cell line by display of an alpha(v) integrin binding peptide on the capsid. Gene Ther, 2001. 8(4): p. 324-31.
33. Yu, Y.A., et al., Visualization of tumors and metastases in live animals with bacteria and vaccinia virus encoding light-emitting proteins. Nat Biotechnol, 2004. 22(3): p. 313-20.
34. Thorne, S.H., R.S. Negrin, and C.H. Contag, Synergistic antitumor effects of immune cell-viral biotherapy. Science, 2006. 311(5768): p. 1780-4.
35. Baril, P., et al., Differential biodistribution of oncolytic poxvirus administered systemically in an autochthonous model of hepatocellular carcinoma. J Gene Med, 2011. 13(12): p. 692-701.
36. Diallo, J.S., et al., Ex vivo infection of live tissue with oncolytic viruses. J Vis Exp, 2011(52).
37. Browne, A.W., et al., Cancer screening by systemic administration of a gene delivery vector encoding tumor-selective secretable biomarker expression. PLoS One, 2011. 6(5): p. e19530.
38. Stokes, G.G., On the Change of Refrangibility of Light Phil. Trans, 1852. 142: p. 463-562.
39. Desmettre, T., J.M. Devoisselle, and S. Mordon, Fluorescence properties and metabolic features of indocyanine green (ICG) as related to angiography. Surv Ophthalmol, 2000. 45(1): p. 15-27.
40. Liebert, A., et al., Non-invasive detection of fluorescence from exogenous chromophores in the adult human brain. Neuroimage, 2006. 31(2): p. 600-8.
41. Hirche, C., et al., Sentinel node biopsy by indocyanine green retention fluorescence detection for inguinal lymph node staging of anal cancer: preliminary experience. Ann Surg Oncol, 2010. 17(9): p. 2357-62.
42. Prasher, D.C., et al., Primary structure of the Aequorea victoria green-fluorescent protein. Gene, 1992. 111(2): p. 229-33.
43. Kricka, L.J. and P.E. Stanley, Scientists awarded Nobel Prize for work with GFP. Luminescence, 2009. 24(1): p. 1.
44. Chalfie, M., et al., Green fluorescent protein as a marker for gene expression. Science, 1994. 263(5148): p. 802-5.
45. Cubitt, A.B., et al., Understanding, improving and using green fluorescent proteins. Trends Biochem Sci, 1995. 20(11): p. 448-55.
46. Heim, R. and R.Y. Tsien, Engineering green fluorescent protein for improved brightness, longer wavelengths and fluorescence resonance energy transfer. Curr Biol, 1996. 6(2): p. 178-82.

47. Konig, K., Multiphoton microscopy in life sciences. J Microsc, 2000. 200(Pt 2): p. 83-104.
48. Fradkov, A.F., et al., Novel fluorescent protein from Discosoma coral and its mutants possesses a unique far-red fluorescence. FEBS Lett, 2000. 479(3): p. 127-30.
49. Shaner, N.C., et al., Improved monomeric red, orange and yellow fluorescent proteins derived from Discosoma sp. red fluorescent protein. Nat Biotechnol, 2004. 22(12): p. 1567-72.
50. Shaner, N.C., et al., Improving the photostability of bright monomeric orange and red fluorescent proteins. Nat Methods, 2008. 5(6): p. 545-51.
51. Shcherbo, D., et al., Bright far-red fluorescent protein for whole-body imaging. Nat Methods, 2007. 4(9): p. 741-6.
52. Shcherbo, D., et al., Far-red fluorescent tags for protein imaging in living tissues. Biochem J, 2009. 418(3): p. 567-74.
53. Lin, M.Z., et al., Autofluorescent proteins with excitation in the optical window for intravital imaging in mammals. Chem Biol, 2009. 16(11): p. 1169-79.
54. Olijslagers, S., et al., Potentiation of a recombinant oncolytic parvovirus by expression of Apoptin. Cancer Gene Ther, 2001. 8(12): p. 958-65.
55. McCart, J.A., et al., Systemic cancer therapy with a tumor-selective vaccinia virus mutant lacking thymidine kinase and vaccinia growth factor genes. Cancer Res, 2001. 61(24): p. 8751-7.
56. Fernandez, M., et al., Genetically engineered vesicular stomatitis virus in gene therapy: application for treatment of malignant disease. J Virol, 2002. 76(2): p. 895-904.
57. Boldogkoi, Z., A. Bratincsak, and I. Fodor, Evaluation of pseudorabies virus as a gene transfer vector and an oncolytic agent for human tumor cells. Anticancer Res, 2002. 22(4): p. 2153-9.
58. Stanziale, S.F., et al., Oncolytic herpes simplex virus-1 mutant expressing green fluorescent protein can detect and treat peritoneal cancer. Hum Gene Ther, 2004. 15(6): p. 609-18.
59. Allen, C., et al., Retargeted oncolytic measles strains entering via the EGFRvIII receptor maintain significant antitumor activity against gliomas with increased tumor specificity. Cancer Res, 2006. 66(24): p. 11840-50.
60. Funston, G.M., et al., Expression of heterologous genes in oncolytic adenoviruses using picornaviral 2A sequences that trigger ribosome skipping. J Gen Virol, 2008. 89(Pt 2): p. 389-96.
61. Wollmann, G., P. Tattersall, and A.N. van den Pol, Targeting human glioblastoma cells: comparison of nine viruses with oncolytic potential. J Virol, 2005. 79(10): p. 6005-22.

62. Advani, S.J., et al., Preferential replication of systemically delivered oncolytic vaccinia virus in focally irradiated glioma xenografts. Clin Cancer Res, 2012. 18(9): p. 2579-90.
63. Donat, U., et al., Preferential colonization of metastases by oncolytic vaccinia virus strain GLV-1h68 in a human PC-3 prostate cancer model in nude mice. PLoS One, 2012. 7(9): p. e45942.
64. Doceul, V., et al., Repulsion of superinfecting virions: a mechanism for rapid virus spread. Science, 2010. 327(5967): p. 873-6.
65. Hiley, C.T., et al., Vascular endothelial growth factor-A promotes Vaccinia virus entry into host cells via activation of the Akt pathway. J Virol, 2012.
66. Herborn, C.U., et al., Clinical safety and diagnostic value of the gadolinium chelate gadoterate meglumine (Gd-DOTA). Invest Radiol, 2007. 42(1): p. 58-62.
67. Marincek, B., Diagnostic improvement in MRI of gynecological neoplasms. J Belge Radiol, 1996. 79(1): p. 13-7.
68. Louie, A.Y., et al., In vivo visualization of gene expression using magnetic resonance imaging. Nat Biotechnol, 2000. 18(3): p. 321-5.
69. Cohen, B., et al., Ferritin as an endogenous MRI reporter for noninvasive imaging of gene expression in C6 glioma tumors. Neoplasia, 2005. 7(2): p. 109-17.
70. Genove, G., et al., A new transgene reporter for in vivo magnetic resonance imaging. Nat Med, 2005. 11(4): p. 450-4.
71. Hasegawa, S., T. Furukawa, and T. Saga, Molecular MR imaging of cancer gene therapy: ferritin transgene reporter takes the stage. Magn Reson Med Sci, 2010. 9(2): p. 37-47.
72. Kim, H.S., et al., In vivo imaging of tumor transduced with bimodal lentiviral vector encoding human ferritin and green fluorescent protein on a 1.5T clinical magnetic resonance scanner. Cancer Res, 2010. 70(18): p. 7315-24.
73. Choi, S.H., et al., Imaging and quantification of metastatic melanoma cells in lymph nodes with a ferritin MR reporter in living mice. NMR Biomed, 2012. 25(5): p. 737-45.
74. Hill, P.J., et al., Magnetic resonance imaging of tumors colonized with bacterial ferritin-expressing Escherichia coli. PLoS One, 2011. 6(10): p. e25409.
75. Geletneky, K., et al., Regression of advanced rat and human gliomas by local or systemic treatment with oncolytic parvovirus H-1 in rat models. Neuro Oncol, 2010. 12(8): p. 804-14.
76. Lavilla-Alonso, S., et al., Adenoviruses with an alphavbeta integrin targeting moiety in the fiber shaft or the HI-loop increase tumor specificity without compromising antitumor efficacy in magnetic resonance imaging of colorectal cancer metastases. J Transl Med, 2010. 8: p. 80.

77. Carroll, N.M., et al., Enhancement of gene therapy specificity for diffuse colon carcinoma liver metastases with recombinant herpes simplex virus. Ann Surg, 1996. 224(3): p. 323-9; discussion 329-30.
78. Steinwaerder, D.S., et al., Tumor-specific gene expression in hepatic metastases by a replication-activated adenovirus vector. Nat Med, 2001. 7(2): p. 240-3.
79. Grote, D., et al., Live attenuated measles virus induces regression of human lymphoma xenografts in immunodeficient mice. Blood, 2001. 97(12): p. 3746-54.
80. Hess, M., et al., Bacterial glucuronidase as general marker for oncolytic virotherapy or other biological therapies. J Transl Med, 2011. 9: p. 172.
81. Weissleder, R., et al., MR imaging and scintigraphy of gene expression through melanin induction. Radiology, 1997. 204(2): p. 425-9.
82. Stritzker, J., et al., Vaccinia virus-mediated melanin production allows MR and optoacoustic deep tissue imaging and laser-induced thermotherapy of cancer. Proc Natl Acad Sci U S A, 2013.
83. Kleijn, A., et al., Distinguishing inflammation from tumor and peritumoral edema by myeloperoxidase magnetic resonance imaging. Clin Cancer Res, 2011. 17(13): p. 4484-93.
84. Hertlein, T., et al., Visualization of abscess formation in a murine thigh infection model of Staphylococcus aureus by 19F-magnetic resonance imaging (MRI). PLoS One, 2011. 6(3): p. e18246.
85. Weibel, S., et al., Imaging of Intratumoral Inflammation during Oncolytic Virotherapy of Tumors by (19)F-Magnetic Resonance Imaging (MRI). PLoS One, 2013. 8(2): p. e56317.
86. Gilad, A.A., et al., Artificial reporter gene providing MRI contrast based on proton exchange. Nat Biotechnol, 2007. 25(2): p. 217-9.
87. Delbeke, D., Oncological applications of FDG PET imaging. J Nucl Med, 1999. 40(10): p. 1706-15.
88. Gambhir, S.S., et al., A tabulated summary of the FDG PET literature. J Nucl Med, 2001. 42(5 Suppl): p. 1S-93S.
89. Beyer, T., et al., A combined PET/CT scanner for clinical oncology. J Nucl Med, 2000. 41(8): p. 1369-79.
90. Serganova, I. and R. Blasberg, Reporter gene imaging: potential impact on therapy. Nucl Med Biol, 2005. 32(7): p. 763-80.
91. Tjuvajev, J.G., et al., Imaging the expression of transfected genes in vivo. Cancer Res, 1995. 55(24): p. 6126-32.
92. Gambhir, S.S., et al., Imaging adenoviral-directed reporter gene expression in living nimals with positron emission tomography. Proc Natl Acad Sci U S A, 1999. 96(5): p. 2333-8.

93. Jacobs, A., et al., Positron emission tomography-based imaging of transgene expression mediated by replication-conditional, oncolytic herpes simplex virus type 1 mutant vectors in vivo. Cancer Res, 2001. 61(7): p. 2983-95.
94. Bennett, J.J., et al., Positron emission tomography imaging for herpes virus infection: Implications for oncolytic viral treatments of cancer. Nat Med, 2001. 7(7): p. 859-63.
95. Tseng, J.C., et al., Tumor-specific in vivo transfection with HSV-1 thymidine kinase gene using a Sindbis viral vector as a basis for prodrug ganciclovir activation and PET. J Nucl Med, 2006. 47(7): p. 1136-43.
96. Brader, P., et al., Imaging of lymph node micrometastases using an oncolytic herpes virus and [F]FEAU PET. PLoS One, 2009. 4(3): p. e4789.
97. Brader, P., et al., Imaging a Genetically Engineered Oncolytic Vaccinia Virus (GLV-1h99) Using a Human Norepinephrine Transporter Reporter Gene. Clin Cancer Res, 2009. 15(11): p. 3791-801.
98. Chen, N., et al., A novel recombinant vaccinia virus expressing the human norepinephrine transporter retains oncolytic potential and facilitates deep-tissue imaging. Mol Med, 2009. 15(5-6): p. 144-51.
99. Jung, H., The sodium/substrate symporter family: structural and functional features. FEBS Lett, 2002. 529(1): p. 73-7.
100. Carrasco, N., Iodide transport in the thyroid gland. Biochim Biophys Acta, 1993. 1154(1): p. 65-82.
101. Dingli, D., et al., Image-guided radiovirotherapy for multiple myeloma using a recombinant measles virus expressing the thyroidal sodium iodide symporter. Blood, 2004. 103(5): p. 1641-6.
102. Goel, A., et al., Radioiodide imaging and radiovirotherapy of multiple myeloma using VSV(Delta51)-NIS, an attenuated vesicular stomatitis virus encoding the sodium iodide symporter gene. Blood, 2007. 110(7): p. 2342-50.
103. Hakkarainen, T., et al., Targeted radiotherapy for prostate cancer with an oncolytic adenovirus coding for human sodium iodide symporter. Clin Cancer Res, 2009. 15(17): p. 5396-403.
104. Haddad, D., et al., Insertion of the human sodium iodide symporter to facilitate deep tissue imaging does not alter oncolytic or replication capability of a novel vaccinia virus. J Transl Med, 2011. 9: p. 36.
105. Touchefeu, Y., P. Franken, and K.J. Harrington, Radiovirotherapy: principles and prospects in oncology. Curr Pharm Des, 2012. 18(22): p. 3313-20.
106. Reddi, H.V., et al., Preclinical efficacy of the oncolytic measles virus expressing the sodium iodide symporter in iodine non-avid anaplastic thyroid cancer: a novel therapeutic agent allowing noninvasive imaging and radioiodine therapy. Cancer Gene Ther, 2012. 19(9): p. 659-65.

107. Opyrchal, M., et al., Effective radiovirotherapy for malignant gliomas by using oncolytic measles virus strains encoding the sodium iodide symporter (MV-NIS). Hum Gene Ther, 2012. 23(4): p. 419-27.
108. Haddad, D., et al., A vaccinia virus encoding the human sodium iodide symporter facilitates long-term image monitoring of virotherapy and targeted radiotherapy of pancreatic cancer. J Nucl Med, 2012. 53(12): p. 1933-42.
109. Ray, P., R. Tsien, and S.S. Gambhir, Construction and validation of improved triple fusion reporter gene vectors for molecular imaging of living subjects. Cancer Res, 2007. 67(7): p. 3085-93.
110. Servais, E.L., et al., Animal models and molecular imaging tools to investigate lymph node metastases. J Mol Med (Berl), 2011. 89(8): p. 753-69.
111. Fong, S.M., et al., Fluorescence-expressing viruses allow rapid identification and separation of rare tumor cells in spiked samples of human whole blood. Surgery, 2009. 146(3): p. 498-505.

3.6 Biomarkers in cancer diagnosis

Biomarkers are specific molecules whose appearance can indicate a regular or pathological process in the human body. The literature distinguishes between diagnostic and therapeutic biomarkers. Diagnostic ones serve as risk indicators predicting the presence or occurance of a disease. In contrast, the indication of a successful treatment can be displayed using therapeutic biomarkers. A simple example of a common biomarker test is the measurement of blood sugar level indicating diabetes. Biomarkers are utilized in approximately every discipline of modern medicine and are extensively used in oncology.

In addition to the previously described imaging methods, biomarker tests belong to the main methods to predict cancer as early as possible. These tests are mostly based on proteins, surface molecules or hormones which can be allocated to the group of tumor markers. These markers are either secreted by cancer cells themselves or by cancer-associated cells like immune cells. Their detection in blood, urine or body tissue leads to further investigations. The increase of biomarker levels in blood are giving a hint to cancer occurrence, but false positive results are common and have to be excluded by utilizing additional diagnostic methods [39]. A widely used tumor marker is prostate-specific antigen (PSA). This glycoprotein enzyme is secreted by epithelial cells of the prostate gland and is present in small amounts in blood of healthy men. An elevated PSA level can give a clue to pathological abnormalities of the prostate [40]. On the other hand, the elevated level of PSA is not a proof of prostate cancer. Likewise many cases of prostate cancer do not exhibit an elevated level of PSA [41]. Hence PSE, comparable to every other tumor marker, acts as a guiding principle but never as a final evidence.

Optimization of existing and development of new biomarker tests are therefore a major focus of state-of-the-art cancer research.

3.7 References

1. Robert Koch-Institut und die Gesellschaft der epidemiologischen Krebsregister in Deutschland e.V., R., *Krebs in Deutschland 2005/2006.* Häufigkeiten und Trends, 2012. 8. Ausgabe.
2. Hanahan, D. and R.A. Weinberg, *The hallmarks of cancer.* Cell, 2000. 100(1): p. 57-70.
3. Robbins, S.L., V. Kumar, and R.S. Cotran, *Robbins and Cotran pathologic basis of disease*. 8th ed. 2010, Philadelphia, PA: Saunders/Elsevier. xiv, 1450 p.
4. Boveri, T., *Concerning the origin of malignant tumours by Theodor Boveri. Translated and annotated by Henry Harris.* J Cell Sci, 2008. 121 Suppl 1: p. 1-84.
5. Boveri, T., *Zur frage der entstehung maligner tumoren*. 1914, Jena,: G. Fischer. 2 p.l., 64 p.
6. Duesberg, P., R. Stindl, and R. Hehlmann, *Explaining the high mutation rates of cancer cells to drug and multidrug resistance by chromosome reassortments that are catalyzed by aneuploidy.* Proc Natl Acad Sci U S A, 2000. 97(26): p. 14295-300.
7. Kops, G.J., B.A. Weaver, and D.W. Cleveland, *On the road to cancer: aneuploidy and the mitotic checkpoint.* Nat Rev Cancer, 2005. 5(10): p. 773-85.
8. Rajagopalan, H. and C. Lengauer, *Aneuploidy and cancer.* Nature, 2004. 432(7015): p. 338-41.
9. Hanahan, D. and R.A. Weinberg, *Hallmarks of cancer: the next generation.* Cell, 2011. 144(5): p. 646-74.
10. Schmitt, C.A., et al., *Dissecting p53 tumor suppressor functions in vivo.* Cancer Cell, 2002. 1(3): p. 289-98.
11. Croce, C.M., *Oncogenes and cancer.* N Engl J Med, 2008. 358(5): p. 502-11.
12. Knudson, A.G., Jr., *Mutation and cancer: statistical study of retinoblastoma.* Proc Natl Acad Sci U S A, 1971. 68(4): p. 820-3.
13. Tucker, T. and J.M. Friedman, *Pathogenesis of hereditary tumors: beyond the "two-hit" hypothesis.* Clin Genet, 2002. 62(5): p. 345-57.
14. Friedenson, B., *The BRCA1/2 pathway prevents hematologic cancers in addition to breast and ovarian cancers.* BMC Cancer, 2007. 7: p. 152.
15. Roukos, D.H., *Genome-wide association studies: how predictable is a person's cancer risk?* Expert Rev Anticancer Ther, 2009. 9(4): p. 389-92.
16. Muller, D., et al., *BRCA1 testing in breast and/or ovarian cancer families from northeastern France identifies two common mutations with a founder effect.* Fam Cancer, 2004. 3(1): p. 15-20.

17. Sasco, A.J., M.B. Secretan, and K. Straif, *Tobacco smoking and cancer: a brief review of recent epidemiological evidence.* Lung Cancer, 2004. 45 Suppl 2: p. S3-9.
18. Su, L.J. and L. Arab, *Alcohol consumption and risk of colon cancer: evidence from the national health and nutrition examination survey I epidemiologic follow-up study.* Nutr Cancer, 2004. 50(2): p. 111-9.
19. Anand, P., et al., *Cancer is a preventable disease that requires major lifestyle changes.* Pharm Res, 2008. 25(9): p. 2097-116.
20. Kushi, L.H., et al., *American Cancer Society Guidelines on Nutrition and Physical Activity for cancer prevention: reducing the risk of cancer with healthy food choices and physical activity.* CA Cancer J Clin, 2006. 56(5): p. 254-81; quiz 313-4.
21. Shore, R.E., *Radiation-induced skin cancer in humans.* Med Pediatr Oncol, 2001. 36(5): p. 549-54.
22. *The 2007 Recommendations of the International Commission on Radiological Protection. ICRP publication 103.* Ann ICRP, 2007. 37(2-4): p. 1-332.
23. Smith-Bindman, R., et al., *Radiation dose associated with common computed tomography examinations and the associated lifetime attributable risk of cancer.* Arch Intern Med, 2009. 169(22): p. 2078-86.
24. Parkin, D.M., *The global health burden of infection-associated cancers in the year 2002.* Int J Cancer, 2006. 118(12): p. 3030-44.
25. Widschwendter, M., et al., *Epigenetic stem cell signature in cancer.* Nat Genet, 2007. 39(2): p. 157-8.
26. Vajdic, C.M. and M.T. van Leeuwen, *Cancer incidence and risk factors after solid organ transplantation.* Int J Cancer, 2009. 125(8): p. 1747-54.
27. Clayton, T.A., et al., *Pharmaco-metabonomic phenotyping and personalized drug treatment.* Nature, 2006. 440(7087): p. 1073-7.
28. Sleeman, J. and P.S. Steeg, *Cancer metastasis as a therapeutic target.* Eur J Cancer, 2010. 46(7): p. 1177-80.
29. Fass, L., *Imaging and cancer: a review.* Mol Oncol, 2008. 2(2): p. 115-52.
30. Scott-Conner, C.E. and D.W. Christie, *Cancer staging using the American Joint Committee on Cancer TNM System.* J Am Coll Surg, 1995. 181(2): p. 182-8.
31. Kufe, D.W., et al., *Cancer medicine 6*. 6th ed. 2003, Hamilton, Ont. ; Lewiston, NY: BC Decker.
32. Hall, E.J. and A.J. Giaccia, *Radiobiology for the radiologist*. 6th ed. 2006, Philadelphia: Lippincott Williams & Wilkins. ix, 546 p.
33. Bucci, M.K., A. Bevan, and M. Roach, 3rd, *Advances in radiation therapy: conventional to 3D, to IMRT, to 4D, and beyond.* CA Cancer J Clin, 2005. 55(2): p. 117-34.

34. Willett, C.G., et al., *Direct evidence that the VEGF-specific antibody bevacizumab has antivascular effects in human rectal cancer.* Nat Med, 2004. 10(2): p. 145-7.
35. Burger, R.A., et al., *Incorporation of bevacizumab in the primary treatment of ovarian cancer.* N Engl J Med, 2011. 365(26): p. 2473-83.
36. Zhang, Q., et al., *Eradication of solid human breast tumors in nude mice with an intravenously injected light-emitting oncolytic vaccinia virus.* Cancer Res, 2007. 67(20): p. 10038-46.
37. Kelly, K.J., et al., *Real-time intraoperative detection of melanoma lymph node metastases using recombinant vaccinia virus GLV-1h68 in an immunocompetent animal model.* Int J Cancer, 2009. 124(4): p. 911-8.
38. Olivier, P., et al., *Guidelines for radioiodinated MIBG scintigraphy in children.* Eur J Nucl Med Mol Imaging, 2003. 30(5): p. B45-50.
39. Krishnan, S.T., Z. Philipose, and G. Rayman, *Lesson of the week: Hypothyroidism mimicking intra-abdominal malignancy.* BMJ, 2002. 325(7370): p. 946-7.
40. Catalona, W.J., et al., *Comparison of digital rectal examination and serum prostate specific antigen in the early detection of prostate cancer: results of a multicenter clinical trial of 6,630 men.* J Urol, 1994. 151(5): p. 1283-90.
41. Kilpelainen, T.P., et al., *False-positive screening results in the Finnish prostate cancer screening trial.* Br J Cancer, 2010. 102(3): p. 469-74.

4. Goals of this thesis

Oncolytic virotherapy shows great potential in revolutionizing cancer treatment. Preclinical and clinical studies proof the oncolytic efficiency particularly with regard to engineered vaccinia viruses.

The goal of this work was to demonstrate the oncolytic effect of vaccinia virus strain GLV-1h68 on the basis of a diagnostic assay to support clinical studies involving GLV-1h68. Furthermore, innovative imaging methods should be investigated in connection with oncolytic vaccinia viruses and therapy concepts should be improved.

For this purpose, the following starting points were applied and investigated:

1) Development and establishment of a biomarker test to demonstrate the therapeutic efficiency of recombinant vaccinia viruses

2) Elaboration and validation of innovative imaging strategies to visualize malignancies parallel to GLV-1h68 treatment

3) Optimization of the oncolytic potential by combining GLV-1h68 with enzyme-activated prodrugs

4) Investigation of additional potential starting points to optimize the diagnostic and therapeutic outcome of oncolytic virotherapy

5. Results

5.1 Beta-glucuronidase as a pharmacokinetic biomarker for oncolytic virotherapy

Bacterial glucuronidase as general marker for oncolytic virotherapy or other biological therapies

Hess M, Stritzker J, Härtl B, Sturm JB, Gentschev I, Szalay AA
J Transl Med. 2011;9:172

The above established glucuronidase-based biomarker assay served as a supportive tool in the following publications:

Vaccinia virus mediated melanin production allows MR and optoacoustic deep tissue imaging and laser induced thermotherapy of cancer

Stritzker J, Kirscher L, Scadeng M, Deliolanis NC, Morscher S, Symvoulidis P, Schaefer K, Zhang Q, Buckel L, Hess M, Donat U, Bradley WG, Ntziachristos V, Szalay AA
Proc Natl Acad Sci U S A. 2013

Virotherapy of canine tumors with oncolytic Vaccinia virus GLV-1h109 expressing an anti-VEGF single-chain antibody

Patil SS, Gentschev I, Adelfinger M, Donat U, Hess M, Weibel S, Nolte I, Frentzen A, Szalay AA
PLoS One. 2012;7:e4747

"Dissertation Based on Several Published Manuscripts"

Statement of individual author contributions.

Publication (complete reference): **Hess M**, Stritzker J, Härtl B, Sturm JB, Gentschev I, Szalay AA. Bacterial glucuronidase as general marker for oncolytic virotherapy or other biological therapies. *J Transl Med*. 2011;9:172
Authors' contributions
MH and JS conceived the study, designed, performed and analyzed all experiments and wrote the manuscript. JBS and BH participated in live animal studies. IG participated in manuscript writing. AAS participated in conceiving the study and writing the manuscript. All authors read and approved the final version of the manuscript.

Jochen Stritzker	
Barbara Härtl	
Julia B. Sturm	
Ivaylo Gentschev	
Aladar A. Szalay	

JOURNAL OF TRANSLATIONAL MEDICINE

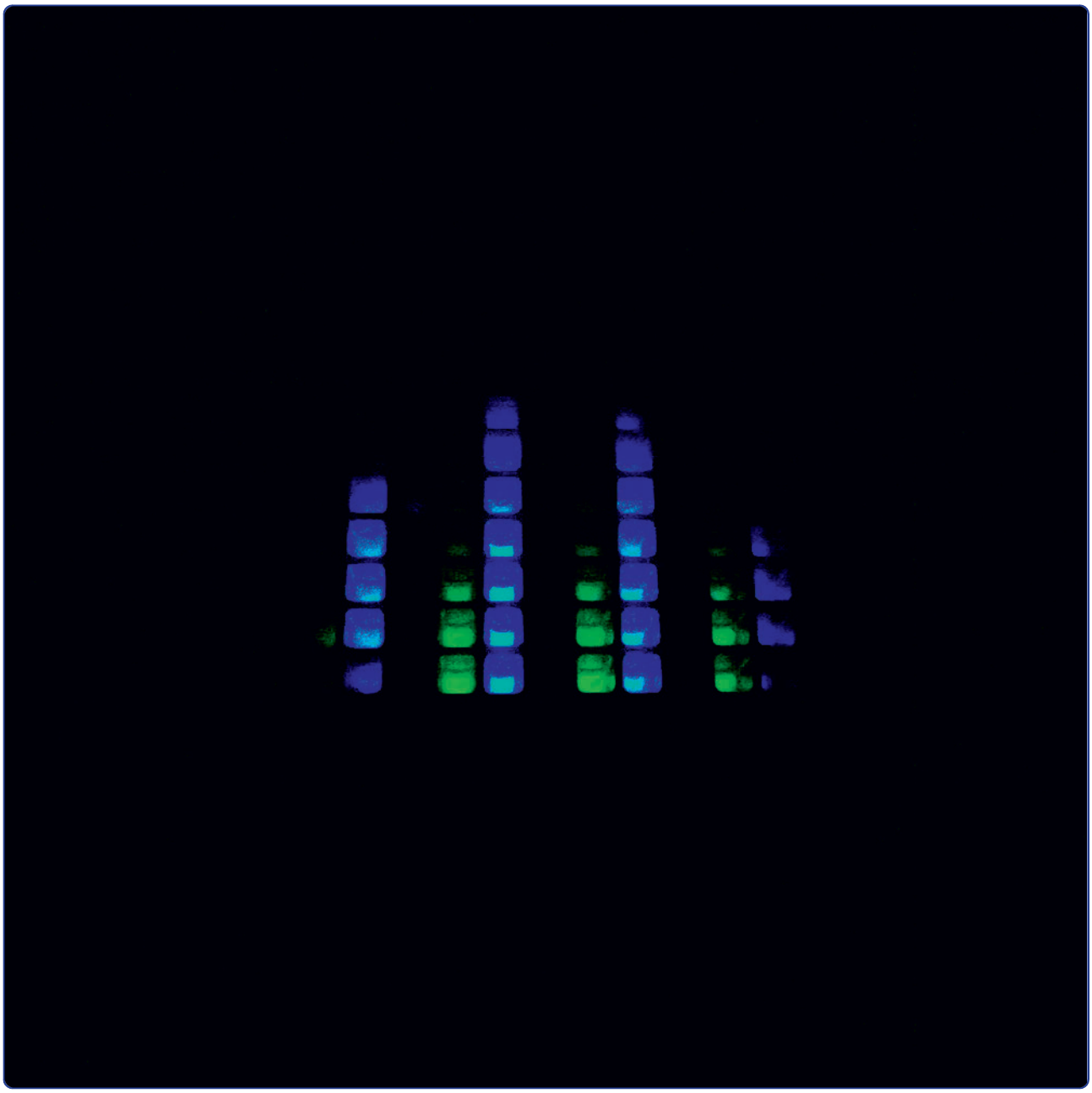

Bacterial glucuronidase as general marker for oncolytic virotherapy or other biological therapies

Hess *et al.*

BioMed Central

Hess *et al. Journal of Translational Medicine* 2011, **9**:172
http://www.translational-medicine.com/content/9/1/172 (11 October 2011)

Hess et al. Journal of Translational Medicine 2011, 9:172
http://www.translational-medicine.com/content/9/1/172

JOURNAL OF TRANSLATIONAL MEDICINE

RESEARCH Open Access

Bacterial glucuronidase as general marker for oncolytic virotherapy or other biological therapies

Michael Hess[1†], Jochen Stritzker[1,2,3†], Barbara Härtl[1,2], Julia B Sturm[1], Ivaylo Gentschev[1,3] and Aladar A Szalay[1,3,4*]

Abstract

Background: Oncolytic viral tumor therapy is an emerging field in the fight against cancer with rising numbers of clinical trials and the first clinically approved product (Adenovirus for the treatment of Head and Neck Cancer in China) in this field. Yet, until recently no general (bio)marker or reporter gene was described that could be used to evaluate successful tumor colonization and/or transgene expression in other biological therapies.

Methods: Here, a bacterial glucuronidase (GusA) encoded by biological therapeutics (e.g. oncolytic viruses) was used as reporter system.

Results: Using fluorogenic probes that were specifically activated by glucuronidase we could show 1) preferential activation in tumors, 2) renal excretion of the activated fluorescent compounds and 3) reproducible detection of GusA in the serum of oncolytic vaccinia virus treated, tumor bearing mice in several tumor models. Time course studies revealed that reliable differentiation between tumor bearing and healthy mice can be done as early as 9 days post injection of the virus. Regarding the sensitivity of the newly developed assay system, we could show that a single infected tumor cell could be reliably detected in this assay.

Conclusion: GusA therefore has the potential to be used as a general marker in the preclinical and clinical evaluation of (novel) biological therapies as well as being useful for the detection of rare cells such as circulating tumor cells.

Keywords: beta-glucuronidase, oncolytic virus, cancer, reporter, fluorescent probe

Background

The regained interest in oncolytic viruses over the past several years led to an enormous leap in the field with more and more oncolytic viruses to be described and yet to come. Not only were those viruses genetically altered to attenuate their virulence, to improve their safety profile and enhance their tumor specificity, but they also were equipped with additional genes for e.g. cytotoxins, cytokines, prodrug converting enzymes and reporter genes that improved the overall performance of these viruses [1,2]. Among those, vaccinia virus is one of the most promising candidates and has several advantages: Since this large DNA virus encodes e.g. its own DNA polymerase it is able to replicate in the cytoplasm of infected host cells thereby minimizing the risk of DNA integration into the host genome. Moreover, vaccinia virus displays a broad host cell range, rapid spread and a high capacity (up to 25 kbp) for genetic payload of foreign DNA [3]. Of note and importance regarding the safety of vaccinia virus, is also its billion-fold use in humans during the eradication program of smallpox, as well as the fact that vaccinia virus is not a human pathogen. On top of that, recombinant vaccinia virus strains (rVACVs) specifically colonize solid tumors in mice while not infecting other organs [4-7]. Therefore, its use in human patients was pursued and first human trials have already been carried out successfully [8-11].

A reliable monitoring of successful tumor colonization in humans would have an enormous impact not only on clinical trials, but also to predict possible outcomes of oncolytic virus therapy. In this aspect, we and others used different kind of reporter genes for optical (e.g. [5]), or radiological (e.g. [12-15]) imaging modalities. This enabled visualization of virus replication within live

* Correspondence: aaszalay@genelux.com
† Contributed equally
[1]Department of Biochemistry, Biocenter, University of Würzburg, Würzburg, Germany
Full list of author information is available at the end of the article

animal models. However, as optical imaging has strong limitations in penetration depth and radiological imaging is time consuming and requires the need of specialized personnel and expensive equipment, a cheap and simple method with short turn-around-times is urgently needed. In particular, if this method could also be used in other biological therapy approaches.

Beta-glucuronidases catalyze the hydrolysis of ß-D-glucuronides into the corresponding D-glucuronate and alcohol. While the mammalian enzymes with a pH-optimum under acidic conditions (pH 4 to 5) have strongly reduced capacity at normal (neutral) tissue pH, the *E. coli* enzyme encoded by *gusA* works optimal in the range of pH 6.8 to 7.7 [16].

Its first use as a (fusion-)reporter gene was described by Jefferson et al. [17,18] and was extensively used in plant physiology studies. In mammals, bacterial glucuronidase was mainly used in prodrug studies, due to the very low abundance of human glucuronidase in human serum [19]. Several strategies were successfully employed: e.g. fusion of cancer specific antibody-fragments with beta-glucuronidase [20] or tumor selective expression of the enzyme using bacteria [21] or adenoviruses [22,23]. The reporter gene properties of the enzyme were not studied as extensively in animals. However, two independent approaches were published that looked at the potential of using beta-glucuronidase as a target structure for radiotracers in positron-emission-tomography [24,25]. In another study, a membrane-anchored form of a mouse-glucuronidase was used in combination with the fluorescein di-beta-D-glucuronide (FDGlcU) which was hydrolyzed to a fluorescent reporter that could be used to assess the location and persistence of gene expression in vivo [26].

Here, we show that beta-glucuronidase in combination with fluorogenic substrates cannot only be used for localization of enzyme expression, but also as a general biomarker for foreign protein expression in serum samples. Consequently, the described test-system could be applied to all kinds of biological therapies which depend on heterologous gene expression.

Materials and methods

For evaluation of the described glucuronidase assay it was necessary to confirm the heterologous gene expression of the described vaccinia virus strain by Western blot analysis as well as immuno-staining studies in cell culture and infected tumor sections. The assay itself (described in the "Fluorogenic probes and detection of fluorescence products" section) was tested with purified enzyme as well as with samples from vaccinia virus injected animals.

Cell culture

Human A549 lung cancer cells (ATCC No. CCL-185) were cultured in RPMI-1640 medium containing 10% fetal bovine serum (FBS) and 1% antibiotic-antimycotic solution (PAA Laboratories, Cölbe, Germany) under standard cell culture conditions (37°C, 5% CO_2). MTH52c is derived from a malignant small-cell canine carcinoma of the mammary gland [27] and cultured in DMEM supplemented with antibiotic-antimycotic solution and 20% FBS.

Vaccinia viruses

The attenuated vaccinia virus strain GLV-1h68 was purified as previously described [4]. For generation of control viruses, *lacZ* and *gusA* of GLV-1h68 were replaced by nonrelevant gene constructs to create viruses negative for beta-galactosidase (rVACV-LacZ$^-$) and beta-glucuronidase (rVACV-GusA$^-$) respectively (Additional File 1, Figure S1).

Infection of cell cultures

Two days before infection, cells were seeded in 6-well plates for western blot analysis or 12-well plates containing sterile cover slips for microscopy studies. 90% confluent cell layers were either mock treated or infected with GLV-1h68, rVACV-LacZ$^-$ or rVACV-GusA$^-$ at a multiplicity of infection (MOI) of 0.1 for 1 h at 37°C and 5% CO_2 in medium containing 2% FBS. Afterwards the infection medium was aspirated and replaced by standard cell culture medium.

Western blot analysis

For detection of proteins, infected cells were harvested and lysed in SDS sample buffer at 6, 12, 24 and 48 hours post-infection (hpi). Lysates were separated by 10% SDS-Polyacrylamide gel electrophoresis and subsequently transferred onto a nitrocellulose membrane (Whatman GmbH, Dassel, Germany). After blocking in 5% skim milk in PBS, the membrane was incubated with anti-beta-glucuronidase rabbit polyclonal antibody (G5420, Sigma-Aldrich, Schnelldorf, Germany), anti-beta-galactosidase rabbit polyclonal antibody (A-11132, Molecular Probes, Leiden, Netherlands), anti-GFP rabbit polyclonal antibody (sc-8334, Santa Cruz, Heidelberg, Germany) or anti-beta-actin mouse monoclonal antibody (ab6276, Abcam, Cambridge, UK). The first antibodies were detected using horseradish peroxidase-conjugated anti-mouse (ab6728, Abcam, Cambridge, UK) or anti-rabbit (ab6721, Abcam, Cambridge, UK) secondary antibodies, followed by enhanced chemiluminescence detection.

X-Gal/X-GlcU staining and microscopy studies

For the analysis of expression and activity of beta-galactosidase and beta-glucuronidase respectively, A549 cells were seeded on coverslips and infected with 200 PFU GLV-1h68, rVACV-LacZ$^-$ or rVACV-GusA$^-$ per well.

After incubation for 2 days, cells were fixed using 4% paraformaldehyde and washed twice in PBS. Staining solutions consisted of 40 µl X-Gal (5-bromo-4-chloro-3-indolyl-β-D-galactoside, Invitrogen, Karlsruhe, Germany) and X-GlcU (5-bromo-4-chloro-3-indolyl-β-D-glucuronide, Invitrogen, Karlsruhe, Germany) respectively in dimethylformamide (40 mg ml^{-1}), ferricyanide (12 mM $K_3Fe(CN)_6$), 5.2 mM $MgCl_2$ and ferrocyanide solution (12 mM $K_4Fe(CN)_6$). Coverslips were stained with either X-Gal or X-GlcU solution and incubated for 24 h at 37° C before mounting in Mowiol. Images were taken with a Zeiss Axiovert 200 M microscope.

Histology and immunofluorescence

For histological analysis, snap-frozen tumors were fixed in 4% paraformaldehyde/PBS overnight at 4°C. Samples were embedded in 5% (w/v) low-melt agarose (Appli-Chem, Darmstadt, Germany) und 100 µm sections were cut using a Leica VT1000S Vibratome (Leica, Heerbrugg, Switzerland) as described before [28]. After permeabilizing in 0.3% Triton X-100/PBS, sections were incubated with Hoechst 33342, anti-beta-glucuronidase rabbit polyclonal antibody (G5420, Sigma-Aldrich, Schnelldorf, Germany) and anti-beta-galactosidase chicken polyclonal antibody (ab9361, Abcam, Cambridge, UK) before staining with Cy-5-conjugated donky anti-rabbit and Cy-3 conjugated donky anti-chicken secondary antibodies (Jackson ImmunoResearch, West Grove, PA). Mowiol-embedded sections were examined using a Leica MZ 16 FA Stereo-Fluorescence Microscope equipped with a Leica DC500 Digital Camera. Digital Images were processed with Photoshop 7.0 (Adobe Systems, San Jose, CA) and merged to yield pseudocolored pictures.

Animal studies

A549 and MTH52c xenograft tumors were developed in 6- to 8-week-old nude mice (NCI:Hsd:Athymic Nude *Foxn1*^{nu}, Harlan Borchem, Germany) by implanting 5 × 10^6 cells subcutaneously in the right abdominal flank. Two to three weeks after implantation, mice were anesthetized with isoflurane and injected with a viral dose of 5 × 10^6 PFU GLV-1h68, rVACV-LacZ$^-$ or rVACV-GusA$^-$ in 100 µl PBS via the retro-orbital sinus vein.

Blood and urine collection of mice was carried out under anesthesia by a heparinised capillary pipet (No. 554/20, Assistent, Sondheim, Germany) via the retro-orbital sinus vein for blood and a bladder catheter (No. 381312, Becton Dickinson, Heidelberg, Germany) for urine respectively.

All animal experiments were carried out in accordance with protocols approved by the Regierung von Unterfranken (Würzburg, Germany) (protocol number AZ 55.2-2531.01-17/08) and/or the the Institutional Animal Care and Use Committee (IACUC) of Explora BIOLABS, located in San Diego Science Center (San Diego, USA) (protocol number: EB08-003).

Fluorogenic probes and detection of fluorescence products

The lyophilized fluorogenic probes FDGlcU, FDG and 4-Methylumbelliferyl-b-D-glucuronide (4-MUG) (Invitrogen, Karlsruhe, Germany) were dissolved in DMSO (36.5 mM). For in-vivo studies, 5 µl of each stock dilution was mixed with 195 µl PBS and injected intraperitoneally. Whole body and urine fluorescence analysis was performed using a Maestro EX imaging system (CRI, Woburn, MA). For serum analysis, the collected mouse serum was diluted 1:15 with PBS and 80 µl of each sample were mixed with of either 2.5 µg FDGlcU or 1.5 µg 4-MUG if not otherwise indicated. Human serum of healthy individuals (Zen-Bio Inc, Research Triangle, NC) was obtained from whole blood and 10 µl were used in the described assay. After incubation for 1 h at 37°C (if not otherwise indicated), fluorescence was read in Lumox 384-well plates (Sarstedt, Nümbrecht, Germany) using an Infinite 200 Pro Microplate Reader (Tecan, Crailsheim, Germany) or a Spectra Max M5 (Molecular Devices, Sunnyvale, USA) and fluorescence intensities are listed as relative fluorescence units.

Results

Biological therapies, like e.g. oncolytic virotherapy, are dependend on the expression of genes that are not functionally expressed in the respective patient. We recently described the use the rVACV strain GLV-1h68 in combination with a prodrug seco-analog of duocarmycin SA which is activated by the virus encoded beta-galactosidase [29]. Although very promising results were observed in cell culture, the synergistic effect in tumor bearing mice were less pronounced, which was also true for a bacterial glucuronidase activatable version of the prodrug (Hess et al, unpublished). Among other potential reasons for this observation was a non-favorable pharmacokinetic of the prodrugs. Therefore, we wanted to analyze the activation and pharmacokinetics of other beta-galactosidase or glucuronidase substrates that could actually be visualized by optical imaging.

As fluorescent probes can be directly detected in small animals, the compounds FDG (substrate for the beta-galactosidase LacZ) as well as FDGlcU (a glucuronidase substrate) were injected in tumor bearing mice that had previously been injected with oncolytic rVACV (GLV-1h68) encoding both enzymes. Upon cleavage the probes were converted to fluorescein which resulted in a change of their fluorescent properties that was readily detectable with a small animal fluorescence imaging

system (Figure 1A). Animals that were previously injected with PBS or the control rVACV strains not expressing beta-galatosicase (rVACV-LacZ$^-$) and glucuronidase (rVACV-GusA$^-$) respectively served as controls. It became evident that each fluorogenic probe could indeed be activated in the tumor and that this activation is dependent on the expression of LacZ and GusA respectively (Figure 1A and 1C). The maximum fluorescein fluorescence in the tumor was observed 120 min after intraperitoneal injection (Figure 1B). Upon intravenous FDGlcU-injection the maximum fluorescence was already observed 20 min post injection (Additional File

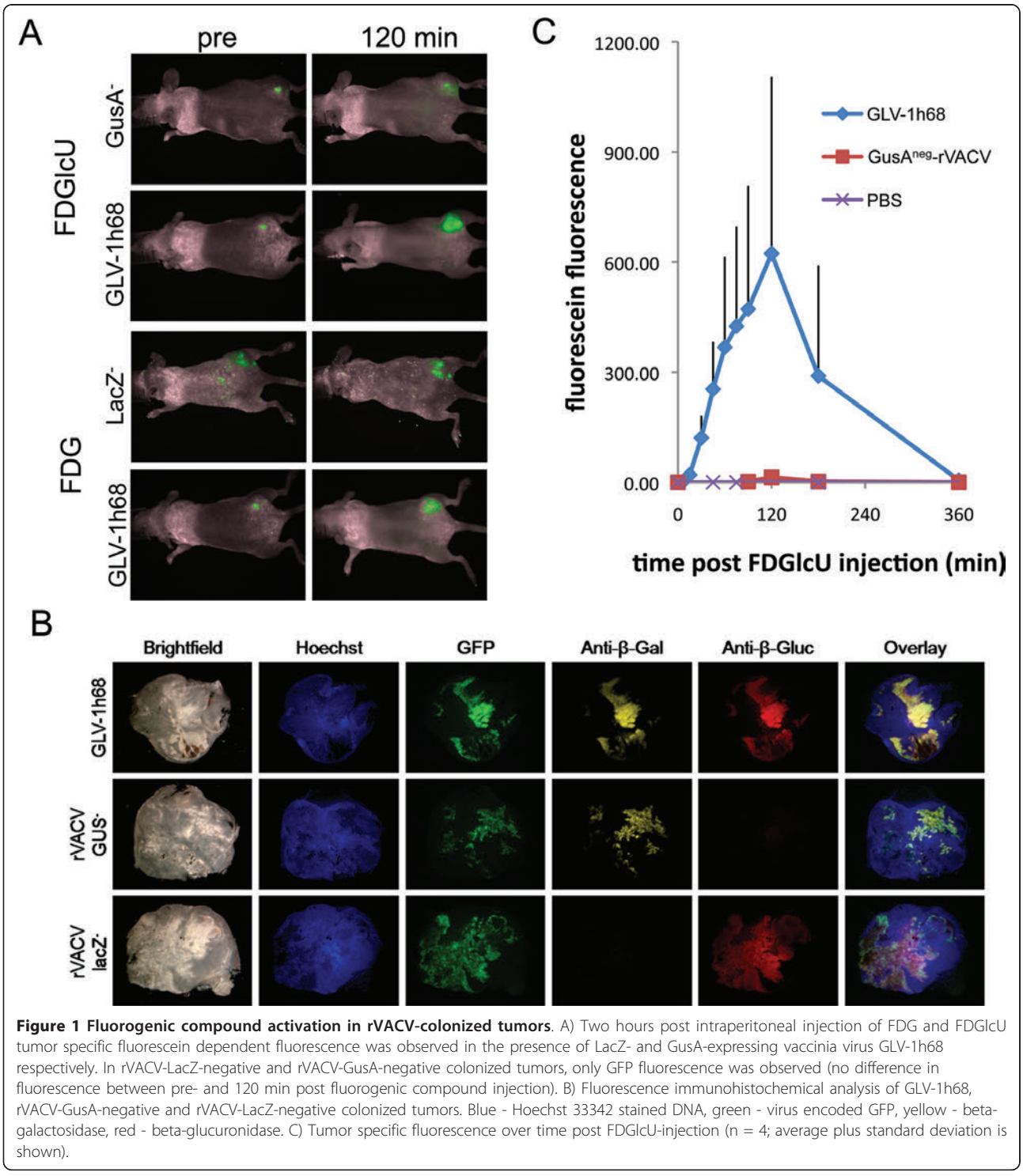

Figure 1 Fluorogenic compound activation in rVACV-colonized tumors. A) Two hours post intraperitoneal injection of FDG and FDGlcU tumor specific fluorescein dependent fluorescence was observed in the presence of LacZ- and GusA-expressing vaccinia virus GLV-1h68 respectively. In rVACV-LacZ-negative and rVACV-GusA-negative colonized tumors, only GFP fluorescence was observed (no difference in fluorescence between pre- and 120 min post fluorogenic compound injection). B) Fluorescence immunohistochemical analysis of GLV-1h68, rVACV-GusA-negative and rVACV-LacZ-negative colonized tumors. Blue - Hoechst 33342 stained DNA, green - virus encoded GFP, yellow - beta-galactosidase, red - beta-glucuronidase. C) Tumor specific fluorescence over time post FDGlcU-injection (n = 4; average plus standard deviation is shown).

2, Fig. S2). About 6 hours post injection (hpi), the GFP-dependent fluorescence remained while most of the compound specific fluorescence was gone (Figure 1A and 1B).

Consequently it was investigated how the produced fluorescein was removed from the tumor. Possible explanations could be fluorescein instability in or compound excretion from the tumor.

In favour of (renal) excretion was the presence of fluorescein in the urine of injected mice. Moreover, when fluorescein itself was injected directly into the tumor the compound accumulated in the bladder and was then secreted with the urine (data not shown) while it disappeared from the tumor.

The presence of the activated probe in the urine of GLV-1h68 injected tumor bearing mice offered the possibility to evaluate this as a possible biomarker for successful tumor colonization. To test this, mice were anesthesized and urine was isolated via a bladder cathether before and 90 minutes after i.p. injection of FDGlcU. Indeed, fluorescein was present in urine of GLV-1h68 treated tumor bearing animals but could not be observed in FDGlcU injected control mice that either had non-colonized or rVACV-GusA$^-$ colonized tumors (Figure 2A, B). Therefore, one could establish a test for the presence of GLV-1h68 in tumors of live mice with a simple urine test after systemic injection of FDGlcU. Nevertheless, we did not proceed to establish a urine based test system as the injection of FDGlcU in human patients seemed unlikely.

Although fluorescein obviously was renally excreted, it was also investigated whether active enzymes that were specifically produced in the tumor tissue leaked out and were then present in the serum of GLV-1h68 injected tumor bearing mice leading to additional (non-tumor specific) cleavage of FDGlcU. To investigate this, the serum of tumor bearing mice which were previously injected with the GusA encoding strain GLV-1h68 was incubated with FDGlcU or 4-MUG. Both substances can be hydrolysed by glucuronidase to the fluorescent products fluorescein and 4-MU respectively. As latter has excitation and emission maxima of 365 nm and 455 nm respectively, it was not suitable for optical *in vivo* imaging and therefore only used in *in vitro* studies. In our experiments, no fluorescence was observed when mice were injected with PBS or GusA-negative control rVACV while the fluorescent compounds clearly were detectable after co-incubation with serum derived from GLV-1h68 injected mice (Figure 3A). The serum therefore contained active (non-secreted, but shed) enzymes that were produced in the tumor tissue.

Theoretically, this does pave the way to a simple blood test that could be used to distinguish tumor bearing from healthy patients and/or to distinguish between successful from unsuccessful tumor colonization of GusA-encoding oncolytic virus strains in cancer bearing patients. To confirm this, we retrospectively tested serum samples (n = 99) from different tumor xenograft models (GI-101A, A549, DU-145, PANC-1, HT-29) that were collected in our lab over about 4 years from mice injected with PBS (n = 33) or treated for different periods of time (7 to 53 days) with several GusA-positive (n = 53) or -negative (n = 13) rVACV (Figure 3B). The test of these probes confirmed a significant ($p < 0.001$) difference between the GusA containing group and those that did not result in GusA-production. As the test was done in retrospect, we could not confirm/exclude successful tumor colonization in those mice which had

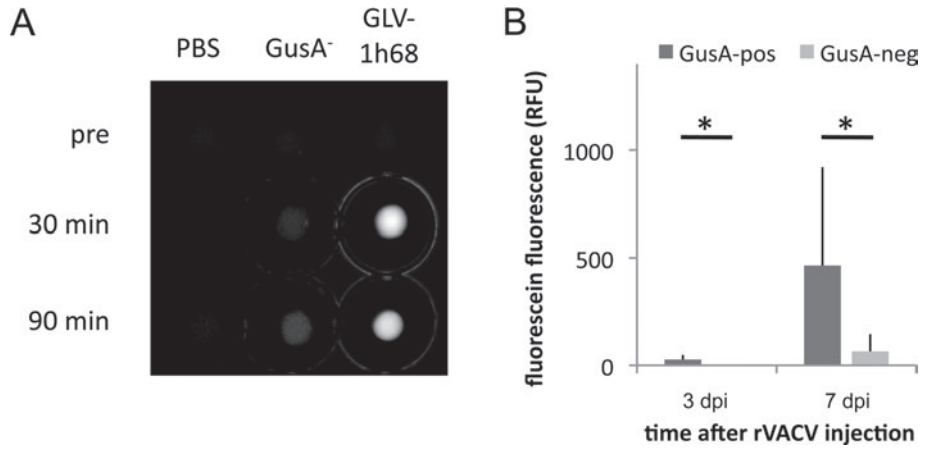

Figure 2 Analysis of urine samples derived from mice before, 30 min and 90 min post FDGlcU injection respectively. A) Five µl urine were analyzed in the Maestro Imaging system. Unmixed fluorescein specific fluorescence is shown. B) Three and seven days post rVACV injection urine was sampled before and 90 min post FDGlcU injection. Average plus standard deviation of fluorescein specific fluorescence of GusA-positive (n = 6 for 3 dpi and n = 8 for 7 dpi) and GusA-negative (n = 4) rVACV colonized tumors. * indicates $p < 0.05$.

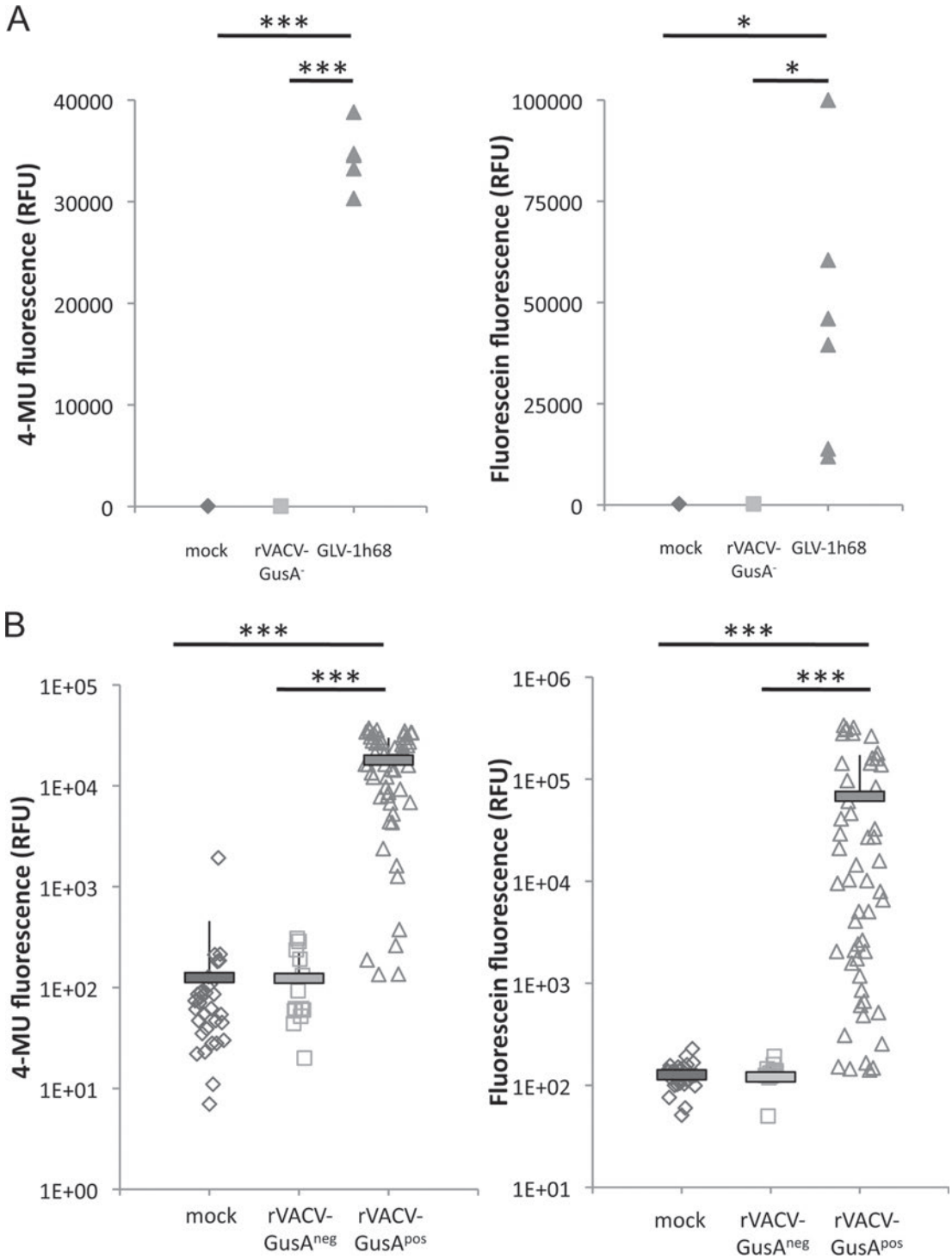

Figure 3 Glucuronidase specific fluorigenic compound activation in serum of tumor bearing mice. A) Tumor bearing mice were mock injected (n = 2) or injected with GLV-1h68 (n = 6) and rVACV-GusA-negative (n = 6) respectively. Seven days later 5 μl serum was co-incubated for 1 h at 37°C with 4-MUG and FDGlcU respectively and subsequently specific fluorescence was determined. B) Retrospective serum analysis. Serum samples (n = 99) from different tumor xenograft models (GI-101A, A549, DU-145, PANC-1, HT-29) were retrospectively tested. Samples were derived from mock (n = 33) injected mice or mice treated for different periods of time (7 to 53 days) with several GusA-positive (n = 53) or -negative (n = 13) rVACV. * indicates $p < 0.03$; *** indicates $p < 0.001$.

GusA-negative results in the blood test. This could explain the negative results for 5 of the GusA-rVACV injected tumor bearing mice.

Next, it was investigated whether one could confidently decide via the blood test if a tumor was colonized or not. Tumor bearing mice (n = 5) were systemically injected with a low dose (1×10^5 PFU) of GLV-1h68. This dose was known to result in colonization of only some tumors while other tumors do not get colonized at all. Serum was then isolated 1, 3, 7, 10 and 14 days later, before mice were sacrificed and tumor colonization was tested by conventional plaque assay confirming the results observed by the FDGlcU/4-MUG based blood test (Figure 4A). The very same 2 out of 5 mice were found to have GLV-1h68 in their tumors as well as being positive in the FDGlcU/4-MUG based blood tests.

In another experiment we tested the suitability of the blood test to differentiate between tumor bearing and control tumor free mice. Unexpectedly, seven days post injection of GLV-1h68 in non-tumor bearing mice low but significant glucuronidase activity was detected in the serum of tumor free mice. Closer examination of those mice revealed GFP expression in the paws of 2 mice (data not shown). Therefore, the mice were sacrificed and a plaque assay of several organs was used to find the origin of glucuronidase production (Table 1). Apart from the two infected paws virus was reproducibly isolated in low concentration from ovaries of non-tumor bearing mice. Interestingly, ovaries of tumor bearing mice were essentially free of virus.

Background expression of glucuronidase in healthy subjects would of course exclude using this test system for detection of tumors if no difference existed that allowed differentiation between cancer patients and healthy individuals. Time course studies in male (n = 12 tumor bearing and 12 tumor free) and female mice (n = 24 tumor bearing and 6 tumor free) over a period of 14-16 days in which blood was taken every other day (in one half of the mice blood was taken on even, in the other on uneven days post virus injection), again showed low levels of glucuronidase present in the serum of tumor free mice. These were similar to those observed in tumor bearing mice until 8 days post virus injection (Figure 4B and Additional File 3, Fig. S3). After that however, significant changes occurred. While the glucuronidase activity in the serum of tumor free mice decreased, the fluorescence signal in the tumor bearing animal probes increased.

Taken together, 9 days after injection of the virus it was possible to decide with confidence whether A) an existing tumor was successfully colonized and/or B) a tumor was present in the *gusA* encoding rVACV injected mouse.

In a next step the sensitivity and performance of the described test was evaluated in *in vitro* studies regarding its clinical translatability. We found a positive correlation between the fluorescence signal intensities and increasing A) glucuronidase concentration, B) substrate (FDGlcU or 4-MUG) concentration and C) incubation time (Additional File 4, Fig. S4). The data also revealed that very low glucuronidase concentrations could be detected using the fluorogenic FDGlcU or 4-MUG substrates which should allow detection of lysed tumor cells not only in mice but also in humans. Feasibility in the presence of human serum was shown by running the assay in the presence or absence of 10 µl human serum (Additional File 5, Fig. S5). The data revealed that neither the sensitivity nor the fluorescence intensity of the assay was changed in the presence of human serum.

As the presence of glucuronidase relies on the production by infected cancer cells, the minimal amount of infected cancer cells was tested that was needed to generate a positive fluorescent signal. For this, A549 cells were infected with GLV-1h68 or control-rVACV. One day later, the amount of infected cells was determined by counting and flow cytometry and the cells were diluted and seeded in half-log dilutions in 384-well plates with concentrations varying from approx. 1.0 to 1000 infected cells/well and co-incubated with 6.3 µg FDGlcU and 3.4 µg 4-MUG respectively. To obtain high sensitivity, the probes were incubated at 37°C over night and analyzed the next day (Figure 5). Surprisingly, even a single infected cancer cell could be readily detected using this test when using 4-MUG as a substrate. This allowed us to calculate the potential sensitivity of the described test for the detection of tumors in human patients using two different approaches: 1) Assuming that more serum (e.g. 50 µl) would be used when testing the system on human patient samples, and an average total blood volume of about 4.7 liters, only approx. 10^5 infected cancer cells would be sufficient to generate a detectable fluorescent signal. 2) The fluorescent signal generated from a single cancer cell was similar to that obtained from 0.2 units glucuronidase. Increasing the sensitivity by adding more fluorescent substrate 0.05 units glucuronidase were easily detectable, corresponding to a concentration of 1 unit glucuronidase/ml serum (again using 50 µl serum/test) or 4700 units/average blood volume of a human patient. Therefore, as low as 2.4×10^4 infected cancer cells would be sufficient for a positive signal.

Discussion

Biological therapies including stem cell therapy, gene therapy, immunotherapy, oncolytic virotherapy etc. are gaining more and more impact in e.g. regenerative medicine, immunology, oncology and treating various

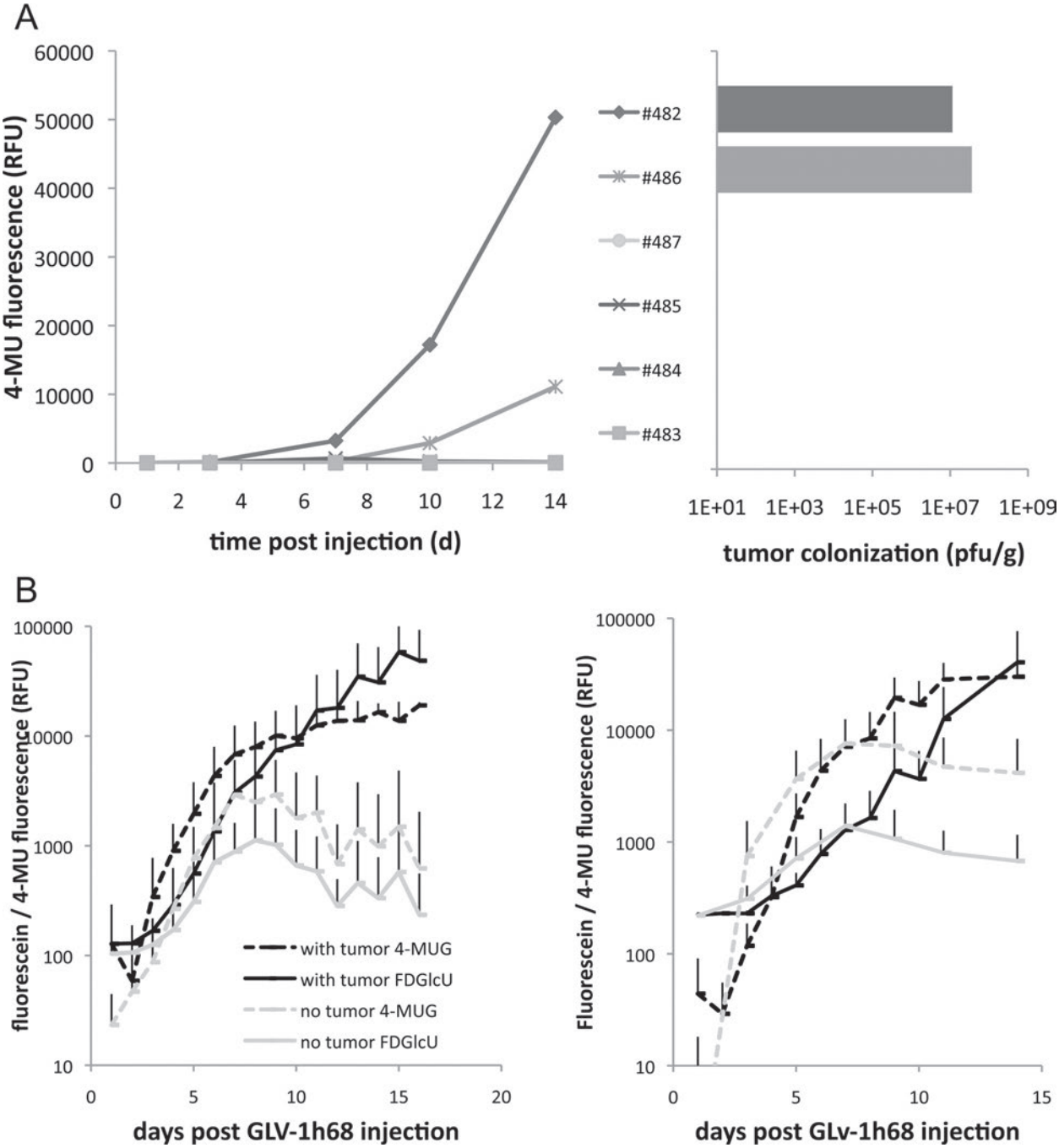

Figure 4 Signal generation is both dependent on presence of tumors and *gusA*-encoding rVACV. A) Confirmation of successful tumor colonization after low-dose injection of 1×10^5 pfu GLV-1h68. In the left panel time dependent 4-MU fluorescence is shown for individual sera of rVACV injected tumor bearing mice. The sera of two mice (#482 and #486) resulted in generation of significant amounts of 4-MU. Viral titer analysis of tumors from the same mice revealed that only those mice (#482 and #486) had virus colonized tumors which also resulted in generation of 4-MU. B) Tumor bearing (black) and non-tumor bearing (grey) control male (left panel) and female (right panel) mice were injected with 5×10^6 pfu GLV-1h68 into the retro-orbital sinus vein. Analysis of sera revealed conversion of the fluorigenic compounds FDGlcU (solid lines) and 4-MUG (broken lines) in all mice. Significant differences ($p < 0.05$) between tumor bearing and control mice was observed after 9 dpi. Results show average plus standard deviation of fluorescein and 4-MU fluorescence.

Table 1 Viral distribution in tumor bearing and non-tumor bearing mice 14 dpi

	pfu/g tissue									fluorescence	
mouse #	tumor	blood	ovaries	spleen	kidneys	liver	lung	brain	paw	4-MU	fluorescein
1	NA	ND	ND	ND	ND	ND	ND	ND	2.10E+06	8599	1179
2	NA	ND	2500	ND	ND	ND	ND	100	ND	4418	607
3	NA	ND	5300	ND	ND	ND	ND	20	ND	6775	855
4	NA	ND	12000	ND	100	ND	ND	ND	5.00E+05	14587	2641
5	NA	ND	8800	ND	ND	100	ND	ND	ND	4325	483
6	NA	ND	ND	ND	ND	0	ND	ND	ND	5272	667
7	2.70E+07	ND	ND	40	ND	ND	20	ND	ND	40812	168977
8	5.15E+07	ND	ND	100	ND	ND	ND	ND	ND	43732	61137
9	2.65E+07	ND	ND	ND	100	ND	ND	ND	ND	43866	43572
10	9.00E+06	ND	20	20	100	ND	80	ND	ND	38449	135454
11	8.50E+06	ND	ND	ND	20	ND	ND	ND	ND	41645	28754

NA - not applicable. ND - not detectable. Detection limit 20 pfu/g.

diseases. All of these require the expression of certain genes that usually are not or only weakly expressed in the targeted tissue. While progress in terms of biological effectiveness is made in each field, no common reporter system exists which is cost-efficient, easy to use in clinical laboratories and at the same time allows short turn-around-times.

In our studies we used oncolytic rVACV strains as a model to investigate the potential of a (bacterial) beta-glucuronidase in combination with fluorogenic probes to be used as a general reporter system in biological therapies. The bacterial glucuronidase was chosen as reporter gene, since the pH in blood (pH of about 7.4) is in the pH-optimum range (pH 6.8 - 7.7) of the bacterial enzyme [16] while mammalian beta-glucuronidases are most active at pH 4 to 5 and present almost exclusively in lysosomes. Moreover, the bacterial enzyme displays much higher specific activity compared to the human beta-glucuronidase [30]. On the other hand, bacterial enzymes usually have much higher immunogenicity than their mammalian counterparts and thus might be hindered in their efficacy [31]. Consequently, the group of S. Roffler selected mutants of human beta-glucuronidase with enhanced activity at neutral pH [30] and fused this protein to single chain humanized antibodies for enhanced antibody-directed enzyme prodrug therapy [32]. Therefore, it should also be possible to use this optimized human beta-glucuronidase in the detection system described herein.

Furthermore, the possibility to direct active beta-glucuronidase into the cytoplasm (this study and many others, e.g. [17]), attach it to the cell surface (e.g. [23,33]), or secrete from producing cells (e.g. [32,34]) offers a number of different potential applications.

Cytoplasm associated beta-glucuronidase seems to be a very attractive marker for oncolytic viruses. Not only does presence of glucuronidase in the serum show successful tumor colonization, but also indicates a therapeutic effect: Active enzyme can only get in the serum when (tumor) cells are lysed. Future studies will show if responding and non-responding tumors can be differentiated using the described test system.

The detection of cell surface associated beta-glucuronidase could be helpful in studies relying on transfection of cells or following bacteria or parasite infections in which blood-borne pathogens express a membrane- or cell-wall-anchored glucuronidase. Also, the previously mentioned (non-membrane passing) prodrug therapies would benefit from detection of beta-glucuronidase in the blood: The enzyme would only be observed upon

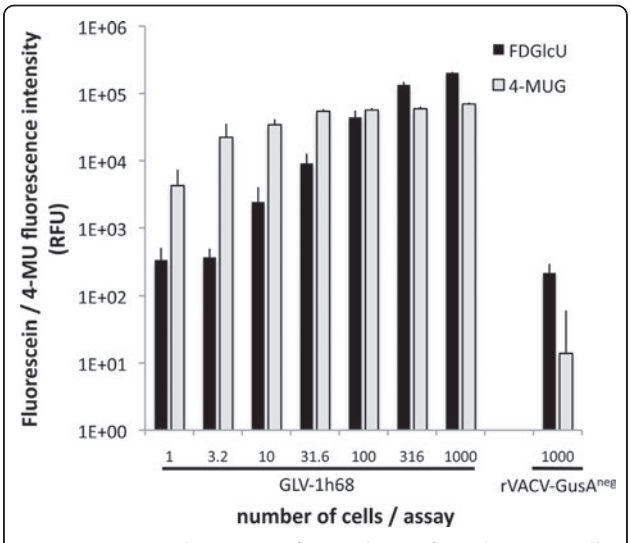

Figure 5 Minimal amount of GLV-1h68 infected cancer cells necessary for positive detection. A549 cells were infected with GLV-1h68 or control-rVACV (rVACV-GusA^{neg}). One day later, the amount of infected cells was determined by flow cytometry and the cells were seeded in half-log dilutions in 384-well plates with concentrations varying from 1.0 to 1000 cells/well and co-incubated with FDGlcU and 4-MUG respectively. Data represent average plus standard deviation (n = 6).

successful prodrug treatment as only then, the active enzyme is released from the tumor.

Secreted beta-glucuronidase could be used as a simple marker for cell survival. Genetically altered cells should secrete active enzyme as long as they are viable. Again, a small number of cells would be sufficient for detection and the amount of beta-glucuronidase in the blood should be correlating with the amount of cells producing the enzyme. Therefore, it will be possible to monitor e.g. stem cell therapies, tissue regeneration etc.

In each case one will have to decide whether the achieved enzyme concentration is sufficient to be detected in the respective assays. Here, we calculated that theoretically only 2.4×10^4 vaccinia virus infected cancer cells might be enough to be detected in humans. With a diameter of 50 μm/cell this would correspond to a volume of only 1.6 mm^3. Of course, it can be argued that in patients this number might be higher, as e.g. not all virus infected cells will release all of their enzymes into the blood stream upon lysis. But even if the number of infected cells is 10 or even 100-fold higher, the tumor diameter would only be 3.1 and 6.7 mm, respectively. Nevertheless, only clinical trials such as those in which GLV-1h68 is currently evaluated for safety in human cancer patients [11], will determine whether the proposed detection system can be translated to a clinical setting.

Presumably, similar evaluations will be necessary when applying the presented beta-glucuronidase test in other applications such as in infectious disease studies, stem cell research/therapy etc. both in basic as well as in translational research.

Conclusions

Taken together, we demonstrated that glucuronidase (in our case encoded by rVACV) in combination with fluorogenic probes has the potential to be used as a general reporter system for heterologous gene expression in biological therapies. Our results provide evidence that the described system cannot only be used for imaging of tumors in the body, but also to confirm viral colonization of these tumors or even the diagnosis of tumors in screening studies.

Additional material

Additional file 1: Figure S1. Viral strains used in this manuscript. A) Schematic virus constructs. The viral F14.5L, thymidine kinase and hemagluttinin encoding genes of the wild type Lister strain were replaced by the indicated marker genes. B) Verification of marker gene expression by Western blot analysis at 6, 12, 24 and 48 hours post A549 cell infection respectively (multiplicity of infection 0.5). Beta-actin served as loading control. C) X-Gal and X-Gluc staining of single viral plaques. GLV-1h68 encodes both beta-galactosidase and beta-glucuronidase, while control strains lack one or the other gene.

Additional file 2: Figure S2. Time dependent conversion of FDGlcU in the same mouse injected with GLV-1h68. A A549 tumor-bearing mouse was injected with GLV-1h68 10 days before FDGlcU injection was performed. Intraperitoneal (i.p.) injection (lower row pictures) occurred 24 hours before intravenous (i.v.) injection (upper row pictures). This allowed the fluorescence signal to decline completely before getting the kinetics in the very same mouse.

Additional file 3: Figure S3. Individual mouse data from Figure 4B. Tumor bearing (red) and non-tumor bearing (grey) control male (upper panels) and female (lower panels) mice were injected with 5×10^6 pfu GLV-1h68. Analysis of sera revealed conversion of the fluorigenic compounds FDGlcU (left panels) and 4-MUG (right) in all mice.

Additional file 4: Figure S4. Positive correlation between the fluorescence signal intensities and increasing glucuronidase concentration, fluorogenic substrate concentration (left panels, 4-MUG in A, FDGlcU in B) and incubation time (right panels).

Additional file 5: Figure S5. Glucuronidase assay results independent from presence of human serum. Increasing amounts of *E. coli* glucuronidase were co-incubated with 4-MUG (upper panel) or FDGlcU (lower panel) in the presence or absence of human serum. Serum samples from 3 different healthy individuals were tested in parallel. **Cover art**. The cover shows the generation of fluorescent products from fluorigenic probes upon cleavage by beta-glucuronidase. From bottom to top decreasing concentrations of beta-glucuronidase were co-incubated with 4-Methylumbelliferyl-b-D-glucuronide, Fluorescein-di-beta-D-glucuronide or without fluorigenic probe in a 384-well plate. The blue compound 4-Methylumbelliferyl and the green Fluorescein were excited using UV-light and photographed without the use of additional emission filters. The very sensitive assay is able to detect picogram amounts of beta-glucuronidase - sufficient for detection of a single beta-glucuronidase expressing cell - as described by Hess et al. in this issue.

List of abbreviations

FBS: fetal bovine serum; FDG: *Fluorescein* di-β-D-galactopyranoside; FDGlcU -fluorescein di-β-D-glucuronide; GFP: Green fluorescent protein; GusA: bacterial glucuronidase; hpi: hours post-infection; LacZ: bacterial beta-galactosidase; MOI: multiplicity of infection; 4-MUG: 4-Methylumbelliferyl-b-D-glucuronide; PFU: plaque forming units; rVACV: recombinant vaccinia virus strain; X-Gal: 5-bromo-4-chloro-3-indolyl-β-D-galactoside; X-GlcU 5-bromo-4-chloro-3-indolyl-β-D-glucuronide.

Acknowledgements

We like to thank Q. Zhang, N. Chen, T. Trevino and J. Aguilar for providing all rVACV, A. Seidensal and J. Langbein for excellent technical assistance. This work was supported by Genelux Corporation (R&D facility in San Diego, CA, USA) and Genelux GmbH, a Service Grant to the University of Würzburg, Germany also funded by Genelux Corp., San Diego, USA as well as a grant of the "Bundesministerium für Bildung und Forschung" in the MoBiTech initiative (grant number 13N4051). JS, BH, IG and AAS are employees and shareholders of Genelux Corporation and Genelux GmbH respectively. MH and JBS are supported by graduate stipends from Genelux Corporation, San Diego.

Author details

[1]Department of Biochemistry, Biocenter, University of Würzburg, Würzburg, Germany. [2]Genelux GmbH, Bernried, Germany. [3]Genelux Corporation, San Diego, CA, USA. [4]Department of Radiation Oncology, Moores Cancer Center, University of California, San Diego, La Jolla, CA, USA.

Authors' contributions

MH and JS conceived the study, designed, performed and analyzed all experiments and wrote the manuscript. JBS and BH participated in live animal studies. IG participated in manuscript writing. AAS participated in conceiving the study and writing the manuscript. All authors read and approved the final version of the manuscript.

Competing interests

The research was supported by the Research and Development Division of Genelux Corp., San Diego, USA, and a Service Grant to the University of

Würzburg, Germany also funded by Genelux Corp., San Diego, USA as well as a grant of the "Bundesministerium für Bildung und Forschung" in the MoBiTech initiative (grant number 13N4051). JS, BH, IG and AAS are employees and shareholders of Genelux Corporation and Genelux GmbH respectively. The funders had no role in study design, data collection and analysis, decision to publish, or preparation of the manuscript. No competing interests exist for MH and JBS.

Received: 8 August 2011 Accepted: 11 October 2011
Published: 11 October 2011

References

1. Kirn DH, Thorne SH: **Targeted and armed oncolytic poxviruses: a novel multi-mechanistic therapeutic class for cancer.** *Nat Rev Cancer* 2009, **9**:64-71.
2. Garcia-Aragoncillo E, Hernandez-Alcoceba R: **Design of virotherapy for effective tumor treatment.** *Curr Opin Mol Ther* 2010, **12**:403-411.
3. Moss B: **Genetically engineered poxviruses for recombinant gene expression, vaccination, and safety.** *Proc Natl Acad Sci USA* 1996, **93**:11341-11348.
4. Zhang Q, Yu YA, Wang E, Chen N, Danner RL, Munson PJ, Marincola FM, Szalay AA: **Eradication of solid human breast tumors in nude mice with an intravenously injected light-emitting oncolytic vaccinia virus.** *Cancer Res* 2007, **67**:10038-10046.
5. Yu YA, Shabahang S, Timiryasova TM, Zhang Q, Beltz R, Gentschev I, Goebel W, Szalay AA: **Visualization of tumors and metastases in live animals with bacteria and vaccinia virus encoding light-emitting proteins.** *Nat Biotechnol* 2004, **22**:313-320.
6. Puhlmann M, Brown CK, Gnant M, Huang J, Libutti SK, Alexander HR, Bartlett DL: **Vaccinia as a vector for tumor-directed gene therapy: biodistribution of a thymidine kinase-deleted mutant.** *Cancer Gene Ther* 2000, **7**:66-73.
7. Gentschev I, Stritzker J, Hofmann E, Weibel S, Yu YA, Chen N, Zhang Q, Bullerdiek J, Nolte I, Szalay AA: **Use of an oncolytic vaccinia virus for the treatment of canine breast cancer in nude mice: preclinical development of a therapeutic agent.** *Cancer Gene Ther* 2009, **16**:320-328.
8. Heo J, Breitbach CJ, Moon A, Kim CW, Patt R, Kim MK, Lee YK, Oh SY, Woo HY, Parato K, *et al*: **Sequential Therapy With JX-594, A Targeted Oncolytic Poxvirus, Followed by Sorafenib in Hepatocellular Carcinoma: Preclinical and Clinical Demonstration of Combination Efficacy.** *Mol Ther* 2011, **19**:1170-1179.
9. Liu TC, Hwang T, Park BH, Bell J, Kirn DH: **The targeted oncolytic poxvirus JX-594 demonstrates antitumoral, antivascular, and anti-HBV activities in patients with hepatocellular carcinoma.** *Mol Ther* 2008, **16**:1637-1642.
10. Park BH, Hwang T, Liu TC, Sze DY, Kim JS, Kwon HC, Oh SY, Han SY, Yoon JH, Hong SH, *et al*: **Use of a targeted oncolytic poxvirus, JX-594, in patients with refractory primary or metastatic liver cancer: a phase I trial.** *Lancet Oncol* 2008, **9**:533-542.
11. Pedersen J, Karapanagiotou L, Alam S, Puglisi M, Britton L, Sassi S, Mansfield D, Yap T, De-Bono J, Harrington K: **Preliminary results of a Phase 1 study of intravenous administration of GL-ONC1 Vaccinia virus in patients with advanced solid cancer with real time imaging.** 6th NCRI Cancer Conference; BT Convention Center, Liverpool, UK; 2010.
12. Bennett JJ, Tjuvajev J, Johnson P, Doubrovin M, Akhurst T, Malholtra S, Hackman T, Balatoni J, Finn R, Larson SM, *et al*: **Positron emission tomography imaging for herpes virus infection: Implications for oncolytic viral treatments of cancer.** *Nat Med* 2001, **7**:859-863.
13. Chen N, Zhang Q, Yu YA, Stritzker J, Brader P, Schirbel A, Samnick S, Serganova I, Blasberg R, Fong Y, Szalay AA: **A novel recombinant vaccinia virus expressing the human norepinephrine transporter retains oncolytic potential and facilitates deep-tissue imaging.** *Mol Med* 2009, **15**:144-151.
14. Dingli D, Peng KW, Harvey ME, Greipp PR, O'Connor MK, Cattaneo R, Morris JC, Russell SJ: **Image-guided radiovirotherapy for multiple myeloma using a recombinant measles virus expressing the thyroidal sodium iodide symporter.** *Blood* 2004, **103**:1641-1646.
15. Haddad D, Chen NG, Zhang Q, Chen CH, Yu YA, Gonzalez L, Carpenter SG, Carson J, Au J, Mittra A, *et al*: **Insertion of the human sodium iodide symporter to facilitate deep tissue imaging does not alter oncolytic or replication capability of a novel vaccinia virus.** *J Transl Med* 2011, **9**:36.
16. Fang W, Vikerpuur M, Sandholm M: **A fluorometric beta-glucuronidase assay for analysis of bacterial growth in milk.** *Vet Microbiol* 1995, **46**:361-367.
17. Jefferson RA, Burgess SM, Hirsh D: **beta-Glucuronidase from Escherichia coli as a gene-fusion marker.** *Proc Natl Acad Sci USA* 1986, **83**:8447-8451.
18. Jefferson RA, Kavanagh TA, Bevan MW: **GUS fusions: beta-glucuronidase as a sensitive and versatile gene fusion marker in higher plants.** *EMBO J* 1987, **6**:3901-3907.
19. Stahl P, Fishman W: **Beta-D-glucuronidase.** In *Methods in enzymatic analysis.* Edited by: JB, MG. Weinheim, Germany: Verlag Chemie; 1984:246-256.
20. Wang SM, Chern JW, Yeh MY, Ng JC, Tung E, Roffler SR: **Specific activation of glucuronide prodrugs by antibody-targeted enzyme conjugates for cancer therapy.** *Cancer Res* 1992, **52**:4484-4491.
21. Cheng CM, Lu YL, Chuang KH, Hung WC, Shiea J, Su YC, Kao CH, Chen BM, Roffler S, Cheng TL: **Tumor-targeting prodrug-activating bacteria for cancer therapy.** *Cancer Gene Ther* 2008, **15**:393-401.
22. de Graaf M, Pinedo HM, Oosterhoff D, van der Meulen-Muileman IH, Gerritsen WR, Haisma HJ, Boven E: **Pronounced antitumor efficacy by extracellular activation of a doxorubicin-glucuronide prodrug after adenoviral vector-mediated expression of a human antibody-enzyme fusion protein.** *Hum Gene Ther* 2004, **15**:229-238.
23. Huang PT, Chen KC, Prijovich ZM, Cheng TL, Leu YL, Roffler SR: **Enhancement of CPT-11 antitumor activity by adenovirus-mediated expression of beta-glucuronidase in tumors.** *Cancer Gene Ther* 2011, **18**:381-389.
24. Tzou SC, Roffler S, Chuang KH, Yeh HP, Kao CH, Su YC, Cheng CM, Tseng WL, Shiea J, Harm IH, *et al*: **Micro-PET imaging of beta-glucuronidase activity by the hydrophobic conversion of a glucuronide probe.** *Radiology* 2009, **252**:754-762.
25. Antunes IF, Haisma HJ, Elsinga PH, Dierckx RA, de Vries EF: **Synthesis and evaluation of [18F]-FEAnGA as a PET Tracer for beta-glucuronidase activity.** *Bioconjug Chem* 2010, **21**:911-920.
26. Su YC, Chuang KH, Wang YM, Cheng CM, Lin SR, Wang JY, Hwang JJ, Chen BM, Chen KC, Roffler S, Cheng TL: **Gene expression imaging by enzymatic catalysis of a fluorescent probe via membrane-anchored beta-glucuronidase.** *Gene Ther* 2007, **14**:565-574.
27. Sterenczak KA, Willenbrock S, Barann M, Klemke M, Soller JT, Eberle N, Nolte I, Bullerdiek J, Murua Escobar H: **Cloning, characterisation, and comparative quantitative expression analyses of receptor for advanced glycation end products (RAGE) transcript forms.** *Gene* 2009, **434**:35-42.
28. Stritzker J, Weibel S, Hill PJ, Oelschlaeger TA, Goebel W, Szalay AA: **Tumor-specific colonization, tissue distribution, and gene induction by probiotic Escherichia coli Nissle 1917 in live mice.** *Int J Med Microbiol* 2007, **297**:151-162.
29. Seubert CM, Stritzker J, Hess M, Donat U, Sturm JB, Chen N, von Hof JM, Krewer B, Tietze LF, Gentschev I, Szalay AA: **Enhanced tumor therapy using vaccinia virus strain GLV-1h68 in combination with a beta-galactosidase-activatable prodrug seco-analog of duocarmycin SA.** *Cancer Gene Ther* 2011, **18**:42-52.
30. Chen KC, Wu CH, Chang CY, Lu WC, Tseng Q, Prijovich ZM, Schechinger W, Liaw YC, Leu YL, Roffler SR: **Directed evolution of a lysosomal enzyme with enhanced activity at neutral pH by mammalian cell-surface display.** *Chem Biol* 2008, **15**:1277-1286.
31. Sharma SK, Bagshawe KD, Melton RG, Sherwood RF: **Human immune response to monoclonal antibody-enzyme conjugates in ADEPT pilot clinical trial.** *Cell Biophys* 1992, **21**:109-120.
32. Chen KC, Wu SY, Leu YL, Prijovich ZM, Chen BM, Wang HE, Cheng TL, Roffler SR: **A humanized immunoenzyme with enhanced activity for glucuronide prodrug activation in the tumor microenvironment.** *Bioconjug Chem* 2011, **22**:938-948.
33. Heine D, Muller R, Brusselbach S: **Cell surface display of a lysosomal enzyme for extracellular gene-directed enzyme prodrug therapy.** *Gene Ther* 2001, **8**:1005-1010.
34. Weyel D, Sedlacek HH, Muller R, Brusselbach S: **Secreted human beta-glucuronidase: a novel tool for gene-directed enzyme prodrug therapy.** *Gene Ther* 2000, **7**:224-231.

doi:10.1186/1479-5876-9-172
Cite this article as: Hess *et al.*: Bacterial glucuronidase as general marker for oncolytic virotherapy or other biological therapies. *Journal of Translational Medicine* 2011 **9**:172.

Figure S1

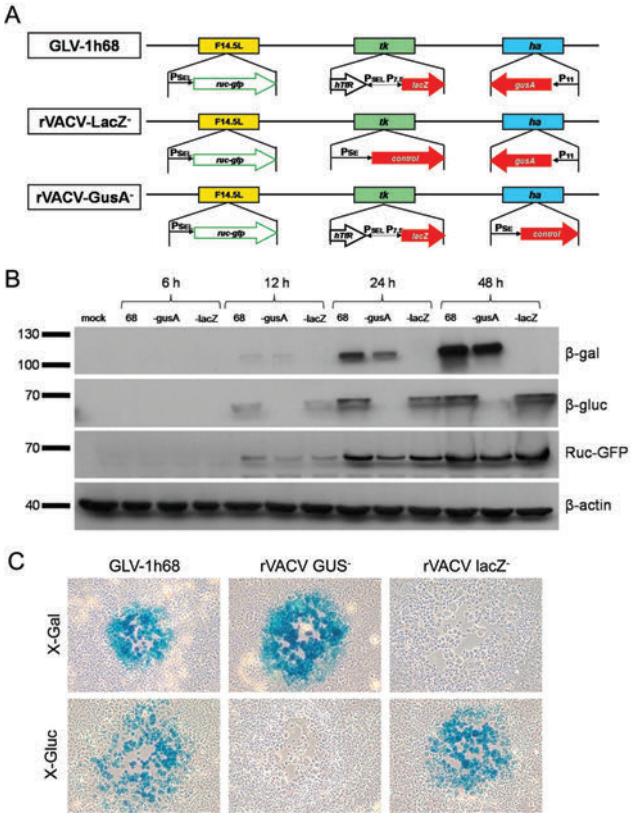
A
GLV-1h68
rVACV-LacZ-
rVACV-GusA-
F14.5L
tk
ha
B
6 h
12 h
24 h
48 h
mock
68
-gusA
-lacZ
130
100
70
70
40
β-gal
β-gluc
Ruc-GFP
β-actin
C
GLV-1h68
rVACV GUS-
rVACV lacZ-
X-Gal
X-Gluc

Figure S2

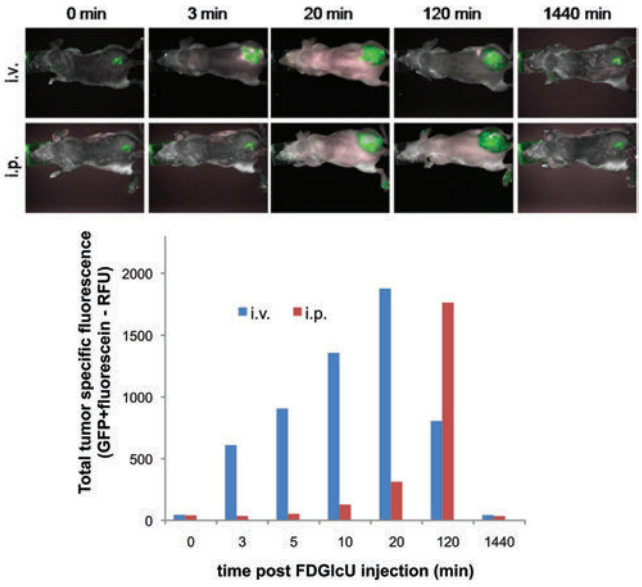
0 min
3 min
20 min
120 min
1440 min
i.v.
i.p.
Total tumor specific fluorescence (GFP+fluorescein - RFU)
2000
1500
1000
500
0
i.v.
i.p.
0
3
5
10
20
120
1440
time post FDGlcU injection (min)

Figure S3

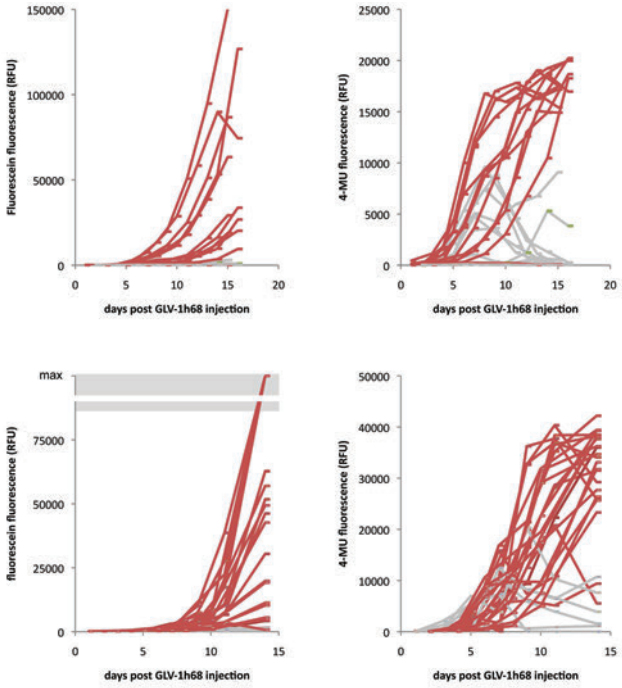
Fluorescein fluorescence (RFU)
150000
100000
50000
0
0
5
10
15
20
days post GLV-1h68 injection
4-MU fluorescence (RFU)
25000
20000
15000
10000
5000
0
0
5
10
15
20
days post GLV-1h68 injection
fluorescein fluorescence (RFU)
max
75000
50000
25000
0
0
5
10
15
days post GLV-1h68 injection
4-MU fluorescence (RFU)
50000
40000
30000
20000
10000
0
0
5
10
15
days post GLV-1h68 injection

Figure S4

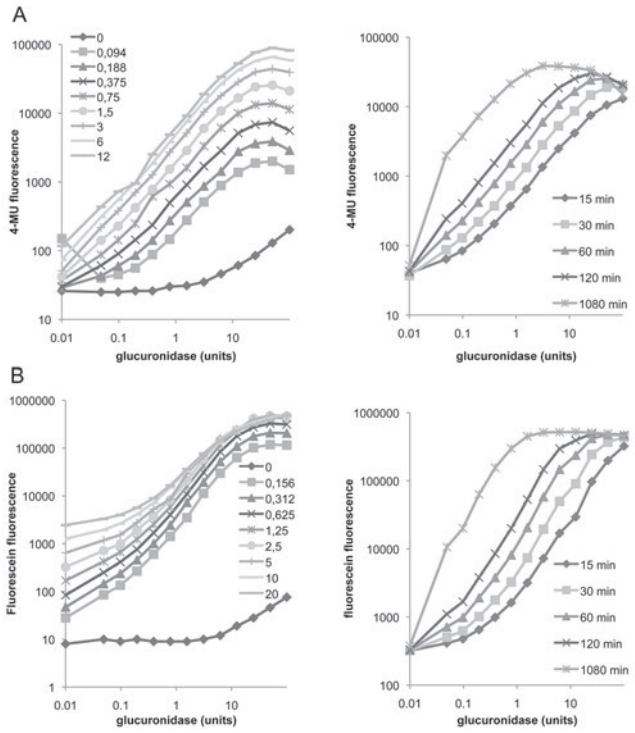
A
0
0,094
0,188
0,375
0,75
1,5
3
6
12
4-MU fluorescence
glucuronidase (units)
15 min
30 min
60 min
120 min
1080 min
B
0
0,156
0,312
0,625
1,25
2,5
5
10
20
Fluorescein fluorescence
fluorescein fluorescence

Figure S5

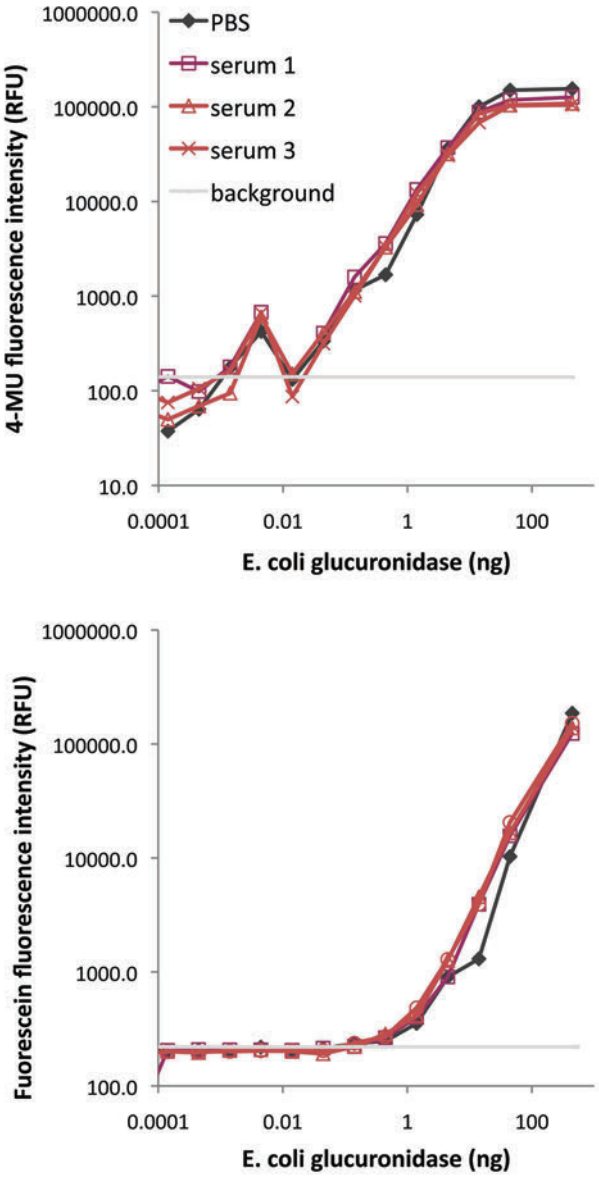
1000000.0
100000.0
10000.0
1000.0
100.0
10.0
4-MU fluorescence intensity (RFU)
PBS
serum 1
serum 2
serum 3
background
0.0001
0.01
1
100
E. coli glucuronidase (ng)
1000000.0
100000.0
10000.0
1000.0
100.0
Fuorescein fluorescence intensity (RFU)
0.0001
0.01
1
100
E. coli glucuronidase (ng)

Publication (complete reference): Stritzker J, Kirscher L, Scadeng M, Deliolanis NC, Morscher S, Symvoulidis P, Schaefer K, Zhang Q, Buckel L, **Hess M**, Donat U, Bradley WG, Ntziachristos V, Szalay AA. Vaccinia virus mediated melanin production allows MR and optoacoustic deep tissue imaging and laser induced thermotherapy of cancer. *Proc Natl Acad Sci U S A*. 2013
Authors' contributions
J.S., M.S., N.C.D., and V.N. designed research; J.S., L.K., M.S., N.C.D., S.M., P.S., K.S., **M.H.**, and U.D. performed research; J.S., L.K., M.S., N.C.D., S.M., P.S., Q.Z., L.B., U.D., and V.N. contributed new reagents/analytic tools; J.S., L.K., M.S., N.C.D., S.M., P.S., K.S., and A.A.S. analyzed data; and J.S., M.S., N.C.D., S.M., Q.Z., W.G.B., and A.A.S. wrote the paper.

Jochen Stritzker	
Lorenz Kirscher	
Miriam Scadeng	
Nicolaos C. Deliolanis	
Stefan Morscher	
Panagiotis Symvoulidis	
Karin Schaefer	
Qian Zhang	
Lisa Buckel	
Ulrike Donat	
William G. Bradley	
Vasilis Ntziachristos	
Aladar A. Szalay	

Vaccinia virus-mediated melanin production allows MR and optoacoustic deep tissue imaging and laser-induced thermotherapy of cancer

Jochen Stritzker[a,b,1], Lorenz Kirscher[b], Miriam Scadeng[c], Nikolaos C. Deliolanis[d,e], Stefan Morscher[d,f], Panagiotis Symvoulidis[d], Karin Schaefer[d], Qian Zhang[a], Lisa Buckel[b], Michael Hess[b], Ulrike Donat[b], William G. Bradley[g], Vasilis Ntziachristos[d], and Aladar A. Szalay[a,b,h,1]

[a]Genelux, San Diego, CA 92109; [b]Department of Biochemistry, Biocenter, University of Würzburg, 97074 Würzburg, Germany; [c]Center for Functional MRI, University of California at San Diego, La Jolla, CA 92093; [d]Institute for Biological and Medical Imaging, Helmholtz Zentrum München and Technische Universität München, 85764 Neuherberg, Germany; [e]Fraunhofer Project Group for Automation in Medicine and Biotechnology, 68167 Mannheim, Germany; [f]iThera Medical, 85764 Neuherberg, Germany; [g]Department of Radiology, University of California at San Diego Medical Center, San Diego, CA 92103; and [h]Department of Radiation Oncology, Moores Cancer Center, University of California at San Diego, La Jolla, CA 92093

Edited* by Roger Y. Tsien, University of California at San Diego, La Jolla, CA, and approved January 14, 2013 (received for review October 1, 2012)

We reported earlier the delivery of antiangiogenic single chain antibodies by using oncolytic vaccinia virus strains to enhance their therapeutic efficacy. Here, we provide evidence that gene-evoked production of melanin can be used as a therapeutic and diagnostic mediator, as exemplified by insertion of only one or two genes into the genome of an oncolytic vaccinia virus strain. We found that produced melanin is an excellent reporter for optical imaging without addition of substrate. Melanin production also facilitated deep tissue optoacoustic imaging as well as MRI. In addition, melanin was shown to be a suitable target for laser-induced thermotherapy and enhanced oncolytic viral therapy. In conclusion, melanin as a mediator for thermotherapy and reporter for different imaging modalities may soon become a versatile alternative to replace fluorescent proteins also in other biological systems. After ongoing extensive preclinical studies, melanin overproducing oncolytic virus strains might be used in clinical trials in patients with cancer.

translational medicine | personalized medicine | diagnosis | photoacoustic | whole-body imaging

Theranostics are considered a key to personalized medicine combining therapy and diagnosis in a single agent. However, "stand-alone" theranostics resulting from engineered gene expression have not been developed yet. Theranostic agents are generally comprised of dual/multifunctional nanoparticles that can be visualized noninvasively in real time by an imaging modality and at the same time are loaded with (chemo-)therapeutic agents. Some of these particles have also been equipped with molecules that enable their targeting of specific receptors (e.g., arthritis and cancer). However, most of them still need to be improved in terms of specificity as well as increased concentrations at the target site.

Insertion of reporter genes to oncolytic viruses resulted in another class of theranostic agents. Oncolytic viruses are characterized by their largely tumor cell-specific replication, resulting in tumor cell lysis and efficient tumor regression. Tumor selectivity is an inherent property of a number of viruses such as Newcastle disease virus, parvovirus, and vaccinia virus. These could be enhanced, for example, by deletion of viral genes, which are dispensable in malignant cells, or by production of surface receptors that bind ligands that are highly expressed on tumor cells (1).

The vaccinia virus strain GLV-1h68 was effective in treating more than 40 tumor xenograft models in mice, shown to be safe in a recently completed phase I trial upon systemic injection to human cancer patients (2), and is currently undergoing several additional phase I/II trials (www.clinicaltrials.gov). This strain also carries genes that allow optical detection via GFP and *Renilla* luciferase expression (3) and further encodes enzymes (β-gal and glucuronidase) that can be monitored in the serum of tumor-bearing mice (4) as well as in the blood of humans with cancer. In addition, it was shown to enhance the therapeutic effect of this oncolytic vaccinia virus strain when an antiangiogenic single-chain antibody was encoded by the virus (5). Here, the oncolytic vaccinia virus strain GLV-1h68 served as backbone for the insertion of key genes in melanogenesis. We speculated that introduction of melanogenesis into tumor cells might render them visible as a result of melanin overproduction by optical as well as optoacoustic imaging (6) and might facilitate therapy. Furthermore, it is well known that melanotic melanomas generate high signal on T1-weighted magnetic resonance images (7, 8), probably as a result of trapping of paramagnetic transition metal ions (9). Previously published cell culture data also encouraged us to use the production of melanin as a reporter for MRI (9–11). Targeted melanin overproduction as a reporter for optoacoustic imaging or MRI in live animals or humans has not yet been established. The goal therefore was to use the vaccinia virus strain GLV-1h68 as an example for a vehicle equipped with genes for melanin overproduction and use the produced melanin as an (additional) theranostic mediator.

Results

Gene-Evoked Melanin Production. In a pilot study, cDNAs of the key enzymes in melanogenesis, namely tyrosinase (*Tyr*), tyrosinase-related protein 1 (*Tyrp1*), and dopachrome tautomerase (*DCT*; also known as *Tyrp2*) were inserted into a mammalian expression vector. Production of melanin in HeLa cells was observed only when the tyrosinase encoding plasmid DNA was introduced (Fig. S1). Cotransformation of the *Tyrp1* plasmid resulted in production of a darker (eu-)melanin (12), whereas DCT expression did not seem to have any influence on the produced melanin. Therefore, tyrosinase alone, or in combination with *Tyrp1*, was inserted into the vaccinia virus genome under control of a synthetic early (SE) or the much stronger synthetic early/late (SEL) promoter. Upon infection with the newly generated recombinant vaccinia virus (rVACV) strains, cells produced significant amounts of melanin (Fig. 1*A*). Optical density measurements of

Author contributions: J.S., M.S., N.C.D., and V.N. designed research; J.S., L.K., M.S., N.C.D., S.M., P.S., K.S., M.H., and U.D. performed research; J.S., L.K., M.S., N.C.D., S.M., P.S., Q.Z., L.B., U.D., and V.N. contributed new reagents/analytic tools; J.S., L.K., M.S., N.C.D., S.M., P.S., K.S., and A.A.S. analyzed data; and J.S., M.S., N.C.D., S.M., Q.Z., W.G.B., and A.A.S. wrote the paper.

Conflict of interest statement: J.S., Q.Z. and A.A.S. are employees and shareholders of Genelux. S.M. is an employee of iThera Medical.

*This Direct Submission article had a prearranged editor.

Freely available online through the PNAS open access option.

[1]To whom correspondence may be addressed. E-mail: js@genelux.com or aaszalay@genelux.com.

This article contains supporting information online at www.pnas.org/lookup/suppl/doi:10.1073/pnas.1216916110/-/DCSupplemental.

infected cell suspensions (Fig. 1*B*) confirmed what was already visible in the cell pellets: Low amounts of tyrosinase (under control of the SE-promoter) resulted in a light brown coloration of the cells whereas high amounts of tyrosinase (SEL–promoter constructs) led to much darker infected cells.

The darkest (i.e., coal black) cells were consistently observed upon GLV-1h324 infection. Obviously, the additional coexpression of Tyrp1 in low amounts could increase the biosynthesis of the black eumelanin. So far, 16 of 16 tested tumor cell lines (including cells from different cancers and different species) produced melanin when infected with the melanin-rVACV strains. Interestingly, melanin in infected red-fluorescent protein expressing PC-3 (PC-3-RFP) cells almost completely suppressed the RFP fluorescence signal (Fig. S2), probably by absorption of excitation and emission light.

The influence of melanin production on viral replication and virus-mediated cell lysis was determined by measuring the activity of the virus-encoded glucuronidase in cell lysates and in the cell culture supernatant, respectively (4). It was shown that higher amounts of melanin seemed to inhibit viral replication at later time points during infection (Fig. S3*A*). However, melanin did not significantly influence viral cell lysis, which also was confirmed by a cell viability assay (Fig. S3 *B* and *C*). More importantly, the melanin-rVACV strains retained their oncolytic activity, although A549 tumor regression was decelerated compared with the control-rVACV strain GLV-1h68 (Fig. S3*D*). Of note, the net body weight (tumor weight subtracted from whole body weight) as a marker for "well-being" was somewhat higher in the melanin-rVACV groups, even though this was not statistically significant

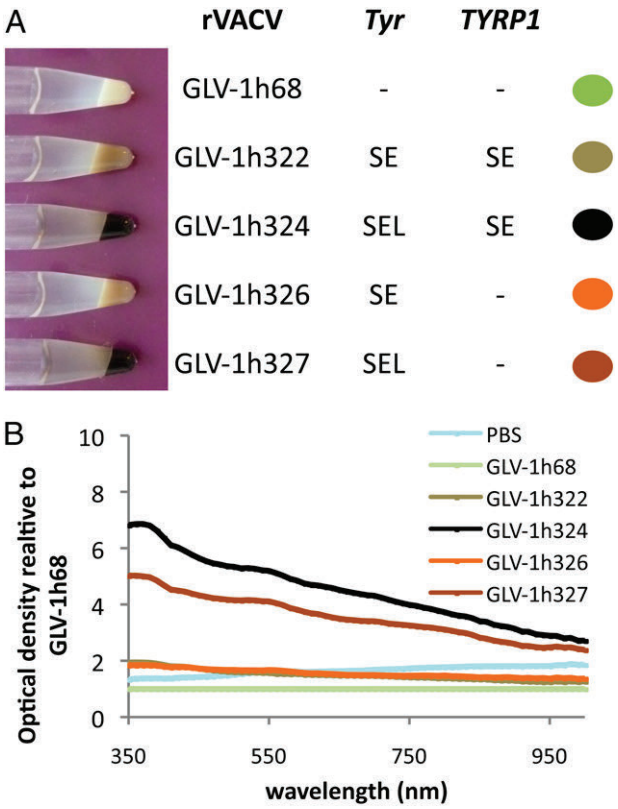

Fig. 1. Production of melanin upon key enzyme expression. (*A*) Pellets of infected CV-1 cells and overview of the infecting rVACV strains encoding Tyr and/or Tyrp1 under control of a weaker SE or strong SEL promoter. The colored dots indicate the color used for each strain in all following figures. (*B*) Optical density measurements over the spectrum from 350 nm to 1,000 nm (in 5-nm increments) were conducted, and the relative optical density compared with the results obtained with GLV-1h68 infected A549 cells was plotted for each data point.

(Fig. S3*D*, *Inset*). Analyses of isolated tumor tissues from perfused mice at the end of the experiments clearly demonstrated that melanin-rVACV colonized tumors, in contrast to controls, produced so much melanin that they appeared coal-black (Fig. S3*E*).

Near-IR Laser-Induced Thermotherapy of Melanin Producing Tumors. As the produced melanin also significantly enhances the absorption of light in the so-called near-IR optical window, which is characterized by low absorption and maximum light penetration in tissues (13), we tested whether we could use a near-IR laser to specifically transfer energy to melanin. The transferred energy would then be converted to thermal energy, eventually heating the melanin-producing cells (and cells in their vicinity) to temperatures causing protein denaturation and cell death, and therefore enabling thermotherapy. Fig. 2 shows that we achieved this by using an 808-nm laser: Whereas mock-infected or control-rVACV–infected tumor cell suspensions warmed up by only approximately 3 °C during 2 min of exposure to the laser light, the melanin-rVACV cell suspension temperature increased by 25 °C for GLV-1h327– and by 41 °C for GLV-1h324–infected cells, respectively, resulting in a temperature higher than 65 °C (Fig. 2*A*, *Upper*). Accordingly, the 120-s laser treatment killed almost all cells in the GLV-1h324–infected aliquot (Fig. 2*A*, *Lower*). When using a single 2-min laser treatment on A549 tumor-bearing mice, the skin on top of the laser-exposed tumor section changed its color (most likely because of the heat inside the tumor underneath) when melanin was expressed in the tumor beneath (Fig. 2*B*), but not in the control-rVACV–injected mice. Tumor size measurements 1 and 5 d after laser therapy revealed the success of this thermotherapy: Whereas the GLV-1h68 control groups did not show significant differences in terms of tumor volume changes, the laser treatment did reduce the tumor volume significantly in GLV-1h324–treated mice compared with tumors that were not exposed to the laser light (Fig. 2*C*). The virus-mediated melanin production in infected tumor cells therefore facilitates near-IR–assisted thermotherapy in addition to the oncolytic virotherapy. Similar results were also achieved by using the B16F10 melanoma cell line (Fig. S4), which naturally produces melanin.

Optoacoustic Imaging of Melanin-Producing Tumors and Metastases. Optoacoustic imaging is an emerging in vivo imaging technology (14, 15), whereby short light energy pulses are absorbed by tissue and converted to thermal energy and subsequently to ultrasound signals that allow high-resolution whole-body imaging. The oncolytic virus mediated production of melanin and its optical absorption in the near-IR enables the imaging of tumors and metastases with this modality. Pellets of cells infected with various melanin-rVACV strains (Fig. 3*A*), for different time points post infection (Fig. 3*B*) and at different dilutions (Fig. 3*C*) showed optoacoustic signals in the near-IR range that were equivalent to optical absorption up to 2 cm^{-1}. These values are one order of magnitude above the 0.3- to 0.5-cm^{-1} tissue optical absorption in near-IR and are comparable with the 2-cm^{-1} absorption of whole blood, thus ensuring sufficient signal to background ratio. In combination with multispectral optoacoustic tomographic (MSOT) imaging of melanin-containing tumors, we were able to generate an image processing algorithm that allowed us to specifically visualize the presence and distribution of melanin not only on the surface but also deep within the mouse body (Fig. S5). With this technique, surface near A549 and PC-3 tumors as well as PC-3-RFP lymph node metastases (Figs. 3 *D* and *E* and S6), which, in a recent study, were shown to be preferentially colonized vs. the primary tumor (16), could be detected in live mice injected with melanin-rVACV.

MR Imaging of Tumors and Metastases upon Melanin Production. Knowing we can produce high amounts of melanin specifically in colonized tumors, we analyzed whether the virus-mediated melanin production would also lead to signal intensity changes in

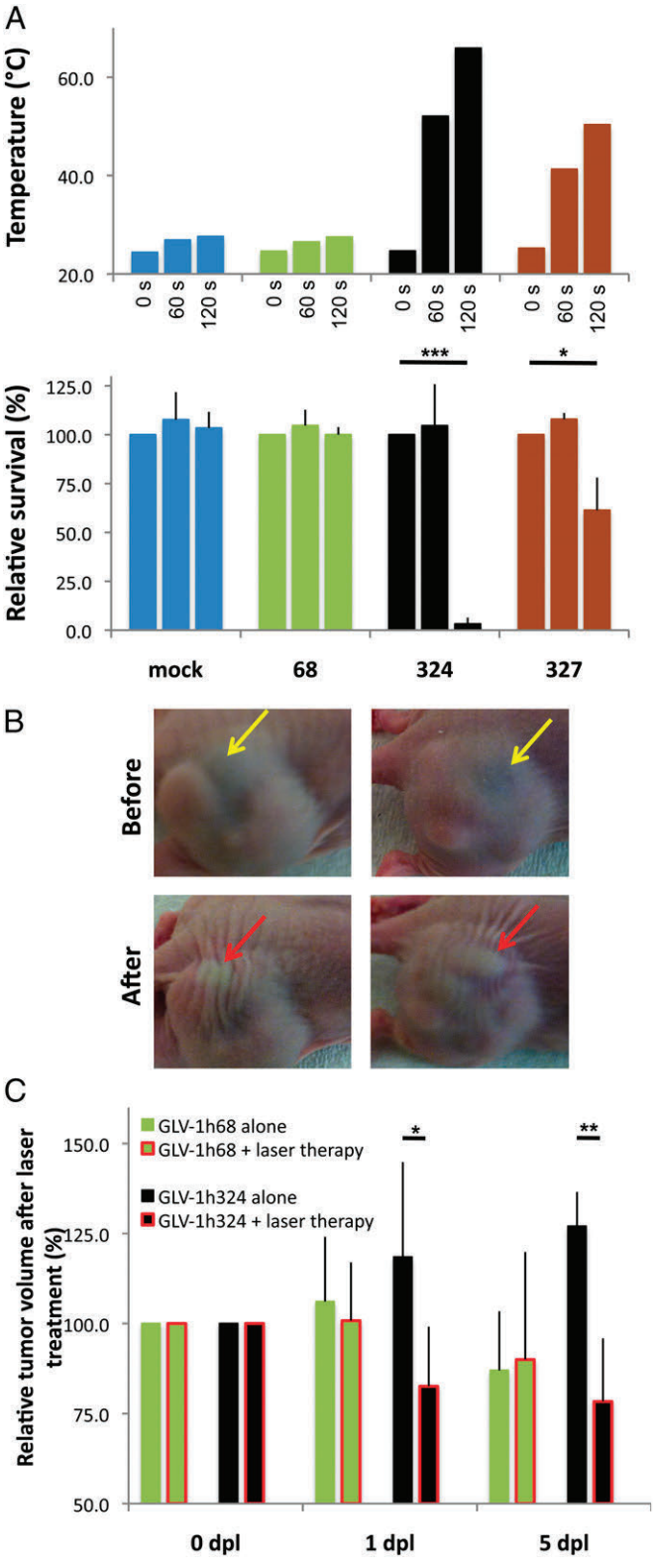

Fig. 2. Melanin biosynthesis facilitates near-IR laser-induced thermotherapy. (*A*) A549 cell suspensions were exposed to 808 nm laser light for 0, 60, and 120 s, respectively. (*Upper*) Measured temperature (in °C) immediately after laser treatment. (*Lower*) Relative survival compared with each non–laser-light–exposed sample (*$P < 0.05$, ***$P < 0.0001$). (*B*) Photographs of laser-treated, melanin-rVACV–injected mice before (*Upper*) and immediately after treatment (*Lower*). The area that was exposed to laser light is indicated by a yellow arrow. The red arrows indicate the same area where tissue damage was observed after treatment. (*C*) Tumor size measurements revealed significant differences in tumor size between the laser-treated and untreated GLV-1h324 subgroups at 1 and 5 d post laser treatment (dpl). No significant differences were observed in the GLV-1h68 subgroups (*$P < 0.05$, **$P < 0.005$).

MR imaging, which, unlike optical imaging, is not alleviated in deep tissues. Indeed, we found a markedly shortened T1 relaxation time when PC-3-RFP or A549 cells were infected with the melanin-rVAVC, but not with GLV-1h68 (Fig. 4 *A* and *C*). Similar to the data already found in optical and optoacoustic analysis, the greatest T1 shortening was also observed by using the GLV-1h324 strain. To determine the lower detection limit, we analyzed twofold serial dilutions of GLV-1h324–infected cells in noninfected A549 cells (Fig. 4*B*). Although no changes were observed when one in 128 cells produced melanin (T1, 1,954 ± 15 ms vs. 1,940 ± 11 ms for noninfected cells), the 1:64-fold dilution significantly reduced the T1 relaxation time (1,860 ± 16 ms). Higher concentration of GLV-1h324–infected cells further decreased T1 relaxation times. When looking at how early T1 relaxation changes occurred after infection, we already found significant reductions after only 24 h post infection, which were even more pronounced after 48 h (Fig. 4*C*). More detailed analysis of GLV-1h324–infected cells revealed a significant T1 shortening after 18 h, but not 12 h, post infection, correlating to what was already observed for the optoacoustic signal (Fig. 3*D*).

Most importantly, the melanin-dependent T1-relaxation changes could be used to generate increased signal in MRI of melanin-rVACV–colonized tumors in live mice (Fig. 4*D*). Although tumors of the control-rVACV–injected mice appeared evenly gray, the melanin-rVACV–colonized A549 tumors were characterized by regions of very high signal (almost white when using the same contrast settings as for the control mice). Moreover, these regions of high signal intensity correlated very well with the melanin distribution in the tumor that could be visualized on the cryosections of the same mice. Tumor regions that (at this time) did not produce melanin because the oncolytic rVACV did not (yet) infect this part of the tumor showed a similar gray level as the tumors of the control mice. Quantitative analysis of T1 maps (Fig. S7) confirmed T1 relaxation time reduction in the melanin-rVACV– compared with control-rVACV–injected mice tumor tissue, but not muscle (Fig. 4*E*).

Consequently, we wanted to know whether we would be able to detect not only relatively large tumors (as shown by the A549 model), but also the smaller PC-3-RFP lymph node metastases. In this study, metastases colonized with melanin-rVACV were shown to exhibit increased intensity in MRI of live mice (Fig. S8) whereas lymph node metastases of PBS solution- or control-rVACV–injected mice had similar gray levels as the primary tumor. The colocalization of increased intensity in MRI and presence of melanin was demonstrated after perfusion and dissection of the mice. Furthermore, immunohistochemistry was used to confirm the presence of rVACV in the lymph node metastases (Fig. S8), demonstrating that melanin was actually produced intracellularly in the metastasized lymph nodes and not transported as free melanin into these structures from the primary tumor.

In addition to the in vivo MR imaging experiments described earlier, we performed MRI analysis of isolated A549 tumors in a clinical 3-T MR instrument to demonstrate that use of melanin production as a reporter could be translated to clinical settings (Fig. S9).

Discussion

Here, we have shown that simple gene-evoked melanin production has the potential to become widely used in several diagnostic (e.g., marker during surgery, for endoscopy, in optoacoustic and MR imaging) as well as in therapeutic (e.g., near-IR light-induced thermotherapy) procedures in the clinic. Whether Tyrp1 should be

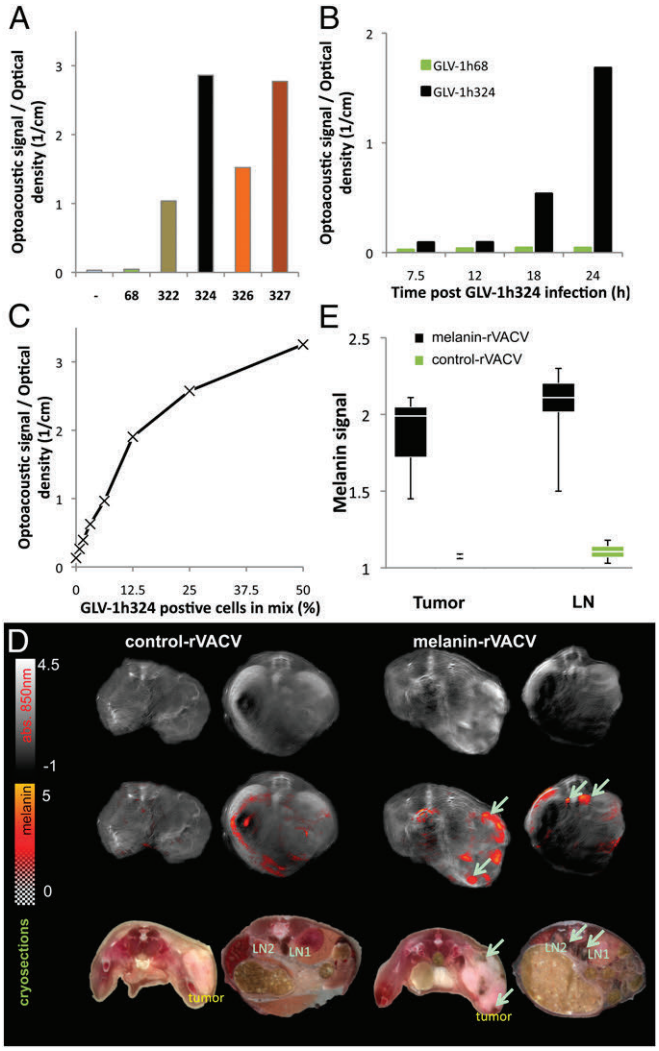

Fig. 3. Optoacoustic imaging of melanin-rVACV in cell cultures and in live mice. (*A*) Three days after infection, PC-3-RFP cell suspensions were analyzed for their optoacoustic signals, which were strongest in GLV-1h324 and GLV-1h327–infected cells. (*B*) Infected A549 cells were analyzed at different times post infection. For GLV-1h324–infected A549 cells, a significant optoacoustic signal increase was observed at 18 h post infection. (*C*) GLV-1h324 infected A549 cells were diluted in uninfected cells and the optoacoustic signal determined. Even at the lowest concentration (one in 128 cells), an optoacoustic signal was detected that was significantly higher than that of control cells. (*D*) MSOT of PC-3-RFP tumor and lymph node metastasis (LN1 and LN2) bearing live mice 14 d after rVACV injection. (*Top*) Background optoacoustic images taken at 850 nm excitation wavelength. (*Middle*) Melanin spatial distribution (pseudocolor) is overlaid on the background images (*Top*) using a variable transparency function as shown in the color bar. The melanin signature was picked up in the melanin-rVACV–injected mice which correlated with the distribution of melanin in the corresponding cryosections (*Bottom*) as indicated by the arrows. (*E*) Quantitative optoacoustic signal intensities for melanin in tumors and lymph nodes as box and whisker plots for three melanin- and two control-VACV–injected mice.

coexpressed in addition to tyrosinase for enhanced eumelanin production in vivo will probably be dependent on the model. Although we detected significant differences in (eu-)melanin production in cell culture, Tyrp1 did not have obvious advantages in virus-colonized tumor models in terms of melanin production. The darker color of eumelanin results in better MSOT contrast, and therefore Tyrp1 coexpression should help when Tyr expression results in pheomelanin biosynthesis. Eumelanin is known to have more efficient binding capacity for certain drugs and metal ions (17), and might also have more potential in storing iron compared with pheomelanin (18). Therefore, eumelanin might give a better MR signal, and, consequently, Tyrp1 expression could be

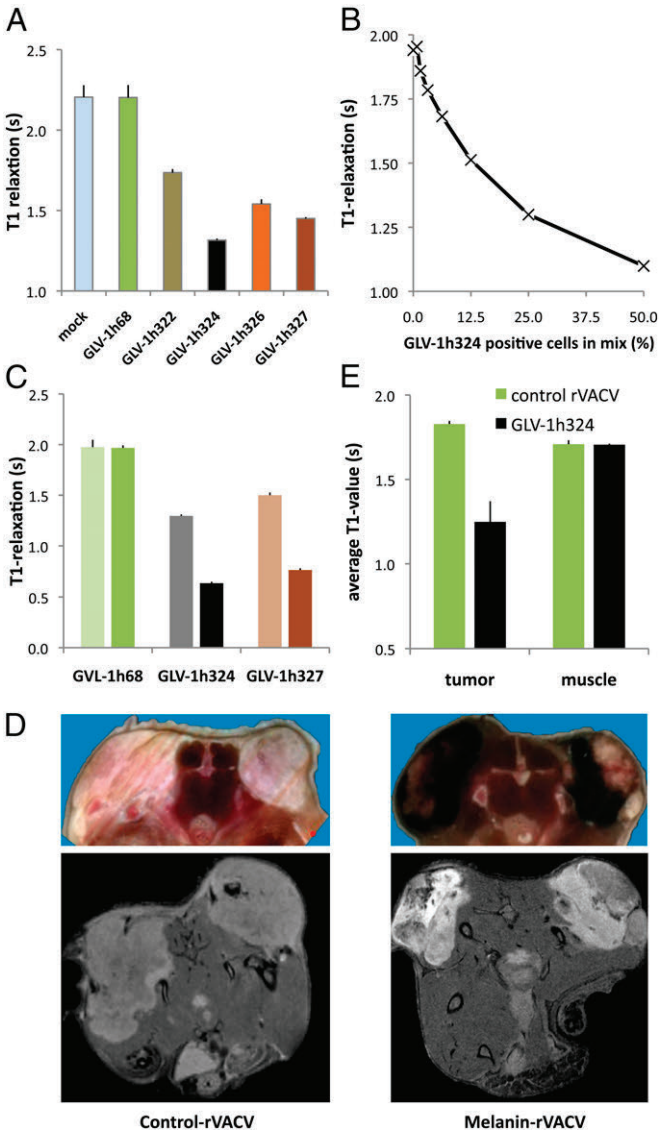

Fig. 4. The production of melanin resulted in bright signal on a T1-weighted MR image by causing T1 shortening. (*A*) T1-relaxation times of harvested PC-3-RFP cell suspensions 3 d after infection. (*B*) Mixtures of GLV-1h324 infected with noninfected A549 cells showed significant T1-relaxation time shortening in the 1:64 dilution (1.56% of infected A549 cells) compared with noninfected A549. (*C*) At 24 h (light colored bars) and 48 h post infection, the T1-relaxtion time was significantly shortened in the melanin-rVACV infected cells, with more decrease at the later time point. (*D*) The grayscale pictures illustrate representative T1-weighted images of live A549 tumor-bearing mice that were injected with GLV-1h68 and GLV-1h324 strains, respectively. The two tumors in each mouse are clearly visible but much brighter in the melanin-rVACV colonized tumors as a result of T1 shortening. (*Upper*) Images obtained after cryoslicing of the same mice show approximately the same section that can be seen on the MR images (*Lower*). The bright regions in the MR images correspond very well with the black melanin areas that were observed in the cryosections of the GLV-1h324–injected mouse, whereas no melanin containing regions in the same tumors appeared as dark as the tumor in MR images of the control mouse. (*E*) The average T1-relaxtion time plus SD of tumors and muscle (control) from two mice in each group was obtained from T1 maps of individual slices.

advantageous in models that do not allow the production of tyrosinase and/or melanin in high concentrations. Compared with fluorescent proteins, melanin can certainly not be used for subcellular protein distribution and interaction analysis, but it has the advantage of being visible by noninvasive deep tissue imaging with MSOT and MRI. In addition, the detection of fluorescent proteins is probably more sensitive than melanin in terms of generated signal per molecule, but melanin is produced enzymatically by the expressed enzyme(s), which allows relatively fast detection by MRI (in our case within 18 h post viral cell infection) with increasing intensity over time. Other advantages vs. fluorescent proteins are the extreme stability of melanin (19), the lack of tissue autofluorescence (in fact, autofluorescence is reduced by melanin, which is another way of detecting the melanin), as well as the fact that no special equipment is needed to visualize the dark pigments. Finally, the ubiquitous presence of melanin in all kingdoms of life suggests that introduction of melanin synthesis as diagnostic/theragnostic marker will be possible in most species, e.g., including plants (20), and should also find translation into clinical settings.

Materials and Methods

Tyrosinase and Tyrp1 expressing melanin-rVACV were constructed using guanine phosphoribosyltransferase selection (21). Optical absorption of cell suspensions was determined in 10-nm increments from 350 nm to 1,000 nm. For MSOT experiments, image acquisition at 11 wavelengths in 15-nm intervals starting from 700 nm and up to 850 nm enabled separation of absorbers with distinct spectral absorption profiles. Melanin distribution could be determined by separating out the background signal of deoxygenated and oxygenated hemoglobin that dominate the contrast in tissue. T1-weighted MRI (multislice–multiecho sequence; repetition time, 927 ms; echo time, 10.6 ms; four excitations; matrix, 256 × 256; field of view, 2.8 cm; slice thickness, 0.5mm; 35 slices) of live mice was performed on a 7-T small animal imaging system. T1 relaxation time maps were acquired on a single slice through the center of the tumors. Thermotherapy of melanin containing material was initiated by a 2-min exposure to 808 nm near-IR laser beam (beam diameter, 5 × 8 mm; laser power, 2.00 W). Detailed experimental procedures are provided in *SI Materials and Methods*.

All animal experiments were carried out in accordance with protocols approved by the Regierung von Unterfranken (Würzburg, Germany; Protocol AZ 55.2–2531.01–17/08) and/or the Institutional Animal Care and Use Committee of Explora BioLabs (located in the San Diego Science Center, San Diego, CA; Protocol EB11-025) and/or the Institutional Animal Care and Use Committee of the University of California at San Diego (Protocol R08335).

ACKNOWLEDGMENTS. The authors thank Jason Aguilar, Sarah Glasl, Uwe Klemm, Johanna Langbein-Laugwitz, and Terry Trevino for their technical assistance and Stanislav Emelianov for helpful discussion. This work was supported by Genelux, iThera Medical, a Service Grant awarded to the University of Würzburg, a Bundesministeriums für Bildung und Forschung Go-Bio award (to V.N.), graduate stipends from the University of Würzburg (to L.K., L.B., and M.H.), a postdoctoral fellowship (to U.D.) from a Research Service Grant awarded by Genelux Corporation to the University of Würzburg, and a European Research Council Senior Investigator Award (to V.N.).

1. Bourke MG, et al. (2011) The emerging role of viruses in the treatment of solid tumours. *Cancer Treat Rev* 37(8):618–632.
2. Pedersen JV, et al. (2011) A phase I clinical trial of a genetically modified and imageable oncolytic vaccinia virus GL-ONC1 with clinical green fluorescent protein (GFP) imaging. *J Clin Oncol* 29(suppl):abstr. 2577.
3. Zhang Q, et al. (2007) Eradication of solid human breast tumors in nude mice with an intravenously injected light-emitting oncolytic vaccinia virus. *Cancer Res* 67(20): 10038–10046.
4. Hess M, et al. (2011) Bacterial glucuronidase as general marker for oncolytic virotherapy or other biological therapies. *J Transl Med* 9:172.
5. Frentzen A, et al. (2009) Anti-VEGF single-chain antibody GLAF-1 encoded by oncolytic vaccinia virus significantly enhances antitumor therapy. *Proc Natl Acad Sci USA* 106(31):12915–12920.
6. Krumholz A, et al. (2011) Photoacoustic microscopy of tyrosinase reporter gene in vivo. *J Biomed Opt* 16(8):080503.
7. Premkumar A, et al. (1996) Metastatic melanoma: Correlation of MRI characteristics and histopathology. *J Magn Reson Imaging* 6(1):190–194.
8. DeJordy JO, Bendel P, Horowitz A, Salomon Y, Degani H (1992) Correlation of MR imaging and histologic findings in mouse melanoma. *J Magn Reson Imaging* 2(6):695–700.
9. Enochs WS, Petherick P, Bogdanova A, Mohr U, Weissleder R (1997) Paramagnetic metal scavenging by melanin: MR imaging. *Radiology* 204(2):417–423.
10. Paproski RJ, Forbrich AE, Wachowicz K, Hitt MM, Zemp RJ (2011) Tyrosinase as a dual reporter gene for both photoacoustic and magnetic resonance imaging. *Biomed Opt Express* 2(4):771–780.
11. Weissleder R, et al. (1997) MR imaging and scintigraphy of gene expression through melanin induction. *Radiology* 204(2):425–429.
12. Slominski A, Tobin DJ, Shibahara S, Wortsman J (2004) Melanin pigmentation in mammalian skin and its hormonal regulation. *Physiol Rev* 84(4):1155–1228.
13. Jöbsis FF (1977) Noninvasive, infrared monitoring of cerebral and myocardial oxygen sufficiency and circulatory parameters. *Science* 198(4323):1264–1267.
14. Ntziachristos V (2010) Going deeper than microscopy: The optical imaging frontier in biology. *Nat Methods* 7(8):603–614.
15. Wang LV, Hu S (2012) Photoacoustic tomography: In vivo imaging from organelles to organs. *Science* 335(6075):1458–1462.
16. Donat U, et al. (2012) Preferential colonization of metastases by oncolytic vaccinia virus strain GLV-1h68 in a human PC-3 prostate cancer model in nude mice. *PLoS ONE* 7(9):e45942.
17. Mårs U, Larsson BS (1999) Pheomelanin as a binding site for drugs and chemicals. *Pigment Cell Res* 12(4):266–274.
18. Ito S (2006) Encapsulation of a reactive core in neuromelanin. *Proc Natl Acad Sci USA* 103(40):14647–14648.
19. Glass K, et al. (2012) Direct chemical evidence for eumelanin pigment from the Jurassic period. *Proc Natl Acad Sci USA* 109(26):10218–10223.
20. Borisjuk L, Rolletschek H, Neuberger T (2012) Surveying the plant's world by magnetic resonance imaging. *Plant J* 70(1):129–146.
21. Falkner FG, Moss B (1988) Escherichia coli gpt gene provides dominant selection for vaccinia virus open reading frame expression vectors. *J Virol* 62(6):1849–1854.

Supporting Information

Stritzker et al. 10.1073/pnas.1216916110

SI Materials and Methods

Construction of Expression Plasmids and Melanin-rVACV Strains. The Multisite Gateway system (Life Technologies) was used to create expression plasmids of tyrosinase (*Tyr*), tyrosinase-related protein 1 (Tyrp1), and dopachrome tautomerase (*DCT*) in pLENTI6/V5-DEST. The cDNA encoding DCT and TYRP1 were obtained from human melanoma cell lines 1936-Mel after mRNA isolation (Qiagen) and reverse transcription using the Revertaid cDNA Synthesis Kit (Fermentas). ds cDNA was then produced by PCR using forward and reverse primers attB1-TYRP1-forward (5′-GGGGACAAGTTTGTACAAAAAAGCAGGCTG-CCACCGCCATGAGTGCTCCTAAACTCCTCT-3′) and attB2-TYRP1-reverse (5′-GGGGACCACTTTGTACAAGAAAGCT-GGGTTTGTTAGACCACAGACTGATTAGG-3′), respectively, for TYRP1, and attB1-DCT-forward (5′-GGGGACAAGT-TTGTACAAAAAAGCAGGCTGCCACCGCCATGAGCCCC-CTTTGG-3′) and attB2-DCT-reverse (5′-GGGGACCACTT-TGTACAAGAAAGCTGGGTAGCACCCTAGGCTTCTTCTG-TG-3′), respectively, for DCT. The attB1-TYRP1-forward and attB1-DCT-forward primers each contained a Kozak sequence for transcription initiation and attB1 sites for Gateway cloning. The attB2-TYRP1-rev and attB2-DCT-rev primers each contain attB2 sites for Gateway cloning.

The cDNA encoding murine Tyr was obtained by PCR from the pTRETyBS new plasmid (provided by Lluis Montoliu, Centro Nacional de Biotecnologia, Madrid, Spain) using attB1-mTYR-forward (5′-GGGGACAAGTTTGTACAAAAAAGCAGGCT-AGCTTAGTGTAAAACAGGCTGAG-3′) and attB2-mTYR-reverse (5′-GGGGACCACTTTGTACAAGAAAGCTGGGT-AATTCCGGAAATTCACAATGAAGTAAG-3′). The attB1-mTYR-forward primer contained an attB1 site and the attB2-mTYR-reverse contained an attB2 site for Gateway cloning.

Each PCR product was BP-cloned into donor vector pDONR221-DEST containing attP sites for recombination with pLENTI6/V5-DEST according to instructions from the manufacturer. Recombination into pLENTI6/V5-DEST was carried out via LR reaction according to the manufacturer's protocol to generate pLENTI6/V5-DCT, pLENTI6/V5-Tyrp1, and pLENTI6/V5-mTyr. Inserted sequences in resulting plasmids were confirmed by sequencing.

The cDNA encoding for Tyr and Tyrp1 were PCR-amplified from the plasmids pLENTI6/V5-Tyr and pLENTI6/V5-Tyrp1, respectively, using the primer pairs Tyr-5 (5′-*GTCGAC*CAC-CATGTTCTTGGCTGTTTTGTATTGCCT-3′)/Tyr-3 (5′-*TT-AATTAA*TCACAGATGGCTCTGATACAGC-3′) or Tyrp1-5 (5′-*GTCGAC*CACCATGAGTGCTCCTAAACTCCTCTCT-3′)/Tyrp1-3 (5′-*TTAATTAA*TTAGACCACAGACTGATTAGGAT-TCTGG-3′). The PCR products were gel-purified and cloned into the pCR-Blunt II-TOPO vector by using a Zero Blunt TOPO PCR Cloning Kit (Invitrogen). The resulting constructs were sequence-confirmed, released with SalI and *Pac*I, and subcloned into pTK-SE and pTK-SEL, respectively. The constructs pTK-SE-Tyr and TK-SEL-Tyr were sequence-confirmed and used to make recombinant viruses GLV-1h326 and GLV-1h327.

The transfer vector for GLV-1h322 was constructed as follows: The SE-Tyr cDNA was released from pTK-SE-Tyr with SacI, and the SE-Tyrp1 cDNA was released from pTK-SE-Tyrp1 with the same cut. The SE-mTyr and SE-Tyrp1 fragments were purified from gel and subjected to ligation with Quick Ligation Kit (New England BioLabs). The ligation products were then used as the template in a PCR with primers SE-Sal-Tyrp1 (5′-TTTTTTT-GCTCGAA*GTCGAC*CACCATGAGTGCTCC-3′) and Ter-PacI-Tyr (5′-GATCGATAAAAA*TTAATTAA*TCACAGATG*GCTCT-G*-3′). The PCR product was then infused with the pTK-SE fragment purified from gel after digestion of pTK-SE-mTyr-1 with SalI and *Pac*I. The infusion reaction as carried out using the In-Fusion PCR Cloning System (Clontech). The resulting construct TK-SE-Tyrp1-SE-Tyr was sequence confirmed, and used to make recombinant virus GLV-1h322.

The transfer vector for GLV-1h324 was constructed as follows: The SEL-Tyr cDNA was released from TK-SEL-Tyr with SacI, and the SE-Tyrp1 cDNA was released from pTK-SE-Tyrp1 with the same cut. The SEL-Tyr and SE-Tyrp1 fragments were purified from gel, ligated, and PCR-amplified with primers SE-Sal-Tyrp1 and Ter-PacI-Tyr. The PCR product was then infused with the pTK-SE fragment purified from gel after digestion of pTK-SE-Tyr with SalI and *Pac*I. The resulting construct TK-SE-Tyrp1-SEL-mTyr was sequence-confirmed and used to make recombinant virus GLV-1h324.

The recombinant vaccinia virus (rVACV) strains encoding Tyr are summarized under the term "melanin-rVACV" in this study.

Cell Culture. All cell lines were cultured in a humidified incubator at 37 °C and 5% CO_2 atmosphere. A549 cells were grown in RPMI medium supplemented with 10% FBS and 1% antibiotic/antimycotic solution (containing 10,000 IU/mL Penicillin, 10,000 μg/mL Streptomycin and 25 μg/mL Amphotericin B). B16F10, HeLa, PC-3, and PC-3-RFP cells were cultured in DMEM with 10% FBS, 1% antibiotic/antimycotic solution, and Blasticidin (10 μg/mL) for PC-3-RFP cells. For transfection and infection studies, cells were seeded 1 d before transfection so that, on the day of transfection, cells were approximately 50% to 70% and 80% to 90% confluent, respectively. Transfection was performed using GeneCellin (BioCellChallenge) according to instructions from the manufacturer. Infections were performed by using the indicated multiplicity of infection (MOI) in DMEM (no phenol red) with 2% FBS for 1 h before changing to DMEM (no phenol red) with 10% FBS.

Optical Density Measurements and Calculations. For optical density measurements, A549 cells which were infected with the indicated virus strains using an MOI of 0.1 were harvested by trypsin digestion and subsequent centrifugation. The cell pellets were resuspended in the same volume of PBS solution, and absorbance was measured in 10-nm increments from 350 nm to 1,000 nm on a SpectraMax M5 reader (Molecular Devices). Relative optical density, compared with GLV-1h68 infected cells, was calculated by dividing the absorbance data from each wavelength through the absorbance data of the GLV-1h68–infected cells at the same wavelength. As mock-infected cells are not killed by infecting virus, more cells were present in the same volume, which explains the higher absorption (also caused by increased scattering) compared with GLV-1h68–infected cells.

Measurement of RFP Fluorescence Signal Reduction by Melanin. Tumor cells in culture infected with GLV-1h68 and melanin-rVACVs, respectively (MOI of 0.1), were harvested by trypsination and centrifugation. Cell pellets were imaged and analyzed in a small animal imager (excitation, 530 nm; emission, 600 nm; Carestream Health) using the Molecular Imaging Second Edition software (version 5.0.6.20; Carestream Health). Background fluorescence was subtracted and data were presented as relative fluorescent units.

Glucuronidase-Based Viral Replication and Cell Killing Assay. All tested rVACV strains in this study encode the *Escherichia coli* glucuronidase gene *gusA* under control of the viral P11 promoter inserted into the viral A56R locus. We can therefore use the intracellular concentration of glucuronidase as a marker for viral replication, and glucuronidase in the cell culture supernatant as a marker for cell lysis (glucuronidase is a nonsecreted protein that will only have access to the supernatant upon cell death). The glucuronidase activity can be easily determined as previously described (1).

Laser-Induced Thermotherapy Treatment. A549 cells in T225 flasks were infected with 5×10^6 pfu of each rVACV strain or not infected. Three days later, cells were harvested by trypsin digest and centrifugation (1,800 × *g*, 5 min), and cell pellets were resuspended in 350 μL DMEM (no phenol red). From each cell suspension, three aliquots of 100 μL were transferred to 1.5 mL reaction tubes. One of these tubes was exposed to the 808-nm laser light (MDL-III-808 with PSU-III-LED power supply; 2,000 mW; Opto Engine) for 60 s, the other was exposed for 120 s, and the third was not exposed to the laser light at all. The temperature of the cell suspensions was measured (if applicable) immediately after exposing to the laser light using an AllTemp digital thermometer (Franmara), and cell viability of diluted samples ($n = 4$) was determined.

In virus (GLV-1h68 and GLV-1h324) colonized A549 tumors, tumors were exposed to laser light (2.00 W, $n = 4$ animals with one tumor in each virus strain group) for 120 s or not exposed to laser light ($n = 5$ in each virus strain group). Tumor volume was determined just before and 1 d and 5 d after laser treatment (50 d post tumor cell implantation and 36 d post virus injection).

B16F10 melanoma tumors were subject to laser treatment (2.00 W for 180 s) 3 d post tumor cell implantation (tumor diameter of approximately 2–3 mm). Five days later, the volume of laser treated and untreated B16F10 tumors was determined ($n = 5$ for each group).

Cell Viability Assays. Cell viability was determined by using MTT (2.5 mg/mL in DMEM without phenol red; Sigma-Aldrich) for adherent cells and 2,3-bis-(2-methoxy-4-nitro-5-sulfophenyl)-2H-tetrazolium-5-carboxanilide (Cell Proliferation Kit II; Roche) for cells in suspension according to instructions from the manufacturer.

Tumor Colonization and Regression Experiments. For tumor formation 1×10^5 B16F10, 5×10^6 A549, or 5×10^6 PC-3-RFP cells were implanted s.c. into athymic nude mice. Tumor volume was calculated from tumor length and width (i.e., as length × width^2 × 0.5). Systemic viral treatment of tumor bearing mice was initiated by injection of 5×10^6 pfu of the virus in 100 μL PBS solution into the retroorbital sinus vein.

In the A549 tumor regression experiment, the viral dose was injected when tumors reached a volume of ~300 mm^3. Tumor growth was monitored weekly. At the end of the experiment (5 wk for PBS solution control mice, 8 wk for rVACV-injected mice), tumors were isolated from perfused mice.

Multispectral Optoacoustic Tomography. The images were acquired by using an inVision128 small animal imaging system (iThera) with a resolution of 150 μm in the imaging plane. Short laser pulses in the nanosecond range with variable wavelength in the near-IR optical window are generated by a wavelength-tunable Nd:yttrium aluminum garnet pumped optical parametric oscillator laser for illumination while an arc-shaped tomographic ultrasound detector array with 128 elements (coverage, 270°; central frequency, 5 MHz; bandwidth, 55%) acquires acoustic signals in the μV range that are converted to digital values with 12-bit accuracy. The transducers are focused cylindrically to collect signals only from a selected imaging plane while the subject can be translated perpendicular to the imaging plane to acquire images from multiple positions (2). For each position and wavelength 25 acquisitions were averaged, resulting in a total acquisition time of 2.5 s per individual image. Tomographic reconstruction algorithms that model detector geometry can produce an accurate image of the acoustic pressure distribution map inside the sample (3). For the in vivo experiments, images were acquired multispectrally by using 11 wavelengths in 15-nm intervals starting from 700 nm up to 850 nm to excite the acoustic signals from tissue. Image processing (i.e., spectral unmixing) enabled the separation of components in the images that correspond to the spatial distributions of absorbers with distinct spectral absorption profiles. In this particular case, the melanin spatial distribution could be determined by separating out the background component of deoxygenated and oxygenated hemoglobin that dominate the absorption contrast in tissue. Spectral unmixing was performed by independent component analysis, which was used as a mean of multispectral processing (4) by using statistical properties inside the multispectral data, and thus adapting to the imaging scenario. To retrieve reproducible results, the method was calibrated on a positive cross-section image by using literature values for the absorption profiles of melanin and hemoglobin (http://omlc.ogi.edu/spectra/). The resulting optimized unmixing matrix was then saved and reapplied for all other datasets to create reproducible results. In Fig. 3*D* and Figs. S5 and S6, the melanin component images are mapped by using a pseudocolor palette and are overlaid on a corresponding background single (850 nm) wavelength image by using a variable transparency function as illustrated by the color bar, on which the checkerboard background symbolizes the maximum contrast colors in the background image. For the in vivo experiments, the animal was mounted in a holder and submerged into a water bath for acoustic coupling between the tissue and the detector. To protect the animal from drowning, it was wrapped by a thin polyethylene membrane while gas anesthesia using isoflurane was supplied through a breathing mask. Live mice were imaged at 2 or 3 wk post virus injection for PC-3-RFP–tumor bearing mice and 4 wk post virus injection for A549 tumor-bearing mice. For Fig. 3*E*, obtained signal intensities were determined and all signals >1 were averaged for each tumor or lymph node metastasis. As could be expected, the area containing signals with melanin signature was much bigger in the melanin-rVACV–injected mice compared with control-rVACV–injected mice.

For cell imaging, ~10^7 cells suspended in 100 μL PBS solution were added to 0.2 mL PCR tubes and slightly centrifuged to form a pellet. The vials were placed in the center of the field of view of the multispectral optoacoustic tomographic (MSOT) imaging system, next to a vial containing black India ink solution with known optical properties ($\mu_a = 0.5$ and 1 cm^{-1}, $\mu'_s = 10$ cm^{-1}) that was used for normalization and absolute quantification of the absorption by cells. The vials were imaged in the 690- to 900-nm range, averaging 30 acquisitions, and the absorption of the cells was determined by normalizing the pixel intensities of the reconstructed images with the ink solution and the background.

Cryosectioning. After in vivo MR or MSOT imaging, mice were perfused with 20 mL PBS solution followed by 10 mL Z-fix (AnaTech) and then frozen at −80 °C. The frozen mouse bodies were then subject to cryosectioning with a CM 1950 cryotome (Leica Microsystems), and each section was photographed, resulting in a stack of images that enabled a 3D reconstruction of the mouse tissue (5). The volume viewer plug-in function in the open-source ImageJ software (National Institutes of Health) was used to find the slices obtained from the MRI results.

MRI. Tumor cells in T225 flasks were infected with rVACVs using a MOI of 0.1 if not otherwise indicated. Mock-infected cells served as control. For infection, virus was diluted in 10 mL DMEM (without phenol red) with 2% FBS, and the cells were infected for 1 h at 37 °C, after which another 10 mL medium (DMEM without phenol red and 20% FBS and 300 μM ferric citrate) were added. If not otherwise indicated, cells were harvested for analysis 3 d after infection and resuspended in PBS solution at a concentration of 1×10^5 cells per 100 μL. Two hundred microliters of this suspension were used for T1-relaxation measurements in a small-animal 7-T MRI scanner (Bruker BioSpec).

Live tumor-bearing mice were imaged 4 wk (A549 tumor model) and 1 or 2 wk (PC-3-RFP tumor model) after virus injection, respectively. Mice were imaged on a 7-T small-animal imaging system (Bruker BioSpec). For each mouse, T1-weighted (T1W) imaging through the tumor was performed [multislice–multiecho sequence, repetition time (TR), 927 ms; echo time (TE), 10.6 ms; four excitations; matrix, 256 × 256; field of view, 2.8 cm; slice thickness, 0.5 mm; 35 slices] and T1 relaxation time maps [rapid aquisition with refocused echos (RARE)-T1+T2-map saturation recovery TR/TE, 5000–200/11–99 ms] were acquired on a single slice through the center of the tumors. The T1 value of each tumor was averaged from the calculated T1 values in each pixel of a manually drawn region of interest, which included the whole tumor. For muscle tissues, average T1 values of a region of interest in the muscle tissue was calculated.

Ex vivo T1W imaging of agarose gel-embedded A549 tumors was obtained by using a 3-T clinical MRI scanner (Discovery MR 750; General Electric) and a T1W sequence as follows: fast relaxation fast spin-echo sequence, slice thickness of 1 mm, TE of 14 ms, TR of 120 ms, three averages, matrix of 256 × 256.

Histology and Immunohistochemistry. PC-3-RFP tumor-bearing mice were perfused as described earlier after MRI. To correlate melanin production in the lymph node metastases with MR signal, internal organs were removed and images were taken. This was followed by decalcification (5 d in Z-fix with 10% formic acid at 4 °C with daily changes of the solution), dehydration, paraffin embedding, and sectioning (10-μm slices). Paraffin sections were transferred on glass slides and subsequent slices within 100 μm were stained with (*i*) hematoxylin (blue; Vector Laboratories) and eosin (red; Carl-Roth), (*ii*) hematoxylin and an anti-rVACV staining [red; rabbit anti-vaccinia A27L first antibody detected by ImmPRESS Reagent (HRP) anti-rabbit stained with ImmPACT AMEC red peroxidase staining solution; Vector Laboratories], (*iii*) the anti-rVACV staining only, or (*iv*) no staining with the brown melanin giving the only contrast.

The specimens were then examined with a stereo-fluorescence microscope (MZ16 FA; Leica) equipped with a digital CCD camera (DC500; Leica) and IM1000 4.0 software (1,300 × 1,030 pixel RGB color images; Leica). Higher-magnification images were obtained by using an Axiovert 200 M microscope equipped with a digital AxioCam MRc5 (Zeiss) and Axiovision 4.5 software (1,293 × 968 fast bin 2 × 2 color; RGB color images). Stainings were visualized by using white light. Digital images were processed with Photoshop 7.0 (Adobe Systems).

Statistical Analysis. A two-tailed Student *t* test was used for statistical analysis. *P* values of ≤0.05 were considered statistically significant.

Ethical Statement. All animal experiments were carried out in accordance with protocols approved by the Regierung von Unterfranken (Würzburg, Germany; Protocol AZ 55.2–2531.01–17/08) and/or the Institutional Animal Care and Use Committee of Explora BioLabs (located in the San Diego Science Center, San Diego, CA; Protocol EB11-025) and/or the Institutional Animal Care and Use Committee of the University of California at San Diego (Protocol R08335).

1. Hess M, et al. (2011) Bacterial glucuronidase as general marker for oncolytic virotherapy or other biological therapies. *J Transl Med* 9:172.
2. Buehler A, Herzog E, Razansky D, Ntziachristos V (2010) Video rate optoacoustic tomography of mouse kidney perfusion. *Opt Lett* 35(14):2475–2477.
3. Rosenthal A, Razansky D, Ntziachristos V (2010) Fast semi-analytical model-based acoustic inversion for quantitative optoacoustic tomography. *IEEE Trans Med Imaging* 29(6):1275–1285.
4. Glatz J, Deliolanis NC, Buehler A, Razansky D, Ntziachristos V (2011) Blind source unmixing in multi-spectral optoacoustic tomography. *Opt Express* 19(4):3175–3184.
5. Sarantopoulos A, Themelis G, Ntziachristos V (2011) Imaging the bio-distribution of fluorescent probes using multispectral epi-illumination cryoslicing imaging. *Mol Imaging Biol* 13(5):874–885.

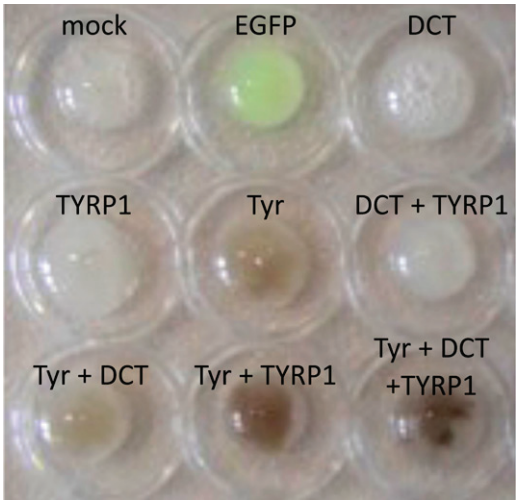

Fig. S1. Melanin production upon expression of key genes in melanogenesis. Photograph of resuspended HeLa cell pellets after transformation with EGFP-, Tyr-, Tyrp1-. and/or DCT-encoding plasmids.

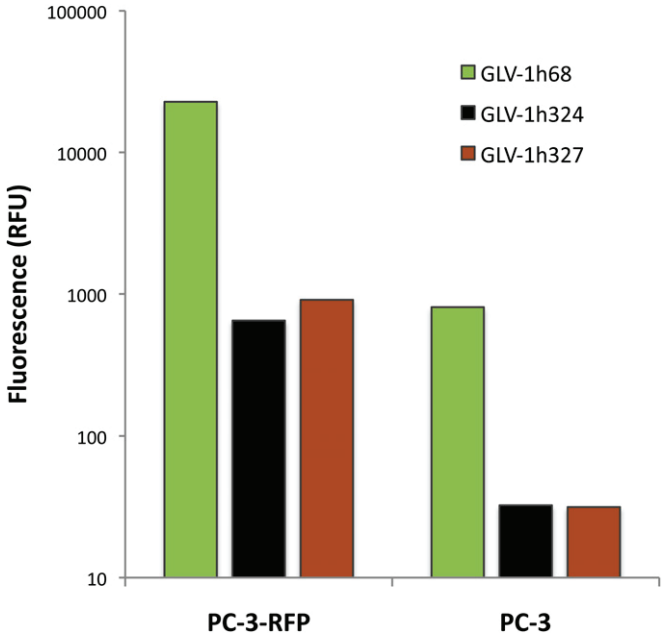

Fig. S2. Biosynthesis of melanin drastically reduces the fluorescent signal of RFP and autofluorescence in melanin-rVACV–infected cells. The RFP fluorescence of the melanin-rVACV–infected PC-3-RFP cells is reduced to the levels of autofluorescence in no RFP-expressing PC-3 control cells. In addition, the autofluorescent signal is also reduced. For the particular experiment, an excitation wavelength of 530 nm and an emission wavelength of 600 nm were used, respectively.

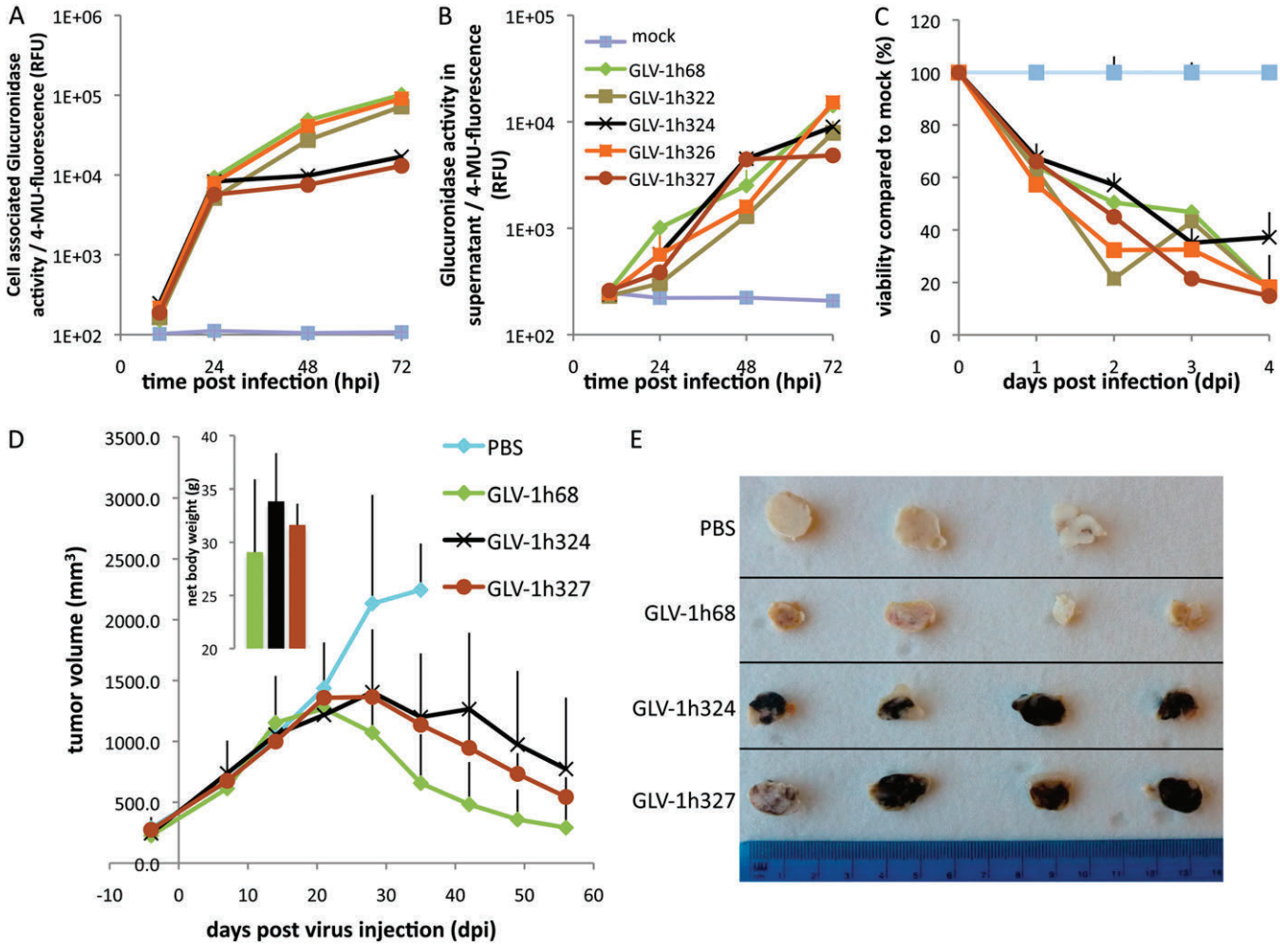

Fig. S3. The biosynthesis of melanin reduces viral replication but not virus-mediated cell lysis or tumor regression. (*A*) Replication assay using cell associated glucuronidase activity as marker for viral replication. Glucuronidase cleaves the 4-MUG substrate to the fluorescent compound 4-MU. (*B*) Presence of non-secreted glucuronidase activity in the supernatant indicates cell lysis. (*C*) Cell viability measured over time by MTT assay. (*D*) A549 tumor volume over time. Tumor regression is decelerated in melanin-rVACV–injected mice compared with control-rVACV–injected mice. Data represent average values plus SD ($n = 8$ tumors in four mice). The average net body weight (mouse weight without tumor; *Inset*) as an indicator for well-being is higher in groups with slower tumor regression. (*E*) Photograph of isolated cut-open tumors at the end of the study (5 wk post injection for PBS control, 8 wk post injection for rVACV-injected groups) clearly demonstrates production of melanin in melanin-rVACV–colonized tumors.

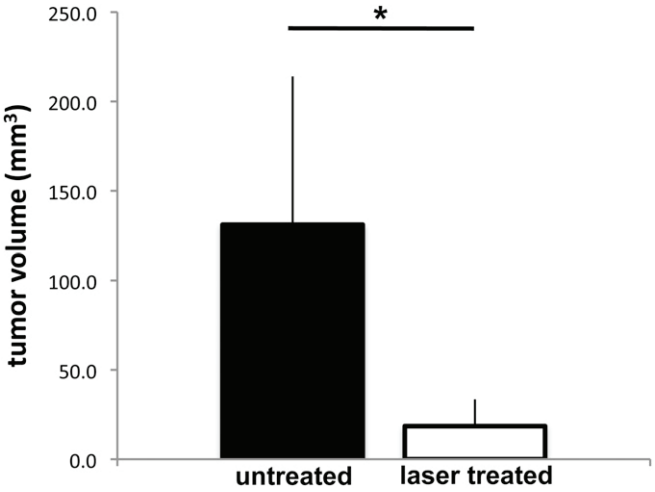

Fig. S4. Near-IR laser-induced thermotherapy treatment of B16F10 melanoma in mice. When tumors reached a diameter of approximately 2 to 3 mm, they were exposed to near-IR laser light (808 nm, 2.00 W) for 3 min or left untreated ($n = 5$ for each group). Five days later, tumor volume was determined, and significant differences (*$P < 0.05$) were observed between the two groups.

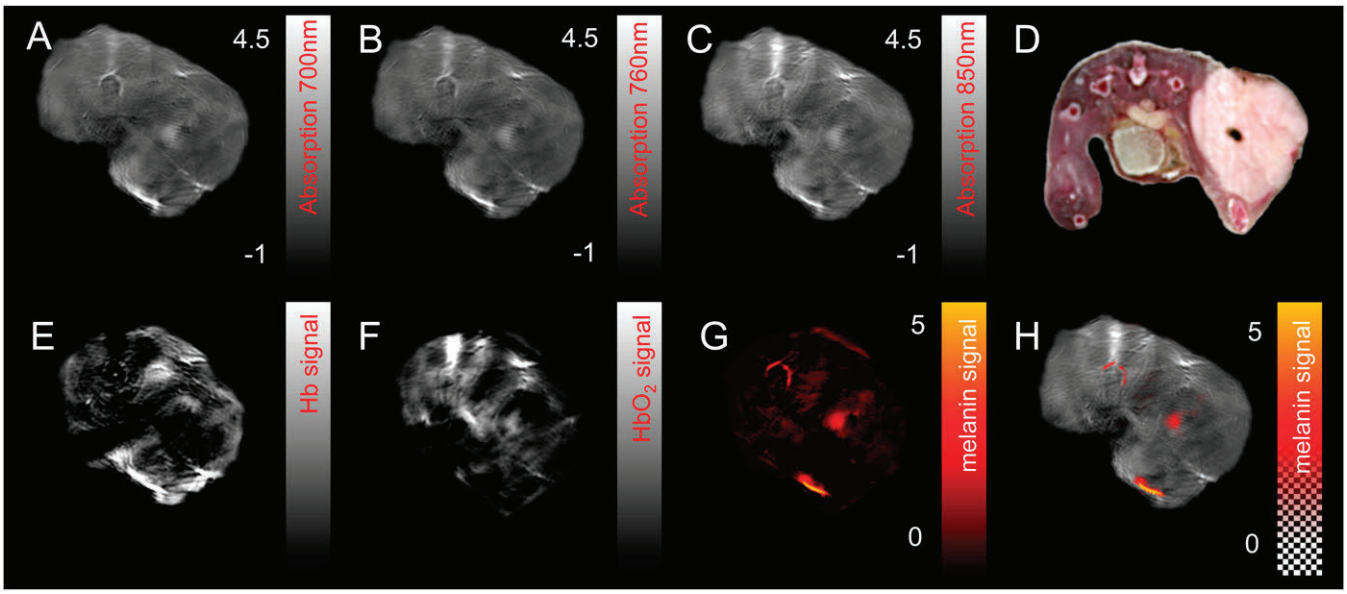

Fig. S5. Generation of melanin-specific MSOT images. Optoacoustic images at characteristic wavelengths (*A*) 700 nm, (*B*) 760 nm, and (*C*) 850 nm do not reveal the distinct absorption of melanin; (*D*) cryosection of the same mouse shown in the other images at approximately the same plane; (*E*) hemoglobin (Hb) signal; (*F*) oxygenated hemoglobin (HbO_2) signal; (*G*) heat map of melanin signal from multispectral imaging; and (*H*) overlay of heat map (*G*) over absorption scan image (*C*) using additional α-blending.

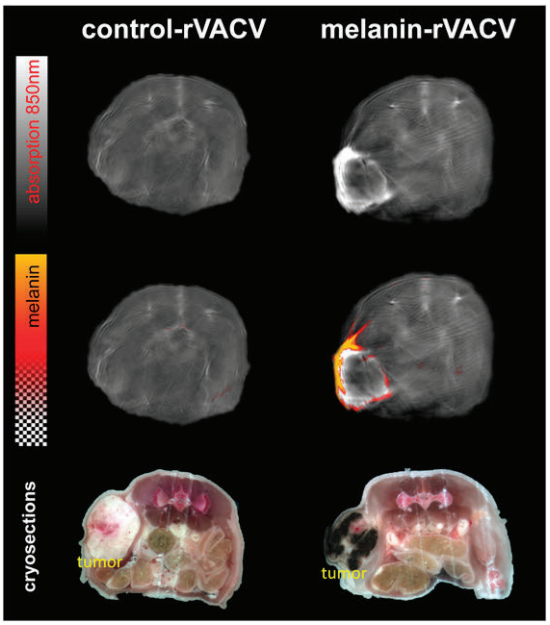

Fig. S6. Detection of melanin production in A549 tumors by multispectral optoacoustic imaging. Melanin is produced throughout the tumor in the melanin-rVACV–injected mouse; however, the optoacoustic melanin signal is mostly detected at the rim of the tumor mass, as a result of the strong absorption of the excitation light that cannot penetrate deeper into the tumor. Control-rVACV–injected mice do not give rise to a melanin signal.

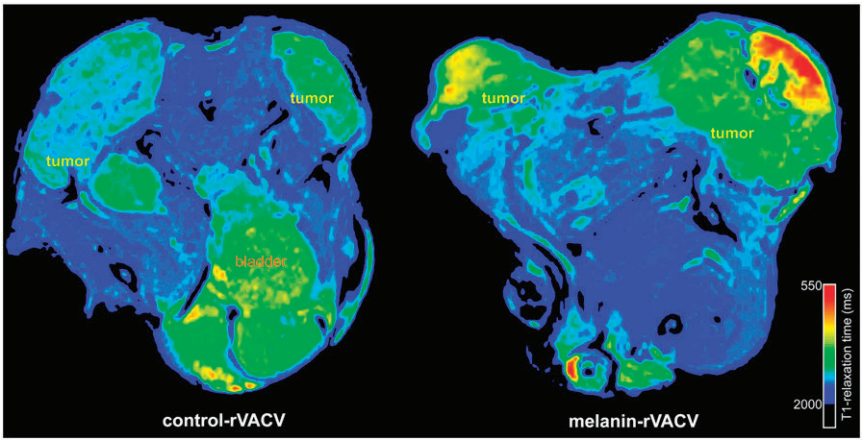

Fig. S7. T1-maps of A549 tumor-bearing mice injected with control- or melanin-rVACV.

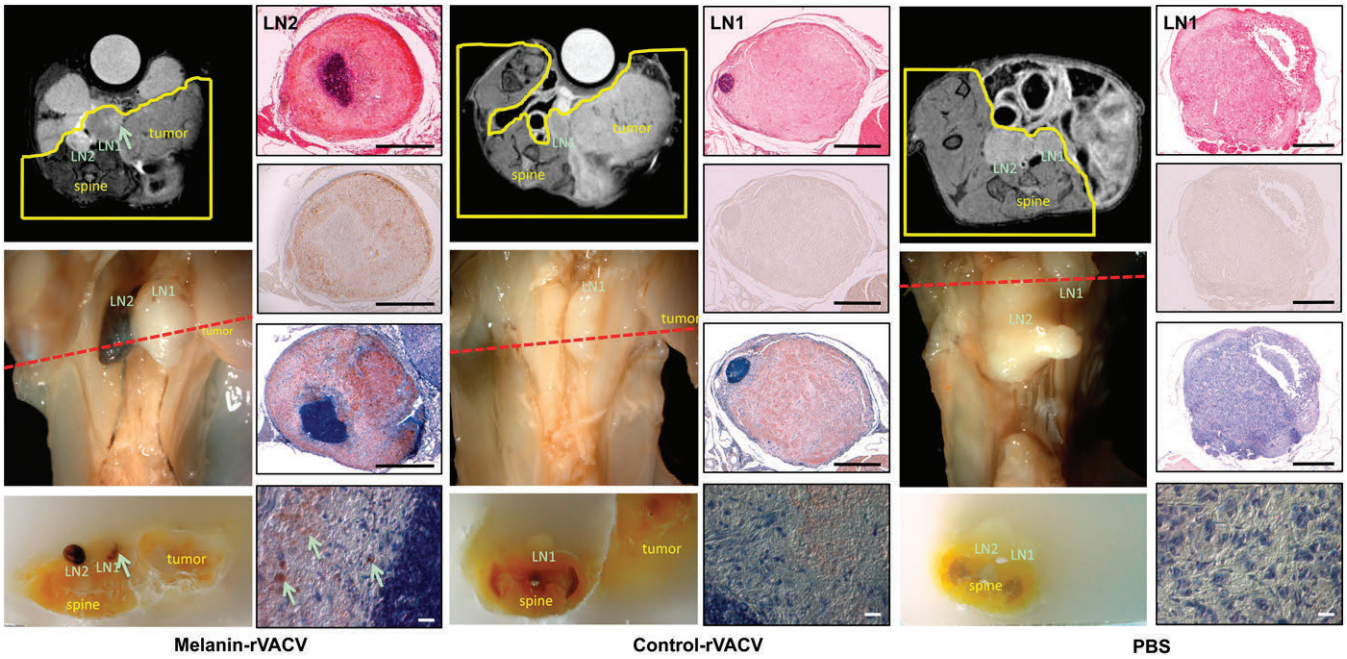

Fig. S8. Analysis of metastases from PC-3-RFP tumor-bearing mice. Magnetic resonance images of live tumor-bearing mice showing spine, tumor, and lymph node metastases (LN1 and LN2; *Top Left*). LN2 in the melanin-rVACV–injected mouse is much brighter than LN1 in the same mouse (which has a brighter region, indicated by the arrow, on the tumor-proximal side) and lymph node metastases of the control-rVACV– or PBS solution-injected mouse, respectively. After perfusion, the internal organs were removed (leaving behind the yellow encircled tissue), and images of the same mice were obtained (*Middle Left*). In the melanin-rVACV–injected mouse, the melanin-producing LN2 is clearly visible, as well as the lymph vessels, which are filled with melanin-containing cancer cells. The red dotted line indicates approximately where the magnetic resonance image was located. The paraffin-embedded mice were cut at the same site (*Bottom Left*), and melanin production colocalized with the bright regions in the lymph node metastases of the magnetic resonance image (indicated by arrows in magnetic resonance image and photograph of paraffin block). Immunohistological analysis of the same lymph nodes are presented (*Right*). (*Right*) From top to bottom, images represent an H&E straining (blue nuclei, red cytoplasm); unstained lymph node slices (melanin is brown); anti-vaccinia virus staining (red) with hematoxylin counterstain (blue); high-resolution image of anti-vaccinia virus staining from above. Melanin is located inside (rVACV-containing) tumor cells [arrows in high-magnification image (*Bottom*)]. In virus-treated lymph node metastases, the virus induces necrosis, and a higher amount of dead cells compared with PBS solution control were detected. (Scale bars: black, 0.5 mm; white, 20 μm.)

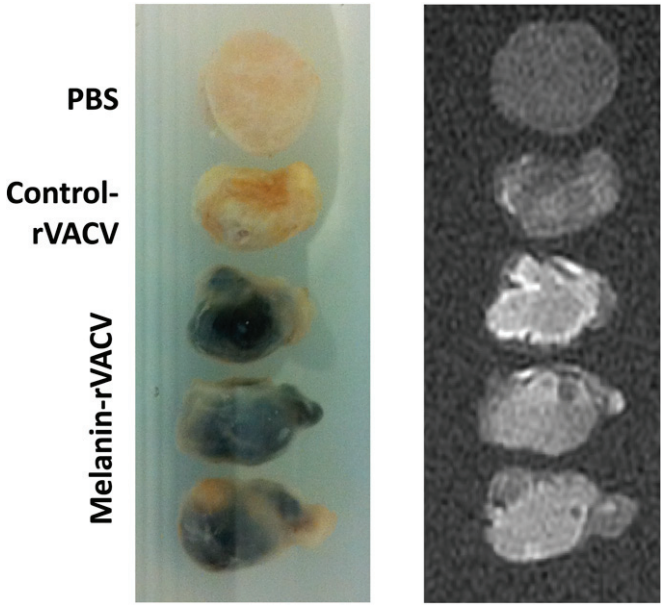

Fig. S9. Melanin-dependent signal enhancement in a clinical 3-T MRI scanner. Isolated A549 tumors were embedded in agarose (*Left*) and scanned at 3 T (*Right*). Melanin-containing regions appear bright on the T1-weighted images, whereas no melanin-containing tumors (or tumor regions) appear darker on the same images.

Publication (complete reference): Patil SS, Gentschev I, Adelfinger M, Donat U, **Hess M**, Weibel S, Nolte I, Frentzen A, Szalay AA. Virotherapy of canine tumors with oncolytic Vaccinia virus GLV-1h109 expressing an anti-VEGF single-chain antibody. *PLoS One*. 2012;7:e47472
Authors' contributions
Conceived and designed the experiments: IG SSP MA UD **MH** AAS. Performed the experiments: SSP IG MA UD **MH** SW. Analyzed the data: IG SSP MA AF AAS. Contributed reagents/materials/analysis tools: UD IN AF. Wrote the paper: IG SSP AAS.

Sandeep S. Patil	
Ivaylo Gentschev	
Marion Adelfinger	
Ulrike Donat	
Stephanie Weibel	
Ingo Nolte	
Alexa Frentzen	
Aladar A. Szalay	

OPEN ACCESS Freely available online

PLOS ONE

Virotherapy of Canine Tumors with Oncolytic Vaccinia Virus GLV-1h109 Expressing an Anti-VEGF Single-Chain Antibody

Sandeep S. Patil[1☯], Ivaylo Gentschev[1,2☯], Marion Adelfinger[1], Ulrike Donat[1], Michael Hess[1], Stephanie Weibel[1], Ingo Nolte[3], Alexa Frentzen[2], Aladar A. Szalay[1,2,4,5,6]*

1 Department of Biochemistry, University of Wuerzburg, Wuerzburg, Germany, **2** Genelux Corporation, San Diego Science Center, San Diego, California, United States of America, **3** Small Animal Clinic, University of Veterinary Medicine, Hannover, Germany, **4** Rudolf Virchow Center for Experimental Biomedicine, University of Wuerzburg, Wuerzburg, Germany, **5** Institute for Molecular Infection Biology, University of Wuerzburg, Wuerzburg, Germany, **6** Department of Radiation Oncology, Moores Cancer Center, University of California San Diego, La Jolla, California, United States of America

Abstract

Virotherapy using oncolytic vaccinia virus (VACV) strains is one promising new strategy for cancer therapy. We have previously reported that oncolytic vaccinia virus strains expressing an anti-VEGF (Vascular Endothelial Growth Factor) single-chain antibody (scAb) GLAF-1 exhibited significant therapeutic efficacy for treatment of human tumor xenografts. Here, we describe the use of oncolytic vaccinia virus GLV-1h109 encoding GLAF-1 for canine cancer therapy. In this study we analyzed the virus-mediated delivery and production of scAb GLAF-1 and the oncolytic and immunological effects of the GLV-1h109 vaccinia virus strain against canine soft tissue sarcoma and canine prostate carcinoma in xenograft models. Cell culture data demonstrated that the GLV-1h109 virus efficiently infect, replicate in and destroy both tested canine cancer cell lines. In addition, successful expression of GLAF-1 was demonstrated in virus-infected canine cancer cells and the antibody specifically recognized canine VEGF. In two different xenograft models, the systemic administration of the GLV-1h109 virus was found to be safe and led to anti-tumor and immunological effects resulting in the significant reduction of tumor growth in comparison to untreated control mice. Furthermore, tumor-specific virus infection led to a continued production of functional scAb GLAF-1, resulting in inhibition of angiogenesis. Overall, the GLV-1h109-mediated cancer therapy and production of immunotherapeutic anti-VEGF scAb may open the way for combination therapy concept i.e. vaccinia virus mediated oncolysis and intratumoral production of therapeutic drugs in canine cancer patients.

Citation: Patil SS, Gentschev I, Adelfinger M, Donat U, Hess M, et al. (2012) Virotherapy of Canine Tumors with Oncolytic Vaccinia Virus GLV-1h109 Expressing an Anti-VEGF Single-Chain Antibody. PLoS ONE 7(10): e47472. doi:10.1371/journal.pone.0047472

Editor: Chandravanu (CV) Dash, Meharry Medical College, United States of America

Received July 6, 2012; **Accepted** September 11, 2012; **Published** October 16, 2012

Funding: The research was supported by the Research and Development Division of Genelux Corporation, San Diego, USA, and a Service Grant to the University of Würzburg, Germany also funded by Genelux Corp., San Diego, USA. IG AF and AAS are employees and shareholders of Genelux. MA, UD, MH and SW were supported by grants of Genelux Corporation. SSP is a graduate fellow and supported by a grant of the German Excellence Initiative to the Graduate School of Life Sciences, University of Wuerzburg. This publication was funded by the German Research Foundation (DFG) and the University of Wuerzburg in the funding programme Open Access Publishing. No additional external funding was received for this study. The funders had no role in study design, data collection and analysis, decision to publish, or preparation of the manuscript.

Competing Interests: I. Gentschev, A. Frentzen and A. A. Szalay have financial interests in Genelux Corporation, and M. Adelfinger U. Donar, M. Hess and S. Weibel were supported by grants of Genelux Corporation. This does not alter the authors' adherence to all the PLOS ONE policies on sharing data and materials. However, no direct financial support was provided by Genelux for the completion of this study.

* E-mail: aaszalay@genelux.com

☯ These authors contributed equally to this work.

Introduction

Cancer is the leading cause of disease-related death in dogs worldwide ([1], National Canine Cancer Foundation). Incidence of cancer ranges from 1 to 2% in the canine population and is currently the leading cause of deaths in dogs older than 10 years [1–2]. The major treatment options available for canine cancers include surgery, radiation therapy, chemotherapy, hyperthermia and photodynamic therapy. Despite progress in the diagnosis and treatment of advanced canine cancer, overall patient treatment outcome has not substantially improved in the past. Therefore, the development of new therapies for advanced canine cancer is a high priority. One of the most promising novel cancer therapies is oncolytic virotherapy. This method is based on the capacity of oncolytic viruses (OVs) to preferentially infect and lyse cancer cells without causing excessive damage to surrounding normal tissues. Several oncolytic viruses including various human and canine adenoviruses, canine distemper virus (CDV) and vaccinia virus strains have been successfully tested for canine cancer therapy in preclinical settings (for review see [3]).

In this study, we analyzed the therapeutic potential of the oncolytic vaccinia virus GLV-1h109 strain in two different xenograft models based on canine soft tissue sarcoma STSA-1 cells [4] and canine prostate carcinoma DT08/40 cells [5]. GLV-1h109 virus was derived from the oncolytic vaccinia virus GLV-1h68 [6] by replacing *lacZ* gene (beta-galactosidase) with GLAF-1 protein encoding gene at *J2R* locus [7]. The *glaf-1* gene encodes the single chain anti-VEGF antibody. GLAF-1 protein, comprises of an Igê light chain leader sequence [8], the V_H chain sequence of

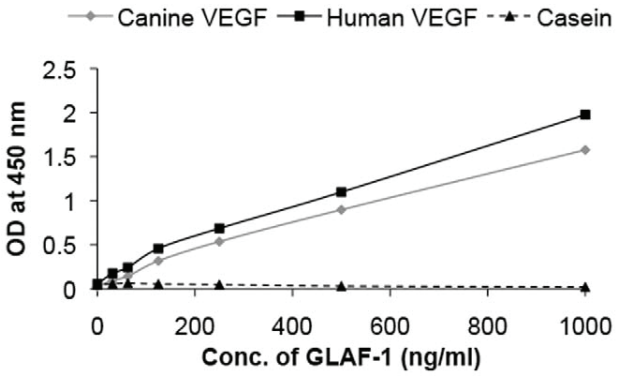

Figure 1. Interaction of purified GLAF-1 antibody with human and canine VEGF. Affinity and cross reactivity of GLAF-1 was demonstrated by ELISA. Equal concentrations of human or canine VEGF (100 ng/well) were coated on ELISA plates. Six two-fold dilutions of purified GLAF-1 protein ranging from 1000 ng/ml to 31.3 ng/ml were incubated with both human and canine VEGF. Plates pre-coated with 1% (w/v) casein (Pierce, 37528) were used as negative control. For further ELISA experimental conditions see material and methods (GLAF-1 ELISA). ODs obtained for various conc. of GLAF-1 against both human and canine VEGF were plotted. ELISA was repeated (n = 3) in an independent experiment.
doi:10.1371/journal.pone.0047472.g001

the G6–31 antibody [9], a $(G_4S)_3$ linker sequence, the V_L chain sequence of the G6–31 antibody [9], and a C-terminal DDDDK sequence [7]. The G6–31 antibody binds both murine (mu) and human (hu) vascular endothelial growth factor (VEGF) with high affinity [9]. The GLAF-1 antibody encoded by VACV strain GLV-h109 is expressed under the control of the vaccinia virus synthetic late (SL) promoter and also recognizes specifically mu and huVEGF [7]. However, cross reactivity of GLAF-1 with VEGF protein from other species was not known. VEGF or VEGF-A is a potent regulator of angiogenesis and therefore several anti-VEGF strategies have been developed for the treatment of human and canine tumors [10] [11,12]. One of the best characterized strategies is the VEGF blockade using the humanized anti-VEGF monoclonal antibody (mAb) bevacizumab (avastin). However, despite very promising preclinical results, bevacizumab has not been shown to provide a benefit in patients with breast cancer (http://www.fda.gov/NewsEvents/Newsroom/PressAnnouncements/ucm279485.htm) or when used in combination with chemotherapy for the treatment of colorectal cancer and non-small-cell carcinoma in humans [13]. The molecular and cellular events underlying resistance to anti-VEGF antibody-based therapy are not completely understood [14]. However, the lack of efficacy of bevacizumab after systemic treatment in patients may be at least attributable to the poor penetration of this antibody into the tumor tissue and metastases. Therefore, new methods or vectors allowing more specific delivery of the anti-VEGF antibodies into the tumor tissue are urgently necessary. We have already shown that the recombinant Vaccinia virus strains (VACV) expressing the GLAF-1 antibody exhibited enhanced tumor inhibition and therapeutic potency, which was comparable to the results seen in combination therapy with separately injected bevacizumab and the parental virus GLV-1h68 [7]. Therefore, the GLV-1h109 virus dependent, intratumoral expression of GLAF-1 may become a new method allowing more optimal continuous delivery of this antibody into tumor tissues in dogs.

Here, we report the virus-mediated oncolytic and immunological effects upon colonization of GLV-1h109 and the constitutive intratumoral GLAF-1 production in STSA-1- and DT08/40 tumor bearing xenograft mice monitored by fluorescence imaging, Western Blot analysis, immunohistochemistry, flow cytometry and ELISA.

Materials and Methods

Ethics Statement

All animal experiments were carried out in accordance with protocols approved by the Institutional Animal Care and Use Committee (IACUC) of Explora Biolabs (San Diego, CA, USA; protocol number: EB11-025) and/or the government of Unterfranken, Germany (permit number: 55.2-2531.01-17/08).

Cell Culture

African green monkey kidney fibroblasts (CV-1) were obtained from the American Type Culture Collection (ATCC). STSA-1 cells were derived from a canine patient with a grade II soft tissue sarcoma [4]. DT08/40 is a canine prostate carcinoma cell line [5].

CV-1 and DT08/40 cells were cultured in DMEM supplemented with antibiotic-solution (100 U/ml penicillin G, 100 units/ml streptomycin) and 10% fetal bovine serum (FBS; Invitrogen GmbH, Karlsruhe, Germany) for CV-1 and 20% FBS for DT08/40. STSA-1 cells were cultured in minimum essential medium with Earle's salts supplemented with 2 mM glutamine, 50 U/mL penicillin G, 50 µg/mL streptomycin, 1 mM sodium pyruvate, 0.1 mM nonessential amino acids (MEM-C), and 10% FBS. All cell lines were cultured at 37°C in a 5% CO_2 humidified incubator.

VEGF ELISA

For the quantitative determination of canine VEGF concentrations in STSA-1 and DT08/40 cell culture supernatants; 5×10^6 cells were cultured under the conditions of MEM and DMEM respectively, containing 10% FBS. Cell culture supernatants were collected at 24 and 48 h and stored at −20°C. Concentrations of VEGF were determined by canine VEGF Quantikine ELISA kit (R&D Systems, Minneapolis, MN, USA) according to the manufacturer's protocol.

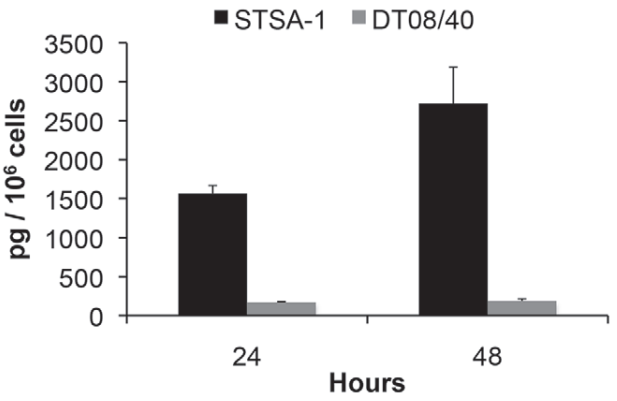

Figure 2. VEGF expression in STSA-1 and DT08/40 canine cancer cells under cell culture conditions. STSA-1 and DT08/40 cells in culture conditions were washed with PBS and cultured in fresh medium with 2% FCS. Culture supernatants were harvested at 24 and 48 h. VEGF levels in supernatants were determined by canine VEGF Quantikine ELISA kit (R&D Systems, Minneapolis, MN, USA). Each value represents the mean (n = 3) +/- standard deviations (SD).
doi:10.1371/journal.pone.0047472.g002

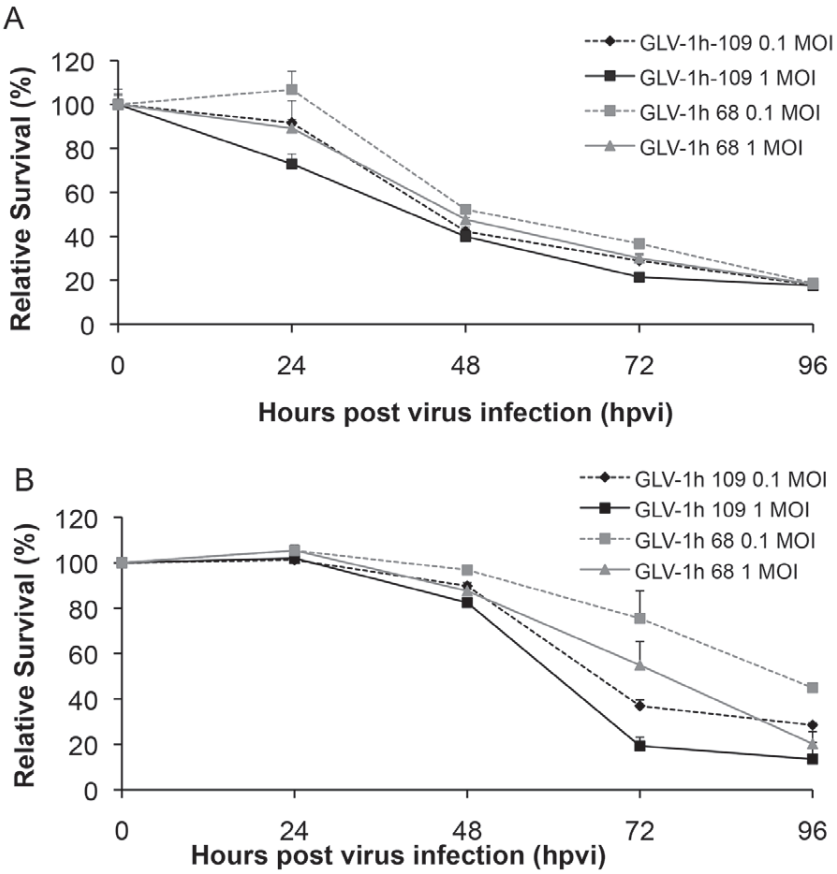

Figure 3. Viability of (A) canine soft tissue sarcoma (STSA-1) and (B) prostate carcinoma (DT08/40) cells after GLV-1h109 or GLV-1h68 infection. Viable cells after infections with two viruses at MOIs of 0.1 and 1.0 were detected using a XTT assay (Cell Proliferation Kit II, Roche Diagnostics, Mannheim, Germany) (Sigma, Taufkirchen, Germany). Mean values (n = 3) and standard deviations are shown as percentages of respective controls. The data represent three independent experiments. There were no significant differences between groups at 72 and 96 hpvi ($P>0.05$).
doi:10.1371/journal.pone.0047472.g003

Virus Strains

GLV-1h68 is an oncolytic vaccinia virus strain designed to locate, enter, colonize and destroy cancer cells without harming healthy tissues or organs [6]. GLV-1h109 is a GLV-1h68-derivative expressing an anti-VEGF single-chain antibody GLAF-1 [7].

Cell Viability Assay

1×10^4 cells/well were seeded in 96-well plates (Nunc, Wiesbaden, Germany). After 24 h in culture, cells were infected with vaccinia virus strains using multiplicities of infection (MOI) of 0.1 and 1.0. The cells were incubated at 37°C for 1 h, then the infection medium was removed and subsequently the cells were incubated in fresh growth medium.

The amount of viable cells after infection was measured using 2,3-bis[2-methoxy-4-nitro-5-sulfophenyl]-2*H*-tetrazolium-5-carboxanilide inner salt (XTT) assay (Cell Proliferation Kit II, Roche Diagnostics, Mannheim, Germany), according to the manufacturer's protocol at 24, 48,72 or 96 h after infection. Quantification of cell viability was performed in an ELISA plate reader (Tecan Sunrise, Tecan Trading AG, Austria) at 490 nm with a reference wavelength of 690 nm. The relative number of viable cells was expressed as percent cell viability. Uninfected cells were used as reference and were considered as 100% viable.

Viral Replication

For the viral replication assay, cells grown in 24-well plates were infected with either GLV-1h68 or GLV-1h109 at an MOI of 0.1. After one hour of incubation at 37°C with gentle agitation every 20 min, the infection medium was removed and replaced by a fresh growth medium. After 1, 12, 24, 48, 72 and 96 hours, the cells and supernatants were harvested. Following three freeze-thaw cycles, serial dilutions of the supernatants and lysates were titered by standard plaque assays on CV-1 cells. All samples were measured in triplicate.

Western Blot Analysis

For detection of proteins, supernatants and infected cells were harvested and resuspended in SDS sample buffer at 24 and 48 hours post virus infection (hpvi). Samples were separated by 10% SDS-Polyacrylamide gel electrophoresis and subsequently transferred onto a nitrocellulose membrane (Whatman GmbH, Dassel, Germany). After blocking in 5% skim milk in PBS, the membrane was incubated with rabbit anti-DDDDK antibody (ab21536, Abcam, Cambridge, UK) for detection of scAb GLAF-1, anti-beta-glucuronidase rabbit polyclonal antibody (G5420, Sigma-Aldrich, Schnelldorf, Germany) or anti-beta-actin mouse monoclonal antibody (ab6276, Abcam, Cambridge, UK). The first antibodies were detected using horseradish peroxidase-conjugated

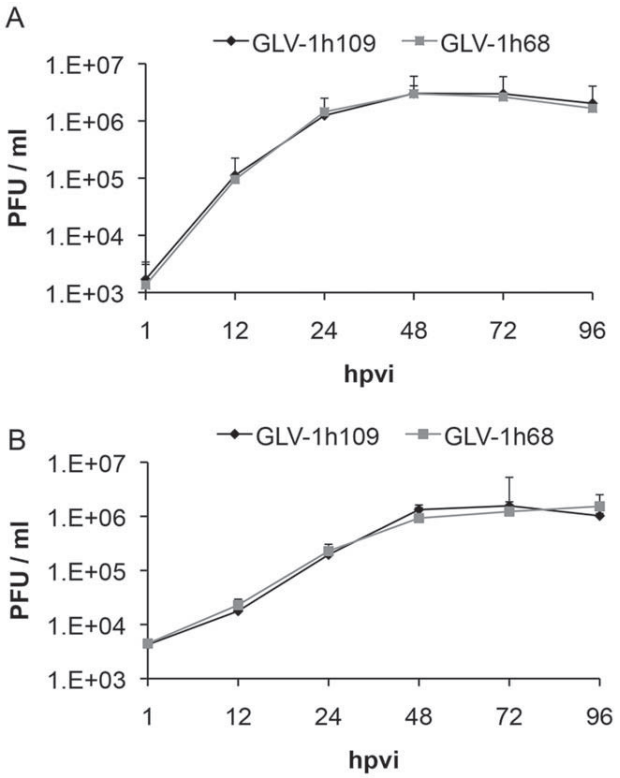

Figure 4. Comparison of the replication capacity of the vaccinia virus strains GLV-1h109 and GLV-1h68 in canine cancer cells. For the viral replication assay, STSA-1 (**A**) or DT08/40 (**B**) cells grown in 24-well plates were infected with either GLV-1h109 or GLV-1h68 at a MOI of 0.1. Cells and supernatants were collected for the determination of virus titers at various time points. Viral titers were determined as pfu per well in triplicates by standard plaque assay in CV-1 cell monolayers. Averages plus standard deviation are plotted. The data represent three independent experiments.
doi:10.1371/journal.pone.0047472.g004

anti-rabbit (ab6721, Abcam, Cambridge, UK) or anti-mouse (ab6728, Abcam, Cambridge, UK) secondary antibodies, followed by enhanced chemiluminescence detection.

Vaccinia Virus-mediated Therapy of STSA-1 and DT08/40 Xenografts

Tumors were generated by implanting either 1×10^6 canine soft tissue sarcoma STSA-1 cells or 5×10^6 canine prostate DT08/40 cells subcutaneously into the right hind leg of 6- to 8-week-old female nude mice [Hsd: Athymic Nude-*Foxn1*^{nu}; Harlan, Holland]. Tumor growth was monitored weekly in two dimensions using a digital caliper. Tumor volume was calculated as [(length × width^2)/2]. When tumor volume reached approximately 600–1000 mm^3 (STSA-1) and 200–400 mm^3 (DT08/40), groups of mice (n = 6) were injected either with 5×10^6 pfu of GLV-1h109 virus or PBS (control) into the tail vein. The significance of the results was calculated by Student's t-test. Results are displayed as means +/- standard deviation (SD). P values of <0.05 were considered significant.

Mice were monitored for change in body weight and signs of toxicity. Blood samples for protein expression analysis (see below) were collected at time points 7, 14, 21 and 28 days post virus injection under anesthesia by a heparinised capillary pipet (No. 554/20, Assistent, Sondheim, Germany) via the retro orbital sinus vein.

Fluorogenic Probes and Detection of Fluorescence Products

The lyophilized fluorogenic probe fluorescein di-beta-D-glucosonide (FDGlcU) (Invitrogen, Karlsruhe, Germany) was dissolved in DMSO (36.5 mM). For analysis of beta glucoronidase in serum, the collected mouse serum was diluted 1:15 with PBS and 80 µl of each sample were mixed with 2.5 µg FDGlcU. After incubation for 1 h at 37°C, fluorescence was read in Lumox 384-well plates (Sarstedt, Nümbrecht, Germany) using an Infinite 200 Pro Microplate Reader (Tecan, Crailsheim, Germany) and fluorescence intensities are listed as relative fluorescence units as described by Hess et al. [15].

GLAF-1 ELISA

The expression of the recombinant GLAF-1 proteins in sera was quantitatively determined by ELISA. For the standard curve, 6 two-fold serial dilutions of purified GLAF-1 protein ranging from 625 ng/ml to 19.5 ng/ml were prepared in PBS/2% FBS. Purified GLAF-1 protein required to obtain the standard curve was produced as described earlier [7]. Ninety-six well plates precoated with recombinant human VEGF (Sigma) were blocked and incubated with standards or 1:25 dilutions of sera samples in triplicates. Following 1.5 h incubation at room temperature, the wells were washed with PBS/0.05% Tween and incubated with a rabbit anti-DDDDK antibody (ab21536, Abcam, Cambridge, UK) for 1 h at room temperature. All wells were washed and incubated with a secondary HRP-conjugated anti-rabbit IgG (Jackson Immuno Research). Color was developed using 3,3,5,5′-tetramethylbenzidine (Sigma), and the reaction was stopped with HCl. Absorbance was read in an Infinite 200 Pro Microplate Reader (Tecan, Crailsheim, Germany) at 450 nm.

Histology and Microscopy

For histological studies, tumors were excised and snap-frozen in liquid nitrogen, followed by fixation in 4% paraformaldehyde/PBS at pH 7.4 for 16 h at 4°C. After dehydration in 10% and 30% sucrose (Carl Roth, Karlsruhe, Germany) specimens were embedded in Tissue-Tek® O.C.T. (Sakura Finetek Europe B.V., Alphen aan den Rijn, Netherlands). Tissue samples were sectioned (10 µm thickness) with the cryostat 2800 Frigocut (Leica Microsystems GmbH, Wetzlar, Germany). Labeling of tissue sections was performed as described in detail elsewhere [16,17].

Endothelial blood vessel cells were stained with a hamster monoclonal anti-CD31 antibody (Chemicon International, Temecula, USA; MAB1398Z). Anti-Mouse Ly-6G (Gr-1, eBioscience, San Diego, USA; 14-5931-81), anti-Mouse F4/80 (Clone BM8, eBioscience) or rabbit anti-DDDDK antibody (ab21536, Abcam, Cambridge, UK) were used to stain myeloid-derived suppressor cells (MDSCs, mainly granulocytes), macrophages or GLAF-1 protein respectively. Cy3- and Cy5-conjugated secondary antibodies (donkey) were obtained from Jackson ImmunoResearch (Pennsylvania, USA).

The fluorescence-labeled preparations were examined using the Leica TCS SP2 AOBS confocal laser microscope equipped with argon, helium-neon and UV laser and the LCS 2.16 software (1024 × 1024 pixel RGB-color images). Digital images were processed with Photoshop 7.0 (Adobe Systems, Mountain View, CA, USA) and merged to yield overlay images.

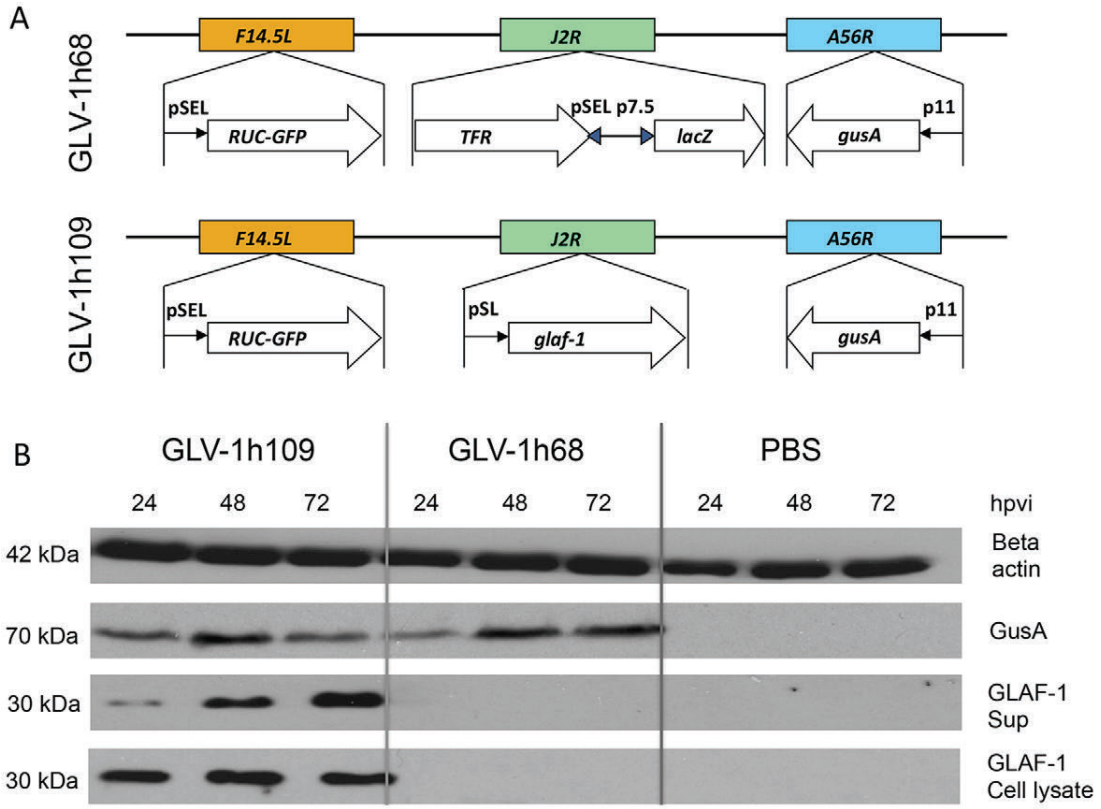

Figure 5. Expression of virus mediated proteins GLAF-1 and GusA in canine soft tissue sarcoma STSA-1 cells. (**A**) Schematic representation of GLV-1h68 and GLV-1h109 according to Frentzen et al [7]. abberations: p11, VACV p11 late promoter; pSEL, VACV SEL promoter; pSE, VACV SE promoter; pSL, VACV SL promoter; p7.5, VACV 7.5 K early/late promoter. (**B**) Western blot analysis of STSA-1 cells infected with either GLV-1h109, GLV1h 68 virus at an MOI of 1 or PBS. Protein fractions from cell lysate and culture supernatant were isolated at different time points and separated by SDS/PAGE. Western blot analysis was performed as described in material and methods.
doi:10.1371/journal.pone.0047472.g005

Measurement of Blood Vessel Density and Fluorescence Intensity of the CD31 Signal in the Tumor Tissue

Blood vessel density was measured in digital images (100× magnification) of CD31-labelled 10-µm-thick tumor cross-sections using Leica TCS SP2 AOBS confocal laser microscope. Eighteen images per tumor were analyzed per staining (3 tumors per group, 3 sections of each tumor and 6 images per section). Exposure time for individual images was adjusted to ensure clear visibility of all detectable blood vessels and decorated with 8 equidistant horizontal lines using Photoshop 7.0. All blood vessels crossing these lines were counted to obtain the vessel density per section.

Fluorescence intensity of the CD31-labelling in 10-µm-thick sections of control tumors and infected and non-infected areas of virus-colonized tumors was measured on digital images (100× magnification) of specimens stained for CD31 immunoreactivity. On the fluorescence microscope, the background fluorescence was set to a barely detectable level by adjusting the gain of the CCD camera before all the images were captured with identical settings. RGB-images were converted into 8-bit gray scale images (intensity range 0–255) using Photoshop 7.0. The fluorescence intensity of the CD31-labeling represented the average brightness of all vessel-related pixels and was measured using Image J software http://rsbweb.nih.gov/ij.

Flow Cytometric (FACS) Analysis

For flow cytometric analysis, three mice from each group were sacrificed by CO_2 inhalation and the tumors were removed. The tumor tissues were minced and incubated individually in 10,000 CDU/ml Collagenase I (Sigma, Steinheim, Germany) and 5 MU/ml DNase I (Calbiochem, Darmstadt, Germany) for 75 min at 37°C and then passed through a 70-µm nylon mesh filter (BD Biosciences, Erembodegem, Belgium).

To block non-specific staining, single cells were preincubated with 0.5 µg of anti-mouse CD16/32 antibody (clone 93, Biolegend, San Diego, USA) per one million cells for 20 min on ice. After that, the cells were incubated at 4°C for 15 min in PBS with 2% FCS in the presence of appropriate dilutions of labeled monoclonal antibodies: anti-mouse MHCII-PE (Clone M5 114.15.2, eBioscience, San Diego, CA, USA), anti-CD11b-PerCPCy5.5 (Clone M1/70, eBioscience, anti-F4/80-APC (Clone BM8, eBioscience), anti-Gr-1-APC (Ly-6G, Clone RB6-8C5, eBioscience). The Anti-Gr-1 mAb (RB6-8C5) has long been used to stain MDSCs and allows the distinction of at least two subsets of granulocytes ($Gr\text{-}1^{high}CD11b^{+}$) and monocytic cells ($Gr\text{-}1^{int}CD11b^{+}$) [18].

Stained cells were subsequently analyzed, using an Accuri C6 Cytometer and FACS analysis software CFlow Version 1.0.227.4 (Accuri Cytometers, Inc. Ann Arbor, MI USA).

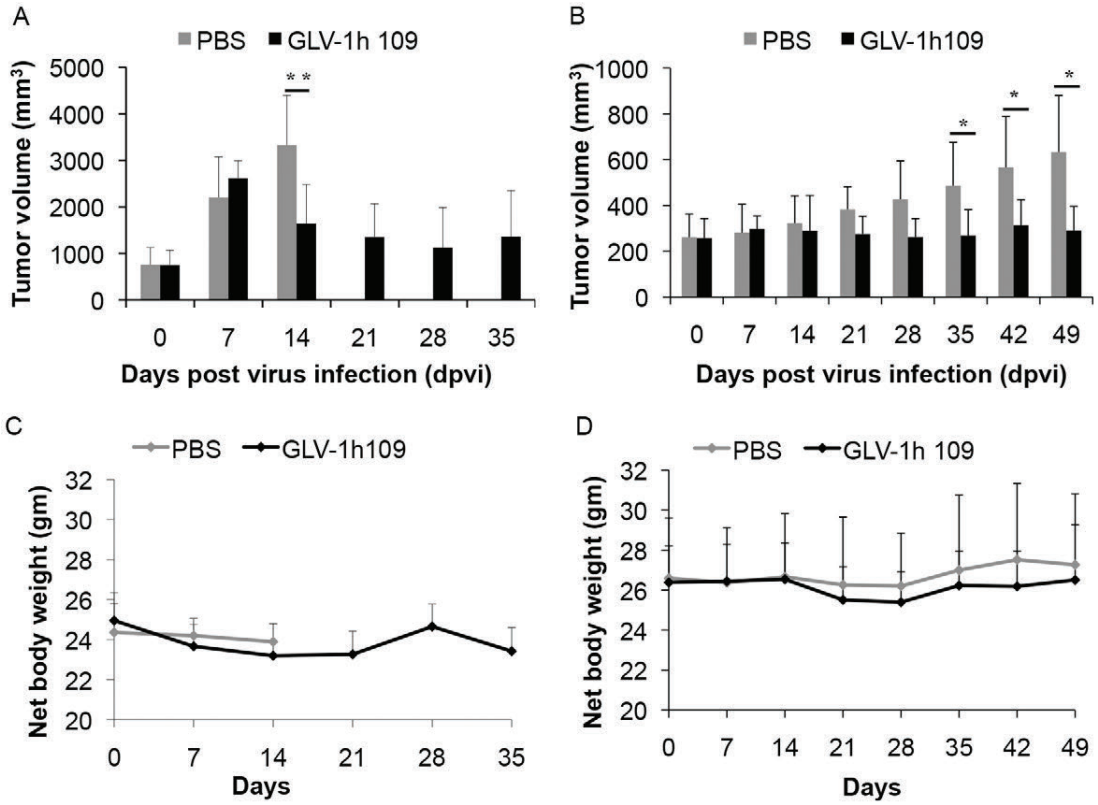

Figure 6. Effects of systemic GLV-1h109 virus injection on tumor growth (A, B) and the body weights (C, D) of STSA-1 or DT08/40 xenografted mice. Two groups each of (**A, C**) STSA-1 tumor-bearing nude mice (n = 6) and (**B, D**) DT08/40 tumor bearing mice (n = 6) were either treated with a single dose of 5×10^6 pfu GLV-1h109 or with PBS (mock control) intravenously (i.v.) into lateral tail vein. The statistical significance was confirmed by Student's t-test where * and ** indicate $P<0.05$ and 0.01 respectively.
doi:10.1371/journal.pone.0047472.g006

Results

The GLAF-1 Antibody Specifically Recognizes Canine VEGF

The anti-VEGF scAb GLAF-1 is directed against human and murine VEGF [7]. Since until now there were no data about the affinity of GLAF-1 to canine (ca) VEGF, we tested the ability of purified GLAF-1 antibody to bind recombinant ca VEGF (R&D System, Minneapolis, MN, USA) by ELISA. The data demonstrated that this antibody is functional and recognized both ca VEGF and hu VEGF with equal efficiency (**Fig. 1**).

STSA-1 and DT08/40 Canine Cancer Cells Express VEGF Under Cell Culture Conditions

VEGF, or specially VEGFA is a potent mediator of both angiogenesis and vasculogenesis in dogs and has been proposed

Table 1. Biodistribution of GLV-1h109 in virus-treated DT08/40-or STSA-1 xenografts at 49 or 35 days post virus injection (dpvi).

PFU/per gram (g) of organ or tumor tissue	DT08/40 xenograft			STSA-1 xenograft		
Mouse No/dpvi	**424/49 dpvi**	**429/49 dpvi**	**433/49 dpvi**	**329/35 dpvi**	**343/35 dpvi**	**335/35 dpvi**
Tumor	2.67E+02	4.53E+03	1.28E+04	1.86E+07	4.95E+07	2.70E+07
Liver	n.d	n.d	n.d	5.38E+01	1.19E+02	4.87E+01
Lung	n.d	n.d	n.d	2.65E+02	9.60E+01	1.05E+02
Heart	n.d	n.d	n.d	n.d	n.d	n.d
Kidney	n.d	n.d	n.d	5.58E+01	n.d	n.d
Spleen	n.d	n.d	n.d	4.72E+01	7.24E+01	3.52E+01

The virus titres were determined by standard plaque assays on CV-1 cells using aliquots of the homogenized organs and were displayed as mean pfu/per gram of organ or tissue. For each organ, two aliquots of 0.1 ml were measured in triplicates.
n. d.: not detected (detection LIMIT >10 pfu/organ).
doi:10.1371/journal.pone.0047472.t001

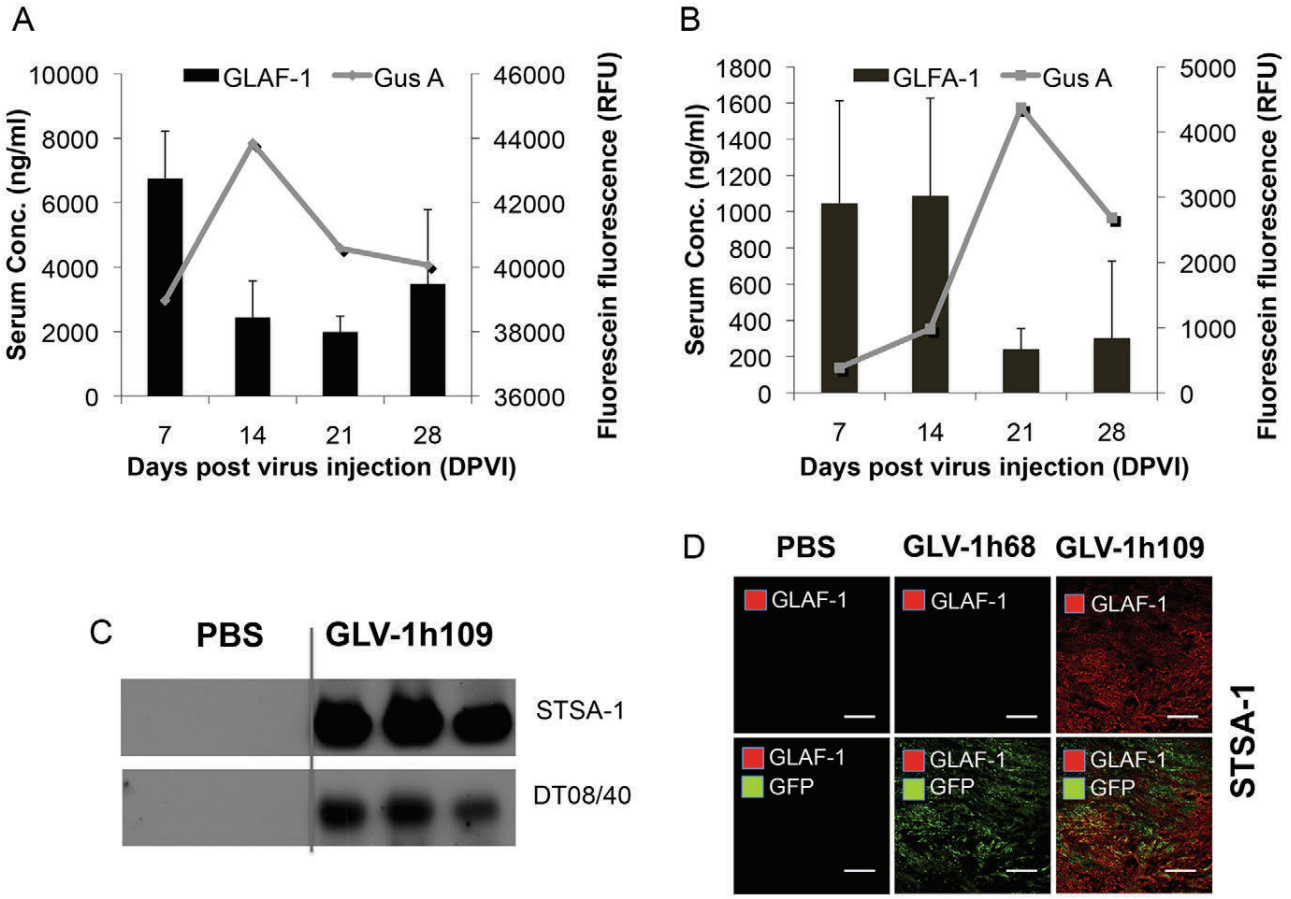

Figure 7. Presence and persistence of the scAb GLAF-1 and GusA in serum (A, B) and tumors (C, D) of GLV-1h109-injected xenograft mice at different time points. A, B: Blood samples were collected at day 7, 14, 21 and 28 from (**A**) STSA-1 and (**B**) DT08/40 tumor bearing mice (n = 6). Expression of GLAF-1 in sera was quantitatively determined using ELISA. GLAF-1 values shown (bars) are mean + SD. GusA activity (represented by lines) was measured by detecting the activation of the fluorogenic compound FDGlcU. **C:** The presence of GLAF-1 in tumor tissue monitored by Western Blot. STSA-1 and DT08/40 tumor-bearing mice injected with GLV-1h109 were sacrificed on day 35 and day 49, respectively. Tumors were collected, and protein fractions from tumor lysate were separated by SDS/PAGE. Western blot analysis was performed using an anti-DDDK antibody. **D:** Localization of GLAF-1 protein in virus-infected STSA-1 tumor areas. Overlays represented the virus infection GFP fluorescence (green)/presence of GLAF-1 (red). Scale bars, 500 µm. (200× magnification).
doi:10.1371/journal.pone.0047472.g007

as a prognostic indicator in several types of canine cancer [19–21]. Therefore we first analyzed the VEGF expression of the two tested canine cancer cell lines under cell culture conditions (**Fig. 2**). Canine VEGF concentrations were determined using a Quantikine ELISA kit (R&D Systems, Minneapolis, MN, USA) developed for detection of canine VEGF, in accordance with the manufacturer's directions. Concentration of VEGF in supernatant was represented as pg/10^6 cells. VEGF levels in the supernatant of STSA-1 cells were 1556.92±103.88 pg/10^6 cells (24 hours) and 2962.19±465.84 pg/10^6 cells (48 hours), while that of DT08/40 cells were 170.85±6.84 pg/10^6 cells (24 hours) and 183.30±28.68 pg/10^6 cells (48 hours). The results revealed that STSA-1 cells produced about 9- to 16-fold more ca VEGF compared to the DT08/40 cells at these two different time points.

Oncolytic Vaccinia Virus GLV-1h109 Virus Efficiently Kills Canine Soft Tissue Sarcoma (STSA-1) and Prostate Carcinoma (DT08/40) Cells

STSA-1 cells were seeded three days prior to infection in 24-well plates and were then infected with either GLV-1h109 or GLV-1h68 (positive control) at MOIs of 1.0 and 0.1, respectively. Cell viability was analyzed at 24, 48, 72 and 96 hours post-virus-infection (hpvi) by XTT-assays (**Fig. 3A**). Ninety-six hours after GLV-1h109-infection at MOIs of 0.1 and 1.0, only 17.8% and 17.5% STSA-1 cells survived the treatment, respectively. At the same time point and MOIs, we found 18.60% and 18.2% viable STSA-1 cells after GLV-1h68 infection.

The oncolytic potentials of GLV-1h109 and GLV-1h68 were additionally tested in DT08/40 cell culture (**Fig. 3B**). In these experimental settings the GLV-1h109 and GLV-1h68 virus infections led to a similar oncolytic efficacy at 96 hpvi and at MOIs of 0.1 and 1.0.

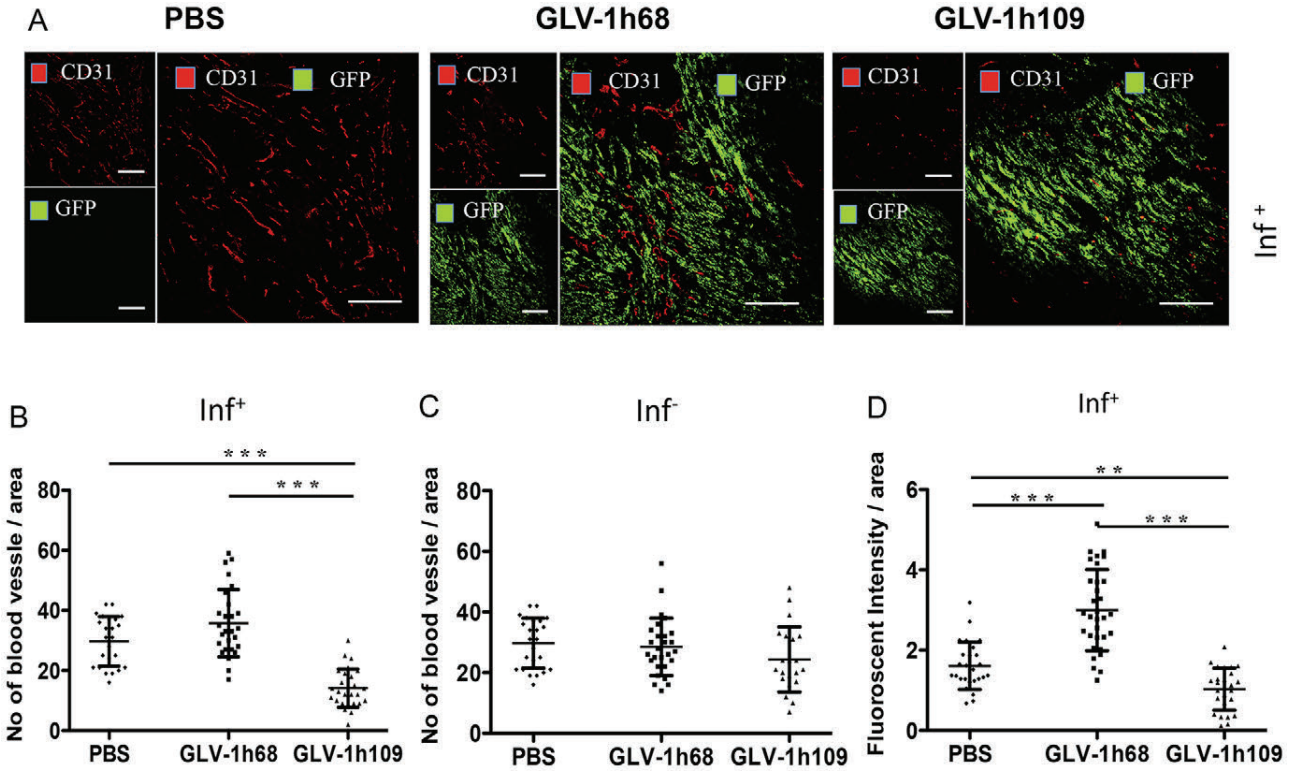

Figure 8. Determination of vascular density using CD31 immunohistochemistry in virus-treated (GLV-1h68, GLV-1h109) and non-treated (PBS) tumors at 7 dpvi. A–C: Blood vessel density in virus-infected (A, B; inf$^+$) and virus non-infected (C; inf$^-$) STSA-1 tumor areas. The vascular density was measured in CD31-labeled tumor cross-sections (n = 3 mice per group, 18 images per mice) and presented as mean values +/- SD. (***P<0.001, **P<0.01, Student's t-test). D: Fluorescence intensity of the CD31 signal in virus-infected (inf$^+$) STSA-1 tumor areas. The fluorescence intensity of the CD31-labelling represented the average brightness of all vessel-related pixels (VRP) and determined as described [3,16]. The fluorescence signal is a rate of CD31 expression in the blood vessels and was measured in 18 images of each tumor (n = 3 mice per group). Shown are the mean values +/-SD. (***P<0.001, **P<0.01, Student's t-test).
doi:10.1371/journal.pone.0047472.g008

The results demonstrated that the GLV-1h109 is oncolytic to both canine cancer cell lines, however the rate of oncolysis was faster in STSA-1 cells than DT08/40 cells.

GLV-1h109 Efficiently Replicates in STSA-1 and DT08/40 Tumor Cells

One of the factors that regulate the oncolytic potential of OVs is their ability to infect and/or efficiently replicate in cancer cells. To determine whether variation in the rate of oncolysis was due to differences in the rate of replication, STSA-1 and DT08/40 cells were infected with either GLV-1h109 or GLV-1h68 at a MOI of 0.1. Standard plaque assay was performed for all samples to determine the viral titers at different time points during the course of infection (**Fig. 4**). The maximum viral titers (total) were observed at 48 hours post virus infection (hpvi) in STSA-1 cells for both GLV-1h68 (2.98×10^6 pfu/ml) and GLV-1h109 (3.01×10^6 pfu/ml) (**Fig. 4A**). In addition, GLV-1h68 and GLV-1h109 viruses can also efficiently infect and replicate in DT08/40 cells with a maximum yield of 1.23×10^6 pfu/ml and 1.56×10^6 pfu/ml at 72 hpvi respectively (**Fig. 4B**). The highest titer of GLV-1h109 in STSA-1 cells at 48 hrs was nearly twice than highest titer of GLV-1h109 in DT08/40 cells at 72 hrs, indicating that GLV-1h109 replicates better and faster in STSA-1 cells (***P = 0.00004; Student's t-test).

However, the replication efficiency of GLAF-1 expressing GLV-1h109 strain was similar to that of the parental GLV-1h68 virus in both the canine cancer cell lines.

GLV-1h109-infected STSA-1 and DT08/40 Cells Express scAb GLAF-1 and Beta Glucuronidase (GusA)

The efficiency of viral expression was also monitored by detecting anti-VEGF scAb GLAF-1 and beta glucuronidase (GusA) proteins in GLV-1h109 infected STSA-1 or DT08/40 cells. For this purpose, 10^6 STSA-1 or DT08/40 cells were infected either with GLV-1h109 or GLV-1h68 (control) at an MOI of 1.0 in 6 well plates. Supernatants and lysates were harvested and analyzed in Western Blot using anti-GLAF-1, anti-GusA or anti-ß-actin antibodies. The ß-actin was used as a loading control and GusA was chosen as an additional protein for monitoring of the viral-dependent protein expression.

The results for virus-infected STSA-1 cells are shown in **Figure 5**. GLAF-1 protein of expected size (30 kDa) was detected in both lysates and supernatants of GLV-1h109-infected STSA-1 cells (**Fig. 5B**). Similar expression of GLAF-1 protein was detected in GLV-1h109 infected DT08/40 (**Figure S1**). No protein of similar size was detected in GLV-1h68 infected or uninfected cells of both cancer types. This is evidence that the GLAF-1 protein was successfully expressed and secreted in both canine cancer cell lines.

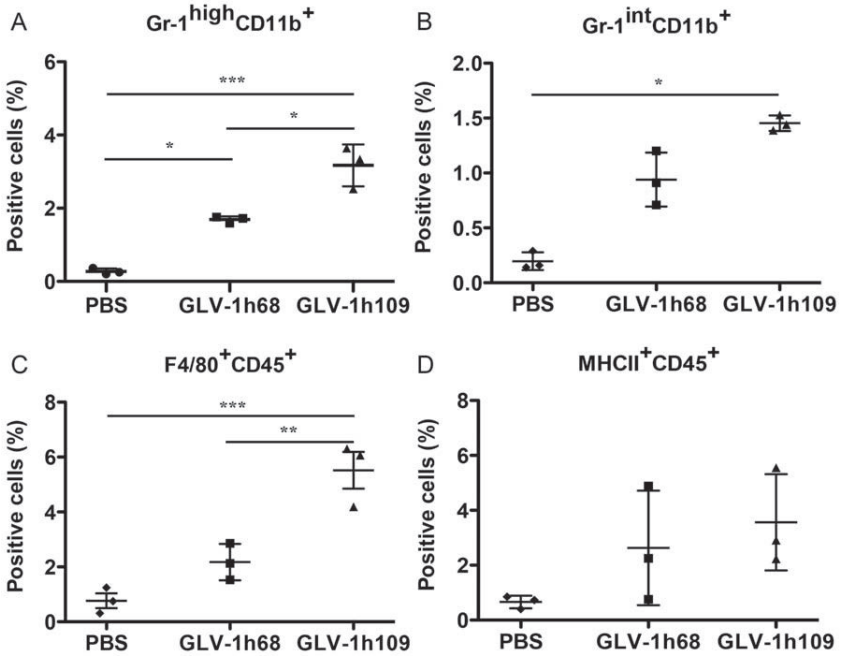

Figure 9. Presence of immune cells in tumors of STSA-1 xenografted mice 7 days after GLV-1h68-, GLV-1h109- or PBS-treatments. Percentage of (A) Gr-1^{high}CD11b^{+} (MDSCs, granulocytes), (B) Gr-1^{int}CD11b^{+} (MDSCs, monocytes), (C) F4/80^{+}CD45^{+} (macrophages) or (D) MHCII^{+}CD45^{+} (mainly B cells, macrophages and dendritic cells) cells in tumors of STSA-1 xenografted mice. Experiments were done twice with at least 3 mice per group. The data are presented as mean values +/- SD. The statistical significance was analyzed using one-way ANOVA followed Bonferronis multiple comparison test (***P<0.001, **P<0.01, *P<0.05). The Anti-Gr-1 mAb (RB6-8C5) has long been used to stain MDSCs and allows the distinction of at least two subsets of granulocytes (Gr-1^{high}CD11b^{+}) and monocytic cells (Gr-1^{int}CD11b^{+}).
doi:10.1371/journal.pone.0047472.g009

Systemic Administration of GLV-1h109 Virus Significantly Regresses Growth of STSA-1 and DT08/40 Derived Tumors in Nude Mice

Female nude mice [Hsd: Athymic Nude-*Foxn1*^{nu}; Harlan, Holland] (n = 6/group) at an age of 6–8 weeks were implanted with 1×10^6 STSA-1 cells. Four weeks post implantation, all mice developed tumors with volumes of 600 to 1000 mm^3. Animals were separated into two groups (n = 6) and were injected with a single dose of GLV-1h109 (5×10^6 pfu) or PBS (100µl) into the tail vein intravenously (i.v.). As shown in **Fig. 6A** the virus treatment led to a significant tumor regression of all GLV-1h109-virus-treated mice. In contrast, due to excessive tumor burden (>3000 mm^3), all animals of the PBS control group were euthanized after 14 dpvi.

The therapeutic effect of GLV-1h109 was also evaluated on the progression of canine prostate carcinoma DT08/40 tumors in nude mice by measuring the tumor volume at various time points. The tumors were generated by implanting 5×10^6 canine prostate carcinoma cells DT08/40 subcutaneously into the right hind leg of 6- to 8-week-old nude mice [Hsd:Athymic Nude-*Foxn1*^{nu}; Harlan, Holland]. Forty-nine days after tumor cell implantation, groups of mice (n = 6/group) were injected (i.v.) either with 5×10^6 pfu of GLV-1h109 virus or PBS (control). Data demonstrated that a single injection with GLV-1h109 vaccinia virus led to significant inhibition of the tumor growth (*p<0.05) of all virus-treated mice in comparison to the control PBS animals (**Fig. 6B**).

Finally, the toxicity of the GLV-1h109 virus was determined by monitoring the relative weight change of mice over time (**Fig. 6C, D**). All GLV-1h109 treated mice showed stable mean weight over the course of studies. There were no signs of virus-mediated toxicity.

Biodistribution of GLV-1h109 Virus and Presence of scAb GLAF-1 in Tumor-bearing Nude Mice

The GLV-1h109 distribution in STSA-1 and DT08/40 xenografts was analyzed at the last time points after virus treatment. **Table 1** summarizes the virus distribution data in both xenograft models. The highest viral titers were identified in primary tumors of virus-treated mice (**Table 1**). Interestingly, the mean GLV-1h109 titers in primary solid tumors of STSA-1 xenografts at 35 dpvi were about 10^4 fold higher than that of DT08/40 xenografts at 49 dpvi. In addition, we found presence of plaque forming units in some organs of virus-injected STSA-1 mice, but not in the virus–treated DT08/40 xenografts. However, the number of GLV-1h109 virus particles in the healthy tissues were negligible; e.g. in whole organs: livers (mean weight 1.2 g) about 89 pfu; lungs (mean weight 0.142 g) about 19 pfu and spleens (mean weight 0.2 g) about 10 pfu at 35 dpvi (Table 1, here the pfu were given per gram of organ). In contrast, we found about 10^4–10^5 fold more GLV-1h109 pfu in solid tumors at this time point, which clearly shows that GLV-1h109 virus displays an enhanced tumor specific replication.

Using fluorogenic probes activated specifically by virus-mediated glucuronidase (GusA), we have recently shown that the detection of GusA in the serum could be used to evaluate successful tumor colonization and/or transgene expression of oncolytic vaccinia virus in tumor-bearing mice [15]. Therefore, in this study we tested the presence and persistence of scAb GLAF-1 protein in combination with the GusA virus marker (**Fig. 7A, B**).

The maximal yield of scAb GLAF-1 in the serum of GLV-1h109-injected STSA-1 xenografts was about nine-fold higher than corresponding DT08/40 xenografts at 7 dpvi. Interestingly, maximal presence of scAb GLAF-1 protein in serum was a week

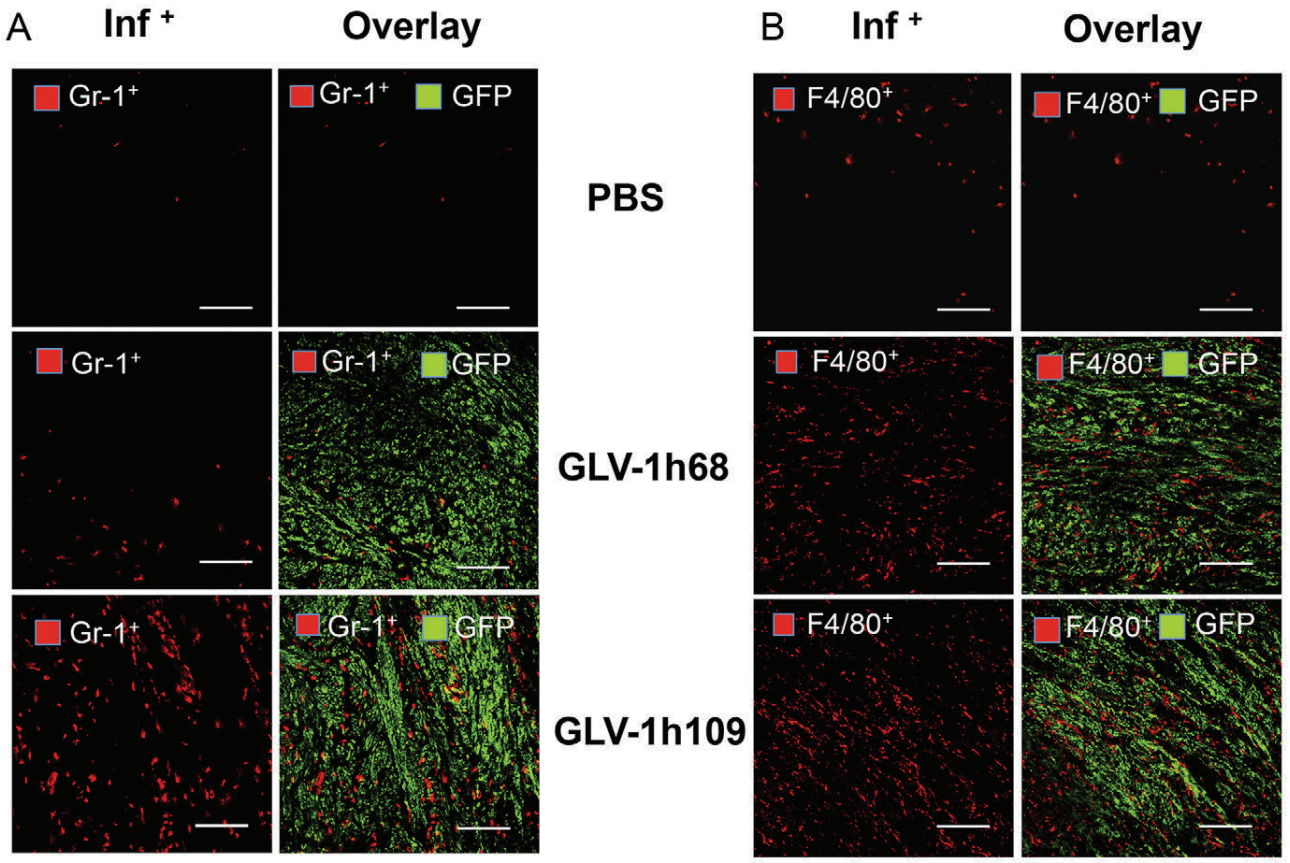

Figure 10. Immunohistochemical staining of infected and uninfected STSA-1 xenograft tumors at 7 dpvi for MDSCs (A) or macrophages (B). Tumor-bearing mice were either infected with GLV-1h109 or GLV-1h68 or mock treated (PBS). Cryosections (10 µm-thick) of tumors were labeled with either anti- Gr-1 (Ly-6G) antibody (**A**) for MDSCs (granulocytes) or anti- F4/80$^+$ antibody (**B**) for macrophages; both red. Virus infection and/or phagocytosis was indicated by GFP fluorescence (green). Overlays represented inf$^+$(Gr-1$^+$)/GFP. Scale bars, 500 µm. (200× magnification).
doi:10.1371/journal.pone.0047472.g010

earlier than the maximal GusA-signal in both the xenograft models (**Fig. 7A, B**). These different kinetics could be due to the fact that GLAF-1 is secreted while GusA is only released to the blood stream via cell lysis. The presence of GLAF-1 in the tumors of GLV-1h109 injected mice was analyzed using Western Blot. The GLAF-1 protein was detected even at the last points of treatment in both xenograft models (**Fig. 7C**). In addition, we clearly detected the GLAF-1 protein in GLV-1h109-treated STSA-1 tumor sections (**Fig. 7D**).

The results demonstrated that analysis of scAb GLAF-1 in the serum could also be used as a pharmacokinetic marker for virus colonization and persistence in GLV-1h109-injected xenograft mice.

Colonization of GLV-1h109 in STSA-1 Tumor Xenograft Significantly Inhibits Development of Tumor Vasculature

STSA-1 cells express 9–16 times more VEGF than DT08/40 cells as well as expression of scAb GLAF-1 was higher in STSA-1 xenografts than DT08/40 xenografts. In addition, an anti-VEGF strategy was successfully evaluated in dogs with canine soft tissue sarcomas [12]. Considering all these factors, the effects of GLV-1h109 on tumor vasculature and tumor microenvironment were tested in STSA-1 xenograft model only.

To test a possible anti-VEGF effect of the GLAF-1 antibody on tumor angiogenesis and vasculogenesis, we analyzed the CD31-positive vascular network in tissue sections of GLV-1h109, GLV-1h68 and PBS-treated STSA-1 tumors by fluorescence microscopy. For this purpose, CD31-labelled cross sections of tumors from PBS-, GLV-1h68- and GLV-1h109- treated mice were used for determination of the vascular density at the day 7 after treatment (**Fig. 8**). The data revealed that the vascular density of GLV-1h109-infected tumors was significantly decreased in comparison to that of GLV-1h68- and PBS -injected control tumors (GLV-1h109 vs. GLV-1h68 ***P = 0.0000672; GLV-1h109 vs. PBS ***P = 0.000255) (**Fig. 8A, B**). Interestingly, a significant reduction of the vascular density was observed in GFP positive areas (**Fig. 8AB; inf$^+$**), but not in the corresponding GFP negative areas of tumor sections (**Fig. 8C; inf$^-$**), indicating that the reduction in vascular density is mediated by virus infection. The vascular density between infected (**inf$^+$**) areas of GLV-1h109 tumor was also significantly lower than non-infected (**inf$^-$**) areas (**inf.$^+$** GLV-1h109 (**Fig. 8B**) vs. **inf$^-$** GLV-1h109 (**Fig. 8C**); ***P = 0.000534). In addition, fluorescence intensity of the CD31 signal was measured in immunohistochemically stained (**inf$^+$**)-sections of STSA-1 tumors (**Fig. 8D**). The results revealed that the fluorescence intensity (vessel-related pixels) of GLV-1h109 virus-infected tumors was significantly decreased in comparison to GLV-1h68 or PBS-injected control tumors (GLV-1h109 vs. PBS

**P = 0.0051; GLV-1h109 vs. GLV-1h68 ***P = 0.00001). This means that only the GLV-1h68 virus colonization led to an up-regulation of CD31 protein. However, there was significant decrease in fluorescence intensity of GLV-1h109-infected tumors, which might be due to the reduction in the vascular density after treatment with this virus.

The results demonstrated that the virus colonization in combination with the scAb GLAF-1 led to local inhibition of the blood vessel development in the GLV-1h109 virus-infected tumor tissue only.

GLV-1h109 Colonization Induces Massive Infiltration of Innate Immune Cells in STSA-1 Xenografts

To investigate potential roles of innate immune cells in the anti-tumor mechanism, we analyzed the effect of virus infection on host immune cells in tumors of STSA1-tumor-bearing mice. Single cell suspensions prepared from STSA-1 tumors, resected 7 days after the treatment were analyzed by flow cytometry for the presence of host immune cells (**Fig. 9**). The presence of various leukocytes was assessed using cellular antigen-specific markers. We used CD45 (leukocyte common antigen), Gr-1 antigen (Ly6C/Ly6G) of MDSCs, CD11b (Mac-1, mainly myeloid cells), F4/80 (macrophages) and MHC II (B cells, monocytes, macrophages and dendritic cells) to visualize the respective cell types in STSA-1 tumors. The tumor-derived Gr-1^{+}CD11b^{+} cells consisted of 2 major subfractions based on differential Gr-1 expression, high (Gr-1$^{high)}$ and intermediate (Gr-1^{int}). It is known that a Gr-1^{high}, mainly composed of immature and mature granulocytes, and a Gr-1^{int}, comprising monocytes and other immature myeloid cells [18]. In these experimental settings we found a significant increase of Gr-1^{high} CD11b^{+}, Gr-1^{int} CD11b^{+} and F4/80^{+}CD45^{+} cells in the GLV-1h109 infected tumors compared with GLV-1h68- or PBS-injected tumors (**Fig. 9A, B, C**). No significant differences were determined in the percentage of MHCII^{+}CD45^{+} cells within GLV-1h109 and GLV-1h68 treated tumors (**Fig. 9D**).

An additional immunohistochemical examination confirmed the increased accumulation of MDSCs and macrophages in GLV-1h109-infected tumors as compared to PBS or GLV-1h68-infected tumors (**Fig. 10**). Interestingly, the MDSCs (mainly Gr-1^{high} granulocytes) cells were mostly co-localized with virus in infected tumor regions (**Fig. 10A**), whereas the macrophages were diffusely distributed throughout the tumor (**Fig. 10B**).

We used the Gr-1^{high} CD11b^{+} cells as markers for monitoring viral infection on a systemic level. For this purpose, a parallel flow cytometric analysis of Gr-1^{high} CD11b^{+} on peripheral blood was performed. There was no significant difference between the number of the Gr-1^{high} CD11b^{+}cells in peripheral blood of the viruses or PBS-infected STSA-1 xenografted mice (**Figure S2**). These data suggest that the changes in granulocytic MDSCs were not systemic, but rather due to a change in recruitment and/or persistence within the tumors.

Finally, we also analyzed the direct virus interaction with cells of the host immune system at 7 dpvi. At this time point, 0.11% and 0.37% of Gr-1^{high} CD11b^{+} (MDSCs, granulocytes), 0.06% and 0.15% of Gr-1^{int}CD11b^{+} (MDSCs, monocytes) and 0.24% and 0.81% of F4/80^{+}CD45^{+} (macrophages) were GFP-positive in GLV-1h68 and GLV-1h109-infected tumors, respectively (**Table 2**). This indicates that either these immune cells were infected with vaccinia virus or they had phagocytized virus-infected tumor cells. We found also that GLV-1h109 more efficiently infects both tumor and host immune cells, compared to GLV-1h68 (**Table 2**).

Discussion

Several oncolytic viruses including adenovirus strains CAV-1 and CAV-2 [22], canine distemper virus [23] and vaccinia virus strains GLV-1h68 and LIVP1.1.1 [4,24,25] have been used for canine cancer therapy in preclinical studies [3,26]. Our data demonstrated that treatment with oncolytic vaccinia virus GLV-1h109 carrying anti-VEGF scAb GLAF-1 regresses the growth of canine prostate carcinoma and canine soft tissue sarcoma xenografts by oncolysis, inhibition of tumor angiogenesis and recruitment of innate immune cells into tumor tissue.

In the current study, we investigated for the first time the oncolytic vaccinia virus strain GLV-1h109 expressing an anti-VEGF single-chain antibody GLAF-1 as a possible therapeutic agent against canine soft tissue sarcoma and canine prostate carcinoma. GLV-1h109 was able to effectively infect, replicate in and lyse these canine cancer cells in culture. The virus infection led to expression of anti-VEGF scAb GLAF-1 protein in both cell lines (**Fig. 5**). Part of the produced scAb GLAF-1 was specifically secreted into the supernatant of the virus-infected cells (**Fig. 5, Figure S1**). The secretion of scAb GLAF-1 by the infected cell might lead to its quick delivery to surrounding tumor tissue and further binding to VEGF (**Fig. 7C**). In addition, tumor-specific virus infection led to a continued presence of scAb GLAF-1 in peripheral blood (**Fig. 7A and B**). Data clearly demonstrated that scAb GLAF-1 could be useful as a pharmacokinetic marker for virus colonization and persistence in GLV-1h109-injected xenograft mice (**Fig. 7**). These findings have also very well demonstrated the application of our virus-based system for efficient expression and distribution of recombinant antibodies in the tumorigenic host. Recently we have reported that virus-encoded scAb GLAF-1 led to an enhanced therapeutic effect in different human tumor xenograft models, compared with oncolytic viral therapy with the prototype strain GLV-1h68 alone [7]. We have postulated that this enhancement may be caused by the continuous production of the anti-VEGF scAb in colonized tumors. This possible VEGF blockade and the proximate anti-angiogenesis effects would enhance therapeutic efficacy. In order to test this assumption, we analysed the virus-mediated oncolytic and immunological effects of GLV-1h109 in xenograft mice bearing STSA-1 tumors. The data have revealed that GLV-1h109 achieved a significant inhibition of tumor growth and damage of tumor tissues in both tested canine xenografts models. One of the most important purposes of the study was to determine whether the virus-encoded scAb GLAF-1 could elicit therapeutic anti-VEGF responses. We selected STSA-1 xenografted mice to study the effects of scAb GLAF-1 on tumor angiogenesis, because the canine soft tissue sarcoma STSA-1 cells have shown a high level of VEGF expression (**Fig. 2**). In addition, we observed a nine-fold higher expression of scAb GLAF-1 in the serum of GLV-1h109-injected STSA-1 xenografted mice than corresponding DT08/40 xenograft-bearing animals at 7 dpvi (**Fig. 7A and 7B**). However, higher serum GLAF-1 concentration in STSA-1 xenografts might be due to the enhanced replication efficacy of GLV-1h109 in STSA-1 cells (**Fig. 4**).

A CD31 immunohistological staining of STSA-1 tumor sections revealed a significant decrease in the number of blood vessels of GLV-1h109 infected tumors, when compared to GLV-1h68- and PBS-injected control tumors at 7 dpvi (**Fig. 8**). The drastic reduction of the vascular density of tumors might be due to the presence of the scAb GLAF-1 in tumor tissue and blood of the GLV-1h109-treated STSA-1 mice. Interestingly, the significant reduction in vascular density was observed in virus-infected areas only. It is considerable that tumor microenvironment character-

Table 2. Percentage of GFP positive cells in virus–treated STSA-1 tumors.

Cell Markers	Virus GLV-1h68	Virus GLV-1h109	P-value GVL-1h68 vs. GVL-1h109	Positive cells
GFP^+	8.67% ±4.5%	14.27% ±1.8%	*(P = 0.039)	total GFP-positive cells
GFP^+/ $Gr\text{-}1^{high}CD11b^+$	0.11% ±0.073%	0.37% ±0.051%	**(P = 0.006)	GFP-positive tumor associated MDSCs (granulocytes)
GFP^+/ $Gr\text{-}1^{int}CD11b^+$	0.06% ±0.043%	0.15% ±0.073%	*(P = 0.042)	GFP-positive tumor associated MDSCs (monocytes)
$GFP^+/F4/80^+CD45^+$	0.24% ±0.072%	0.81% ±0.28%	*(P = 0.028)	GFP-positive tumor associated macrophges

Percentage GFP-positive cells in tumors of STSA-1 xenografted mice 7 days after GLV-1h109- or GLV-1h68-treatments. Experiments were done twice with at least 3 mice per group. The data are presented as mean values +/- standard deviations. The statistical significance was analyzed using two-tailed unpaired Student's test (**P<0.01, *P<0.05).

doi:10.1371/journal.pone.0047472.t002

ized by interstitial hypertension interferes with intratumoral spread (diffusion) of therapeutic agents [27]. The increased interstitial hypertension in the tumor tissue is the result of abnormal vasculature. Unlike normal blood vessels, tumor vasculature is structurally and functionally abnormal [28]. This abnormal vasculature in STSA-1 tumor xenograft might inhibit intratumoral spread of GLAF-1 protein, which could be the reason for its localized effect. Moreover, effect of GLAF-1 showing decreased vascular density in STSA-1 tumor xengrafts is well supported by the previous findings which demonstrated that the treatment with GLV-1h68 and another GLAF-1-negative oncolytic vaccinia virus strain LIVP1.1.1, did not affect the blood vessel density of STSA-1 tumors [4]. We have also shown that GLAF-1 could specifically bind to canine VEGF (**Fig. 1**). Cross reactivity of GLAF-1 with VEGFs from other species apart from human and mouse was not tested. It was important to know whether GLAF-1 could bind and inhibit canine VEGF. The GLAF-1-binding to VEGF from both canine and mouse origins is advantageous in our canine xenograft models, as blocking of the two VEGF forms could be important for therapeutic efficacy [29].

To investigate the GLV-1h109 virus interactions with the host immune cells we analyzed the innate immune response in the early phase of virus infection by flow cytometry. Data demonstrated a significantly increased accumulation of host immune cells including granulocytic MDSCs and macrophages in GLV-1h109–infected tumors as compared to PBS or GLV-1h68-infected tumors (**Fig. 9**). On the other hand, a significant reduction of the blood vessel density of GLV-1h109 treated STSA-1 tumors was observed when compared to both controls; GLV-1h68 and PBS (**Fig. 8**). A possible reason for this phenomenon may be that the GLV-1h109-treatment led to "vascular normalization" in tumor tissue, as described by Winker and colleagues [30]. The "changed" vasculature seems to allow an increased intratumoral infiltration of MDSCs and macrophages in the tumor bed. Interestingly, MDSCs and macrophages may be associated with both pro- and anti-tumoral activities (for reviews, see [31–34]).

Several recent studies have described that virotherapy with vaccinia viruses induces massive tumoral infiltration of MDSCs resembling neutrophils, that may be exerting antitumor effects in vivo through a number of different mechanisms [35–37]. In this context, Breitbach and colleagues have postulated that neutrophils ($Gr\text{-}1^+$ cells) could mediate antitumor effects by the induction of vascular collapse in tumors [36]. In addition, a recent study has identified a cytotoxic population (N1) of tumor associated neutrophils expressing $CD11b^+Ly6G^+$, capable of killing tumor cells [38]. In the current work, we found evidence of direct interactions of vaccinia virus or virus-infected cells with MDSCs and macrophages in the STSA-1 tumor tissue (Table 2; GFP-positive cells). Others and we have recently reported that these interactions may increase the activation and strength of host antitumor immune responses [4,37–39]. Therefore, we think that the interactions of MDSCs and macrophages with vaccinia virus in the tumor bed may be crucial for the success of the virotherapy.

In conclusion, systemic administration of oncolytic vaccinia virus GLV-1h109 expressing an anti-VEGF single-chain antibody led to significant inhibition of angiogenesis and tumor growth as well as to increased infiltration of innate immune cells in the treated canine tumors.

Supporting Information

Figure S1 Expression of GLV-1h109 mediated proteins GLAF-1 and GusA in canine soft tissue sarcoma DT08/40 cells. DT08/40 cells were infected with either GLV-1h109, GLV1h 68 virus at an MOI of 1 or PBS. Protein fractions from cell lysate and culture supernatant were isolated at different time points and separated by SDS/PAGE. Western blot analysis was performed using an anti-DDDDK antibody against scAb GLAF-1 and anti-GusA antibody as described in material and methods.
(TIF)

Figure S2 Presence of $Gr\text{-}1^{high}$ $CD11b^+$cells (granulocytic MDSCs) in peripheral blood of virus-infected and non-infected STSA-1 xenografts at 7 dpvi. Experiments were done twice with at least 3 mice per group. The data are presented as mean values +/- SD.
(TIF)

Acknowledgments

We thank Ms. Johanna Langbein-Laugwitz, Mr. Jason Aguilar and Mr. Terry Trevino for technical support, Dr. Z. Sokolovic for critical reading of the manuscript and Dr U. Fischer and Dr. H. Murua Escobar for helpful discussions.

Author Contributions

Conceived and designed the experiments: IG SSP MA UD MH AAS. Performed the experiments: SSP IG MA UD MH SW. Analyzed the data: IG SSP MA AF AAS. Contributed reagents/materials/analysis tools: UD IN AF. Wrote the paper: IG SSP AAS.

References

1. Merlo DF, Rossi L, Pellegrino C, Ceppi M, Cardellino U, et al. (2008) Cancer incidence in pet dogs: findings of the Animal Tumor Registry of Genoa, Italy. J Vet Intern Med 22: 976–984.
2. Kelsey JL, Moore AS, Glickman LT (1998) Epidemiologic studies of risk factors for cancer in pet dogs. Epidemiol Rev 20: 204–217.
3. Patil SS, Gentschev I, Nolte I, Ogilvie G, Szalay AA (2012) Oncolytic virotherapy in veterinary medicine: current status and future prospects for canine patients. J Transl Med 10: 3.
4. Gentschev I, Adelfinger M, Josupeit R, Rudolph S, Ehrig K, et al. (2012) Preclinical evaluation of oncolytic vaccinia virus for therapy of canine soft tissue sarcoma. PLoS One 7: e37239.
5. Reimann-Berg N, Willenbrock S, Murua Escobar H, Eberle N, Gerhauser I, et al. (2011) Two new cases of polysomy 13 in canine prostate cancer. Cytogenet Genome Res 132: 16–21.
6. Zhang Q, Yu YA, Wang E, Chen N, Danner RL, et al. (2007) Eradication of solid human breast tumors in nude mice with an intravenously injected light-emitting oncolytic vaccinia virus. Cancer Res 67: 10038–10046.
7. Frentzen A, Yu YA, Chen N, Zhang Q, Weibel S, et al. (2009) Anti-VEGF single-chain antibody GLAF-1 encoded by oncolytic vaccinia virus significantly enhances antitumor therapy. Proc Natl Acad Sci U S A 106: 12915–12920.
8. Falkner FG, Moss B (1990) Transient dominant selection of recombinant vaccinia viruses. J Virol 64: 3108–3111.
9. Liang WC, Wu X, Peale FV, Lee CV, Meng YG, et al. (2006) Cross-species vascular endothelial growth factor (VEGF)-blocking antibodies completely inhibit the growth of human tumor xenografts and measure the contribution of stromal VEGF. J Biol Chem 281: 951–961.
10. Ferrara N, Gerber HP, LeCouter J (2003) The biology of VEGF and its receptors. Nat Med 9: 669–676.
11. Folkman J (2007) Angiogenesis: an organizing principle for drug discovery? Nat Rev Drug Discov 6: 273–286.
12. Kamstock D, Elmslie R, Thamm D, Dow S (2007) Evaluation of a xenogeneic VEGF vaccine in dogs with soft tissue sarcoma. Cancer Immunol Immunother 56: 1299–1309.
13. Quesada AR, Medina MA, Alba E (2007) Playing only one instrument may be not enough: limitations and future of the antiangiogenic treatment of cancer. Bioessays 29: 1159–1168.
14. Gerber HP, Ferrara N (2005) Pharmacology and pharmacodynamics of bevacizumab as monotherapy or in combination with cytotoxic therapy in preclinical studies. Cancer Res 65: 671–680.
15. Hess M, Stritzker J, Hartl B, Sturm JB, Gentschev I, et al. (2011) Bacterial glucuronidase as general marker for oncolytic virotherapy or other biological therapies. J Transl Med 9: 172.
16. Weibel S, Stritzker J, Eck M, Goebel W, Szalay AA (2008) Colonization of experimental murine breast tumours by Escherichia coli K-12 significantly alters the tumour microenvironment. Cell Microbiol 10: 1235–1248.
17. Gentschev I, Muller M, Adelfinger M, Weibel S, Grummt F, et al. (2011) Efficient colonization and therapy of human hepatocellular carcinoma (HCC) using the oncolytic vaccinia virus strain GLV-1h68. PLoS One 6: e22069.
18. Peranzoni E, Zilio S, Marigo I, Dolcetti L, Zanovello P, et al. (2010) Myeloid-derived suppressor cell heterogeneity and subset definition. Curr Opin Immunol 22: 238–244.
19. de Queiroz GF, Dagli ML, Fukumasu H, Zavala AA, Matera JM (2010) Vascular endothelial growth factor expression and microvascular density in soft tissue sarcomas in dogs. J Vet Diagn Invest 22: 105–108.
20. Zizzo N, Patruno R, Zito FA, Di Summa A, Tinelli A, et al. (2010) Vascular endothelial growth factor concentrations from platelets correlate with tumor angiogenesis and grading in a spontaneous canine non-Hodgkin lymphoma model. Leuk Lymphoma 51: 291–296.
21. Patruno R, Arpaia N, Gadaleta CD, Passantino L, Zizzo N, et al. (2009) VEGF concentration from plasma-activated platelets rich correlates with microvascular density and grading in canine mast cell tumour spontaneous model. J Cell Mol Med 13: 555–561.
22. Hemminki A, Kanerva A, Kremer EJ, Bauerschmitz GJ, Smith BF, et al. (2003) A canine conditionally replicating adenovirus for evaluating oncolytic virotherapy in a syngeneic animal model. Mol Ther 7: 163–173.
23. Suter SE, Chein MB, von Messling V, Yip B, Cattaneo R, et al. (2005) In vitro canine distemper virus infection of canine lymphoid cells: a prelude to oncolytic therapy for lymphoma. Clin Cancer Res 11: 1579–1587.
24. Gentschev I, Stritzker J, Hofmann E, Weibel S, Yu YA, et al. (2009) Use of an oncolytic vaccinia virus for the treatment of canine breast cancer in nude mice: preclinical development of a therapeutic agent. Cancer Gene Ther 16: 320–328.
25. Gentschev I, Ehrig K, Donat U, Hess M, Rudolph S, et al. (2010) Significant Growth Inhibition of Canine Mammary Carcinoma Xenografts following Treatment with Oncolytic Vaccinia Virus GLV-1h68. J Oncol 2010: 736907.
26. Arendt M, Nasir L, Morgan IM (2009) Oncolytic gene therapy for canine cancers: teaching old dog viruses new tricks. Vet Comp Oncol 7: 153–161.
27. Padera TP, Stoll BR, Tooredman JB, Capen D, di Tomaso E, et al. (2004) Pathology: cancer cells compress intratumour vessels. Nature 427: 695.
28. Jain RK (2001) Delivery of molecular and cellular medicine to solid tumors. Adv Drug Deliv Rev 46: 149–168.
29. Gerber HP, Kowalski J, Sherman D, Eberhard DA, Ferrara N (2000) Complete inhibition of rhabdomyosarcoma xenograft growth and neovascularization requires blockade of both tumor and host vascular endothelial growth factor. Cancer Res 60: 6253–6258.
30. Winkler F, Kozin SV, Tong RT, Chae SS, Booth MF, et al. (2004) Kinetics of vascular normalization by VEGFR2 blockade governs brain tumor response to radiation: role of oxygenation, angiopoietin-1, and matrix metalloproteinases. Cancer Cell 6: 553–563.
31. Gregory AD, Houghton AM (2011) Tumor-associated neutrophils: new targets for cancer therapy. Cancer Res 71: 2411–2416.
32. Nathan C (2006) Neutrophils and immunity: challenges and opportunities. Nat Rev Immunol 6: 173–182.
33. Ruffell B, Affara NI, Coussens LM (2012) Differential macrophage programming in the tumor microenvironment. Trends Immunol 33: 119–126.
34. Ochando JC, Chen SH (2012) Myeloid-derived suppressor cells in transplantation and cancer. Immunol Res.
35. Gil M, Bieniasz M, Seshadri M, Fisher D, Ciesielski MJ, et al. (2011) Photodynamic therapy augments the efficacy of oncolytic vaccinia virus against primary and metastatic tumours in mice. Br J Cancer 105: 1512–1521.
36. Breitbach CJ, Paterson JM, Lemay CG, Falls TJ, McGuire A, et al. (2007) Targeted inflammation during oncolytic virus therapy severely compromises tumor blood flow. Mol Ther 15: 1686–1693.
37. John LB, Howland LJ, Flynn JK, West AC, Devaud C, et al. (2012) Oncolytic virus and anti-4-1BB combination therapy elicits strong antitumor immunity against established cancer. Cancer Res 72: 1651–1660.
38. Fridlender ZG, Sun J, Kim S, Kapoor V, Cheng G, et al. (2009) Polarization of tumor-associated neutrophil phenotype by TGF-beta: "N1" versus "N2" TAN. Cancer Cell 16: 183–194.
39. Gentschev I, Donat U, Hofmann E, Weibel S, Adelfinger M, et al. (2010) Regression of human prostate tumors and metastases in nude mice following treatment with the recombinant oncolytic vaccinia virus GLV-1h68. J Biomed Biotechnol 2010: 489759.

Figure S1

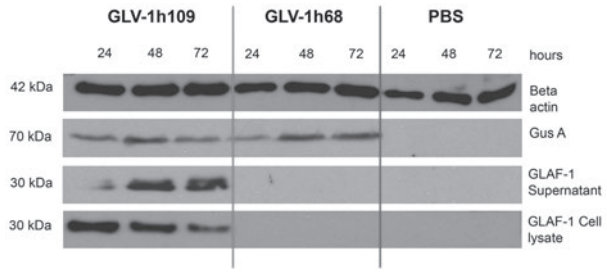
GLV-1h109
GLV-1h68
PBS
24
48
72
24
48
72
24
48
72
hours
42 kDa
Beta actin
70 kDa
Gus A
30 kDa
GLAF-1 Supernatant
30 kDa
GLAF-1 Cell lysate

Figure S2

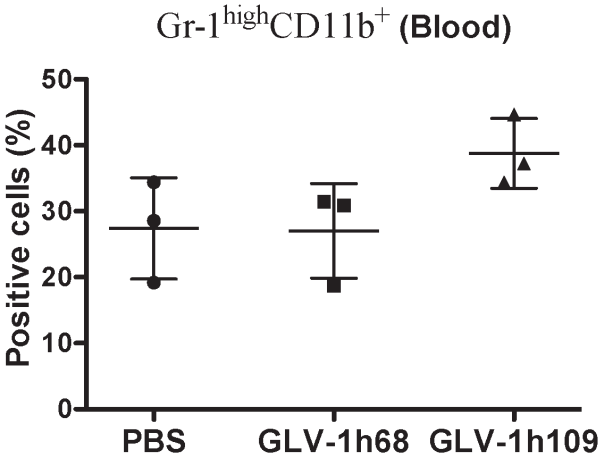
Gr-1highCD11b+ (Blood)
Positive cells (%)
50
40
30
20
10
0
PBS
GLV-1h68
GLV-1h109

5.2 Beta-glucuronidase as a preclinical imaging marker

Bacterial glucuronidase as general marker for oncolytic virotherapy or other biological therapies

Hess M, Stritzker J, Härtl B, Sturm JB, Gentschev I, Szalay AA
J Transl Med. 2011;9:172

(The possibilities of using glucuronidase-activted substrates as optical imaging tools are included in the publication that can be seen in chapter 5.1)

5.3 Vaccinia virus-encoded enzymes as prodrug-activating tools

Enhanced tumor therapy using Vaccinia virus strain GLV-1h68 in combination with a beta-galactosidase-activatable prodrug seco-analog of duocarmycin SA

Seubert CM, Stritzker J, Hess M, Donat U, Sturm JB, Chen N, von Hof JM, Krewer B, Tietze LF, Gentschev I, Szalay AA
Cancer Gene Ther. 2011;18:42-52

Publication (complete reference): Seubert CM, Stritzker J, **Hess M**, Donat U, Sturm JB, Chen N, von Hof JM, Krewer B, Tietze LF, Gentschev I, Szalay AA. Enhanced tumor therapy using Vaccinia virus strain GLV-1h68 in combination with a beta-galactosidase-activatable prodrug seco-analog of duocarmycin SA. *Cancer Gene Ther*. 2011;18:42-52
Authors' contributions
Conceived and designed the experiments: CMS JS AAS. Performed the experiments: CMS JS **MH** UD JBS. Analyzed the data: CMS JS AAS. Contributed reagents/materials/analysis tools: NC JMH BK LFT. Wrote the paper: CMS JS AAS.

Carolin M. Seubert	
Jochen Stritzker	
Ulrike Donat	
Julia B. Sturm	
Nanhai G. Chen	
J. Marian von Hof	
Birgit Krewer	
Lutz F. Tietze	
Ivaylo Gentschev	
Aladar A. Szalay	

Cancer Gene Therapy (2011) 18, 42–52

www.nature.com/cgt

Open

ORIGINAL ARTICLE

Enhanced tumor therapy using vaccinia virus strain GLV-1h68 in combination with a β-galactosidase-activatable prodrug *seco*-analog of duocarmycin SA

CM Seubert[1,5], J Stritzker[1,2,5], M Hess[1], U Donat[1], JB Sturm[1], N Chen[2], JM von Hof[3], B Krewer[3], LF Tietze[3], I Gentschev[1,2] and AA Szalay[1,2,4]

[1]*Department of Biochemistry, Biocenter, University of Würzburg, Würzburg, Germany;* [2]*Genelux Corporation, San Diego, CA, USA;* [3]*Institut für Organische und Biomolekulare Chemie, Georg-August-Universität Göttingen, Göttingen, Germany;* [4]*Department of Radiation Oncology, Moores Cancer Center, University of California, San Diego, La Jolla, CA, USA*

Breast cancer is the most common cause of cancer-related death worldwide, thus remaining a crucial health problem among women despite advances in conventional therapy. Therefore, new alternative strategies are needed for effective diagnosis and treatment. One approach is the use of oncolytic viruses for gene-directed enzyme prodrug therapy. Here, the *lacZ*-carrying vaccinia virus (VACV) strain GLV-1h68 was used in combination with a β-galactosidase-activatable prodrug derived from a *seco*-analog of the natural antibiotic duocarmycin SA. Tumor cell infection with the VACV strain GLV-1h68 led to production of β-galactosidase, essential for the conversion of the prodrug to the toxic compound. Furthermore, drug-dependent cell kill and induction of the intrinsic apoptosis pathway in tumor cells was also observed on combination therapy using the prodrug and the GLV-1h68 strain, despite the fact that VACV strains encode antiapoptotic proteins. Moreover, GI-101A breast cancer xenografts were effectively treated by the combination therapy. In conclusion, the combination of a β-galactosidase-activatable prodrug with a tumor-specific vaccinica virus strain encoding this enzyme, induced apoptosis in cultures of the human GI-101A breast cancer cells, in which a synergistic oncolytic effect was observed. Moreover, *in vivo*, additional prodrug treatment had beneficial effects on tumor regression in GLV-1h68-treated GI-101A-xenografted mice.
Cancer Gene Therapy (2011) **18,** 42–52; doi:10.1038/cgt.2010.49; published online 10 September 2010

Keywords: vaccinia virus; breast cancer; oncolytic virotherapy; prodrug

Introduction

Breast cancer is the most common form of cancer and the second most common cause of cancer-related death in women.[1] In the United States of America, it is estimated that 1.5 million new cases of breast cancer was diagnosed in 2009, and that ~40 400 women will die from breast cancer-related causes alone, despite advances in conventional therapy.[2] Consequently, novel, well-tolerated and more effective therapies are needed to reduce the number of breast cancer-related deaths. Among several strategies to improve currently applied treatments, the use of oncolytic viruses is a very promising therapeutic approach.[3,4]

Correspondence: Dr AA Szalay, Genelux Corporation, San Diego, CA 92109, USA.
E-mail: aaszalay@genelux.com
[5]These authors contributed equally to this work.
Received 26 July 2009; revised 10 May 2010; accepted 19 July 2010; published online 10 September 2010

Regarding the many different oncolytic viral agents used for tumor-directed therapy, vaccinia virus (VACV) has several advantages. This large DNA virus exclusively replicates in the cytoplasm without the need for host DNA-synthesis machinery, thereby excluding the risk of integration into the host genome. It displays rapid spread, a broad range of host cell tropism and a high capacity for genetic payload, with up to 25 kb of foreign DNA.[5] Moreover, the systemic injection of recombinant VACV (rVACV) strains into tumor-bearing mice resulted in high viral titers in tumors, but not in other organs, indicating tumor-specific colonization.[6–8]

Another approach is the use of viruses for gene-directed enzyme prodrug therapy (GDEPT) to improve the selectivity of chemotherapy by enabling cancer cells to convert prodrugs of low cytotoxictiy to highly potent drugs. Because the suicide genes must be expressed selectively in tumor cells to prevent adverse effects in the patient, substantial efforts have been conducted to develop gene transfer vectors specifically targeting tumors. Among these, tumor-specific viruses including adenovirus, sindbis virus, retroviruses, herpes simplex

virus, vesicular stromatitis virus and VACV so far appear to be the best-suited gene transfer vectors (reviewed in Schepelmann and Springer[9]). Using the VACV species, several promising results have already been obtained with replication-competent, cytosine deaminase-expressing VACV strains in combination with the well-described prodrug 5-fluorocytosine.[10–14] Here, a β-galactosidase-expressing VACV strain was used for GDEPT.

The β-galactosidase-encoding *lacZ* gene of *E. coli* was the first widely used reporter gene. It has numerous applications in molecular and cellular biology and has also been used as marker in clinical trials.[15,16] Moreover, a variety of substrate structures were generated to enable detection of β-galactosidase expression in live animals, by optical imaging with near-infrared fluorescent probes,[17,18] by luminescent imaging using a caged D-luciferin–galactoside conjugate,[19] with radionuclide substrates for SPECT imaging[20] and with probes enabling magnetic resonance imaging.[21] As prodrug-mediated tumor therapy has been investigated more extensively, a number of β-galactosidase-activatable prodrugs have also been described, the most promising of which are the *seco*-analogs of the highly cytotoxic natural antibiotics CC-1065 and duocarmycin SA (for a recent review see Tietze and Krewer[22]). However, no experiments have been published in the literature that describes the successful use of these prodrugs in live tumor-bearing animal studies. One of the most promising prodrugs developed so far, namely, the (1*S*)-*seco*-CBI-DMAI-β-D-galactoside 1, showed a high Q IC_{50} value (Q $IC_{50} = IC_{50}$ of prodrug/IC_{50} of prodrug in the presence of the cleaving enzyme, with IC_{50} being the concentration required for 50% growth inhibition of target cells) of 3500 and an IC_{50} value for the corresponding highly cytotoxic drug 2 of 16 pM (Supplementary Figure S1).[23] In this study, this prodrug, in combination with the β-galactosidase-encoding oncolytic VACV strain GLV-1h68, was tested in cell culture and animals, resulting in enhanced breast cancer regression.

Materials and methods

Cell culture and VACV constructs

The GI-101A human breast cancer cells were cultured in RPMI-1640 medium containing 1% HEPES (4-(2-hydroxyethyl)-1-piperazineethanesulfonic acid), 1% sodium pyruvate, 1% antibiotic–antimycotic solution and 20% fetal bovine serum (FBS). The human adenocarcinoma cells MDA-MB-231-CBG (click-beetle luciferase-expressing cells derived from MDA-MB-231; U Donat *et al*., unpublished data) were cultured in Dulbecco's modified Eagle's medium, 10% FBS and 10 μg ml^{-1} blasticidin. Canine breast adenoma ZMTH3 cells were cultured in RPMI-1640 medium containing 20% FBS.

GLV-1h68 was derived from VACV LIVP as described previously.[7] In GLV-1h43, the *lacZ*-containing gene cassette was replaced by a nonrelevant gene-containing cassette. Both strains were developed from the VACV LIVP strain by site-directed insertional mutagenesis. The *F14.5L* locus was replaced by insertion of a *Renilla* luciferase–*GFP* (green fluorescent protein) fusion construct under the control of a synthetic early/late promoter (P_{SEL}). The hemagglutinin (*HA*) gene was replaced by the β-glucuronidase-encoding gene *gusA* and placed under the control of the late promoter P11. The viral thymidine kinase (*TK*) was either replaced by *lacZ*, the gene encoding β-galactosidase, controlled by the VACV early/late P7.5 promoter in GLV-1h68, or by a nonrelevant gene construct in GLV-1h43 (Figure 1a). The virus strains GLV-1h71 and

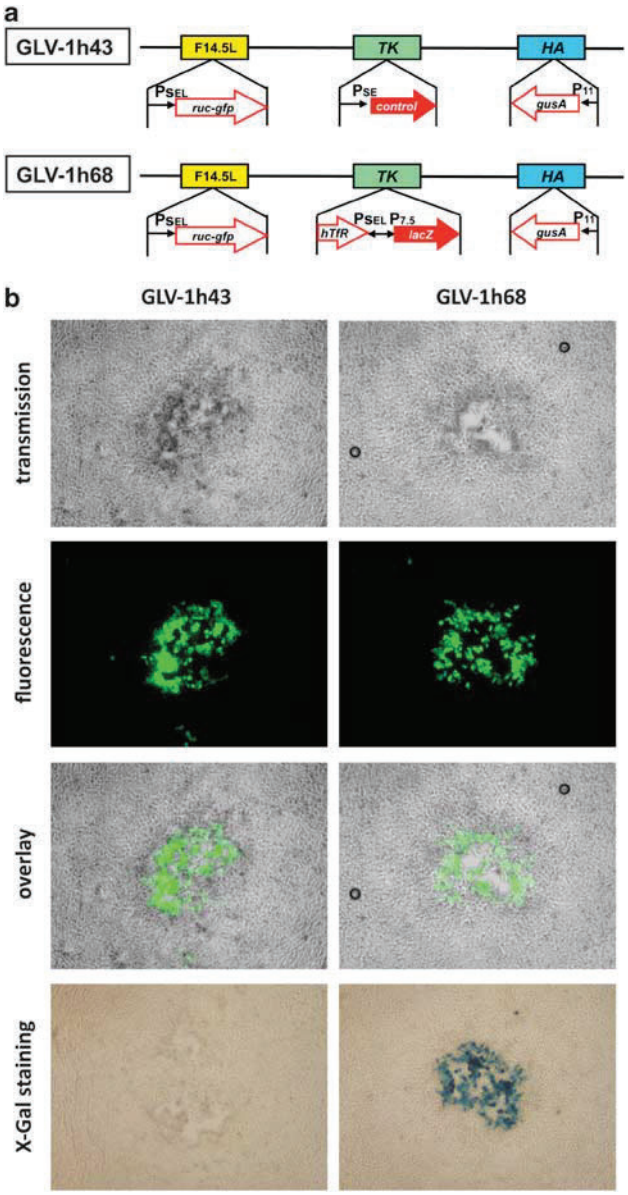

Figure 1 Recombinant vaccinia virus (rVACV) constructs and marker gene expression. (**a**) The wild-type LIVP was used for the generation of modified rVACV with designations of GLV-1h43 and GLV-1h68. *P11*, VACV late P11 promoter; *PE/L*, VACV synthetic early/late promoter; *P7.5*, VACV 7.5 K early/late promoter. (**b**) Expression of the marker gene green fluorescent protein (GFP) could be detected in plaques of both virus strains, whereas staining for X-gal revealed expression of β-galactosidase in GLV-1h68-infected GI-101A cells only. HA, hemagglutinin; TK, thymidine kinase.

GLV-1h85 are the *Ruc-GFP*-negative analogs of GLV-1h68 and GLV-1h43, respectively.

Infections of cell cultures

At 2 days before infection, cells were seeded in six-well plates for RNA and protein isolation, and in 24-well plates for survival and microscopy studies. If not otherwise indicated, the 90% confluent cell layer was mock infected or infected with GLV-1h43 or GLV-1h68 at a multiplicity of infection per cell of 0.05 or 0.5 for 1 h at 37 °C in medium containing 2% FBS. The virus-containing medium was then aspirated and replaced by non-prodrug-containing cell culture medium or medium supplemented with 10 nM of prodrug.

Isolation and detection of proteins

At 6, 12, 24, 48 or 72 h post-infection (hpi), cells were harvested and lysed in SDS sample buffer or in lysis buffer (10 mM Tris (pH 7.4), 150 mM NaCl, 1 mM EDTA, 10 mM HEPES, 0.05% Igepal and 0.75 mM dithiothreitol) supplemented with a proteinase inhibitor cocktail (Roche, Penzberg, Germany). The cell lysates were separated on a 10, 12 or 15% SDS-polyacrylamide electrophoresis gel, and proteins were transferred onto a nitrocellulose transfer membrane (Whatman GmbH, Dassel, Germany). The membrane was then incubated with one of the following: anti-β-actin mouse monoclonal antibody (ab6276, Abcam, Cambridge, UK), anti-β-galactosidase rabbit polyclonal antibody (A-11132, Molecular Probes, Leiden, the Netherlands), anti-cleaved caspase-3 rabbit polyclonal antibody (no. 9661, Cell Signaling Technology, Danvers, MA), anti-full-length caspase-3 rabbit polyclonal antibody, (no. 9662, Cell Signaling Technology), anti-caspase-8 mouse monoclonal antibody (no. 9746, Cell Signaling Technology), anti-caspase-9 rabbit polyclonal antibody (no. 9502, Cell Signaling Technology), anti-GFP rabbit polyclonal (sc-8334, Santa Cruz, Heidelberg, Germany) or anti-cleaved poly (ADP-ribose) polymerase (PARP) mouse monoclonal antibody (51-9000017, BD Pharmingen, Heidelberg, Germany). The first antibodies were then detected using horseradish peroxidase-labeled anti-mouse (ab6728, Abcam) or anti-rabbit (ab6721, Abcam) secondary antibodies, followed by enhanced chemiluminescence.

Quantitative results were obtained using a NightOWL LB 981 imaging system (Berthold Technologies, Bad Wildbad, Germany).

Analysis of RNA expression

At 6, 12, 24, 48 or 72 hpi, cellular RNA was isolated using the RNeasy Mini Kit (Qiagen, Hilden, Germany), followed by DNase treatment using DNA-free Kit (Ambion, Austin, TX). RNA samples were converted to cDNA by RevertAid First Strand cDNA Synthesis Kit (Fermentas, St Leon-Rot, Germany) and analyzed by reverse transcriptase PCR and quantitative PCR using primers for glyceraldehyde 3-phosphate dehydrogenase (from First Strand cDNA Synthesis Kit (Fermentas)); for β-actin, the primers used were forward: 5′-GGAGAA AATCTGGCACCACAC-3′ and reverse: 5′-CCATCTCT TGCTCGAAGTCCA-3′; for *lacZ*, forward: 5′-GGC CAGTTGCGTGACTACC-3′ and reverse: 5′-CCGACA TCGCAGGCTTCTG-3′ for real-time PCR and 5′-CAC GGCATTAAAGTTGTTCTGCTTC-3′ for reverse transcriptase PCR; and for GFP, forward: 5′-GCGTG CAGTGCTTTTCCAG-3′ and reverse: 5′-AGGGCAGA CTGGGTGGAC-3′.

Quantitative PCR was performed using ABsolute QPR SYBR Green Mix (Thermo Scientific, Epsom, UK) in a DNA Engine Opticon CFD-0200 (MJ Research, Waltham, MA) and analyzed using the Opticon Monitor software (MJ Research).

β-Galactosidase assays and X-gal staining

The concentration of cell-associated β-galactosidase, as well as the concentration in the supernatant, was analyzed in a β-galactosidase assay. A standard dilution series was performed over the range of 1×10^{-6}–1 U μl^{-1} β-galactosidase (from *Aspergillus oryzae*—11.2 U mg^{-1}, G5160, Sigma-Aldrich, Steinheim, Germany). Tumor homogenates, blood serum samples, cell lysates and cell culture supernatants were incubated with the staining solution (40 µl X-gal in dimethylformamide (40 mg ml^{-1}), ferricyanide (12 mM K3Fe(CN)6), 5.2 mM MgCl2 and ferrocyanide solution (12 mM K4Fe(CN)6)), and optical density was determined in a Tecan sunrise absorbance reader (Tecan, Crailsheim, Germany).

For X-gal staining, cells on coverslips or tumor sections were incubated with the staining solution overnight at room temperature, washed several times with PBS and mounted in 80% glycerol in PBS.

Histology and fluorescent microscopy

For the microscopical analysis of β-galactosidase and GFP expression, GI-101A cells were seeded on coverslips and infected using 100 plaque-forming units (PFUs) per well. After 2 days, cells were fixed for 2 min using 4% paraformaldehyde and washed in PBS. Subsequently, either direct visualization was performed for GFP or β-galactosidase staining was carried out before microscopical analysis by means of a Leica DMR fluorescence microscope (Leica, Wetzlar, Germany) and a Diagnostic Instruments digital camera model 2.3.1 (Visitron Systems GmbH, Puchheim, Germany) using Meta-Vue 5.0r2 software (Visitron Systems GmbH).

Histology and fluorescence microscopy of tumor sections were performed as described previously.[24] Briefly, snap-frozen GI-101A tumors of GLV-1h43- or GLV-1h68-injected mice were fixed in 4% paraformaldehyde and 100 µm vibratome tissue sections were permeabilized in PBS containing 0.3% Triton X-100. Neighboring sections were then stained using X-gal and Hoechst 33342. After several rinses in PBS, tissue sections were incubated in PBS containing 60% (v/v) glycerol and then mounted in PBS containing 80% (v/v) glycerol.

Tumor specimens were examined with the Stereo-Fluorescence microscope (MZ16 FA, Leica, Heerbrugg, Switzerland) equipped with a digital CCD camera (DC500, Leica). The blue β-galactosidase staining was visualized using white light, whereas GFP and Hoechst

33342 were detected using fluorescence. Digital images (1300×1030 pixel color images) were processed with Photoshop 10.0 (Adobe Systems, San Jose, CA) and merged to yield pseudocolored pictures.

Prodrug synthesis

Prodrug synthesis was performed as described previously[23] and stock solutions of the prodrug were prepared in dimethyl sulfoxide.

Cell viability assay

The amount of viable cells after infection with GLV-1h43 or GLV-1h68 and/or treatment with 10 nM prodrug was measured using 3-(4,5-dimethylthiazol-2-yl)-2,5-diphenyltetrazolium bromide (MTT) (Sigma, Taufkirchen, Germany). At the indicated time points, the medium was replaced by 0.5 ml MTT solution at a concentration of 2.5 mg ml^{-1} MTT dissolved in RPMI 1640 medium without phenol red and incubated for 4 h at 37 °C in a 5% CO_2 atmosphere. After removal of the MTT solution, 1 N HCl diluted in 2-propanol was added and the optical density was then measured at a wavelength of 570 nm. Mock-infected cells served as a reference and were considered as 100% viable.

The rate of apoptosis was determined using the PE-annexin V apoptosis detection kit (BD Biosciences, Heidelberg, Germany) according to the manufacturer's instructions. The analysis was performed on a Epics XL flow cytometer (Beckman Coulter GmbH, Krefeld, Germany) and the data were analyzed using WinMDI 2.8 (Joe Trotter, Scripps Research Institute, La Jolla, CA).

Animal studies

GI-101A xenograft tumors were developed in 6- to 8-week-old female nude mice (NCI:Hsd:Athymic Nude-*Foxn1*^{nu}, Harlan, Borchem, Germany and Indianapolis, IN) by implanting 5×10^6 GI-101A cells subcutaneously on both hind flanks (two tumors per mouse). Tumor growth was recorded once a week in two dimensions using a digital caliper. Tumor volume was calculated as ((length $\times$ width^2)/2) and reported in mm^3. At 30 days after tumor cell implantation, three groups of 12 mice were injected with a single intravenous dose of PBS, or 5×10^6 PFUs of GLV-1h43 or GLV-1h68 in 100 µl of PBS. The 12 mice of each group were subdivided into two groups of six mice that were intraperitoneally injected three times a week with 200 µl of a 1:1 (v/v) mixture of dimethyl sulfoxide and PBS alone or 200 µl of the same mixture containing prodrug (100 nM), starting 6 days after VACV injection.

All animal experiments were carried out in accordance with protocols approved by the Institutional Animal Care and Use Committee of Explora Biolabs (San Diego, CA) or the 'Regierung von Unterfranken' (Würzburg, Germany).

Statistical analysis

The significance of differences between the various groups was determined using a two-tailed unpaired *t*-test (Excel 2008 for Mac, Microsoft, Redmond, WA). A *P*-value <0.05 was considered significant.

Results

β-Galactosidase-activatable prodrug: mechanism of action

The recently described *seco*-duocarmycin SA analog-derived prodrug 1 (Supplementary Figure S1) used in this study was previously shown to be extremely efficient in killing cells in culture.[23] On β-galactosidase activation, prodrug 1 releases a drug with an IC_{50} value of 16 pM that is 3500 times more cytotoxic than the prodrug itself. However, studies have not yet determined whether target cell death also occurred via the same intrinsic apoptosis mechanism as already described for duocarmycin SA.[25–27]

We therefore incubated GI-101A cells with PBS and prodrug alone or prodrug in combination with purified β-galactosidase. In contrast to PBS or prodrug-only treated cells, Hoechst 33342 staining showed nuclear condensation in a high proportion of prodrug and β-galactosidase-treated cells. A parallel staining with propidium iodide, which is only permeant into dead cells, was mostly negative. This indicated an intact cell membrane and supported the notion of apoptosis induction (data not shown).

To validate that the apoptosis was induced, cellular proteins were harvested and analyzed by western blotting using antibodies against cleaved PARP, caspase-3, caspase-8 and caspase-9 (Figure 2). It was obvious that cleaved PARP and cleaved caspase-3, as indicators for apoptosis,[28] were only detectable in cells that were treated with the prodrug in combination with β-galactosidase, but absent in PBS and prodrug-only controls. Furthermore,

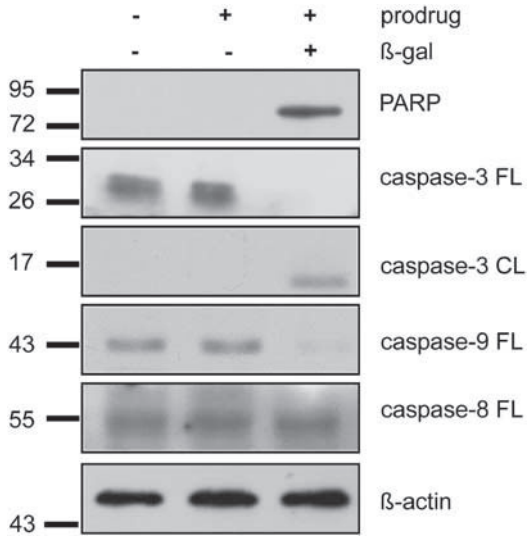

Figure 2 Validation of apoptosis induction on prodrug activation. Western blot analysis with antibodies against cleaved poly (ADP-ribose) polymerase (PARP), full-length (FL) caspase-3, cleaved (CL) caspase-3, full-length caspase-9, full-length caspase-8 and β-actin. Cleaved PARP and cleaved caspase-3, as indicators for apoptosis, were only detectable in both prodrug and β-galactosidase-treated cells. Additionally, full-length caspase-9 concentration significantly decreased because of treatment with prodrug and β-galactosidase, whereas caspase-8 remained uncleaved. Equal protein loading was confirmed by detection of β-actin.

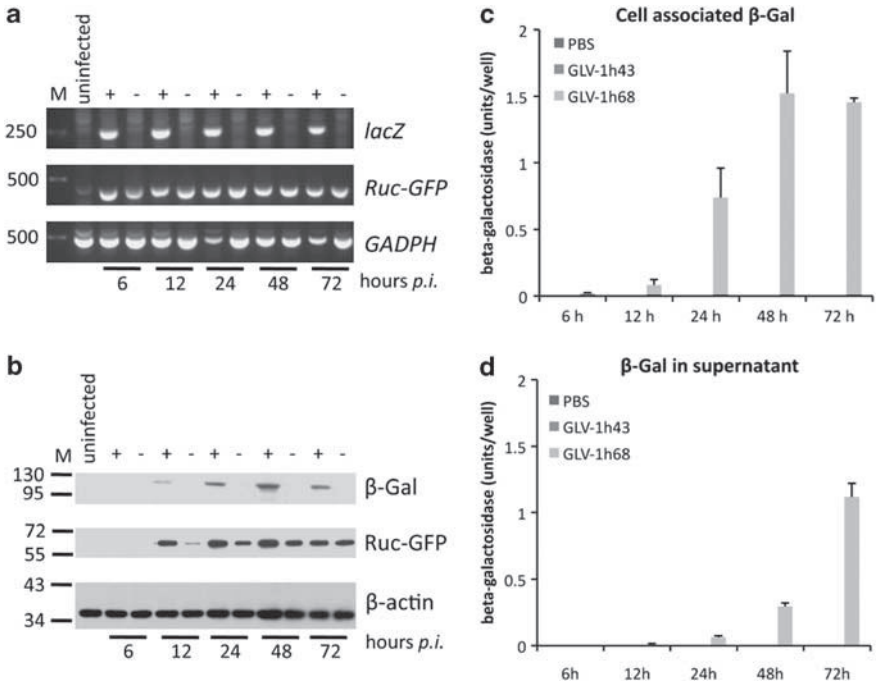

Figure 3 Evaluation of reporter gene expression after infection with recombinant vaccinia virus (rVACV). (**a**) Reverse transcriptase PCR results from mock-infected cells (untreated), GLV-1h68- (68) or GLV-1h43 (43)-infected cells at 6, 12, 24, 48 and 72 hpi using *lacZ*-, green fluorescent protein (GFP)- and glyceraldehyde 3-phosphate dehydrogenase-specific primers. Infection with GLV-1h68 led to production of *Ruc-GFP* and *lacZ*-specific transcripts as early as 6 hpi, whereas in GLV-1h43-infected cells, no *lacZ* transcript could be detected. Both reporter gene transcripts were not detectable in mock-infected cells. (**b**) Western blot analysis using β-galactosidase (β-gal) and Ruc-GFP-specific antibodies, showing no expression of β-galactosidase in GLV-1h43-infected cells. In contrast, both proteins could be detected in GLV-h168-infected cells after 12 hpi. β-galactosidase expression increased up to 48 hpi. Equal protein loading was confirmed by detection of β-actin. (**c**, **d**) Determination of β-galactosidase activity in cell lysates (**c**) and supernatants (**d**) after infection with GLV-1h43, GLV-1h68 and mock infection. Enzyme activity in cell lysates increased up to 48 hpi with GLV-1h68, further supporting the western blot results. In supernatants, no active enzyme could be detected until 12 hpi, but then increased until 72 hpi. As expected, no active enzyme could be detected in mock- or GLV-1h43-infected cells or supernatants at all time periods. PBS, phosphate-buffered saline.

although caspase-8 remained uncleaved, the amount of full-length caspase-9 dropped significantly in prodrug and β-galactosidase-treated cells, indicating that apoptosis is induced via the intrinsic rather than extrinsic pathway.[29,30]

Characterization of rVACV strains GLV-1h68 and GLV-1h43 in cell culture

To test the expression of the reporter proteins Ruc-GFP and β-galactosidase, the human breast cancer cell line GI-101A was infected with the rVACV strains GLV-1h68 or GLV-1h43 (Figure 1a). As previously mentioned, β-galactosidase was used as a prodrug-activating protein in this study.

As expected, expression of GFP could be observed for both strains by fluorescence microscopy, whereas β-galactosidase-specific X-gal staining of plaques was only positive in GLV-1h68-infected GI-101A cells (Figure 1b).

Reverse transcriptase PCR analysis (Figure 3a) and western blotting (Figure 3b) confirmed the virus-mediated expression of the reporter genes. No *Ruc-GFP*- or *lacZ*-specific transcripts or proteins could be detected in mock-infected control cells, whereas both were detectable in GLV-1h68-infected cells. In contrast, infection with GLV-1h43 led to production of Ruc-GFP but not β-galactosidase. Although reporter gene transcripts could be detected as early as 6 hpi, the respective proteins were not detected by western blot until 12 hpi. In addition, real-time PCR revealed an increasing *lacZ* expression until 48 hpi (data not shown), correlating with the western blot analysis (Figure 3b) of GLV-1h68-infected cells.

As the prodrug is converted only by a functional enzyme, we also determined the β-galactosidase activity in cell lysates (Figure 3c) and supernatants (Figure 3d) of mock-, GLV-1h43- and GLV-1h68-infected GI-101A cells. The enzyme activity increased until 48 hpi in the cell lysates, as supported by the western blot results (Figure 3b). In supernatants, no β-galactosidase activity was detected by 12 hpi, but then increased by 72 hpi, probably as a consequence of increased viral cell lysis. In mock- or GLV-1h43-infected cells, no β-galactosidase activity was detectable at any time points.

Furthermore, when coincubating the cell lysates and supernatants of mock-, GLV-1h43- or GLV-1h68-infected cells with uninfected GI-101A cells, the observed prodrug-mediated cell death correlated with the presence of active β-galactosidase (Supplementary Figure S2).

Therefore, a β-galactosidase-specific prodrug should only be activated on GLV-1h68 infection.

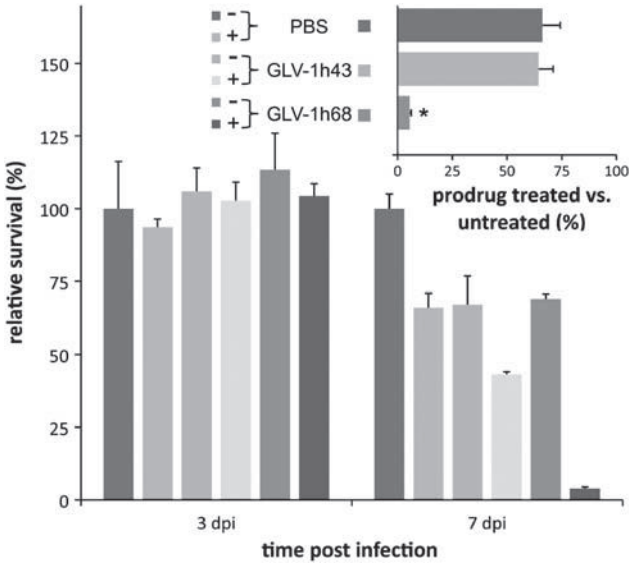

Figure 4 Cell survival studies after prodrug treatment and infection. Cells were infected with a low multiplicity of infection of 0.05 or mock infected and treated with 10 nM prodrug. Non-prodrug-treated cells served as the control. Cell viability was determined by 3-(4,5-dimethylthiazol-2-yl)-2,5-diphenyltetrazolium bromide (MTT)-assays on days 3 and 7 post-infection. On day 3 post-infection, no significant difference in cell viability between the different samples was observed. Combined treatment of cells with GLV-1h68 and prodrug induced a significantly higher tumor cell kill 7 days post-infection compared with infection with GLV-1h68 alone. Although prodrug treatment alone as well as rVACV treatment alone had inhibitory effects when compared with untreated cells (significance not shown), only simultaneous treatment of cells with GLV-1h68 and prodrug contributed to strong synergistic effects and the most efficient cell killing (inset, showing survival of prodrug-treated vs corresponding untreated cells). In each chart, average plus standard deviation ($n=3$) is shown. Asterisk indicates statistical significance ($P<0.05$). PBS, phosphate-buffered saline.

Enhanced tumor cell lysis after GLV-1h68 infection due to prodrug addition

In tumors treated with oncolytic VACV, not every cell is infected and will express β-galactosidase; hence, sufficient prodrug bystander effects are needed for enhancement of oncolysis.[11]

We therefore chose to use a low multiplicity of infection of 0.05 for experiments, applying the prodrug directly in combination with mock-, GLV-1h43- and GLV-1h68-infected cells. The prodrug was added at a concentration of 10 nM immediately after infection. Non-prodrug-treated cells served as controls. Cell survival was analyzed by MTT assays on days 3 and 7 after infection.

As shown in Figure 4, on day 3 post-infection, no significant difference was observed between prodrug-treated or untreated mock-, GLV-1h43- or GLV-1h68-infected cells. Conversely, simultaneous treatment of GI-101A cells with GLV-1h68 and 10 nM of prodrug resulted in significantly higher tumor cell killing at 7 days post-infection compared with GLV-1h68 alone. The prodrug alone had some inhibitory effects on mock- or GLV-1h43-infected GI-101A cells, resulting in an ~30% reduction of cell numbers on day 7 post-infection, when compared with the respective non-prodrug-treated controls. However, only the combination of the prodrug with GLV-1h68 resulted in strong synergistic effects and the most efficient cell killing (Figure 4, inset).

Similar effects were also observed when using other breast tumor cells such as the human breast adenocarcinoma cells MDA-MB-231-CBG and canine breast adenoma ZMTH3 (data not shown).

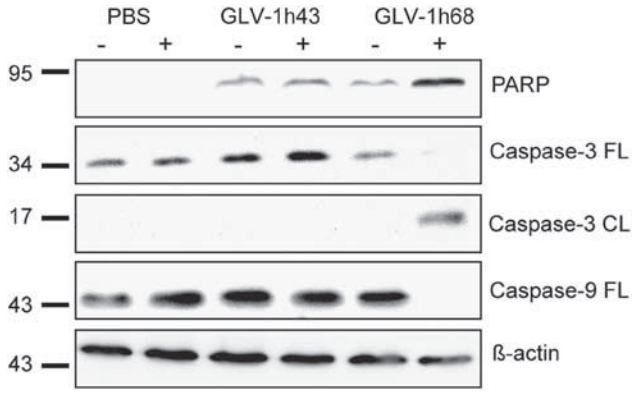

Figure 5 Apoptosis induction in GLV-1h68-infected tumor cells on prodrug treatment. Western blot analysis using specific antibodies against cleaved poly (ADP-ribose) polymerase (PARP), full-length (FL) caspase-3, cleaved (CL) caspase-3, full-length caspase-9 and β-actin. Samples were taken from infected or mock-infected GI-101A cells treated (+) or untreated (−) with 10 nM prodrug. Expression of the apoptosis indicator PARP was significantly higher in GLV-1h68-infected cells treated with prodrug, compared with cells treated with vaccinia virus alone or with GLV-1h43 and prodrug. Uninfected control cells showed almost no expression of PARP. Furthermore, approximately no full-length caspase-3 or caspase-9 could be observed in GLV-1h68-infected cells treated with prodrug, whereas both proteins were present in the other samples. Cleaved caspase-3 was detectable only in those samples retrieved after combined treatment with GLV-1h68 and prodrug. Equal loading of protein was confirmed by detection of β-actin. PBS, phosphate-buffered saline.

Induction of apoptosis in GLV-1h68-infected tumor cells after addition of prodrug

VACV encodes a number of antiapoptotic factors and inhibits both the extrinsic as well as the intrinsic apoptotic pathway (reviewed in Taylor and Barry[31]). To test whether these factors can also prevent cells from (pro)drug-mediated apoptosis, we analyzed the induction of apoptosis by measuring the binding of labeled annexin V using flow cytometry. As both GLV-1h68 and GLV-1h43 result in very high expression levels of the fusion protein Ruc-GFP, which interfered with the flow cytometry measurements, we used two other VACV strains, namely GLV-1h71 (β-galactosidase-positive) and GLV-1h85 (β-galactosidase-negative), which do not express the fluorescent protein. At 3 days post-infection, we detected $59.9 \pm 1.1\%$ annexin V-positive cells in prodrug-treated cells infected with GLV-1h71, but only $39.9 \pm 4.4\%$ cells when GLV-1h85 was used. This corresponded well with $40.2 \pm 1.9\%$ apoptotic cells in GLV-1h71-infected cells that were not treated with

prodrug. Therefore, the enhanced rate in apoptosis could be attributed to the prodrug treatment.

Even clearer results were obtained when analyzing protein lysates of prodrug-treated or untreated mock-, GLV-1h43- and GLV-1h68-infected cells, using western blotting with antibodies against cleaved PARP, caspase-3 and caspase-9 (Figure 5).

The quantitative analysis of the western blots revealed a sevenfold higher concentration of cleaved PARP in cells treated with GLV-1h68 in combination with the prodrug, when compared with cells treated with VACV alone or with GLV-1h43 and the prodrug. In GI-101A cells not infected with rVACV, almost no cleaved PARP was detectable. Even more pronounced was the difference with cleaved caspase-3, which could only be detected in GLV-1h68-infected cells treated with prodrug. On the other hand, an at least threefold less full-length caspase-3 and a sevenfold less full-length caspase-9 was present in GI-101A cells treated with prodrug after infection with GLV-1h68 compared with controls. The induction of apoptosis, therefore, can still be observed in the presence of VACV and is specifically induced in cells treated with prodrug and the β-galactosidase-encoding GLV-1h68 strain.

Enhanced GLV-1h68-mediated oncolysis on prodrug treatment

Next, we investigated the oncolytic potential of a combined treatment using the β-galactosidase-activatable prodrug and the rVACV strain GLV-1h68 in the GI-101A xenograft breast cancer model.

As active β-galactosidase might be released from GLV-1h68-infected tumors into the blood stream and lead to unwanted side effects in other tissues, the β-galactosidase activity in tumors and in blood serum samples was tested in a preliminary experiment. Three GI-101A tumor-bearing mice were injected with GLV-1h68, and at 42 days post-infection, the mice were killed. Tumor homogenates and blood serum samples were then analyzed by β-galactosidase assay. The results revealed high enzyme activity in tumor samples ($\sim 100\,\mathrm{U\,g^{-1}}$ tumor tissue), but undetectable levels in blood serum samples (detection limit: $0.3\,\mathrm{U\,ml^{-1}}$). Therefore, unwanted side effects are unlikely to occur. Thus, we began to determine the effects of the β-galactosidase-activatable prodrug in combination with the *lacZ*-encoding GLV-1h68 strain in live animals.

For this purpose, mice were subcutaneously injected with 5×10^6 GI-101A cells on each flank, which formed tumors of around $450\,\mathrm{mm^3}$ after 30 days. Groups of 12 mice were then intravenously injected with PBS or with 5×10^6 PFUs each of both GLV-1h43 and GLV-1h68 cells. The animals were then subdivided equally into two groups. At 6 days after rVACV injection, prodrug treatment was started in one subgroup, whereas the other subgroup received injections of a 1:1 (v/v) mixture of dimethyl sulfoxide and PBS only (Figure 6).

Tumor size measurements revealed that both rVACV strains showed tumor therapeutic efficacy compared with PBS-injected mice, with the PBS-injected mice having to be killed because of tumor burden between 6 and 9 weeks post-injection. Interestingly, GLV-1h43-mediated tumor therapy was more effective compared with GLV-1h68 treatment. The injection of the prodrug resulted in reduced tumor size in all subgroups when compared with the corresponding non-prodrug-treated animals, although the difference did not reach statistical significance in those groups injected with PBS or the GLV-1h43 strain ($P > 0.15$). In contrast, the subgroup treated with prodrug after injection of the *lacZ*-encoding GLV-1h68 strain had a significantly decreased tumor volume ($P < 0.006$) at 70 days after rVACV injection, when compared with the non-prodrug-treated GLV-1h68-injected control. The tumor size in the prodrug-treated subgroup was reduced close to the initial tumor volume before injection of VACV, whereas the non-prodrug-treated subgroup had an average tumor volume of $\sim 930\,\mathrm{mm^3}$.

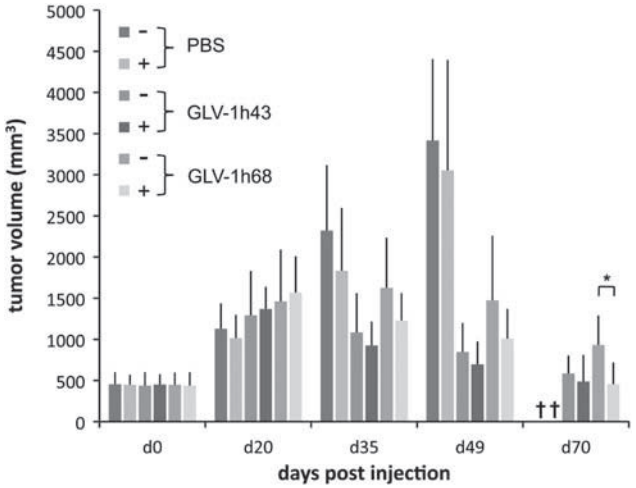

Figure 6 Characterization of tumor progression and oncolysis on recombinant vaccinia virus (rVACV) and prodrug treatment. Groups of 12 GI-101A tumor-bearing mice (two tumors on each) were injected intravenously with phosphate-buffered saline (PBS), or 5×10^6 PFUs of GLV-1h43 and GLV-1h68. Although one subgroup of six mice received prodrug treatment, the other subgroup received injections of 50% dimethyl sulfoxide/50% PBS only. Tumor size was measured weekly until 70 dpi for rVACV-infected mice or until the mice had to be killed because of tumor burden in PBS-injected control groups. Injection of prodrug led to reduced tumor size in all subgroups compared with untreated mice, but reached no statistical significance except in the GLV-1h68-treated group on day 70 after rVACV injection. Depicted are average values plus standard deviation. Asterisk indicates statistical significance ($P < 0.05$) between prodrug-treated and untreated subgroups.

Prodrug treatment: effects on viral tumor colonization

As prodrug conversion and cell killing might lead to inhibition of viral replication or enrichment of *lacZ*-negative mutants of GLV-1h68 within the tumor, both prodrug-treated and untreated tumors of mice were isolated 71 days after rVACV injection, and the amount of virus was determined by standard plaque assay (Supplementary Figure S3a). No significant differences ($P > 0.42$) were observed between prodrug-treated or untreated GLV-1h43- and GLV-1h68-injected mice.

Furthermore, sterile-filtered (0.1 μm) tumor lysates were used to activate prodrug in cell culture experiments (Supplementary Figure S3b). For this purpose, lysates of two tumors per subgroup were diluted in cell culture medium (resulting in lysate of 20 mg tumor tissue in 1 ml cell culture medium). This was then added to GI-101A cells and MTT assays were performed 2 days later. Added prodrug was converted and resulted in cell killing when tumor lysates were derived from mice injected with GLV-1h68, regardless of previous prodrug treatments in the living animals. On the other hand, no killing was observed in non-prodrug-treated GI-101A cells or in cells that were treated with tumor lysates derived from GLV-1h43-injected mice.

In addition, adjacent tumor sections of prodrug-treated GLV-1h43- or GLV-1h68-injected mice were analyzed for the presence of GFP and β-galactosidase activity (Supplementary Figure S3c). Both viral constructs led to large patches of GFP within the tumor tissue, which was depicted using Hoechst 33342 staining. Using X-gal staining, functional β-galactosidase was detected in GLV-1h68-infected tumors only and correlated with the GFP-positive regions. Furthermore, plaques obtained from prodrug-treated GLV-1h68-injected mice and analyzed by X-gal staining revealed that all plaques stained positive for β-galactosidase. Therefore, prodrug treatment did not lead to a selection of GLV-1h68 mutants with nonfunctional β-galactosidase or to a reduction of VACV titers in tumors.

Taken together, our data showed that a combination of the oncolytic, *lacZ*-encoding VACV strain GLV-1h68 with a β-galactosidase-activatable prodrug could induce apoptosis in breast cancer cells and led to accelerated tumor shrinkage in a xenograft mouse model.

Discussion

In this work, the mode of action and the effects of a combination therapy using an oncolytic VACV strain, together with a β-galactosidase-activatable prodrug on tumor regression, were analyzed in a breast cancer xenograft mouse model system. The used human breast cancer cell line GI-101A was derived from cells isolated from a 57-year-old female cancer patient with recurrent, infiltrating ductal adenocarcinoma.[32,33] It has been previously shown that xenograft tumors derived from GI-101A cells are eradicated on treatment with GLV-1h68,[7] the onolytic VACV strain also used in this study.

Cell culture experiments revealed that GLV-1h68 as well as the control virus strain GLV-1h43 lacking the *lacZ* gene insert, both infected and replicated equally well within GI-101A cells (Figure 1 and data not shown). Because only functionally active enzyme leads to conversion of the prodrug, it was important to analyze the increasing β-galactosidase activity in cell lysates and supernatants of GLV-1h68-infected GI-101A cells (Figures 3b–d). Activation of the prodrug was achieved by coincubation with the sterile-filtered, β-galactosidase-containing cell lysates and supernatants, resulting in killing of GI-101A cells (Supplementary Figure S2). Conversely, incubation with samples obtained from mock- or GLV-1h43-infected cells did not change overall survival. Furthermore, the prodrug-mediated killing observed in the presence of sterile-filtered samples proved that the active drug does penetrate cell membranes, suggesting that each cell in the tumor tissue may not necessarily have to express β-galactosidase to become eliminated by the GDEPT.

Strong synergistic effects could also be observed in the combined prodrug and the GLV-1h68 strain treatment using a low multiplicity of infection of 0.05 in GI-101A cells. The prodrug itself also resulted in significant cell inhibition at 7 days post-application when compared with non-prodrug-treated mock- or GLV-1h43-infected cells. Presumably, cell growth was inhibited by the cytotoxicity of the prodrug itself, which is comparable with that of the cytotoxicity of doxorubicin.[23] However, this unspecific cell growth inhibition was much lower when compared with the additive effects observed on prodrug treatment in combination with GLV-1h68 infection. Similar results were also obtained in other human or canine breast cancer cell lines (data not shown). Canine breast cancer cells were also shown to be infected and lysed with GLV-1h68 alone.[34] The use of several breast cancer cell lines, therefore, provided evidence for a broader application spectrum of the combined prodrug rVACV approach. In addition, we also performed low-light imaging with click-beetle luciferase-expressing GI-101A-CBG and MDA-MB-231-CBG cells (data not shown), which supported the results obtained by MTT assays. Taken together, the prodrug has been cleaved on GLV-1h68-mediated expression of β-galactosidase and, thus, resulted in the release of the cytotoxic drug 2 as a *seco*-analog of the antibiotic duocarmycin SA, which was found to penetrate cell membranes and therefore caused bystander effects in breast cancer cells in culture.

It was reported that duocarmycin SA causes sequence-selective alkylation of N3 of adenine in AT-rich sites of the minor groove of DNA and induces apoptosis.[27,35] The DNA damage results in cleavage of full-length caspase-9, subsequent activation of caspase-3 and, ultimately, cell death.[25,26] As shown in Figure 2, apoptosis induction via the intrinsic pathway was confirmed by the detection of cleaved PARP, cleaved caspase-3 and the full-length caspase-8, as well as the decrease of full-length caspase-3 and -9, in cells treated with a mixture of prodrug and purified β-galactosidase.

Notably, it was reported that poxviruses, such as VACV, possess a number of mechanisms counteracting apoptosis (reviewed in Taylor and Barry[31]). Specifically, VACV-infected cells seem to be protected from the intrinsic apoptotic pathway involving cytochrome *c* release and cleavage of caspase-9.[36–40]

We therefore analyzed whether the apoptotic cascade, observed after prodrug treatment in the presence of purified β-galactosidase, was still activated in GLV-1h68-infected cells. Indeed, we were able to detect high amounts of cleaved PARP in GI-101A cells treated with prodrug

and the β-galactosidase-expressing rVACV strain. We found that lower amounts of cleaved PARP were present in controls infected with GLV-1h68 alone or with GLV-1h43 in the presence or absence of prodrug, whereas almost no cleaved PARP could be detected in mock-infected cells. Consequently, rVACV infection probably led to activation of the apoptotic pathway in some of the infected GI-101A cells, but was much higher in GLV-1h68-infected and prodrug-treated cells. The difference was even more pronounced when looking at cleaved caspase-3, which could only be detected in prodrug-treated cells expressing β-galactosidase. In conclusion, apoptosis was not inhibited by the infecting rVACV and caspase-9 cleavage confirmed the activation of the intrinsic pathway.

As we could not formally exclude that only noninfected cells underwent apoptosis because of the observed bystander effect, prodrug-treated GI-101A cells infected with the GLV-1h68 strain were stained with Hoechst 33342 and propidium iodide. Subsequent fluorescence microscopy revealed condensed nuclei also in GFP-containing, PI-negative cells (data not shown), and therefore supported the assumption that the activated prodrug can overcome the rVACV-mediated antiapoptotic mechanisms, at least in some cells. On the other hand, cells infected with rVACV and not undergoing apoptosis were also detected. Such cells will die of the VACV infection and enhance viral shedding, which will contribute to ongoing β-galactosidase production.

A similar mechanism could also explain that the titer of VACV was not decreased significantly on prodrug treatment in tumors of live animals (Supplementary Figure S3a). Another explanation for this observation could be the enrichment of mutants in *lacZ*. This, however, could be excluded as prodrug-treated, GLV-1h68-infected tumors still stained positive using X-gal (Supplementary Figure S3c). Consistently, X-gal staining was used to confirm functional β-galactosidase expression in plaques resulting from VACV titer analysis of prodrug-treated tumors from GLV-1h68-injected mice (data not shown). Finally, the applied prodrug, in contrast to the released active drug, is not able to penetrate cell membranes.[23] Therefore, the activation of the prodrug occurs in the extracellular matrix of the tumor after release of β-galactosidase from VACV-infected (lysed) cells and does not have direct influence on the infection process itself. As reported earlier and illustrated in Figure 3, the β-galactosidase is reasonably stable and remains active after cell lysis. This is also supported by microscopic analysis of tumor sections in which X-gal staining was positive in regions of GFP fluorescence, which were also characterized by low levels of actin staining and therefore lower levels of living cells (data not shown). Furthermore, we showed that the highest proportion of the enzyme remains in the tumor or is inactivated or excreted after obtaining access to the blood circulation. Otherwise, the cleavage of the prodrug had resulted in systemic toxicity. As no sign of malaise or weight loss was observed in prodrug-treated mice when compared with the respective control mice (data not shown), we concluded that the active β-galactosidase released from the tumor was negligible.

Taken together, the injected GLV-1h68 strain could replicate in tumors of live mice, regardless of prodrug therapy and did not lose its necessary ability to express functional β-galactosidase. Even more importantly, prodrug treatment of GLV-1h68-injected mice resulted in effects leading to additional tumor regression, although these were in the range of the GLV-1h43 treatment. For unknown reasons, the latter seemed to be more efficient than GLV-1h68 regarding tumor therapy. However, prodrug treatment could not significantly enhance the therapeutic effect, as GLV-1h43 does not encode β-galactosidase.

On the basis of the cell culture results, we have however expected stronger synergistic tumor regression effects in GLV-1h68- and prodrug-injected mice. In previous studies, two reasons, which also could apply to our tumor model system, have already been discussed regarding this discrepancy.[10] First, the authors suggested that the rapid kinetics of oncolytic VACV replication might functionally overlap with the used cytosine deaminase/5-fluorocytosine prodrug system. This might also apply to the β-galactosidase/prodrug combination that we used. Second, the authors argued that administration of 5-fluorocytosine may have inhibited the viral replication, thus reducing the antitumoral cytotoxicity induced by the oncolytic virus itself. This effect has already been reported by McCart *et al*.,[14] which is in contrast to our system, as we did not observe inhibition of viral replication in prodrug-treated animals (Supplementary Figure S3a). A reason for this difference might be extracellular activation of the β-galactosidase-activatable prodrug. The 5-fluorocytosine, on the other hand, was cleaved inside the VACV-infected cells. Therefore, the generated 5-fluorouracil may have interfered with viral replication. It would be interesting to directly compare secreted cytosine deaminase or membrane-penetrating β-galactosidase-activatable prodrugs using the currently available rVACV/GDEPT approaches to evaluate the requirements of enzyme and prodrug location in the tumor microenvironment.

Other theoretical problems could be the stability of the prodrug within the body and the immune response generated by VACV. We showed that the prodrug is not inactivated in serum containing cell culture medium; however, we cannot formally exclude a faster breakdown of the prodrug *in vivo*. The immunological effects generated by GLV-1h68 in immunocompromized nude mice as well as in an immunocompetent mouse model have been described elsewhere.[34,41–45] We do not expect immunological effects to have any influence on the described prodrug system in our model system. One could think about the generation of antibodies against β-galactosidase that could inactivate the enzyme. As we were able to show β-galactosidase activity using β-galactosidase-activated fluorescent probes in tumors of live mice (J Stritzker, M Hess *et al*., in preparation), we think that the generation of antibodies to β-galactosidase will not have a significant role, but might

actually help to make the therapy more tumor specific, as low concentration of β-galactosidase leaking out of the tumor would be cleared efficiently.

The selectivity of certain VACV strains, such as derivates of the Lister strain, to replicate within tumor tissues lead to large tumor to background ratios of $>10^4$,[7,34] resulting in specific expression of prodrug-converting enzymes within tumor tissues. Such ratios can hardly be achieved by the use of tumor-specific antibodies, which can also be linked to prodrug-activating enzymes. Furthermore, the amount and location of functional β-galactosidase can be controlled before addition of the prodrug by fluorescent imaging using β-galactosidase-dependent probes (J Stritzker and M Hess *et al*., in preparation).

Taken together, a combined treatment using gene-directed prodrug therapy and rVACV strains such as GLV-1h68 holds great promise for successful tumor therapy; however, further research is needed to find and optimize GDEPT/rVACV systems.

Conflict of interest

JS, NC, IG and AAS have financial interests in Genelux Corporation. CMS, UD and JBS were supported by grants of Genelux Corporation.

Acknowledgements

The authors thank Terry Trevino, Jason Aguilar and Johanna Langbein for excellent technical assistance, Marion Adelfinger for animal care, Birgit Bergmann and Linda Böhme for antibodies, Detlev Schindler and Richard Friedel for support on flow cytometry and Andrea Feathers and Dana Haddad for editorial help. BK thanks the Deutsche Telekom Foundation for a PhD scholarship. The research was supported by Genelux Corporation, San Diego, USA.

References

1 Lostumbo L, Carbine N, Wallace J, Ezzo J. Prophylactic mastectomy for the prevention of breast cancer. *Cochrane Database Syst Rev* 2004; CD002748.
2 American Cancer Society. Cancer facts and figures 2009. 2009. http://www.cancer.org.
3 Kumar S, Gao L, Yeagy B, Reid T. Virus combinations and chemotherapy for the treatment of human cancers. *Curr Opin Mol Ther* 2008; **10**: 371–379.
4 Vaha-Koskela MJ, Heikkila JE, Hinkkanen AE. Oncolytic viruses in cancer therapy. *Cancer Lett* 2007; **254**: 178–216.
5 Moss B. Genetically engineered poxviruses for recombinant gene expression, vaccination, and safety. *Proc Natl Acad Sci USA* 1996; **93**: 11341–11348.
6 Puhlmann M, Brown CK, Gnant M, Huang J, Libutti SK, Alexander HR *et al*. Vaccinia as a vector for tumor-directed gene therapy: biodistribution of a thymidine kinase-deleted mutant. *Cancer Gene Ther* 2000; **7**: 66–73.
7 Zhang Q, Yu YA, Wang E, Chen N, Danner RL, Munson PJ *et al*. Eradication of solid human breast tumors in nude mice with an intravenously injected light-emitting oncolytic vaccinia virus. *Cancer Res* 2007; **67**: 10038–10046.
8 Yu YA, Shabahang S, Timiryasova TM, Zhang Q, Beltz R, Gentschev I *et al*. Visualization of tumors and metastases in live animals with bacteria and vaccinia virus encoding light-emitting proteins. *Nat Biotechnol* 2004; **22**: 313–320.
9 Schepelmann S, Springer CJ. Viral vectors for gene-directed enzyme prodrug therapy. *Curr Gene Ther* 2006; **6**: 647–670.
10 Chalikonda S, Kivlen MH, O'Malley ME, Eric Dong XD, McCart JA, Gorry MC *et al*. Oncolytic virotherapy for ovarian carcinomatosis using a replication-selective vaccinia virus armed with a yeast cytosine deaminase gene. *Cancer Gene Ther* 2008; **15**: 115–125.
11 Erbs P, Findeli A, Kintz J, Cordier P, Hoffmann C, Geist M *et al*. Modified vaccinia virus Ankara as a vector for suicide gene therapy. *Cancer Gene Ther* 2008; **15**: 18–28.
12 Foloppe J, Kintz J, Futin N, Findeli A, Cordier P, Schlesinger Y *et al*. Targeted delivery of a suicide gene to human colorectal tumors by a conditionally replicating vaccinia virus. *Gene Ther* 2008; **15**: 1361–1371.
13 Gnant MF, Puhlmann M, Alexander Jr HR, Bartlett DL. Systemic administration of a recombinant vaccinia virus expressing the cytosine deaminase gene and subsequent treatment with 5-fluorocytosine leads to tumor-specific gene expression and prolongation of survival in mice. *Cancer Res* 1999; **59**: 3396–3403.
14 McCart JA, Puhlmann M, Lee J, Hu Y, Libutti SK, Alexander HR *et al*. Complex interactions between the replicating oncolytic effect and the enzyme/prodrug effect of vaccinia-mediated tumor regression. *Gene Ther* 2000; **7**: 1217–1223.
15 Puumalainen AM, Vapalahti M, Agrawal RS, Kossila M, Laukkanen J, Lehtolainen P *et al*. Beta-galactosidase gene transfer to human malignant glioma *in vivo* using replication-deficient retroviruses and adenoviruses. *Hum Gene Ther* 1998; **9**: 1769–1774.
16 Griscelli F, Opolon P, Saulnier P, Mami-Chouaib F, Gautier E, Echchakir H *et al*. Recombinant adenovirus shedding after intratumoral gene transfer in lung cancer patients. *Gene Ther* 2003; **10**: 386–395.
17 Tung CH, Zeng Q, Shah K, Kim DE, Schellingerhout D, Weissleder R. *In vivo* imaging of beta-galactosidase activity using far red fluorescent switch. *Cancer Res* 2004; **64**: 1579–1583.
18 Josserand V, Texier-Nogues I, Huber P, Favrot MC, Coll JL. Non-invasive *in vivo* optical imaging of the lacZ and luc gene expression in mice. *Gene Ther* 2007; **14**: 1587–1593.
19 Wehrman TS, von Degenfeld G, Krutzik PO, Nolan GP, Blau HM. Luminescent imaging of beta-galactosidase activity in living subjects using sequential reporter-enzyme luminescence. *Nat Methods* 2006; **3**: 295–301.
20 Lee KH, Byun SS, Choi JH, Paik JY, Choe YS, Kim BT. Targeting of lacZ reporter gene expression with radioiodine-labelled phenylethyl-beta-d-thiogalactopyranoside. *Eur J Nucl Med Mol Imaging* 2004; **31**: 433–438.
21 Louie AY, Huber MM, Ahrens ET, Rothbacher U, Moats R, Jacobs RE *et al*. *In vivo* visualization of gene expression using magnetic resonance imaging. *Nat Biotechnol* 2000; **18**: 321–325.
22 Tietze LF, Krewer B. Novel analogues of CC-1065 and the duocarmycins for the use in targeted tumour therapies. *Anticancer Agents Med Chem* 2009; **9**: 304–325.
23 Tietze LF, von Hof JM, Krewer B, Muller M, Major F, Schuster HJ *et al*. Asymmetric synthesis and biological

evaluation of glycosidic prodrugs for a selective cancer therapy. *ChemMedChem* 2008; **3**: 1946–1955.
24 Stritzker J, Weibel S, Hill PJ, Oelschlaeger TA, Goebel W, Szalay AA. Tumor-specific colonization, tissue distribution, and gene induction by probiotic *Escherichia coli* Nissle 1917 in live mice. *Int J Med Microbiol* 2007; **297**: 151–162.
25 Hirota M, Fujiwara T, Mineshita S, Sugiyama H, Teraoka H. Distamycin A enhances the cytotoxicity of duocarmycin A and suppresses duocarmycin A-induced apoptosis in human lung carcinoma cells. *Int J Biochem Cell Biol* 2007; **39**: 988–996.
26 Tada-Oikawa S, Oikawa S, Kawanishi M, Yamada M, Kawanishi S. Generation of hydrogen peroxide precedes loss of mitochondrial membrane potential during DNA alkylation-induced apoptosis. *FEBS Lett* 1999; **442**: 65–69.
27 Wrasidlo W, Johnson DS, Boger DL. Induction of endonucleolytic DNA fragmentation and apoptosis by the duocarmycins. *Bioorg Med Chem Lett* 1994; **4**: 631–636.
28 Nicholson DW, Ali A, Thornberry NA, Vaillancourt JP, Ding CK, Gallant M *et al*. Identification and inhibition of the ICE/CED-3 protease necessary for mammalian apoptosis. *Nature* 1995; **376**: 37–43.
29 Debatin KM. Apoptosis pathways in cancer and cancer therapy. *Cancer Immunol Immunother* 2004; **53**: 153–159.
30 Kim R. Recent advances in understanding the cell death pathways activated by anticancer therapy. *Cancer* 2005; **103**: 1551–1560.
31 Taylor JM, Barry M. Near death experiences: poxvirus regulation of apoptotic death. *Virology* 2006; **344**: 139–150.
32 Hurst J, Maniar N, Tombarkiewicz J, Lucas F, Roberson C, Steplewski Z *et al*. A novel model of a metastatic human breast tumour xenograft line. *Br J Cancer* 1993; **68**: 274–276.
33 Rathinavelu P, Malave A, Raney SR, Hurst J, Roberson CT, Rathinavelu A. Expression of mdm-2 oncoprotein in the primary and metastatic sites of mammary tumor (GI-101) implanted athymic nude mice. *Cancer Biochem Biophys* 1999; **17**: 133–146.
34 Gentschev I, Stritzker J, Hofmann E, Weibel S, Yu YA, Chen N *et al*. Use of an oncolytic vaccinia virus for the treatment of canine breast cancer in nude mice: preclinical development of a therapeutic agent. *Cancer Gene Ther* 2009; **16**: 320–328.
35 Boger DL, Johnson DS, Yun W, Tarby CM. Molecular basis for sequence selective DNA alkylation by (+)- and ent-(−)-CC-1065 and related agents: alkylation site models that accommodate the offset AT-rich adenine N3 alkylation selectivity. *Bioorg Med Chem* 1994; **2**: 115–135.
36 Taylor JM, Quilty D, Banadyga L, Barry M. The vaccinia virus protein F1 L interacts with Bim and inhibits activation of the pro-apoptotic protein Bax. *J Biol Chem* 2006; **281**: 39728–39739.
37 Stewart TL, Wasilenko ST, Barry M. Vaccinia virus F1L protein is a tail-anchored protein that functions at the mitochondria to inhibit apoptosis. *J Virol* 2005; **79**: 1084–1098.
38 Wasilenko ST, Banadyga L, Bond D, Barry M. The vaccinia virus F1L protein interacts with the proapoptotic protein Bak and inhibits Bak activation. *J Virol* 2005; **79**: 14031–14043.
39 Wasilenko ST, Meyers AF, Vander Helm K, Barry M. Vaccinia virus infection disarms the mitochondrion-mediated pathway of the apoptotic cascade by modulating the permeability transition pore. *J Virol* 2001; **75**: 11437–11448.
40 Wasilenko ST, Stewart TL, Meyers AF, Barry M. Vaccinia virus encodes a previously uncharacterized mitochondrial-associated inhibitor of apoptosis. *Proc Natl Acad Sci USA* 2003; **100**: 14345–14350.
41 Kelly KJ, Brader P, Woo Y, Li S, Chen N, Yu YA *et al*. Real-time intraoperative detection of melanoma lymph node metastases using recombinant vaccinia virus GLV-1h68 in an immunocompetent animal model. *Int J Cancer* 2009; **124**: 911–918.
42 Gentschev I, Hofmann E, Donat U, Weibel S, Adelfinger M, Raab V *et al*. Regression of human prostate tumors and metastases in nude mice following treatment with the recombinant oncolytic vaccinia virus GLV-1h68. *J Biomed Biotechnol* 2010; e-pub ahead of print 23 June 2010; doi:10.1155/2010/736907.
43 Worschech A, Chen N, Yu YA, Zhang Q, Pos Z, Weibel S *et al*. Systemic treatment of xenografts with vaccinia virus GLV-1h68 reveals the immunologic facet of oncolytic therapy. *BMC Genomics* 2009; **10**: 301.
44 Worschech A, Haddad D, Stroncek DF, Wang E, Marincola FM, Szalay AA. The immunologic aspects of poxvirus oncolytic therapy. *Cancer Immunol Immunother* 2009; **58**: 1355–1362.
45 Worschech A, Kmieciak M, Knutson KL, Bear HD, Szalay AA, Wang E *et al*. Signatures associated with rejection or recurrence in HER-2/neu-positive mammary tumors. *Cancer Res* 2008; **68**: 2436–2446.

Supplementary Information accompanies the paper on Cancer Gene Therapy website (http://www.nature.com/cgt)

Figure S1

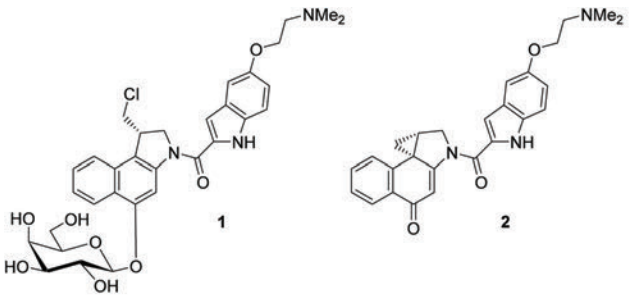

Figure S2

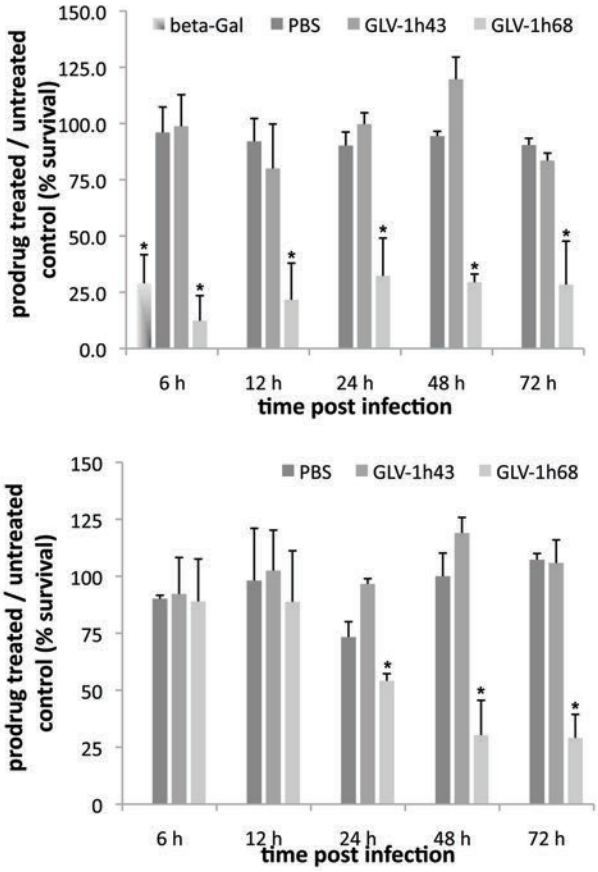
beta-Gal
PBS
GLV-1h43
GLV-1h68
prodrug treated / untreated control (% survival)
150.0
125.0
100.0
75.0
50.0
25.0
0.0
6 h
12 h
24 h
48 h
72 h
time post infection
PBS
GLV-1h43
GLV-1h68
prodrug treated / untreated control (% survival)
150
125
100
75
50
25
0
6 h
12 h
24 h
48 h
72 h
time post infection

Figure S3

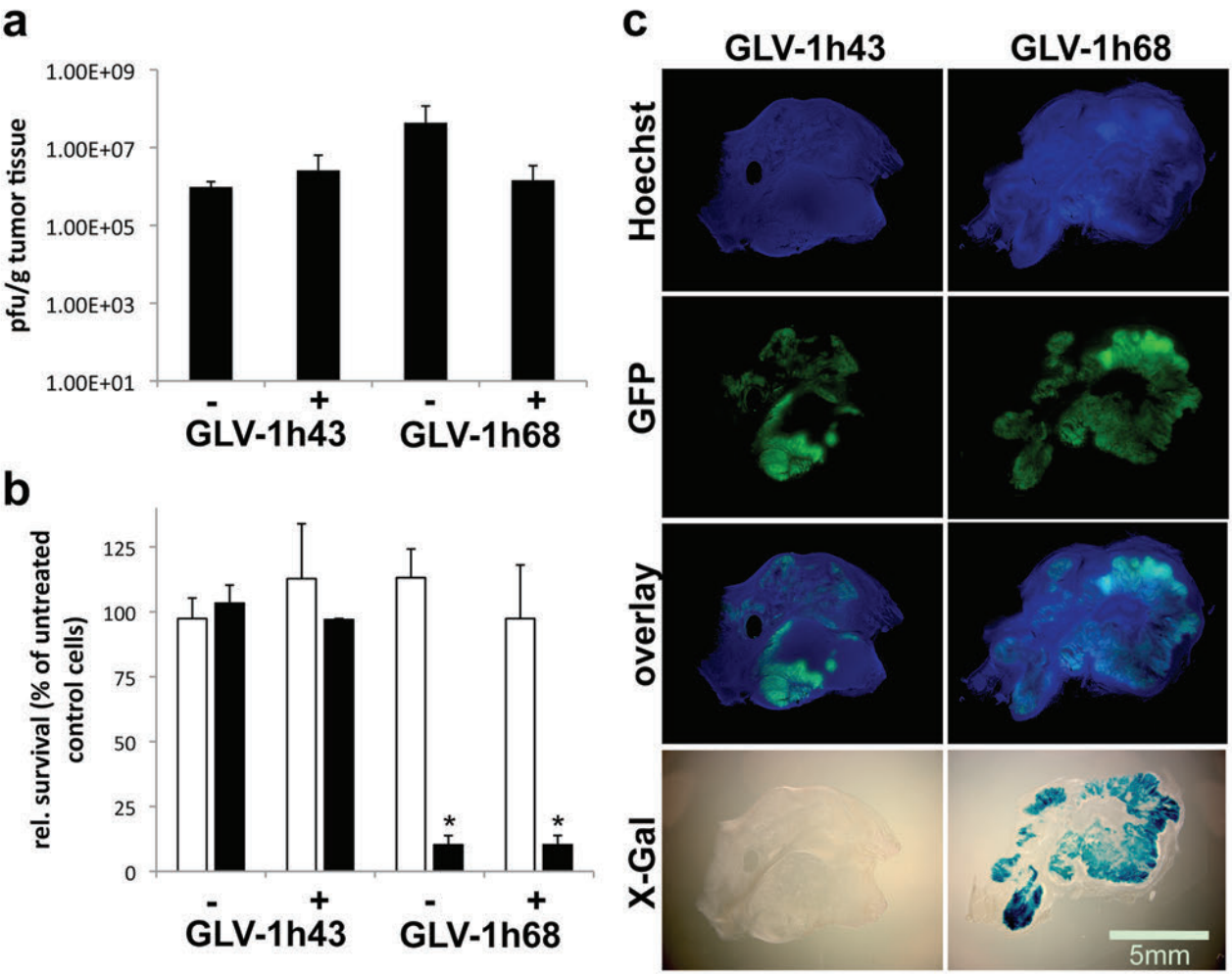
a
1.00E+09
1.00E+07
1.00E+05
1.00E+03
1.00E+01
pfu/g tumor tissue
-
+
-
+
GLV-1h43
GLV-1h68
b
rel. survival (% of untreated control cells)
125
100
75
50
25
0
*
*
-
+
-
+
GLV-1h43
GLV-1h68
c
GLV-1h43
GLV-1h68
Hoechst
GFP
overlay
X-Gal
5mm

Supplementary figure S1. Structure of the galactosidic prodrug 1 and its corresponding drug 2.

Supplementary figure S2. Tumor cell killing due to active beta-galactosidase in lysates and supernatants of GLV-1h68-infected cells. GI-101A tumor cells were treated with sterile filtered lysates (**a**) or supernatants (**b**) of mock- (PBS), GLV-1h43-, and GLV-1h68-infected cells respectively and treated with 10 nM prodrug. Two days later cell survival was analyzed by MTT assays and compared to non-prodrug treated controls. The addition of recombinant beta-galactosidase (beta-Gal) served as a positive control. Each sample was analyzed in triplicate. Averages plus standard deviations are shown. Asterisks indicate statistical significance ($p<0.05$) for both comparison against mock- or GLV-1h43-infection derived probes.

Supplementary figure S3. Correlation of prodrug treatment and viral tumor colonization. (**a**) The concentration of viral particles in rVACV-infected tumors was determined by standard plaque assay and displayed no significant differences between prodrug-treated or untreated infected mice. (**b**) Tumor cell killing due to active beta-galactosidase in lysates of GLV-1h68-infected tumors. GI-101A tumor cells were treated with sterile filtered lysates of GLV-1h43- or GLV-1h68-infected tumors from mice, which were previously treated with prodrug (+) or left untreated (-). The cells were either left untreated (white bars) or treated with 10nM prodrug (black bars). Two days later cell survival was analyzed by MTT assays and compared to non-tumor lysate, non-prodrug treated control cells. For each group 2 tumor lysates were analyzed in

parallel, each of which in duplicate. Astersiks indicate statistical significant differences ($p<0.05$) between GLV-1h43 and GLV-1h68 treated tumors, regardless of previous prodrug treatment. (**c**) Adjacent tumor sections analyzed for the presence of GFP or beta-galactosidase. Large patches of the fluorescent protein were visible within the tumor tissue regardless of whether tumors were infected with GLV-1h43 or GLV-1h68. Functional beta-galactosidase was detected in GLV-1h68-infected tumors only.

5.4 Additional aspects of oncolytic virotherapy

Within the time frame of this thesis, the author was engaged in further research, which will be presented in this section.

Imaging of intratumoral inflammation during oncolytic virotherapy of tumors by 19F-magnetic resonance imaging (MRI)

Weibel S, Basse-Luesebrink TC, Hess M, Hofmann E, Seubert CM, Langbein- Laugwitz J, Gentschev I, Sturm VJF, Ye Y, Kampf T, Jakob PM, Szalay AA
PLoS One. 2013;10.1371/journal.pone.0056317

Preferential colonization of metastases by oncolytic Vaccinia virus strain GLV-1h68 in a human PC-3 prostate cancer model in nude mice

Donat U, Weibel S, Hess M, Stritzker J, Härtl B, Sturm JB, Chen NG, Gentschev I, Szalay AA
PLoS One. 2012;7:e45942

Functional hyper-IL-6 from Vaccinia virus-colonized tumors triggers platelet formation and helps to alleviate toxicity of mitomycin C enhanced virus therapy

Sturm JB, Hess M, Weibel S, Chen NG, Yu YA, Zhang Q, Donat U, Reiss C, Gambaryan S, Krohne G, Stritzker J, Szalay AA
J Transl Med. 2012;10:9

Significant growth inhibition of canine mammary carcinoma xenografts following treatment with oncolytic Vaccinia virus GLV-1h68

Gentschev I, Ehrig K, Donat U, Hess M, Rudolph S, Chen N, Yu YA, Zhang Q, Bullerdiek J, Nolte I, Stritzker J, Szalay AA

J Oncol. 2010;2010:736907

Publication (complete reference): Weibel S, Basse-Luesebrink TC, **Hess M**, Hofmann E, Seubert CM, Langbein-Laugwitz J, Gentschev I, Sturm VJF, Ye Y, Kampf T, Jakob PM, Szalay AA. Imaging of intratumoral inflammation during oncolytic virotherapy of tumors by 19F-magnetic resonance imaging (MRI). *PLoS One*. 2013;10.1371/journal.pone.0056317
Authors' contributions
Programmed software routines: TCBL VJFS TK. Approved the final manuscript: IG. Conceived and designed the experiments: SW TCBL **MH** EH CS PMJ AAS. Performed the experiments: SW TCBL **MH** EH CS JL. Analyzed the data: SW TCBL IG YY TK. Contributed reagents/materials/analysis tools: PMJ AAS. Wrote the paper: SW TCBL.

Stephanie Weibel	
Thomas Basse-Lüsebrink	
Elisabeth Hofmann	
Carolin M. Seubert	
Johanna Langbein-Laugwitz	
Ivaylo Gentschev	
Volker J. F. Sturm	
Yuxiang Ye	
Thomas Kampf	
Peter M. Jakob	
Aladar A. Szalay	

OPEN ACCESS Freely available online

PLOS ONE

Imaging of Intratumoral Inflammation during Oncolytic Virotherapy of Tumors by ^{19}F-Magnetic Resonance Imaging (MRI)

Stephanie Weibel[1☯], Thomas Christian Basse-Luesebrink[1,2,3☯], Michael Hess[1], Elisabeth Hofmann[1], Carolin Seubert[1], Johanna Langbein-Laugwitz[1], Ivaylo Gentschev[1,7], Volker Jörg Friedrich Sturm[2], Yuxiang Ye[2], Thomas Kampf[2], Peter Michael Jakob[2,3], Aladar A. Szalay[1,4,5,6,7]*

1 Department of Biochemistry, Biocenter, University of Wuerzburg, Wuerzburg, Germany, **2** Department of Experimental Physics 5, University of Wuerzburg, Wuerzburg, Germany, **3** Research Center for Magnetic Resonance Bavaria e.V., Wuerzburg, Germany, **4** Rudolf Virchow Center, Research Center for Experimental Biomedicine, and, **5** Institute for Molecular Infection Biology, University of Wuerzburg, Wuerzburg, Germany, **6** Department of Radiation Medicine and Applied Sciences, University of California San Diego Health System, La Jolla, California, United States of America, **7** Genelux Corporation, San Diego Science Center, San Diego, California, United States of America

Abstract

Background: Oncolytic virotherapy of tumors is an up-coming, promising therapeutic modality of cancer therapy. Unfortunately, non-invasive techniques to evaluate the inflammatory host response to treatment are rare. Here, we evaluate ^{19}F magnetic resonance imaging (MRI) which enables the non-invasive visualization of inflammatory processes in pathological conditions by the use of perfluorocarbon nanoemulsions (PFC) for monitoring of oncolytic virotherapy.

Methodology/Principal Findings: The Vaccinia virus strain GLV-1h68 was used as an oncolytic agent for the treatment of different tumor models. Systemic application of PFC emulsions followed by ^{1}H/^{19}F MRI of mock-infected and GLV-1h68-infected tumor-bearing mice revealed a significant accumulation of the ^{19}F signal in the tumor rim of virus-treated mice. Histological examination of tumors confirmed a similar spatial distribution of the ^{19}F signal hot spots and CD68^{+}-macrophages. Thereby, the CD68^{+}-macrophages encapsulate the GFP-positive viral infection foci. In multiple tumor models, we specifically visualized early inflammatory cell recruitment in Vaccinia virus colonized tumors. Furthermore, we documented that the ^{19}F signal correlated with the extent of viral spreading within tumors.

Conclusions/Significance: These results suggest ^{19}F MRI as a non-invasive methodology to document the tumor-associated host immune response as well as the extent of intratumoral viral replication. Thus, ^{19}F MRI represents a new platform to non-invasively investigate the role of the host immune response for therapeutic outcome of oncolytic virotherapy and individual patient response.

Citation: Weibel S, Basse-Luesebrink TC, Hess M, Hofmann E, Seubert C, et al. (2013) Imaging of Intratumoral Inflammation during Oncolytic Virotherapy of Tumors by ^{19}F-Magnetic Resonance Imaging (MRI). PLoS ONE 8(2): e56317. doi:10.1371/journal.pone.0056317

Editor: Eric A. Weaver, Mayo Clinic, United States of America

Received August 3, 2012; **Accepted** January 8, 2013; **Published** February 18, 2013

Funding: This work was supported by a research grant and a service grant from Genelux Corporation (R&D facility in San Diego, CA, USA) awarded to the University of Wuerzburg, Germany. The funders had no role in study design, data collection and analysis, decision to publish, or preparation of the manuscript.

Competing Interests: This work was supported by grants from Genelux Corporation (R&D facility in San Diego, CA, USA). SW, TCBL, EH, and CS received a postdoctoral fellowship, MH received a graduate fellowship by Genelux Corporation awarded to the University of Wuerzburg, Germany. IG and AAS are salaried employees of Genelux Corporation and have personal financial interests in Genelux Corporation. All authors fully adhere to all the PLOS ONE ploicies on sharing data and materials.

* E-mail: aaszalay@genelux.com

☯ These authors contributed equally to this work.

Introduction

Oncolytic virotherapy of tumors is based on the lytic destruction of solid tumors mediated by infection of the malignant tissue by tumor-specific viruses [1–4]. Today, a multitude of different virus strains with oncolytic potential are described in the literature and promising pre-clinical data as well as clinical trial reports from oncolytic virotherapy are available [5–7]. In addition to the oncolytic tissue destruction massive inflammation within the tumor microenvironment occurs, which is primarily directed against the virus [8–10]. However, virus-mediated cell lysis also leads to the release of tumor-associated antigens, which may finally stimulate an anti-tumoral immune response [11,12]. So far, it is well known that oncolytic virotherapy is accompanied by a host immune response, however, the individual time course, the polarization of the immune response, and the effect on the therapeutic efficacy remain to be elucidated.

In practice, a longitudinal, non-invasive quantification of the intratumoral inflammation during oncolytic virotherapy may provide substantial benefits to therapeutic monitoring, tumor diagnostics and indirect virus imaging as well as to the optimization of new therapeutic virus strains. Recently, ^{19}F/^{1}H MRI was introduced as a novel and promising non-invasive

imaging modality of different inflammatory conditions in rodent models of cardiac ischemia [13], allograft rejection [14], LPS-induced pulmonary inflammation [15], inflammatory bowel disease [16], neuro-inflammation [17] and bacterial abscess formation [18]. In practice a single intravenous injection of an emulsified perfluorocarbon (PFC) predominantly lead to the phagocytic uptake by the monocyte-macrophage system followed by their detection via ^{19}F MRI [19]. As a consequence of the progressive infiltration of PFC-labeled immune cells into inflamed tissues, the foci of inflammation can be localized as hotspots and morphologically correlated to the anatomical or patho-physiological context with the help of ^{1}H images [19,20].

Although recent advances in the visualization of inflammatory processes using different imaging modalities were reported [21–23], ^{19}F MRI has several advantages especially compared to contrast agent based ^{1}H MRI. First, no detectable fluorine signal is present in tissues enabling background-free ^{19}F MRI of the exogenous ^{19}F marker [20] and the directly acquired ^{19}F signal facilitates the quantification of the marker amount [24]. Second, the ^{1}H signal is not altered compared to other contrast agents making the assessment of other quantitative ^{1}H parameters feasible [18]. Therefore, ^{19}F MRI is a promising modality for imaging of inflammation combined with high anatomical resolution (^{1}H) in the context of oncolytic virotherapy.

The abundance of inflammatory cells is a hallmark of cancer, and their importance in cancer development and progression have been demonstrated in numerous studies [25,26]. Of particular importance are macrophages due to their high phenotypic heterogeneity reaching from cytotoxic M1-polarized macrophages, which can theoretically harm tumor tissues to M2-polarized macrophages (tumor-associated macrophages, TAMs), which promote tumorigenesis [27]. The destruction of TAMs or the reprogramming of tumor-promoting M2 to cytotoxic M1 macrophages represents a current immunotherapeutic strategy against cancer [28]. Since colonization of solid tumors with systemically injected oncolytic viruses induces macrophage-recruitment this treatment may interfere with the polarization of macrophages by confronting the host with a variety of pathogen-associated molecular patterns (PAMPs) [12].

To the best of our knowledge, PFC nanoemulsions have not yet been used to target, visualize and monitor viral tumor infection and oncolytic virotherapy of tumors. Consequently, in this proof-of-principle study ^{19}F MRI was applied to analyze tumor-bearing mice treated with the oncolytic Vaccinia virus (VACV) GLV-1h68. This oncolytic virus strain was previously described as a powerful agent to treat various types of cancer [29–31]. The presented results suggest ^{19}F MRI as a non-invasive methodology to document the tumor-associated host immune response as well as the extent of intratumoral viral replication.

Materials and Methods

Ethics Statement

All animal experiments were carried out in accordance with protocols approved by the Institutional Animal Care and Use Committee (IACUC) of Explora Biolabs (San Diego, CA, USA, protocol number EB08-003) or the government of Unterfranken (Würzburg, Germany, protocol number AZ 55.2-2531.01-17/08). Both the Institutional Animal Care and Use Committee of Explora Biolabs and the government of Unterfranken specifically approved this study.

Cell Lines

The human 1936-MEL melanoma cell line was originally isolated from late-stage metastases of patient 888 [32] and kindly provided to us by F. M. Marincola (National Institutes of Health, Bethesda, MD, USA). 1936-MEL cells were cultured in RPMI-1640 supplemented with 10% fetal bovine serum (FBS), 100 Units/ml penicillin, and 100 µg/ml streptomycin (PAA Laboratories, Cölbe, Germany). Human A549 lung carcinoma cells (ATCC No. CCL-185) were cultured in RPMI-1640 containing 10% FBS and 100 Units/ml penicillin, and 100 µg/ml streptomycin. GI-101A human ductual breast adenocarcinoma cells [33,34] were kindly provided by A. Aller (Rumbaugh-Goodwin Institute for Cancer Research, Inc., FL, USA) and cultured in RPMI-1640 supplemented with 5 ng/ml β-estradiol and 5 ng/ml progesterone (Sigma Aldrich, Taufkirchen, Germany), 1 mM sodium pyruvate, 10 mM HEPES, 20% FBS, 100 Units/ml penicillin, and 100 µg/ml streptomycin. All cells were maintained at 37°C and 5% CO_2.

Virus

The construction of the attenuated Vaccinia virus strain GLV-1h68 was previously described by Zhang et al. [31]. Briefly, three expression cassettes (encoding for *Renilla* luciferase-GFP fusion protein, β-galactosidase and β-glucuronidase) were recombined into the *F14.5L*, *J2R* and *A56R* loci, respectively, of the LIVP strain virus genome. Viruses were propagated in CV-1 cells and purified through sucrose gradients.

Tumor Inoculation, Administration of the Virus, Application of Perfluorocarbon (PFC)

Six-week-old female athymic nude *Foxn1^{nu}* mice were obtained from Harlan Laboratories (Boxmeer, Netherlands or Indianapolis, IN, USA). 1936-MEL (7×10^5/100 µl PBS), A549 (5×10^6/100 µl PBS), and GI-101A tumor cells (5×10^6/100 µl PBS) were subcutaneously (s.c.) injected into the abdominal right flank. At different time points after injection, the tumor volume was calculated as length×width^2×0.52. For all experiments, tumors were grown up to 100–300 mm^3 in size before viral administration. A single viral dose of 1×10^7 plaque forming units (p.f.u.) in 100 µl PBS was injected intravenously (i.v.) via the tail vein.

The emulsified ^{19}F perfluorocarbon (PFC) solution (VS-1000H, Celsense, Inc., Pittsburgh, PA, USA) with a mean particle size of approximately 145 nm [18] was directly i.v. injected as 20% v/v emulsion (100 µl) into tumor-bearing mice. The injection time points of each individual experiment are indicated in the corresponding figure legend.

In vivo MRI

In vivo ^{1}H and ^{19}F MRI measurements were performed on a 7 Tesla Bruker Biospec System (Bruker BioSpin GmbH, Reinstetten, Germany) at room temperature using a 40 mm diameter home-built double resonant ^{1}H/^{19}F birdcage. For *in vivo* imaging the animals received inhalation anesthesia (1–2% isoflurane) during the measurement. Animals were placed together with a reference tube containing a mixture of the above described PFC emulsion and H_2O in a home-built measurement container according to safety regulations.

In all experiments ^{1}H MRI was performed prior to ^{19}F imaging to enable correlation of the ^{19}F signal distribution into the anatomical context. Thus, 3D ^{1}H turbo-spin-echo (TSE) and 3D ^{1}H multi-spin-echo (MSE) experiments were performed. For *in vivo* ^{19}F imaging 3D TSE sequences were performed after the ^{1}H experiments.

Table 1. Parameters for the different *in vivo* ^{1}H MRI experiments.

Model	Fig	Sequence	TE [ms]	TR [ms]	TF	NE	MTX	FOV [mm]
1936-MEL	1 B,C,D	TSE	30	1000	10	1	100×150×125	20×30×25
1936-MEL	3 B/4 A	TSE	30	1000	10	1	100×150×125	20×30×25
A549	5 A,B	MSE	4.4*	250	1	28	64×96×80	20×30×25

Acronyms: Fig = figure, TE = echo time, TR = repetition time, TF = turbo factor of TSE experiments, NE = number of echoes for MSE experiments, MTX = imaging matrix, FOV = field-of-view.
*In case of the MSE experiments TE labels the echo time of the first echo and the inter echo time.
doi:10.1371/journal.pone.0056317.t001

The parameters for the different ^{1}H *in vivo* experiments are listed in table 1. No averaging was applied when ^{1}H data was acquired.

The parameters for the different ^{19}F *in vivo* animal experiments are presented in table 2. For each animal the total *in vivo* MRI protocol time was <2h.

Ex vivo MRI

After completion of the *in vivo* experiments the 1936-MEL tumors were excised and snap-frozen in liquid N_2 and stored at −80°C. For *ex vivo* ^{19}F MRI measurements followed by histology the tumors were fixed in 4% paraformaldehyde/PBS pH 7.4 for 16 h at 4°C and rinsed in PBS followed by embedding and dehydration in 10% Sucrose/5% w/v low-melting point agarose/PBS.

In a first set of experiments, focusing on the 1936-MEL tumor model, all infected tumors (n = 3) were placed together in a single 15 ml tube (Greiner Bio-One GmbH, Frickenhausen, Germany) embedded in 10% Sucrose/5% w/v low-melting point agarose/PBS. The corresponding control tumors (n = 3) were placed in an additional 15 ml tube. Both tubes were placed together in the measurement coil to enable measurement of all tumor specimens in only one ^{1}H and one ^{19}F scan. The same embedding procedure was used for all other *ex vivo* measurements, however, for those experiments tumor specimen were placed in individual tubes (50 ml tubes: 1936-MEL; 15 ml tubes: GI-101-A) together with a reference tube containing PFC emulsion and H_2O. Thus, for these tumor samples *ex vivo* MRI was performed individually. The same hardware as for *in vivo* MRI was used for the *ex vivo* measurement of 1936-MEL tumor specimen.

Ex vivo ^{1}H and ^{19}F MRI measurements of the GI-101A samples were performed on a 11.7 Tesla Bruker AMX System (Bruker BioSpin GmbH, Reinstetten, Germany) at room temperature using a 17 mm diameter home-built double-tunable ^{1}H/^{19}F birdcage.

Similar to *in vivo* measurements, ^{1}H 3D TSE experiments were used to obtain anatomical background information. *Ex vivo* ^{1}H experiments were followed by ^{19}F 3D TSE imaging. The chosen ^{1}H and ^{19}F *ex vivo* imaging parameters are presented table 3 and 4. No averaging was applied for *ex vivo* ^{1}H MRI experiments.

Post Processing of MRI Datasets

Post processing was performed using home-written routines in MATLAB (The MathWorks Inc., Natick, MA, USA) if not mentioned otherwise.

Figure preparation. For anatomical correlation of the *in vivo* A549 ^{19}F data, a summed image of all echo images was calculated for each ^{1}H MSE experiment. Prior to summation, the echo images were pixel-wise weighted with the calculated T_2 time assuming a mono-exponential decay ($S(t) = S_0 \exp(-t/T_2)$; $S(t)$ = signal; t = time).

All ^{19}F datasets were zerofilled to the matrix sizes of the respective ^{1}H datasets. The SNR of the zerofilled ^{19}F data were calculated following reference [35] for low SNR data. For better visualization the maximum of the shown 2D images of the 3D ^{19}F datasets were scaled to a specific maximal SNR which is indicated in the respective figure legends. For ^{1}H/^{19}F overlay images a SNR threshold of 4.5 was chosen for the ^{19}F data. Additionally, remaining, isolated ^{19}F signal pixels were removed.

Regarding the 3D overlay reconstruction, ^{19}F data were zerofilled as described above. The 3D ^{1}H and the zerofilled ^{19}F data were scaled to their respective maxima. The zerofilled 3D ^{19}F data were set to a threshold as described above. Afterwards a 3D overlay dataset was generated. The overlay dataset was additionally masked by only selecting the animal area. The animal mask was manually generated with the help of the ^{1}H 3D data. After the described pre-preparation of the 3D overlay data in MATLAB, the data were transferred to MeVisLab (MeVis Medical Solutions AG, Bremen, Germany) where the 3D surface reconstruction was performed. For the visual correlation of the *ex vivo* MRI data and histology results only tissue slices from the tumor middle were compared.

Quantitative analysis of the ^{19}F MRI data. For quantitative analysis of the *in vivo* MRI time course in 1936-MEL tumor-bearing mice, ratios of the total ^{19}F SNR of the tumor and the tumor volume (^{19}FTVR) were generated. Since from each group only n = 2 animals were measured at 9 dpi, this parameter was

Table 2. Parameters for the different *in vivo* ^{19}F MRI experiments.

Model	Fig	Sequence	TE [ms]	TR [ms]	TF	NA	MTX	FOV [mm]
1936-MEL	1 B,C,D	TSE	4	1000	48	60	40×48×32	20×30×25
1936-MEL	3 B/4 A	TSE	4	1000	48	60	40×48×32	25×30×20
A549	5 A,B	TSE	4	1000	48	75	40×48×32	25×30×20

Acronyms (in addition to table 1): NA = number of averages.
doi:10.1371/journal.pone.0056317.t002

Table 3. Parameters for the different *ex vivo* ^{1}H MRI experiments.

Model	Fig	Sequence	TE [ms]	TR [ms]	TF	MTX	FOV [mm]
1936-MEL	1 E,F/1S A,B	TSE	81	1000	20	300×200×100	60×40×20
1936-MEL	2 B/4 C	TSE	35.5	1000	10	200×150×125	40×30×25
GI-101A	5 C,D	TSE	34	500	8	192×128×128	30×20×20

Acronyms (see table 1 and 2).
doi:10.1371/journal.pone.0056317.t003

only calculated for 7 and 11 dpi (n = 4 animals per group). The tumor regions were manually selected with the help of the fully resolved ^{1}H images. SNR maps of the zerofilled ^{19}F data were generated as described above. Only ^{19}F signal pixels within the predefined regions-of-interest (ROI) having an SNR≥4.5 were regarded and single ^{19}F signal pixels were removed. The total ^{19}F SNR was evaluated by summation of all pixels remaining after the pre-preparation/−selection procedure. The ^{19}F SNR data were additionally normed to the mean SNR of the corresponding reference. For each animal the corresponding ^{19}FTVRs of 7 and 11 dpi were individually regarded. Thus, for each pair (day 7 and 11), the ^{19}FTVRs were normed to the maximum value and the slope between both values was calculated assuming a linear relationship.

Similar as for *in vivo* MRI of 1936-MEL tumor-bearing animals, ratios of the total ^{19}F SNR of the tumor and the tumor weight (^{19}FTWR) were generated for *in vivo* MRI of A549 tumors and *ex vivo* MRI of 1936-MEL/GI-101-A tumor-bearing animals. Thus, SNR maps of the original ^{19}F data were generated for quantitative analysis as described above. Overlays were generated with the help of the original ^{19}F data (^{19}F SNR≥4.5) and downscaled ^{1}H data. This was done to select ROIs which excluded ^{19}F signal from other regions (e.g. lymph nodes).

Additionally, for VACV infected animals having 1936-MEL tumors a correlation of the *ex vivo* ^{19}F signal area with the GFP positive area was performed. Thus, for each tumor sample, the middle slice of the tumors was chosen using the original ^{19}F data. Furthermore, ROIs of the tumor region were manually selected with the help of downscaled ^{1}H data. In a next step, the number of signal pixels in the ROIs having a SNR≥4.5 was calculated. Single ^{19}F signal pixels were removed. In a final step, the percentage of the ^{19}F signal containing volume in regard to the tumor volume of the selected slice was calculated.

Immunohistochemistry

Following *ex vivo* ^{19}F MRI measurements histology was performed. Briefly, the paraformaldehyde-fixed and in 10% Sucrose/5% w/v low-melting point agarose/PBS embedded tumors were further dehydrated in 30% sucrose/PBS for 12 h and finally embedded in Tissue-Tek® O.C.T. (Sakura Finetek Europe B.V., Alphen aan den Rijn, Netherlands). Tumor samples were sectioned (15 µm) with the cryostat 2800 Frigocut (Leica Microsystems GmbH, Wetzlar, Germany). Antibody-labeling was performed following fixation in ice-cold acetone. The primary antibody was incubated for 1 h. After washing with PBS, sections were labeled for 30 min with the secondary antibody and finally mounted in Mowiol 4–88.

Fluorescence Microscopy

The fluorescence-labelled preparations were examined using the MZ16 FA Stereo-Fluorescence microscope (Leica) equipped with the digital DC500 CCD camera and the Leica IM1000 4.0 software (1300×1030 pixel RGB-color images) as well as the Leica TCS SP2 AOBS confocal laser microscope equipped with an argon, helium-neon and UV laser and the LCS 2.16 software (1024×1024 pixel RGB-color images). Digital images were processed with Photoshop 7.0 (Adobe Systems, Mountain View, CA, USA) and merged to yield overlay images.

Fluorescence Intensity and Immune Cell Density Measurements

The fluorescence intensity of the CD68-labelling or the percentage of the CD68-positive tumor area in 15-µm-thick cryostat sections of control and GLV-1h68-colonized tumors was measured on digital images (x10 objective or x40 objective, x1 ocular) of specimens stained for CD68 immuno-reactivity. On the fluorescence microscope, the background fluorescence was set to a barely detectable level by adjusting the gain of the CCD camera before all the images were captured with identical settings. The fluorescence intensity of the CD68-labelling was determined in RGB images and represented the mean brightness of all pixels (intensity range 20–255) and was measured using ImageJ software (http://rsbweb.nih.gov/ij). The whole area of the tumor cross-section was determined by manually drawing ROIs using ImageJ.

The immune cell density was determined either in microscopic images of whole tumor cross-sections (x10 objective, x1 ocular) by quantification of the positive labelled area using ImageJ software or by direct counting of CD68-positive immune cells in multiple areas of different tumor sections obtained with the confocal laser microscope (x20 objective, x10 ocular). On the fluorescence

Table 4. Parameters for the *ex vivo* ^{19}F MRI experiments.

Model	Fig	Sequence	TE [ms]	TR [ms]	TF	NA	MTX	FOV [mm]
1936-MEL	1 E,F/1S A,B	TSE	5	1000	64	450	96×64×32	60×40×20
1936-MEL	2 B/4 C	TSE	4.3	1000	48	90	64×48×40	40×30×25
GI-101A	5 C,D	TSE	6.2	1000	64	60	96×64×64	30×20×20

Acronyms (see table 1 and 2).
doi:10.1371/journal.pone.0056317.t004

microscope, for each image the fluorescence signal was set to a clearly detectable level by individually adjusting the gain of the CCD camera before the images were captured. All RGB-images were equally adjusted and converted into 8-bit gray scale images using Photoshop 7.0. Positive pixels (intensity range 0–255) of the CD68-labelling were measured using ImageJ software. The immune cell density was shown as positive area/tumor section for whole tumor sections or as number of positive cells/field of view and presented as mean values with standard deviations.

Antibodies

Immune cells were labeled either using rat anti-mouse CD68 (monocytes, tissue macrophages, dendritic cells; Abcam, Cambridge, UK), rat anti-mouse CD11b (myeloid cells, NK, T^{act}, B cell subset; eBioscience, San Diego, CA, USA), rat anti-mouse MHCII antibody (B cells, dendritic cells, monocytes, macrophages; eBioscience) and rat-anti Ly-6G antibody (mainly neutrophils, myeloid cells; eBioscience).

The Cy3-conjugated secondary antibodies (donkey) were obtained from Jackson ImmunoResearch (West Grove, PA, USA). Hoechst 33342 (Sigma Aldrich) was used to label nuclei in tissue sections.

Statistics

A two-tailed Students *t* test was used for statistical analysis of different quantitative parameters described above. Pearsons rank correlation was used to determine the correlation coefficient r. *p* values of <0.05 were considered statistically significant.

Results

PFC Accumulates in 1936-MEL Melanomas during Oncolytic Virotherapy

To test the applicability of ^{19}F MRI to monitor virus-induced inflammation during oncolytic virotherapy, we used 1936-MEL melanoma-bearing mice and administered VACV (GLV-1h68) i.v. followed by i.v. injection of emulsified PFC at day 4 and day 6 pi and MR imaging at 8 dpi (Fig. 1A). The tumor area was localized by ^{1}H images followed by acquisition of anatomically matching ^{19}F images in mock-infected control (Fig. 1B, n = 2) as well as VACV-treated animals (Fig. 1C, n = 2). The corresponding ^{1}H/^{19}F overlay *in vivo* images revealed intense hot spots of the ^{19}F signal located at the tumor periphery in VACV-colonized animals compared to only few ^{19}F-positive hot spots in the mock-infected control animals. The 3D ^{1}H/^{19}F overlay reconstruction of the abdomen of a VACV-infected mouse clearly showed an accumulation of PFC at the tumor margin (partial/hollow sphere) enabling tumor localization as well as localization of the adjacent lymph nodes (Fig. 1D). *Ex vivo* ^{1}H/^{19}F MRI imaging of excised tumors followed by CD68- and Ly-6G-immunohistology revealed a similar spatial distribution pattern of the ^{19}F signal and CD68-positive monocytes/macrophages in both groups of mice (Fig. 1E, F, n = 3). However, in VACV-colonized tumors the macrophage-containing hot spots (^{19}F^{+}/CD68^{+}) accumulate around the viral infected GFP-positive areas in the tumor periphery, whereas in control animals the CD68-positive macrophages and the corresponding ^{19}F signal were generally distributed with lower signal intensity throughout the tumor tissue. Moreover, there were also Ly-6G-positive neutrophils located around the viral infected GFP-positive areas forming the inner part of the invading immune cell front. Analysis of the CD68-fluorescence signal intensity of whole tumor cross-sections by histology revealed a significantly enhanced fluorescence intensity in VACV-infected compared to mock-infected tumors (Fig. 1G; n = 3, p = 0.026).

The detailed histological analysis further showed that the ^{19}F-positive/CD68-positive areas were also positive for CD11b and MHCII which confirm the affiliation to monocyte/macrophage populations (Figure S1).

Altogether, the results demonstrate that non-invasive ^{19}F MRI can specifically visualize VACV-mediated spatial changes in the myeloid cell populations of tumors which may either due to recruitment or redistribution of tumoral myeloid cells.

PFC and CD68^{+}-macrophage Accumulation in 1936-MEL Melanomas during the Early Time Course of Infection (0–8 dpi)

To identify the timing of PFC accumulation in 1936-MEL melanomas after VACV-treatment, we performed a time course study of PFC accumulation during early infection stages (0, 2, 4, 6, and 8 dpi). Each group was injected with one dose of PFC 4 days before tumors were harvested and *ex vivo* MRI was performed (Fig. 2A). Immediately before (0 dpi) and 2 days pi no ^{19}F signal was detectable by MRI (Fig. 2B). However, 4 days pi the first ^{19}F-positive patches were detectable in the VACV-treated tumors which further increased at day 6 and 8 pi (Fig. 2B). Interestingly, in contrast to the 4 dpi tumors the distribution pattern of the ^{19}F hot spots of the 6 and 8 dpi tumors differed and ^{19}F hot spots were mostly located in close proximity to the tumor rim. Therefore, for robust detection of viral-induced ^{19}F accumulation we suggest 2–4 dpi as the optimal injection time point for PFC in 1936-MEL tumor-bearing mice followed by ^{19}F MR imaging 6–8 days post VACV injection.

To confirm the MRI results, we performed immuno-histological analysis of the CD68^{+}-macrophage population in tumor sections at all time points. CD68-positive cells were detectable in all investigated tumors with no significant difference of the total CD68-positive tumor area during the infection time course (Fig. 2C, F). Interestingly, the distribution pattern of the CD68-positive cells was notably different in 0–4 dpi and 6–8 dpi tumors changing from an intra- and peritumoral scattered pattern to a strong accumulation of macrophages at the tumor margin. Detailed analysis of the intratumoral and the peripheral tumor areas revealed a significant increase in the CD68^{+}-macrophage population in the tumor margin concomitant with increasing viral spreading (Fig. 2D, G) and a significant loss of the intratumoral CD68^{+}-macrophage population (Fig. 2E, H).

Long-term Imaging of PFC Accumulation – a Spatio-temporal Analysis

To analyze the stability and/or the spatial distribution of the ^{19}F signal pattern over time, we injected PFC only once at day 4 pi in mock- and VACV-treated groups of 1936-MEL tumor-bearing mice and performed ^{19}F MRI at day 7, 9, and 11 dpi. During these time points tumor growth arrests in VACV-treated animals in contrast to the continuously increasing tumor volume of the mock-infected group (Fig. 3A). In each group the ^{19}F signal distribution pattern was similar during the imaging period (Fig. 3B). However, the ^{19}FTWR (total ^{19}F SNR of the tumor/tumor weight) was significant higher in VACV-treated at 11 dpi compared to mock-treated tumor-bearing animals as determined by *ex vivo* ^{19}F MRI (Fig. 3C; n = 7–8, p = 0.031). Moreover, quantification of the ^{19}F signal over time revealed a tendential ^{19}FTVR (total ^{19}F SNR of the tumor/tumor volume) signal decrease during the time course in both tested groups, in which the mock-infected group showed a significant higher decrease than the VACV-treated group (Fig. 3D; n = 4, p = 0.038).

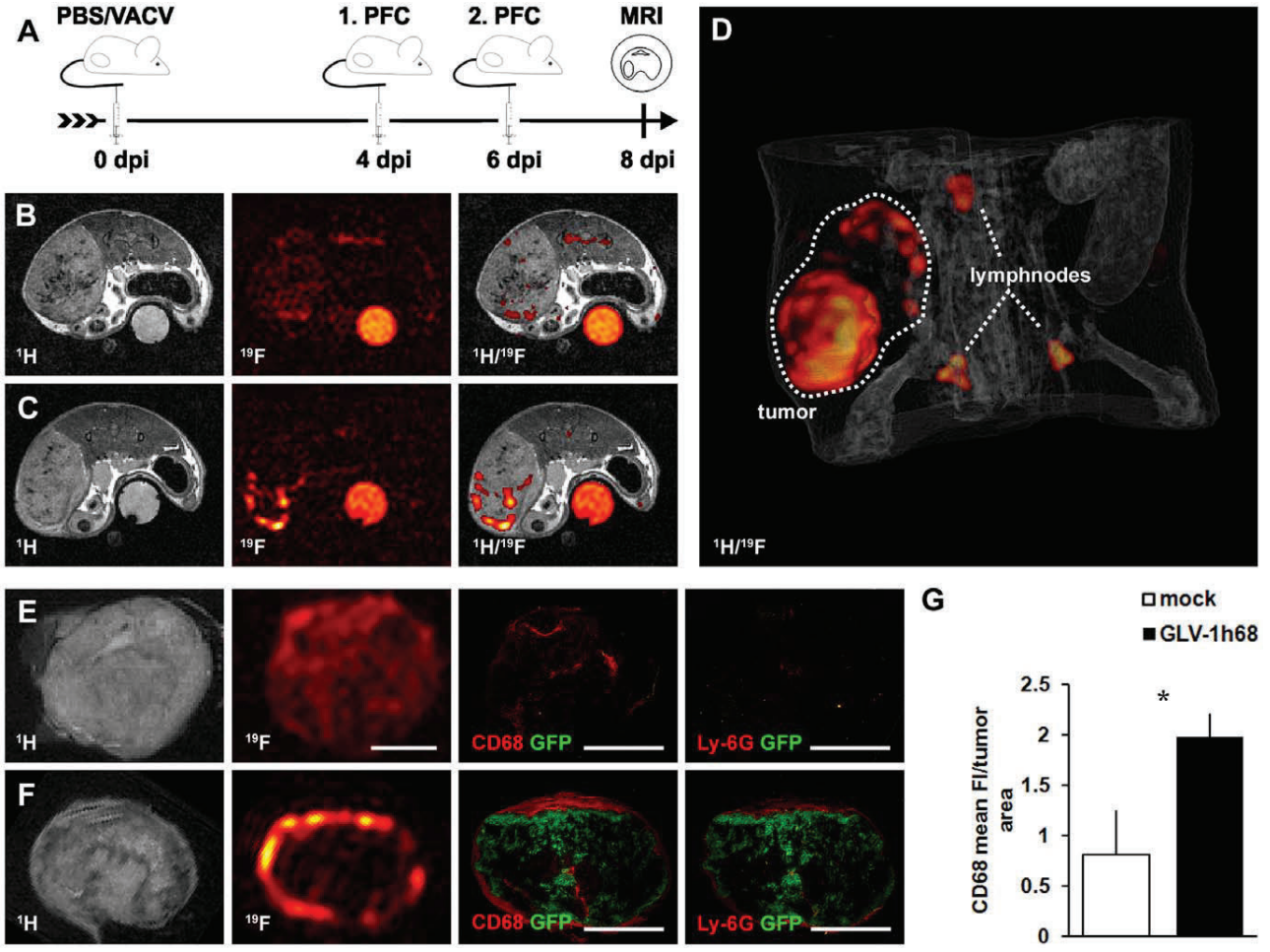

Figure 1. Visualization of viral tumor colonization by ^{19}F MRI-based imaging of inflammation. (**A**) timeline - 1936-MEL melanoma-bearing athymic nude mice were i.v. injected with either 1×10^{7} pfu of GLV-1h68 or PBS as control. Emulsified PFC was i.v. administered at day 4 and 6 pi followed by ^{19}F MRI at 8 dpi. (**B, C**) representative ^{1}H, ^{19}F, and overlayed ^{1}H/^{19}F *in vivo* images of a mock-infected tumor-bearing mouse (**B**) showing a low ^{19}F signal throughout the tumor tissue with few signal hot spots and a corresponding GLV-1h68-infected tumor-bearing mouse (**C**) revealing intense ^{19}F signal accumulation in the tumor rim 8 dpi. (**D**) 3D ^{1}H/^{19}F overlay reconstruction of the abdomen of a VACV-infected mouse clearly showed the partial/hollow sphere-like accumulation of PFC at the tumor margin and the adjacent lymph nodes. (**E, F**) representative *ex vivo* ^{1}H, ^{19}F images as well as corresponding histologically prepared tumor sections (CD68, Ly-6G) demonstrating the distribution of the CD68^{+}-macrophage/Ly-6G^{+}-neutrophil population and the ^{19}F signal of a mock-infected tumor (**E**) and a GLV-1h68-infected tumor (**F**); GLV-1h68 infection corresponds to the GFP-expressing tumor area. (**G**) GLV-1h68-colonized tumors showed increased CD68-fluorescence intensity (FI) compared to mock-infected control tumors as determined in histologically prepared tumor sections (n = 3; p = 0.026). Shown are the mean values +/− standard deviations. The ^{19}F signal intensity in B and C was scaled to SNR = 30 and in E and F to SNR = 75. The asterisk indicates a significant difference between experimental groups (*$p<0.05$; Students *t* test). All images are representative examples. Scale bars represent 5 mm.
doi:10.1371/journal.pone.0056317.g001

Importantly, both the ^{19}F-positive area (Fig. 3E; r = 0.882, p = 0.004) as well as the CD68-positive area (Fig. 3F; r = 0.720, p = 0.044) in tumor sections of VACV-treated animals positively correlated with the degree of VACV-infection as determined by the GFP-positive tumor area enabling indirect intratumoral virus detection.

Non-macrophage-related PFC Accumulation in Large, Mock-infected Control Tumors

During our study, we noticed that some large, mock-infected tumors can incorporate substantial PFC amounts after intravenous PFC application. This could interfere with the reliable detection of virus-mediated immune cell recruitment. However, this group of mainly large tumors showed a different distribution pattern of the ^{19}F signal compared to the previously shown scattered intratumoral ^{19}F pattern of mock-infected control tumors as shown in Fig. 1E. The analysis of different ^{1}H/^{19}F overlay axial slices of the abdomen revealed that the ^{19}F signal accumulation also appeared in non-tumorous areas and was mostly located outside of the malignant tissue in abdominal cross-sections (Fig. 4A). Interestingly, the investigation of the phenotype of these large, mock-infected tumor-bearing animals revealed that these mice developed peritumoral hematoma and even bloody tumors in comparison to VACV-treated tumor-bearing mice (Fig. 4B). Direct comparison of the ^{1}H/^{19}F signal pattern of large, mock-infected tumors and VACV-infected tumors by *ex vivo* MRI showed that the ^{19}F signal accumulated in the outermost part of the tumor rim in the mock-infected animals, whereas ^{19}F hot spots accumulated deeper into the tumor tissue in VACV-treated animals (Fig. 4C). Histological analysis revealed a similar pattern

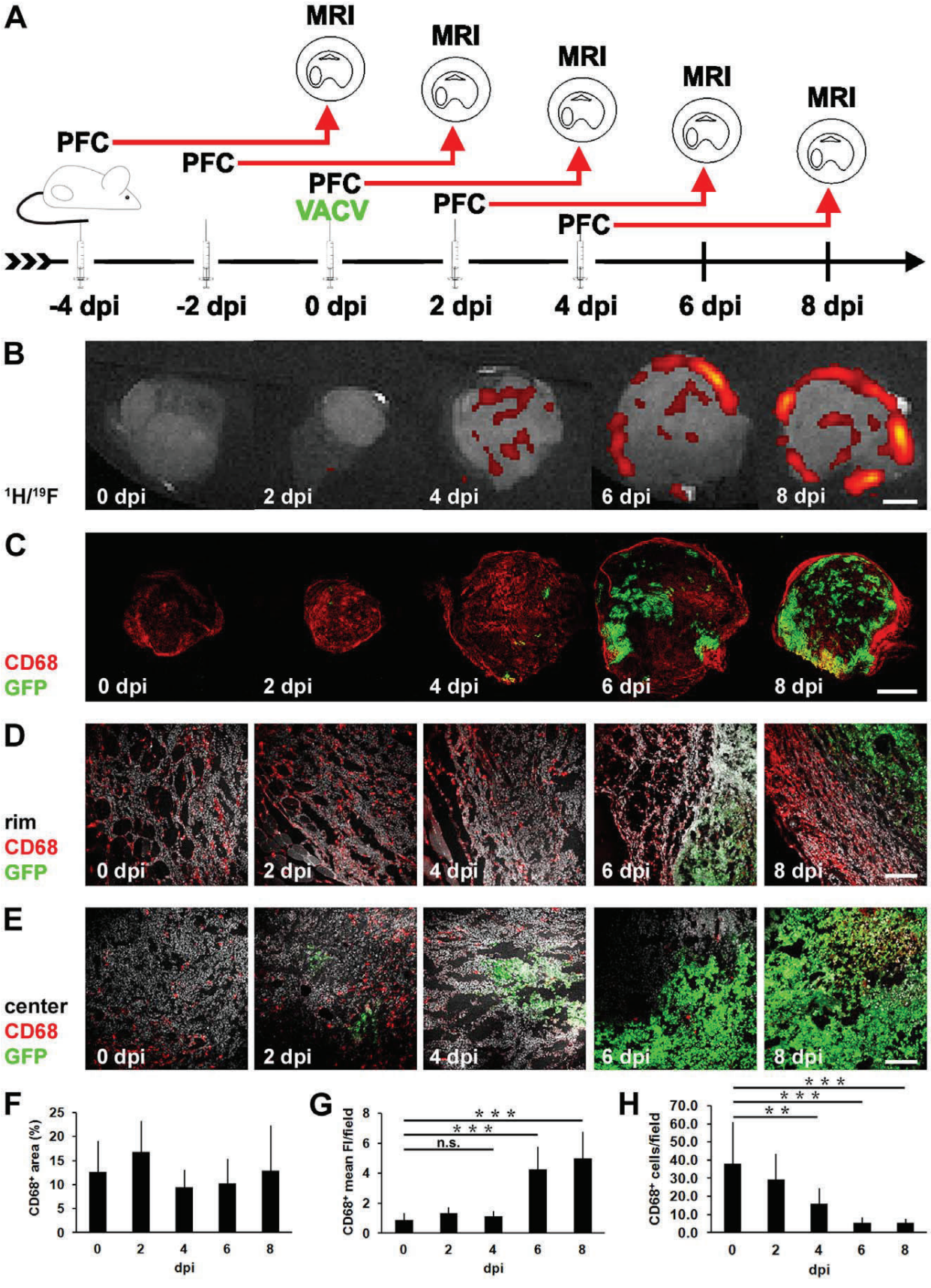
A
MRI
MRI
MRI
MRI
MRI
PFC
PFC
PFC
VACV
PFC
PFC
-4 dpi
-2 dpi
0 dpi
2 dpi
4 dpi
6 dpi
8 dpi
B
^{1}H/^{19}F
0 dpi
2 dpi
4 dpi
6 dpi
8 dpi
C
CD68
GFP
0 dpi
2 dpi
4 dpi
6 dpi
8 dpi
D
rim
CD68
GFP
0 dpi
2 dpi
4 dpi
6 dpi
8 dpi
E
center
CD68
GFP
0 dpi
2 dpi
4 dpi
6 dpi
8 dpi
F
CD68^{+} area (%)
dpi
G
CD68^{+} mean FI/field
n.s.
dpi
H
CD68^{+} cells/field
dpi

Figure 2. PFC and CD68$^+$-macrophage accumulation during early infection time course (0–8 dpi). (**A**) timeline - 1936-MEL melanoma-bearing athymic nude mice were i.v. injected with emulsified PFC in each case 4 days before tumors were harvested. 1×10^7 pfu of GLV-1h68 was i.v. administered at day 0 and tumors were harvested for *ex vivo* ^{19}F MRI at 0, 2, 4, 6 and 8 dpi (2 tumors/time point). (**B**) representative ^{1}H/^{19}F images of 1936-MEL tumors at 0, 2, 4, 6, and 8 dpi analyzed by *ex vivo* ^{19}F MRI revealed first detectable ^{19}F signal at day 4 pi further increasing at day 6 and 8 pi; 6 and 8 dpi-infected tumors showed enhanced accumulation of the ^{19}F signal at the tumor rim. (**C, F**) corresponding histologically prepared tumor sections labelled with anti-CD68 antibody to visualize the tumoral macrophage population at day 0, 2, 4, 6, and 8 dpi revealed no significant difference in the total CD68$^+$ tumor area (%) at the different time points (8 tumor sections/time point). (**D, G**) confocal-laser microscopic images of the corresponding tumor sections taken from the tumor periphery (rim) showed a similar density of CD68$^+$-macrophages/CD68 fluorescence intensity (FI) in 0–4 dpi tumors and a significant increase at 6 and 8 dpi (12 tumor areas/time point). (**E, H**) corresponding confocal-laser microscopic images of tumor sections taken from the intratumoral tissue (center) showed a significant decrease in the density of CD68$^+$-macrophages during the time course of infection (12 tumor areas/time point). Shown are the mean values +/− standard deviations. The signal intensity of all presented ^{19}F images was scaled to SNR = 30. Asterisks indicate a significant difference between experimental groups (n.s. = not significant, $^{**}p<0.01$, $^{***}p<0.001$; Students *t* test). All images are representative examples. Scale bars represent 2 mm (B, C) and 300 μm (D, E).
doi:10.1371/journal.pone.0056317.g002

of CD68$^+$-macrophage populations and ^{19}F hot spots only for the VACV-treated tumors and no matching was found for mock-infected tumors (Fig. 4D).

^{19}F-MRI-based Imaging of VACV-induced Recruitment of Macrophages in Different Tumor Models

Since different tumor types as well as individual tumors of the same origin can greatly vary in their content of phagocytic macrophages, the polarization of the macrophage status and the immune-related response to therapy [36,37], we decided to test our concept in different tumor models. Thus, we chose the A549

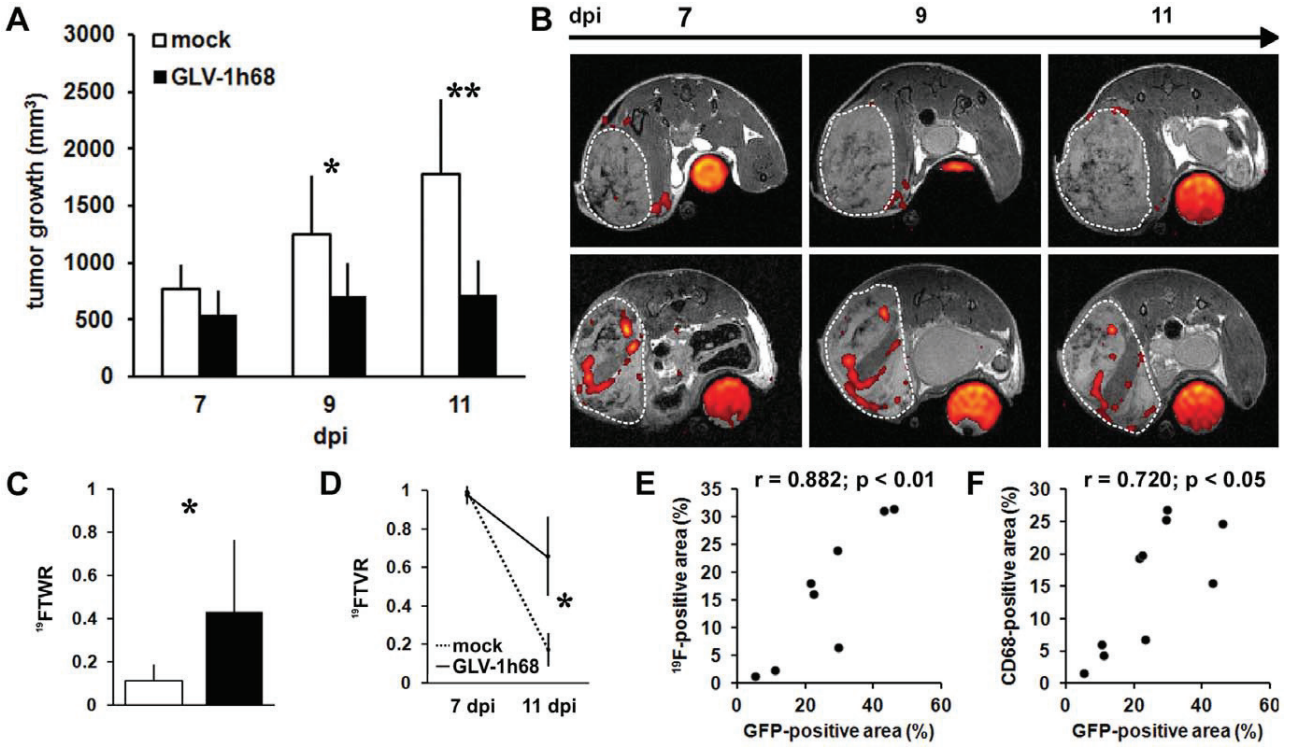

Figure 3. Long term PFC accumulation and correlation to viral tumor load. The mice were either mock-infected or treated with 1×10^7 pfu GLV-1h68 (i.v.) and i.v. injected with emulsified PFC at day 4 pi. (**A**) 1936-MEL tumor growth was monitored by measuring the tumor volume of 7–8 mice in each group revealing a continuous tumor growth in the mock-infected group and a stable disease in the GLV-1h68-treated group. Shown are the mean values +/− standard deviations. (**B**) representative ^{1}H/^{19}F images of 1936-MEL tumor-bearing mice either mock-infected (upper row) or treated with GLV-1h68 (lower row) and i.v. injected with emulsified PFC at day 4 pi. *In vivo* ^{19}F MRI was performed at day 7, (9), and 11 pi of n = 4 (n = 2) mice of each group. (**C**) quantitative evaluation of the ^{19}FTWRs of *ex vivo* ^{19}F MRI measurements of mock-infected and GLV-1h68-treated 1936-MEL tumors at 11 dpi revealed a significant difference between both groups (n = 7/8; p = 0.031). (**D**) quantitative evaluation of the ^{19}FTVR decrease (7 to 11 dpi) of mock-infected and GLV-1h68-treated 1936-MEL tumors during the time course study measured by *in vivo* ^{19}F MRI revealed a significant difference between both groups (n = 4; p = 0.038). (**E, F**) significant positive correlation of either the amount of the ^{19}F-positive area determined in 625 μm-thick MRI sections (**E**) or the CD68-positive area determined in 15 μm-thick histological sections (**F**) with the extent of viral infection as determined by the GFP-expressing area in corresponding 15 μm-thick tumor sections (Pearsons correlation coefficient PFC/GFP: r = 0.882; p = 0.004; CD68/GFP: r = 0.720; p = 0.044). Shown are the mean values +/− standard deviations. The signal intensity of all presented ^{19}F images was scaled to SNR = 30. Asterisks indicate a significant difference between experimental groups ($^*p<0.05$, $^{**}p<0.01$; Students *t* test). All images are representative examples.
doi:10.1371/journal.pone.0056317.g003

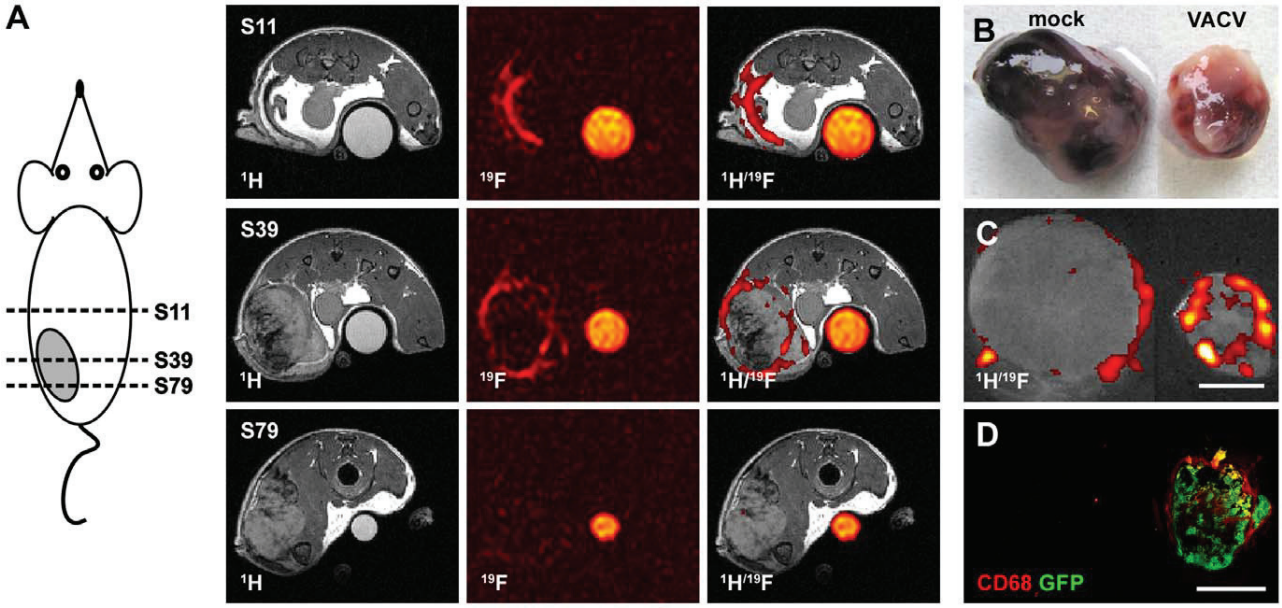

Figure 4. PFC also accumulates in peritumoral hematomas of mock-infected animals bearing large 1936-MEL tumors independently of CD68^{+}-macrophages. (**A**) mock-infected 1936-MEL tumor-bearing mouse i.v. injected with emulsified PFC at 4 dpi. *In vivo* ^{19}F MRI 7 dpi revealed an accumulation of the ^{19}F signal in axial slices of the abdomen far-out from the tumor region (S11), in some tumorous sections (S39), whereas other tumor-containing sections did not reveal ^{19}F accumulation (S79). (**B**) morphological analysis of PFC-accumulating mock-infected animals revealed large hematomas in the peritumoral areas compared to GLV-1h68-treated tumors. (**C, D**) *ex vivo* ^{1}H/^{19}F images of mock-infected and GLV-1h68-infected tumors revealed a similar distribution pattern of the ^{19}F signal (**C**) and the CD68^{+}-macrophage population (**D**) only for the GLV-1h68-treated tumors. The signal intensity of all presented ^{19}F images was scaled to SNR = 30. All images are representative examples. Scale bars represent 5 mm.
doi:10.1371/journal.pone.0056317.g004

lung carcinoma model bearing few macrophages as well as the GI-101A breast adenocarcinoma model harboring a substantial population of tumor-associated macrophages before treatment (unpublished results). Despite these immunological differences, in both tumor types a significant increase in the ^{19}F signal due to VACV-treatment was detectable in comparison to the mock-infected animal group (Fig. 5, Figure S2).

In addition we wanted to emphasize, that the use of ^{19}F PFC as cellular contrast agent should not prevent the utilization of quantitative ^{1}H parameters. Exemplarily, ^{1}H T_2 maps were acquired for the A549 lung carcinoma model (Fig. 5B, D)

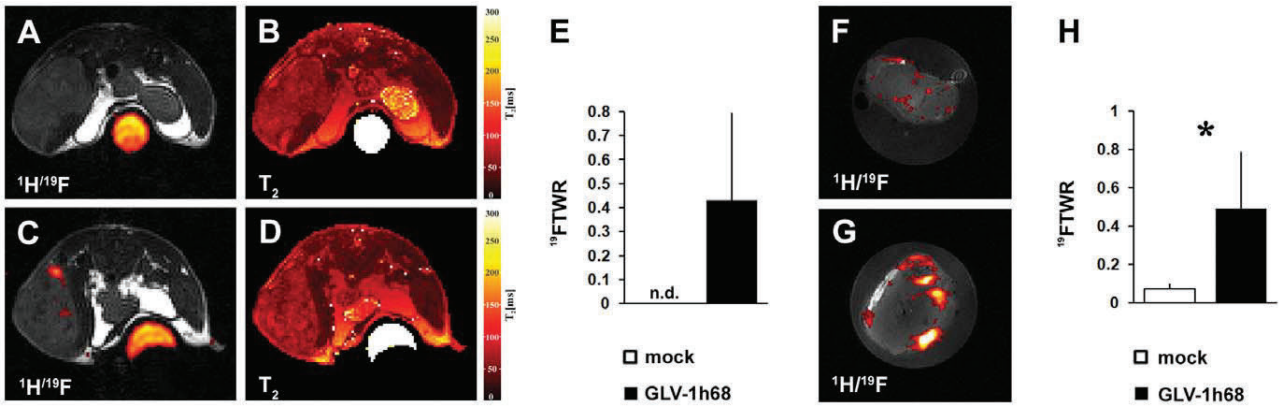

Figure 5. GLV-1h68-induced accumulation of intratumoral PFC is also detectable in lung carcinomas and breast adenocarcinomas. (**A–D**) ^{1}H/^{19}F overlay and ^{1}H T_2 images of mock-infected (**A, B**) and GLV-1h68-infected (**C, D**) A549 lung carcinoma-bearing mice were analyzed 7 dpi by *in vivo* ^{19}F MRI (PFC, 4 dpi). (**E**) quantitative evaluation of the ^{19}FTWR of *in vivo* ^{19}F MRI measurements of mock-infected and GLV-1h68-treated A549 tumors at 7 dpi revealed a detectable ^{19}FTWR only in VACV-treated tumors (n = 4). (**F–H**) mock-infected (**F**) and GLV-1h68-infected (**G**) GI-101A breast adenocarcinoma-bearing mice were analyzed 10 dpi by *ex vivo* ^{19}F MRI (PFC injection, 7 dpi). (**H**) quantitative evaluation of the ^{19}FTWR of *ex vivo* ^{19}F MRI measurements of mock-infected and GLV-1h68-treated GI-101A tumors at 10 dpi revealed a significant difference between both groups (n = 4–5; p = 0.033). Shown are the mean values +/− standard deviations. The signal intensity of all presented ^{19}F images was scaled to SNR = 30. Asterisk indicate a significant difference between experimental groups (n.d. = not detectable; *$p<0.05$; Students *t* test). All images are representative examples.
doi:10.1371/journal.pone.0056317.g005

indicating the possible integration of other quantitative ^{1}H MRI parameters to facilitate tumor characterization [38].

In summary, the ^{19}F-MRI-based imaging of tumoral VACV-colonization is applicable in different tumor models and possesses high potential for monitoring oncolytic therapy. However, the great diversity of the microenvironment of different tumor models and even individual tumors implies for future work a specific and thus personalized imaging modality applying ^{19}F MRI before and after starting the oncolytic treatment.

Discussion

We have shown that the VACV-induced infiltration of myeloid cells into different tumor models is reliably detectable by ^{19}F MRI. Therefore, we suggest that ^{19}F MRI may be used in the future as a novel tool to quantitatively and non-invasively monitor the innate immune response in tumors following oncolytic virotherapy. Thus, this imaging technique can be readily investigated as a surrogate measure to monitor viral tumor colonization and also therapeutic response. To the best of our knowledge, this is the first report of utilizing PFC nanoparticles in combination with ^{19}F MRI for detection of myeloid cell infiltration into tumors undergoing oncolytic virotherapy. Other investigators have reported the use of PFC nanoparticles to monitor inflammatory conditions in different other pathological situations [13–18]. Recently, Kleijn [39] used a Gadolinium (Gd)-based agent targeting the inflammatory enzyme myeloperoxidase (MPO) in a similar approach to detect oncolytic virus-associated tumor inflammation by MRI. However, ^{19}F MRI has several advantages compared to contrast agent based ^{1}H MRI including no background in tissues [20], the possibility of direct quantification of the marker amount [24] and the unaltered ^{1}H signal making the assessment of other quantitative ^{1}H parameters more feasible [18].

In the present study, ^{19}F MRI as well as the histological examination of mock-infected tumors revealed a diffuse distribution of both the ^{19}F signal and the CD68^{+}-macrophages throughout the tumor. In this respect, the so called enhanced permeability and retention (EPR) effect, which is a microenvironmental characteristic of solid tumors leading to the passive and unspecific accumulation of a variety of macromolecules and nanoparticles, may enhance the accumulation of PFC in large mock-infected control tumors [40]. However, the direct comparison to VACV-treated tumors clearly showed that the viral tumor colonization significantly altered the ^{19}F signal distribution as well as the signal intensity. In VACV-treated tumors the ^{19}F-positive hot spots, which showed a similar distribution pattern as the CD68^{+}-macrophage population, encapsulated the viral infection focus and formed a "partial/hollow sphere" localized to the tumor rim. In this regard, 3D-reconstructions of the abdominal region of VACV-treated tumor-bearing mice enable a straightforward localization of the tumorous regions. Since GLV-1h68 preferentially colonizes metastases [41] this imaging modality may be useful to detect metastases. In accordance with previous findings [13,17], we further observed a strong ^{19}F signal in the adjacent lymph nodes of tumors in 1936-MEL-bearing animals also indicating the potential of this imaging modality for the localization of sentinel lymph nodes. In future studies, we will especially analyze ^{19}F-positive lymph nodes and clarify whether these lymph nodes are already metastasized or sites of an ongoing inflammatory immune cell activation.

Recent studies combining blood density gradient centrifugation and ^{1}H/^{19}F MRI showed that i.v. applied PFCs are predominantly taken up within the blood stream by monocytes but to a minor degree also by B-cells and neutrophils [13,15]. After uptake, especially PFC-labelled neutrophils and macrophages migrate to sites of ongoing inflammation, where monocytes/macrophages are the predominant PFC-labelled cell fraction [15,19]. In ^{19}F-positive hot spots of VACV-treated tumors both monocyte-derived macrophages (CD68, CD11b, MHCII) as well as neutrophils (Ly-6G) were detectable, however, clearly spatially separated in different areas of the invading immune cell front. Neutrophils were localized in the inner part of the immune cell immigrants, whereas macrophages were located in the surrounding outer area. Since neutrophils are the first actors at the infection site followed by monocytes/macrophages [42] the here observed accumulation pattern of both immune cell populations implies that both populations are recruited in a timely different fashion to the VACV-infected tumor rather than re-distributed within the tumor tissue.

The time course study from 0 to 8 dpi based on ^{19}F MRI and histological analysis of VACV-treated tumors revealed discrepancies between the spatio-temporal ^{19}F accumulation and the CD68^{+}-macrophage population during the course of infection. The ^{19}F signal was first detectable at 4 dpi further increasing in the tumor rim at day 6 and 8 pi, whereas the CD68^{+}-macrophage population was at all investigated time points detectable, however, either distributed throughout the whole tumor (0–4 dpi) or mostly located with a high density at the tumor rim (6–8 dpi). Further, the microscopic analysis revealed that the intratumoral macrophage population significantly decreases whereas the peritumoral population increases during the course of infection and with increasing viral spreading. These results indicate that the resident TAM population may be directly eliminated from the tumor tissue by viral infection and simultaneously a second VACV infection-induced population of ^{19}F-positive macrophages was recruited from the circulation to the tumor encapsulating the infection focus. The lack of the ^{19}F accumulation early after infection may be responsible either to the lower phagocytic activity of the resident macrophage population [37] or to the reduced vessel permeability in these tumors avoiding significant intratumoral accumulation of PFC after injection. Since the presence of TAMs in several cancer types correlates strongly with a poor outcome [43] studies were already performed to develop a clinically applicable, non-invasive diagnostic assay for visualization of TAMs in tumors based on MRI and clinically applicable iron oxide nanoparticles [44]. In the present study, however, the results indicate that, rather than labelling the intratumoral TAMs, PFC nanoparticles may label mainly the immune cells in the circulation which immigrate into the tumor after viral colonization.

The observed decrease of the ^{19}FTVRs during the time course study could be mainly explained by the continuous tumor growth in the mock-infected group. However, in VACV-treated animals the average tumor volume remained stable during the imaging period. Therefore, the decrease in the ^{19}FTVRs in VACV-treated mice may be either due to an emigration of PFC-labelled macrophages to e.g. draining lymph nodes, which could also explain the observed ^{19}F signal in the sentinel lymph nodes (Fig.1 D) or to the loss of freely accumulated PFC via efferent lymphatics. For the immuno-therapeutic effect of oncolytic virotherapy, emigration of phagocytic cells from the tumor to adjacent lymph nodes may offer a way to activate an adaptive anti-tumoral immune response via tumor antigen presentation to B- and T cells and should be further investigated in future studies.

The examination of the ^{19}F-positive area and the extent of the viral spreading determined by the GFP-expression revealed a significant positive correlation for both parameters indicating that ^{19}F MRI during oncolytic virotherapy enables indirect monitoring of viral replication. This would be beneficial for non-invasive

monitoring of intratumoral viral replication in pre-clinical and in future clinical studies, since ^{19}F MRI provides a whole organ visualization circumventing the problems associated with small sample biopsies such as false-negative or -positive results of viral replication. For future studies using ^{19}F MRI for monitoring of oncolytic virotherapy, we suggest a specific personalized imaging modality applying ^{19}F MRI before and after starting the oncolytic treatment to avoid misinterpretation of unspecific PFC accumulation as we have shown in tumor-associated hematoma.

For correlation purposes only tissue slices from the tumor middle and the same orientation were always chosen for histological sections and ex-vivo ^{19}F images. However, due to the different slice thickness and possible alignment errors of the histological section and the MRI data, the correlation remains limited. In the future, as has been done with ^{1}H MRI [45], sophisticated ^{19}F MRI coils should be developed to improve the correlation of ^{19}F MRI and histology.

Since we could show that ^{19}F MRI enables the detection of viral tumor colonization and immune cell recruitment to tumors in different tumor types with different immunological context, we assume that the here described imaging modality may also be useful in the future for clinical applications. Thorne previously discussed that it is also likely that systemic measurements of the level and type of immune response induced by the viral treatment may ultimately be used either as an early prognostic indicator of therapeutic response, or may help elucidate the immune properties of the tumor being treated, and so assist in the design of subsequent immunotherapeutic treatments [46]. In the same manner, we propose that ^{19}F MRI may have the potential to be used for therapeutic monitoring and as prognostic indicator for the therapeutic outcome.

Supporting Information

Figure S1 Co-localization of the ^{19}F signal with monocytes/macrophages and neutrophils. Representative *ex vivo* ^{1}H/^{19}F overlays as well as corresponding histologically prepared tumor sections demonstrating a similar distribution pattern of the CD68^{+}- (monocytes/macrophages), MHCII^{+}- (antigen-presenting cells such as dendritic cells (DCs), macrophages and B cells), CD11b^{+}- (myeloid cells), Ly-6G^{+}-population (neutrophils) and the ^{19}F signal of a mock-infected tumor **(A)** and a GLV-1h68-infected tumor **(B)**. The ^{19}F signal intensity was scaled to SNR = 75. All images are representative examples. Scale bars represent 5 mm.
(TIF)

Figure S2 GLV-1h68-induced accumulation of intratumoral PFC and CD68 histology of breast adenocarcinomas. (A–D) ^{1}H/^{19}F overlay images (left row) and CD68 histology (right row) of mock-infected **(A, B)** and GLV-1h68-infected **(C, D)** GI-101A breast adenocarcinoma-bearing mice analyzed 10 dpi by *ex vivo* ^{19}F MRI (PFC injection, 7dpi). GFP corresponds to GLV-1h68 infection of the tumor tissue. The signal intensity of all presented ^{19}F images was scaled to SNR = 30. All images are representative examples.
(TIFF)

Acknowledgments

The authors thank Jason Aguilar, Sabine Voll and Tobias Hertlein for excellent technical assistance, Saskia Wittber for animal care, and Anna Vilter for building the coil for the 11.7 Tesla system.

Author Contributions

Programmed software routines: TCBL VJFS TK Approved the final manuscript: IG. Conceived and designed the experiments: SW TCBL MH EH CS PMJ AAS. Performed the experiments: SW TCBL MH EH CS JL. Analyzed the data: SW TCBL IG YY TK. Contributed reagents/materials/analysis tools: PMJ AAS. Wrote the paper: SW TCBL.

References

1. Bourke MG, Salwa S, Harrington KJ, Kucharczyk MJ, Forde PF, et al. (2011) The emerging role of viruses in the treatment of solid tumours. Cancer Treat Rev 37: 618–632.
2. Urruticoechea A, Alemany R, Balart J, Villanueva A, Vinals F, et al. (2010) Recent advances in cancer therapy: an overview. Curr Pharm Des 16: 3–10.
3. Vaha-Koskela MJ, Heikkila JE, Hinkkanen AE (2007) Oncolytic viruses in cancer therapy. Cancer Lett 254: 178–216.
4. Parato KA, Senger D, Forsyth PA, Bell JC (2005) Recent progress in the battle between oncolytic viruses and tumours. Nat Rev Cancer 5: 965–976.
5. Liu TC, Galanis E, Kirn D (2007) Clinical trial results with oncolytic virotherapy: a century of promise, a decade of progress. Nat Clin Pract Oncol 4: 101–117.
6. Rowan K (2010) Oncolytic viruses move forward in clinical trials. J Natl Cancer Inst 102: 590–595.
7. Russell SJ, Peng KW, Bell JC (2012) Oncolytic virotherapy. Nat Biotechnol 30: 658–670.
8. Weibel S, Raab V, Yu YA, Worschech A, Wang E, et al. (2011) Viral-mediated oncolysis is the most critical factor in the late-phase of the tumor regression process upon vaccinia virus infection. BMC Cancer 11: 68.
9. Fulci G, Dmitrieva N, Gianni D, Fontana EJ, Pan X, et al. (2007) Depletion of peripheral macrophages and brain microglia increases brain tumor titers of oncolytic viruses. Cancer Res 67: 9398–9406.
10. Fulci G, Breymann L, Gianni D, Kurozomi K, Rhee SS, et al. (2006) Cyclophosphamide enhances glioma virotherapy by inhibiting innate immune responses. Proc Natl Acad Sci U S A 103: 12873–12878.
11. Prestwich RJ, Errington F, Diaz RM, Pandha HS, Harrington KJ, et al. (2009) The case of oncolytic viruses versus the immune system: waiting on the judgment of Solomon. Hum Gene Ther 20: 1119–1132.
12. Prestwich RJ, Harrington KJ, Pandha HS, Vile RG, Melcher AA, et al. (2008) Oncolytic viruses: a novel form of immunotherapy. Expert Rev Anticancer Ther 8: 1581–1588.
13. Flogel U, Ding Z, Hardung H, Jander S, Reichmann G, et al. (2008) In vivo monitoring of inflammation after cardiac and cerebral ischemia by fluorine magnetic resonance imaging. Circulation 118: 140–148.
14. Flogel U, Su S, Kreideweiss I, Ding Z, Galbarz L, et al. (2011) Noninvasive detection of graft rejection by in vivo (19) F MRI in the early stage. Am J Transplant 11: 235–244.
15. Ebner B, Behm P, Jacoby C, Burghoff S, French BA, et al. (2010) Early assessment of pulmonary inflammation by 19F MRI in vivo. Circ Cardiovasc Imaging 3: 202–210.
16. Kadayakkara DK, Ranganathan S, Young WB, Ahrens ET (2012) Assaying macrophage activity in a murine model of inflammatory bowel disease using fluorine-19 MRI. Lab Invest 92: 636–645.
17. Weise G, Basse-Luesebrink TC, Wessig C, Jakob PM, Stoll G (2011) In vivo imaging of inflammation in the peripheral nervous system by (19)F MRI. Exp Neurol 229: 494–501.
18. Hertlein T, Sturm V, Kircher S, Basse-Lusebrink T, Haddad D, et al. (2011) Visualization of abscess formation in a murine thigh infection model of Staphylococcus aureus by 19F-magnetic resonance imaging (MRI). PLoS One 6: e18246.
19. Temme S, Bonner F, Schrader J, Flogel U (2012) (19) F magnetic resonance imaging of endogenous macrophages in inflammation. Wiley Interdiscip Rev Nanomed Nanobiotechnol 4: 329–343.
20. Stoll G, Basse-Lusebrink T, Weise G, Jakob P (2012) Visualization of inflammation using (19) F-magnetic resonance imaging and perfluorocarbons. Wiley Interdiscip Rev Nanomed Nanobiotechnol.
21. Miller JC, Thrall JH (2004) Clinical molecular imaging. J Am Coll Radiol 1: 4–23.
22. Tawakol A, Migrino RQ, Bashian GG, Bedri S, Vermylen D, et al. (2006) In vivo 18F-fluorodeoxyglucose positron emission tomography imaging provides a noninvasive measure of carotid plaque inflammation in patients. J Am Coll Cardiol 48: 1818–1824.
23. Hyafil F, Cornily JC, Feig JE, Gordon R, Vucic E, et al. (2007) Noninvasive detection of macrophages using a nanoparticulate contrast agent for computed tomography. Nat Med 13: 636–641.
24. Srinivas M, Turner MS, Janjic JM, Morel PA, Laidlaw DH, et al. (2009) In vivo cytometry of antigen-specific t cells using 19F MRI. Magn Reson Med 62: 747–753.

25. de Visser KE, Eichten A, Coussens LM (2006) Paradoxical roles of the immune system during cancer development. Nat Rev Cancer 6: 24–37.
26. Mantovani A, Allavena P, Sica A, Balkwill F (2008) Cancer-related inflammation. Nature 454: 436–444.
27. Mantovani A, Sozzani S, Locati M, Allavena P, Sica A (2002) Macrophage polarization: tumor-associated macrophages as a paradigm for polarized M2 mononuclear phagocytes. Trends Immunol 23: 549–555.
28. Heusinkveld M, van der Burg SH (2011) Identification and manipulation of tumor associated macrophages in human cancers. J Transl Med 9: 216.
29. Advani SJ, Buckel L, Chen NG, Scanderbeg DJ, Geissinger U, et al. (2012) Preferential replication of systemically delivered oncolytic vaccinia virus in focally irradiated glioma xenografts. Clin Cancer Res 18: 2579–2590.
30. Gentschev I, Muller M, Adelfinger M, Weibel S, Grummt F, et al. (2011) Efficient colonization and therapy of human hepatocellular carcinoma (HCC) using the oncolytic vaccinia virus strain GLV-1h68. PLoS One 6: e22069.
31. Zhang Q, Yu YA, Wang E, Chen N, Danner RL, et al. (2007) Eradication of solid human breast tumors in nude mice with an intravenously injected light-emitting oncolytic vaccinia virus. Cancer Res 67: 10038–10046.
32. Sabatino M, Zhao Y, Voiculescu S, Monaco A, Robbins P, et al. (2008) Conservation of genetic alterations in recurrent melanoma supports the melanoma stem cell hypothesis. Cancer Res 68: 122–131.
33. Hurst J, Maniar N, Tombarkiewicz J, Lucas F, Roberson C, et al. (1993) A novel model of a metastatic human breast tumour xenograft line. Br J Cancer 68: 274–276.
34. Greer S, Alvarez M, Mas M, Wozniak C, Arnold D, et al. (2001) Five-chlorodeoxycytidine, a tumor-selective enzyme-driven radiosensitizer, effectively controls five advanced human tumors in nude mice. Int J Radiat Oncol Biol Phys 51: 791–806.
35. Gudbjartsson H, Patz S (1995) The Rician distribution of noisy MRI data. Magn Reson Med 34: 910–914.
36. Lewis CE, Pollard JW (2006) Distinct role of macrophages in different tumor microenvironments. Cancer Res 66: 605–612.
37. Movahedi K, Laoui D, Gysemans C, Baeten M, Stange G, et al. (2010) Different tumor microenvironments contain functionally distinct subsets of macrophages derived from Ly6C(high) monocytes. Cancer Res 70: 5728–5739.
38. Morchel P, Melkus G, Yaromina A, Zips D, Baumann M, et al. (2010) Correlating quantitative MR measurements of standardized tumor lines with histological parameters and tumor control dose. Radiother Oncol 96: 123–130.
39. Kleijn A, Chen JW, Buhrman JS, Wojtkiewicz GR, Iwamoto Y, et al. (2011) Distinguishing inflammation from tumor and peritumoral edema by myeloperoxidase magnetic resonance imaging. Clin Cancer Res 17: 4484–4493.
40. Fang J, Nakamura H, Maeda H (2011) The EPR effect: Unique features of tumor blood vessels for drug delivery, factors involved, and limitations and augmentation of the effect. Adv Drug Deliv Rev 63: 136–151.
41. Donat U, Weibel S, Hess M, Stritzker J, Hartl B, et al. (2012) Preferential Colonization of Metastases by Oncolytic Vaccinia Virus Strain GLV-1h68 in a Human PC-3 Prostate Cancer Model in Nude Mice. PLoS One 7: e45942.
42. Soehnlein O, Lindbom L (2010) Phagocyte partnership during the onset and resolution of inflammation. Nat Rev Immunol 10: 427–439.
43. Bingle L, Brown NJ, Lewis CE (2002) The role of tumour-associated macrophages in tumour progression: implications for new anticancer therapies. J Pathol 196: 254–265.
44. Daldrup-Link HE, Golovko D, Ruffell B, Denardo DG, Castaneda R, et al. (2011) MRI of tumor-associated macrophages with clinically applicable iron oxide nanoparticles. Clin Cancer Res 17: 5695–5704.
45. Meadowcroft MD, Zhang S, Liu W, Park BS, Connor JR, et al. (2007) Direct magnetic resonance imaging of histological tissue samples at 3.0T. Magn Reson Med 57: 835–841.
46. Thorne SH (2011) Immunotherapeutic potential of oncolytic vaccinia virus. Immunol Res 50: 286–293.

Figure S1

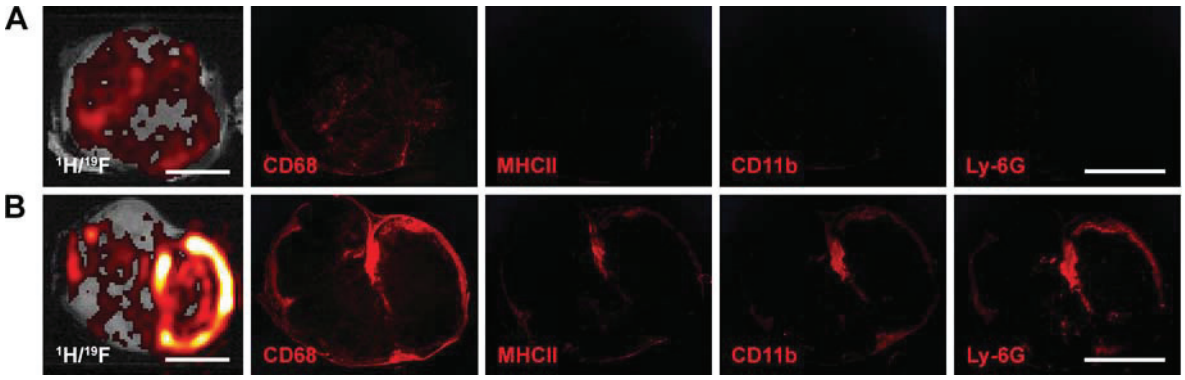

Figure S2

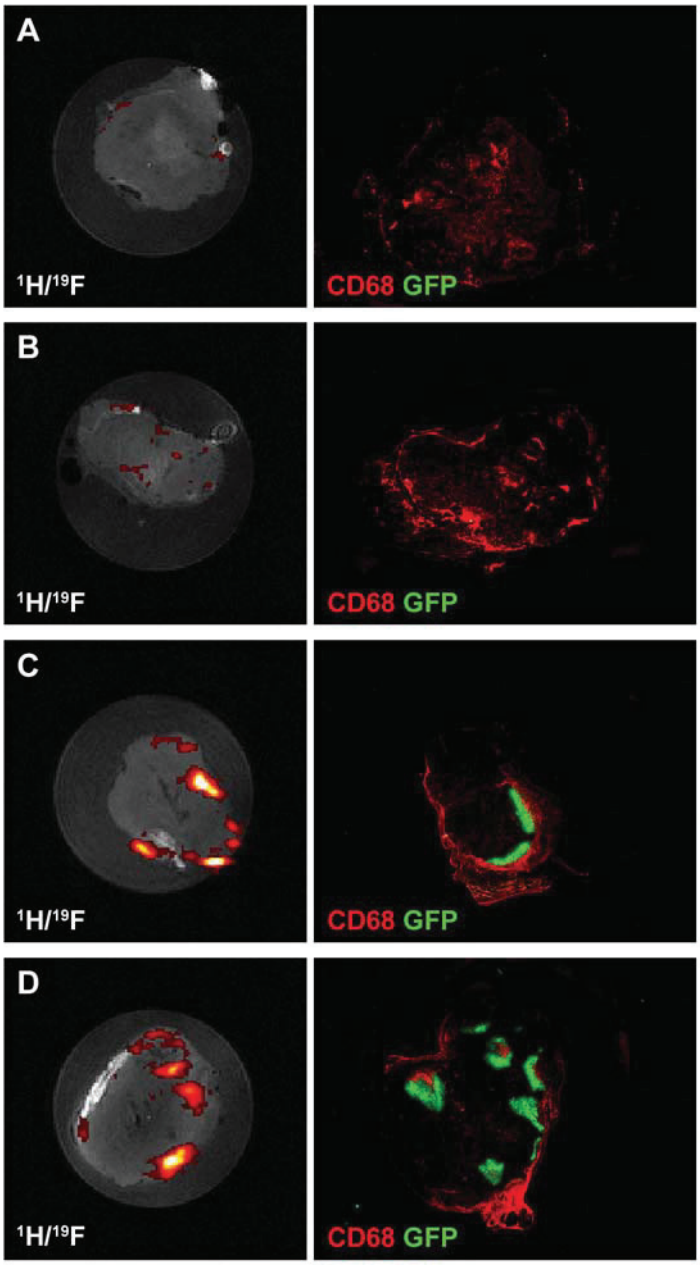
A
$^{1}H/^{19}F$
CD68 GFP
B
$^{1}H/^{19}F$
CD68 GFP
C
$^{1}H/^{19}F$
CD68 GFP
D
$^{1}H/^{19}F$
CD68 GFP

Publication (complete reference): Donat U, Weibel S, **Hess M**, Stritzker J, Härtl B, Sturm JB, Chen NG, Gentschev I, Szalay AA. Preferential colonization of metastases by oncolytic Vaccinia virus strain GLV-1h68 in a human PC-3 prostate cancer model in nude mice. *PLoS One*. 2012;7:e45942
Authors' contributions
Conceived and designed the experiments: UD AAS SW JS IG. Performed the experiments: UD **MH** JBS. Analyzed the data: UD SW. Contributed reagents/materials/analysis tools: NGC. Wrote the paper: UD SW **MH** AAS JS BH.

Ulrike Donat	
Stephanie Weibel	
Jochen Stritzker	
Barbara Härtl	
Julia B. Sturm	
Nanhai G. Chen	
Ivaylo Gentschev	
Aladar A. Szalay	

OPEN ACCESS Freely available online

PLOS ONE

Preferential Colonization of Metastases by Oncolytic Vaccinia Virus Strain GLV-1h68 in a Human PC-3 Prostate Cancer Model in Nude Mice

Ulrike Donat[1], Stephanie Weibel[1], Michael Hess[1], Jochen Stritzker[1,2], Barbara Härtl[1,4], Julia B. Sturm[1], Nanhai G. Chen[2,3], Ivaylo Gentschev[1,2], Aladar A. Szalay[1,2,3,4,5]*

1 Institute of Biochemistry, University of Würzburg, Würzburg, Germany, **2** Genelux Corporation, San Diego Science Center, San Diego, California, United States of America, **3** Department of Radiation Oncology, Rebecca & John Moores Comprehensive Cancer Center, University of California San Diego, San Diego, California, United States of America, **4** Genelux GmbH, Bernried, Germany, **5** Rudolph Virchow Center for Experimental Biomedicine and Institute Molecular Infection Biology, University of Würzburg, Würzburg, Germany

Abstract

Recently, we showed that the oncolytic vaccinia virus GLV-1h68 has a significant therapeutic potential in treating lymph node metastases of human PC-3 prostate carcinoma in tumor xenografts. In this study, underlying mechanisms of the virus-mediated metastases reduction were analyzed. Immunohistochemistry demonstrated that virus-treatment resulted in a drastically decrease of blood and lymph vessels, representing essential routes for PC-3 cell migration, in both tumors and metastases. Thus, GLV-1h68 drastically reduced essential routes for the metastatic spread of PC-3 cells. Furthermore, analysis of viral distribution in GLV-1h68-injected tumor-bearing mice by plaque assays, revealed significantly higher virus titers in metastases compared to solid tumors. To elucidate conditions potentially mediating the preferential viral colonization and eradication of metastases, microenvironmental components of uninfected tumors and metastases were compared by microscopic studies. These analyses revealed that PC-3 lymph node metastases showed increased vascular permeability, higher proliferation status of tumor cells as determined by BrdU- and Ki-67 assays and lesser necrosis of PC-3 cells than solid tumors. Moreover, an increased number of immune cells ($MHCII^+/CD68^+$ macrophages, $MHCII^+/CD19^+$ B lymphocytes) combined with an up-regulated expression of pro-inflammatory cytokines was observed in metastases in comparison to primary PC-3 tumors. We propose that these microenvironmental components mediated the metastatic tropism of GLV-1h68. Therefore, vaccinia virus-based oncolytic virotherapy might offer a novel treatment of metastatic prostate carcinomas in humans.

Citation: Donat U, Weibel S, Hess M, Stritzker J, Härtl B, et al. (2012) Preferential Colonization of Metastases by Oncolytic Vaccinia Virus Strain GLV-1h68 in a Human PC-3 Prostate Cancer Model in Nude Mice. PLoS ONE 7(9): e45942. doi:10.1371/journal.pone.0045942

Editor: Maciej S. Lesniak, The University of Chicago, United States of America

Received June 25, 2012; **Accepted** August 23, 2012; **Published** September 25, 2012

Funding: These authors have no support or funding to report.

Competing Interests: Drs. Jochen Stritzker, Nanhai G. Chen, Ivaylo Gentschev and Aladar A. Szalay are employees of Genelux Corporation and have financial interests in Genelux Corporation. Dr. Barbara Härtl is an employee of Genelux GmbH. Genelux Corporation also provided a Service Grant to the University of Würzburg. Dr. Ulrike Donat and Dr. Stephanie Weibel are recipients of a postdoctoral fellowship. Dr. Julia Sturm and Mr. Michael Hess are recipients of a graduate fellowship from the University of Würzburg. The funders had no role in study design, data collection and analyses, decision to publish, or preparation of the manuscript. There are no patents or products in development or marketed products to declare. This does not alter the authors' adherence to all the PLOS ONE policies on sharing data and materials, as detailed online in the guide for authors.

* E-mail: aaszalay@genelux.com

Introduction

According to current studies, more than 90% of cancer patients die due to direct or indirect effects of metastases. Patient's prognosis is therefore immediately connected to the metastatic stage of the carcinoma [1]. Metastatic tumor cells infiltrate healthy tissues and cross vessel barriers to access lymphatic or blood circulation. The tendency of a tumor cell to enter lymphatic or blood vessels depends on the ability to adhere to specific structures, such as reticular fibers in the subcapsular sinus of a draining lymph node or endothelial cells that line blood vessels [2].

Prostate cancer is known to metastasize to bones, lungs and lymph nodes [3,4]. It represents the second leading cause of cancer-related death in men. Since prostate cancer proceeds asymptomatically, the diagnosis is often made when metastases have already formed. Current treatment strategies for metastases are similar to those used for primary tumors [1]. Treatment of advanced prostate carcinoma is performed via conventional chemo- and radiotherapy. Unfortunately, these treatments often result in the development of resistant tumors and metastases [5,6]. Furthermore, it has been shown that keeping growth of the solid tumor at bay can promote rather than suppress the formation of metastases [7]. Combating both formation and growth of metastases is therefore the key to success in cancer treatment.

Accordingly, oncolytic virotherapy is one of the most promising novel strategies in fighting both: solid tumors and metastases. Oncolytic viruses are able to selectively replicate in cancer cells, resulting in destruction of tumor tissue, but leaving healthy tissues unharmed [8]. In 2007, Zhang *et al.* first described the attenuated recombinant vaccinia virus GLV-1h68 [9,10]. The oncolytic effect of this virus has been shown in breast, pancreatic and prostate tumor xenografts [10–12]. Furthermore, Gentschev *et al.* demon-

strated, in principle, the great therapeutic potential of GLV-1h68 in treating lymph node metastases originating from the prostate carcinoma cell line PC-3 [11].

In this study, we characterized the underlying mechanisms of the virus-mediated reduction of metastases. For a detailed analysis, we first visualized metastatic spread of PC-3 cells in the lymph system of nude mice by inserting the *mRFP1*-gene encoding the red fluorescent protein under control of the CMV promoter into the tumor cell genome. Upon viral injection into PC-3-RFP tumor-bearing mice, we demonstrated that virus treatment dramatically decreased the amount of blood and lymph vessels, which are essential routes for metastatic spread of tumor cells, in tumors as well as in metastases [13,14]. Furthermore, we detected significantly higher virus titers in PC-3 lymph node metastases than in solid tumors and we showed that renal lymph node metastases were colonized to an even higher degree than lumbar ones. To our knowledge, this viral tropism to metastases has, so far, not been described in the literature. Therefore, we set out to analyze mechanisms leading to the preferential viral colonization. In this context, several microenvironmental aspects, such as tumor and metastases vasculature and perfusion, proliferative status and extent of PC-3 cell necrosis, immune cell burden as well as cytokine expression in primary tumors and lymph node metastases were analyzed.

Materials and Methods

Cell Lines

The human prostate carcinoma cell line PC-3 (DSMZ ACC465) was cultured in RPMI 1640 (PAA Laboratories, Cölbe, Germany) supplemented with 10% FCS (PAA Laboratories, Cölbe, Germany) and 1% penicillin-streptomycin solution (PAA Laboratories, Cölbe, Germany). PC-3-RFP cells were cultured under same conditions except for adding 10 µg/ml blasticidin. The African green monkey kidney fibroblast cell line CV-1, obtained from the American Type Culture Collection (ATCC CCL-70), was cultured in DMEM High Glucose (PAA Laboratories, Cölbe, Germany) supplemented with 10% FCS and 1% penicillin-streptomycin solution. Human epithelial kidney cells (293FT) were kindly provided by P. Hill (University of Nottingham, originally obtained from Invitrogen) and cultured in RPMI 1640 supplemented with 10% FCS and 2 mM L-glutamine (PAA Laboratories, Cölbe, Germany).

Generation of PC-3-RFP Cells

The cDNA sequence of the red fluorescent protein (*mRFP1*) was inserted into the PC-3 cell genome using Vira Power^{TM} Lentiviral Expression System Kit (Invitrogen GmbH, Germany) in accordance with the manufacturer's instructions. The *mRFP1*-encoding plasmid pCR-TK-SEL-mRFP was provided by Q. Zhang (Genelux Corporation, San Diego) and used to generate the *mRFP1*-containing lentiviral vectors as described previously [15]. Replication-incompetent *mRFP1*-encoding lentiviruses were produced in 293FT cells by a co-transfection of the plasmids pLP1, pLP2, pLP/VSVG that supply lentiviral structural and replication proteins and the pLENTI6/V5-DEST-mRFP expression plasmid using Lipofectamine^{TM}2000. After transduction of PC-3 cells with mRFP-encoding lentiviruses and blasticidin (10 µg/ml) selection, one stable RFP-expressing PC-3 clone was selected and RFP-expression in >98% of all cells was confirmed by flow cytometry.

Virus Strain

The attenuated vaccinia virus strain GLV-1h68 was constructed as described previously by Zhang *et al.* [10]. Three expression cassettes encoding for *Renilla* luciferase-GFP fusion protein, β-galactosidase, or β-glucuronidase were recombined into the *F14.5L*, *J2R* and *A56R* loci, respectively, of the parental LIVP virus genome. GLV-1h68 was propagated in CV-1 cells and purified through sucrose gradients.

Tumor Implantation and Virus Administration

Tumors were generated by implanting 2×10^6 PC-3 or PC-3-RFP cells in 100 µl PBS subcutaneously into the right abdominal flank of 6–8 weeks old female athymic nude *Foxn1^{nu}* mice (Harlan Winkelmann GmbH, Borchen, Germany). A single dose of 1×10^7 plaque forming units (pfu) GLV-1h68 in 100 µl PBS was injected intravenously (i.v.). For studying the viral colonization of PC-3-RFP metastases, GLV-1h68 was administrated after abdominal lymph node metastases were palpable; usually 45–60 days after PC-3-RFP cell implantation, to mimic the advanced stage of prostate carcinoma. Since the advanced stage of the disease is associated with weight loss independent of viral infection, weight was measured twice a week and mice were sacrificed before standard rates were exceeded. The analyzed treatment periods did not exceed 14 days. After virus injection the health status of the mice did not change.

All animal experiments were approved by the government of Unterfranken, Germany (protocol number AZ 55.2-2531.01-17/08) and/or the Institutional Animal Care and Use Committee (IACUC) of Explora BIOLABS, located in San Diego Science Center (San Diego, USA) (protocol numbers: EB08-003; EB11–25).

Detection of Human PC-3 Cells in Lymph Nodes via RT-PCR

The presence of human PC-3 cells in enlarged lumbar and renal lymph nodes was analyzed by RT-PCR using primers for human β-actin as described previously [11]. A lymph node was defined to be enlarged when the maximal diameter exceeded 2 mm.

Fluorescence Imaging of Tumors and Lymph Node Metastases

Images of GLV-1h68 or PBS treated PC-3-RFP tumor-bearing mice were taken either with the Maestro EX Imaging System (Caliper, Hopkinton, MA, USA) or with a MZ16 FA Stereo-Fluorescence Microscope (Leica, Wetzlar, Germany). For imaging of mice with the Maestro EX Imaging System, animals were anesthetized using 2–3% isoflurane. Digital images were processed with Photoshop 7.0 (Adobe Systems, Mountain View, USA).

Analysis of Viral Titers in Tumors and Metastases

The amount of virus particles in tumor and metastases lysates was determined by standard plaque assays. Therefore, PC-3 tumors and metastases were excised 3, 7 and 14 days after GLV-1h68 injection, minced and 2 volumes of lysis buffer (50 mM Tris-HCl with 2 mM EDTA, pH 7.4) supplemented with 2 mM phenylmethylsulfonyl fluoride and proteinase inhibitor cocktail (Roche Diagnostics GmbH, Penzberg, Germany) were added. Samples were homogenized using a Fastprep Shredder (Thermo Scientific, Karslruhe). After 3 freeze and thaw cycles followed by sonication serial dilutions were titrated on confluent CV-1 cells in 24-well plates. All samples were measured in duplicates.

Immunohistochemistry

For histology, tumors and metastases were excised and fixed for 16 h in 4% paraformaldehyde/PBS, pH 7.4. Preparation of 100 µm sections and labeling procedures were performed as

described previously [16] using the Leica VT1000 Vibratom (Leica, Heerbrugg, Switzerland). After labeling, tissue sections were mounted in Mowiol 4–88 (Sigma-Aldrich, Taufkirchen, Germany). Tissue samples were sectioned (10 µm thickness) with the cryostat 2800 Frigocut (Leica, Wetzlar, Germany). After dehydration in 10% and 30% sucrose (Carl Roth, Karlsruhe, Germany) specimens were embedded in Tissue-Tek® O.C.T. (Sakura Finetek Europe B.V., Alphen aan den Rijn, Netherlands). Cryosections were stored at −80°C and incubated with primary antibodies for 1 h. After washing with PBS, sections were stained for 1 h with secondary antibodies and finally mounted in Mowiol 4–88.

Antibodies and Reagents

Endothelial blood vessels were stained with a hamster monoclonal anti-CD31 antibody (Chemicon International, Temecula, USA; MAB1398Z) and endothelial lymph vessels with a rabbit polyclonal anti-LYVE-1 antibody (Abcam, Cambridge, UK; ab14917). Non-specific rat-IgG (Jackson Immunoresearch, Pennsylvania, USA; 01200003) was used to analyze the permeability of blood vessels in PC-3-RFP tumors and metastases. Therefore, 10 mg/kg rat-IgG were injected intravenously (i.v.) into PC-3-RFP tumor-bearing mice. Six hours post injection mice were sacrificed and 100 µm sections of tumors and metastases were prepared. Labeling of antigen presenting cells was performed with a monoclonal rat anti-MHC Class II (I-A/I-E) antibody (eBioscience, San Diego, USA; 14–5321). B cells were stained with a rat monoclonal anti-CD19 antibody (Abcam, Cambridge, UK; ab25232), macrophages with a rat monoclonal anti-CD68 antibody (Abcam, Cambridge, UK, ab53444). The proliferation marker Ki-67 was labeled with a rabbit polyclonal anti-Ki-67 antibody (Abcam, Cambridge, UK; ab15580). For analyzing BrdU incorporation into the DNA of PC-3-RFP cells in tumors and metastases, 120 mg/kg BrdU were injected intraperitoneally (i.p.). Three hours later, tumors and metastases were excised and 10 µm sections were prepared. Labeling was performed using rat monoclonal anti-BrdU antibody (Abcam, Cambridge, UK; ab6326) after 30 min incubation with 2 M HCl and washing in PBS. Nuclei were Hoechst 33342-labeled (Sigma Aldrich, Taufkirchen, Germany). DyLight488-, DyLight549- and DyLight 649-conjugated secondary antibodies (donkey) were obtained from Jackson ImmunoResearch (Pennsylvania, USA). All primary and secondary antibodies were diluted 1:100 in PBS in the case of 10 µm sections or in PBS/0.3% Triton-X-100 in the case of 100 µm sections.

Fluorescence Microscopy

Microscopic studies were used to compare tumor vasculature, cell proliferation status and specific immune cell populations of tumors as well as of metastases. To examine the fluorescence-labeled tumor and metastasis sections, the following microscopes were used: A stereo-fluorescence microscope MZ16 FA (Leica) equipped with a digital CCD camera and the Leica IM1000 4.0 software (1300×1030 pixel RGB-color images), a TCS SP2 AOBS confocal laser microscope (Leica) equipped with the LCS 2.16 software (1024×1024 pixel RGB-color images) and a Axiovert 200 M microscope (Zeiss) with Axiovision 4.5 software (1388×1040 pixel gray scale images). Digital images were processed with Photoshop 7.0 (Adobe Systems, USA) and merged to yield pseudo-colored pictures.

Analyses of Digital Fluorescence Images

For analyses of digital images of tumor, LN and RN sections, it is important to note that there was one tumor per mouse, but the number of lumbar and renal lymph node metastases differed from mouse to mouse. In most cases 2 LNs and 2 RNs were present per mouse. Per tumor or metastasis images of 2 sections were analyzed, whereby data obtained from all lumbar lymph node metastases were merged to LN and data obtained from all renal lymph nodes were merged to RN.

Measurement of lymph and blood vessel density. Lymph and blood vessel density was measured in digital images (×80 and ×100 magnification) of anti-LYVE-1 and anti-CD31 stained 100 µm sections. Eight images per tumor, LN and RN were analyzed per staining. Exposure time for individual images was adjusted to ensure clear visibility of all detectable blood and lymph vessels and decorated with 8 equidistant horizontal lines using Photoshop 7.0. All lymph or blood vessels crossing these lines were counted to obtain the vessel density per section.

Measurement of blood vessel diameters. Blood vessel diameter measurement was performed using digital images (×100 magnification) of 100 µm sections stained with anti-CD31 using Leica IM1000 4.0 software. Images of tumors and lymph node metastases were obtained with individual exposure times to get optimal CD31 signals and exclude signal-dependent variability of vessel diameter. Individual images were overlaid with three equidistant horizontal lines and the diameters of all blood vessels crossing these lines were measured. Blood vessel diameters were determined in 4 images per tumor, LN and RN.

Quantification of section labeling. To quantify the permeability of blood vessels, digital images (×160 magnification) of 100 µm histology sections of tumors and metastases were analyzed. The total area positive for IgG (labeled with anti-rat-DyLight488) was determined in 16 different regions per sample. The amount of necrotic tissue in PC-3 tumors or metastases was determined in digital images of 100 µm sections. Nuclei were labeled with Hoechst 33342. The fraction of a section not stained by Hoechst due to nuclei degradation was defined as necrotic area. In this case, images of 2 whole sections per sample were analyzed. The amount of MHC-II, CD19 and CD68 positive cells in PC-3 tumors and metastases was measured in digital images of 10 µm sections. Two whole section images per sample were analyzed. Analyses of the amount of IgG, necrotic tissue and MHC-II-, CD19- and CD68-positive cells in digital images were performed using ImageJ software (http://rsbweb.nih.gov/ij) after converting RGB-images into 8-bit gray scale images using Photoshop 7.0.

Measurement of fluorescence intensity. Measurement of the CD31 and Ki-67 intensity was done in digital images of 100 µm and 10 µm sections of PC-3 tumors and metastases. For each staining, 8 different images per sample were acquired with identical settings. RGB-images were converted into 8-bit gray scale with an intensity range from 0–255. The fluorescence intensity of CD31 and Ki-67 stainings represents the average brightness of all staining related pixels and was measured using ImageJ. Images of CD31 staining were taken at 100x, images of Ki-67 at 400x magnification.

Protein Isolation and Characterization

Protein lysates of PC-3-RFP tumors, lumbar and renal lymph node metastases of 3 mice 49 days after tumor cell implantation were analyzed with an immune-related protein antigen profiling (RodentMAP® v2.0, Rules Based Medicine, Austin, USA) using antibody linked beads. Lysates were performed as described previously [11]. Results were normalized based on total protein concentration.

Statistical Analysis

A two-tailed Student's *t* test was used for statistical analysis. *P* values of ≤ 0.05 were considered statistically significant. Asterisks indicate a significant difference between experimental groups (* indicates $p \leq 0.05$; ** indicates $p \leq 0.01$; *** indicates $p \leq 0.001$).

Results

Visualization of the Metastatic Spread of PC-3-RFP Tumor Cells via the Lymphatic System in Nude Mice

To analyze the metastatic spread of PC-3 cells within nude mice, it was necessary to establish primary tumors by implanting 2×10^6 RFP-expressing PC-3 cells subcutaneously into the right flank of nude mice. About 70 days after implantation we visualized metastasized tumor cells in lumbar (LN) and renal (RN) lymph nodes in living PC-3-RFP tumor-bearing mice (Figure 1a). Besides detection in lumbar and renal lymph nodes, PC-3-RFP cells were also visualized in vessels connecting the lymph node pairs (Figure 1b). To figure out whether these vessels are lymphatic or blood vessels immunohistological stainings were performed. Labeling of LYVE-1 (lymphatic marker) and CD31 (blood vessel marker) in tissue sections clearly revealed a lymphatic origin of these tumor cell-containing vessel-like structures (Figure 1c).

Taken together, we visualized the metastatic spread of PC-3-RFP tumor cells from the defined primary tumor site at the right flank to regional lumbar and distant renal lymph nodes in nude mice.

Additionally, a time-based correlation between the formation of lymph node metastases and the density of lymph vessels in the corresponding PC-3 tumors was shown. Over time, a continuous increment of lymph nodes positive for metastasized PC-3 cells was observed (Figure 1d). Simultaneously, lymph vessel density in PC-3 tumors increased (Figure 1e) indicating coherence between the amount of lymph vessels in solid tumors and lymph node metastases formation.

GLV-1h68 Treatment Dramatically Decreases the Blood and Lymph Vessel Density in PC-3-RFP Tumors and Metastases

Recently, it has been shown that GLV-1h68 treatment of PC-3 tumor-bearing mice results in a significant reduction of lymph node metastases [11]. Additionally, we showed that GLV-1h68 is also an efficient agent in treating PC-3 lung metastases, which mainly arose by metastatic spread of PC-3 cells via the hematogenous route (Figure S1). To understand the therapeutic potential of GLV-1h68, we analyzed the effect of viral treatment on tumor-associated blood and lymph vessels since those play an essential role as routes for metastatic spread to distant organs and lymph nodes [13,14].

For CD31-positive blood as well as for LYVE-1-positive lymph vessels a significant reduction of the vessel density in PC-3 tumors, LNs, and RNs was observed due to intravenous (i.v.) injection of GLV-1h68 (Figure 2). Blood vessel density measurements revealed a reduction of the density by 46% in tumors and LNs and by 60% in RNs in vaccinia virus-injected mice, respectively (Figure 2a and b). Similar results were obtained for the lymph vessel density (Figure 2c and d) indicating that the effect of GLV-1h68 was strongest in renal lymph node metastases.

In summary, the results clearly indicate that oncolytic tumor tissue destruction in PC-3 tumors and metastases is significantly enhanced by eradication of tumor vasculature as well as lymphatic vessels.

Preferential Colonization of Lymph Node Metastases Compared to Primary PC-3 Tumors by GLV-1h68

Since we have observed a stronger reduction of blood and lymph vessel densities in renal lymph node metastases in comparison to primary tumors, we set out to investigate viral colonization patterns of primary tumors, LNs and RNs. To achieve this goal, PC-3-RFP tumor-bearing mice were injected i.v. with 1×10^7 plaque forming units (pfu) GLV-1h68. To mimic the situation of advanced-stage cancer patients and to ensure the presence of metastases in lymph nodes we injected vaccinia virus in the final stage of the disease 55 days post tumor cell implantation. Multispectral imaging of tumors and metastases revealed clear GFP signals in tumors, LNs and RNs already 3 days post virus injection (dpi). Surprisingly, the GFP intensity was the highest in RNs, followed by LNs and then solid tumors (Figure 3a). Based on these findings we assume a more efficient colonization of lymph node metastases by GLV-1h68 compared to primary PC-3 tumors.

For further analysis, viral colonization patterns for tumors, LNs and RNs were studied in a time course at day 3, 7 and 14 after virus injection by plaque assays. Indeed, it was shown that there were significantly higher viral titers in lymph node metastases compared to primary PC-3-RFP tumors at all three time points (Figure 3b). Interestingly, at 3 and 7 dpi RNs were colonized in a higher degree than LNs. At day 7 post virus injection 1.4×10^9 pfu of GLV-1h68 per gram tissue were determined in RNs. In contrast, only 28% of RN virus concentration was detected in LNs and as little as 2% in primary tumors. After two weeks, the initial differences in viral titers between LNs and RNs were no longer detectable.

Additionally, microscopic analysis of PC-3-RFP tumor and metastases sections revealed, as expected from higher viral titers, also higher GFP signals in metastases in contrast to solid tumors 7 days post GLV-1h68 injection (Figure 3c). Furthermore, we showed that the preferential colonization of metastases compared to solid tumors by GLV-1h68 is not restricted to lumbar and renal lymph node metastases. Higher GFP signals and viral titers were also observed in inguinal (IN) and sciatic (SN) lymph node metastases (Figure S2). In addition, the investigation of a different route of virus injection revealed similar GLV-1h68 colonization patterns 7 days after intra tumoral (i.t.) injection (Figure S3).

Taken together, these results indicated a highly selective colonization of metastases by GLV-1h68 when compared to primary tumors.

Analysis of Microenvironmental Factors in Primary Tumors and Metastases Necessary for Enhanced Viral Concentrations in Lymph Node Metastases

To find reasons for the enhanced viral colonization of lymph node metastases, we analyzed the status of PC-3 tumors and metastases before vaccinia virus injection occurred. Various differences in the microenvironment of tumors and metastases that might be crucial for the virus to colonize metastases in a higher degree than tumors had been considered. Therefore, vasculature, proliferative status of PC-3 cells, extent of necrosis, immune cells and cytokine expression in tumors, LNs and RNs were analyzed in uninfected PC-3-RFP tumor-bearing mice. To mimic the situation of advanced-stage cancer patients when diagnosis of cancer usually occurs, we analyzed microenvironmental parameters in the final stage of the disease between 45–60 days post tumor cell implantation.

Increased vascular permeability in lymph node metastases. First of all, we analyzed whether differences occur

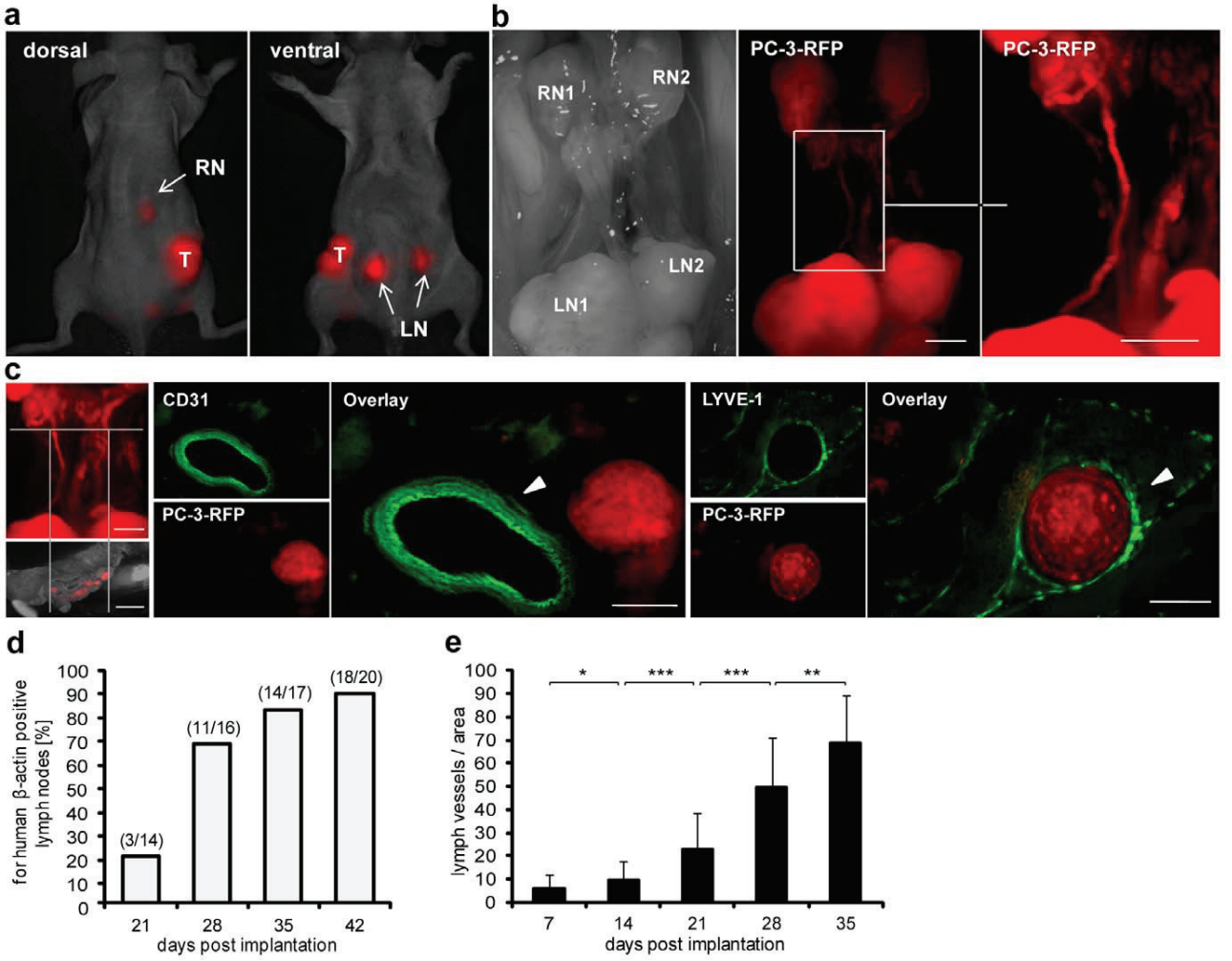

Figure 1. Metastatic spread and correlation between metastases formation and tumor lymph vessel density. 2×10^6 PC-3 or PC-3-RFP cells were implanted into the right flank of nude mice. (a) Real time imaging of a living nude mouse bearing a PC-3-RFP tumor 70 days post implantation, dorsal and ventral view. T, tumor; LN, lumbar lymph node metastases; RN, renal lymph node metastases. (b) Lumbar (LN1, LN2) and renal (RN1, RN2) lymph node metastases in the abdomen of a PC-3-RFP solid tumor-bearing mouse 65 days post implantation. Right picture: migration of PC-3-RFP cells between LN and RN. (c) 100 μm cross sections of the part between LNs and RNs stained with anti-CD31 and anti-LYVE-1 antibody, respectively. (d) For human β-actin positive lymph nodes 21, 28, 35 and 42 days post implantation of PC-3 cells and (e) density of lymph vessels in corresponding primary PC-3 tumors. Tumors, lumbar and renal lymph nodes of 4 mice were analyzed per time point. To determine the lymph vessel density, 100 μm sections of PC-3 tumors were prepared and 2 sections were stained with anti-LYVE-1 antibody. Four images (x 80 magnification) per section were analyzed as described in material and methods. Scale bars represent 2 mm (b and left picture c) and 200 μm (right pictures c). All images are representative examples.
doi:10.1371/journal.pone.0045942.g001

in the vasculature regarding density and permeability of vessels between tumors and metastases, leading to a higher initial amount of viral particles within the different tumor tissues. Histology of PC-3-RFP tumors, LNs and RNs was performed and blood vessels were labeled with CD31. Although, no differences in blood vessel density between tumors and metastases were observed 57 days post tumor cell implantation (Figure 2a PBS group), the fluorescence intensity of the CD31 staining was significantly higher in LNs and RNs in comparison to solid tumors (Figure 4a). In general, the blood vessel marker CD31 is highly up-regulated on endothelial cells in inflamed tissues or at sites of ongoing leukocyte transmigration and is associated with higher vascular permeability [17]. Therefore, a detailed microscopic study of blood vessels concerning vessel diameter and vascular permeability in tumors compared to those in metastases was performed. Significantly, LNs and RNs revealed higher blood vessel diameters (mean diameter 15 μm) than solid PC-3-RFP tumors (mean diameter 10 μm) (Figure 4b). To find out whether these dilated blood vessels indeed contribute to higher vascular permeability in lymph node metastases, the extravasation patterns of intravenously injected rat-IgGs were analyzed histologically. Interestingly, significant higher amounts of extravasated IgG were detected in metastases (mean IgG-positive area about 60%) compared to tumors (mean IgG-positive area 25%). However, no significant differences of blood vessel permeability between LNs and RNs were observed (Figure 4c).

These results indicate that the enhanced vascular permeability may result in an increased initial number of viral particles in metastases compared to primary tumors.

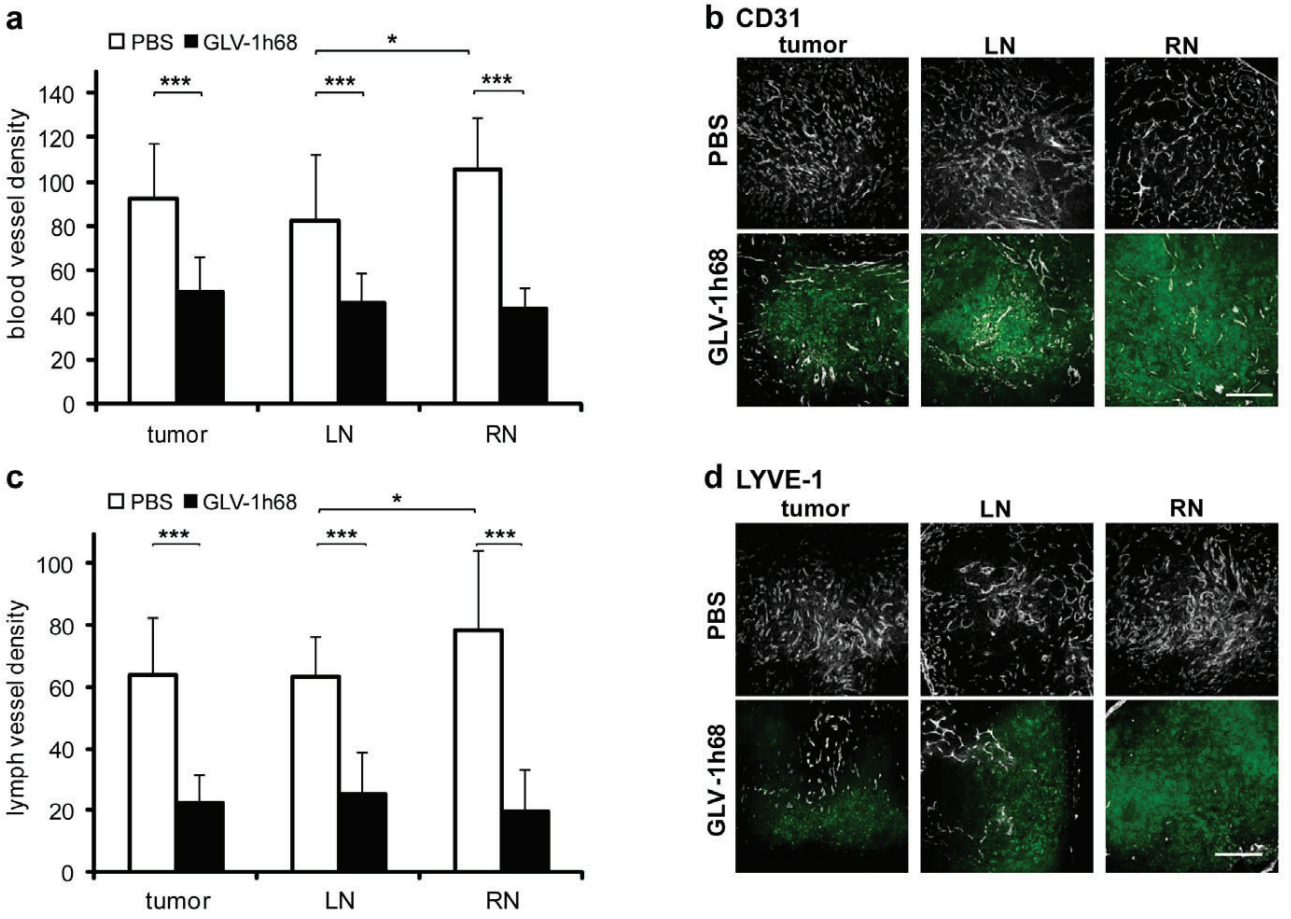

Figure 2. Blood and lymph vessel density in PC-3 tumors and lymph node metastases. Analysis was performed 57 days after implantation of 2×10^6 PC-3 cells and 7 days after injection of 1×10^7 pfu GLV-1h68. To determine blood and lymph vessel density, 100 μm sections of tumors, LNs and RNs of 5 PBS- and 5 GLV-1h68-treated mice were stained with anti-CD31 or anti-LYVE-1 antibody. Blood and lymph vessels were counted in 4 images (×100 magnification) from each of 2 sections per sample. (a) Blood vessel density in PC-3 tumors/metastases and (b) representative images of anti-CD31 stained sections. Blood vessels are shown in grayscale, by GLV-1h68 expressed GFP in green. (c) Lymph vessel density in PC-3 tumors/metastases and (d) representative images of anti-LYVE-1 stained sections. Lymph vessels are shown in grayscale, by GLV-1h68 expressed GFP in green. Scale bars represent 500 μm.
doi:10.1371/journal.pone.0045942.g002

Metastases exhibited an increased proliferation index and lowered necrosis. Since expression of thymidine kinase (TK) positively correlates with the rate of cell proliferation [18] and vaccinia virus replication depends on cellular TK levels [19], the proliferation status of PC-3 cells could directly influence viral replication. For this reason we determined and compared the proliferation index of PC-3-RFP cells in tumors, LNs and RNs by Ki-67 and BrdU assays. Interestingly, we found that the fluorescence intensity of the Ki-67 staining was significantly higher in lymph node metastases than in solid tumors (Figure 5a). Also, marked differences were observed between RNs and LNs, whereby RNs showed distinctly higher Ki-67 fluorescence intensity than LNs.

In addition, we injected BrdU i.p. which ultimately entered the tumors and metastases via the blood vessels. As shown above, there was a significant higher permeability of blood vessels in lymph node metastases compared to the tumor. Therefore, we analyzed and compared only LNs and RNs, due to the general higher perfusion with BrdU in metastases than in tumors. As shown in Figure 5b, a significant higher number of BrdU positive cells was observed in RNs (73+/−15 BrdU-positive cells/area) than in LNs (48+/−26 BrdU-positive cells/area). Furthermore, analysis of necrosis revealed that the area of necrotic tissue was significantly smaller in LNs and RNs than in solid PC-3-RFP tumors (Figure 5c). Approximately 23% of the tumor tissue was necrotic, in contrast to 9% of the LN and 13% of the RN tissue, respectively. However, no significant differences were detected between LNs and RNs.

Thus, a higher proliferation status of PC-3-RFP cells in metastases along with lower levels of necrosis seemed to be favorable for viral replication and dissemination.

High density of MHC-II, CD19 and CD68 positive cells in lymph node metastases. Lymph nodes represent a target structure for metastasizing prostate cancer cells. Since lymph nodes are essential organs of the immune system where antigen presentation as well as B cell activation and proliferation takes place [20], three antigen presenting immune cell populations were analyzed in lymph node metastases and compared to primary tumors: MHCII- (as monocyte, macrophage, DCs and B cell marker), CD19- (as a B cell marker) and CD68- (as a macrophage marker) positive cells. The MHC-II staining revealed an increased density of antigen presenting cells in RNs compared to LNs and

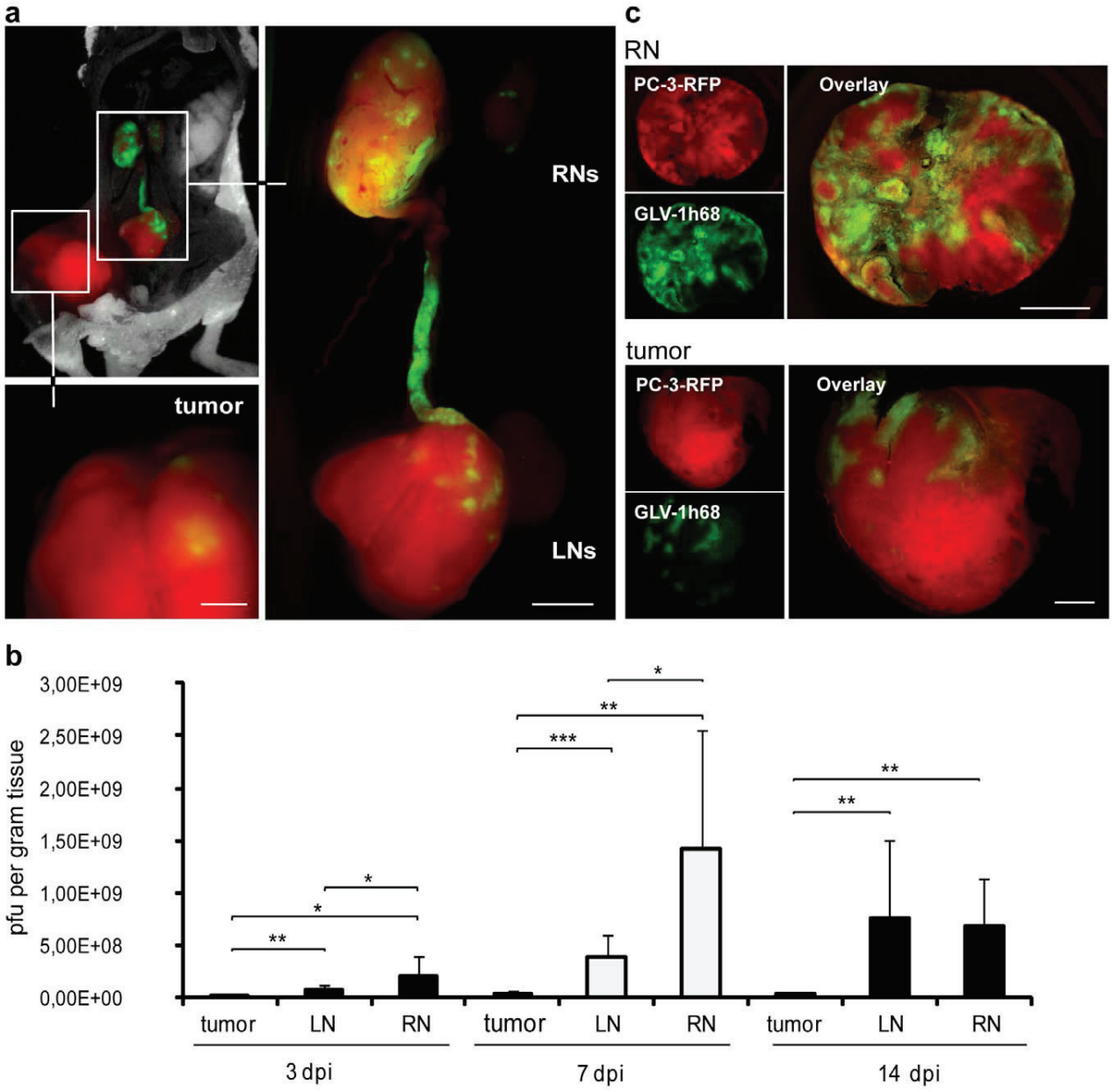

Figure 3. Colonization of lymph node metastases and PC-3-RFP tumors by GLV-1h68. 1×10^7 pfu GLV-1h68 were i.v. injected into PC-3-RFP tumor-bearing mice. (a) PC-3-RFP tumor-bearing mouse 3 days after injection of GLV-1h68. (b) Virus titers in PC-3-RFP tumors, LNs and RNs 3, 7 and 14 days after injection of GLV-1h68. Virus injection was performed 55 days post tumor cell implantation. Tumors and lymph node metastases of 6 mice were analyzed per group (n = 6). (c) 100 µm sections of a PC-3-RFP tumor and a renal lymph node metastasis 77 days post implantation and 7 days after virus injection. PC-3-RFP cells are shown in red, by GLV-1h68 expressed GFP in green. All images are representative examples. Scale bars represent 1 mm (b) and 2 mm (c).
doi:10.1371/journal.pone.0045942.g003

solid tumors (Figure 6a). Furthermore, quantifying MHC-II, CD19 and CD68 stainings resulted in significant increases from tumors to LNs and to RNs in all three cases (Figure 6b, c and d).

In conclusion, we found that the further the distance of a lymph node metastasis from the solid tumor the higher the density of MHC-II-, CD19- and CD68-positive cells in the tissues.

Pro-inflammatory signature in lymph node metastases. To analyze the influence of the increased amount of immune cells in metastases, we studied biomarker expression in PC-3-RFP lymph node metastases and in primary tumors of 3 individual mice 49 days after tumor cell implantation using a mouse immune-related protein antigen profiling. Altogether 58 biomarkers were analyzed. We did not observe differences in the cytokine profile of LNs and RNs. Therefore, the data of both were merged und compared to data obtained from primary tumors. The profiling revealed in lymph node metastases a significant ($p<0.05$) up-regulation of 20 biomarkers, amongst others, a variety of pro-inflammatory cytokines (Table 1) compared to solid tumors. Significant higher levels of chemokines which attract macrophages, neutrophils and dendritic cells, such as IP-10,

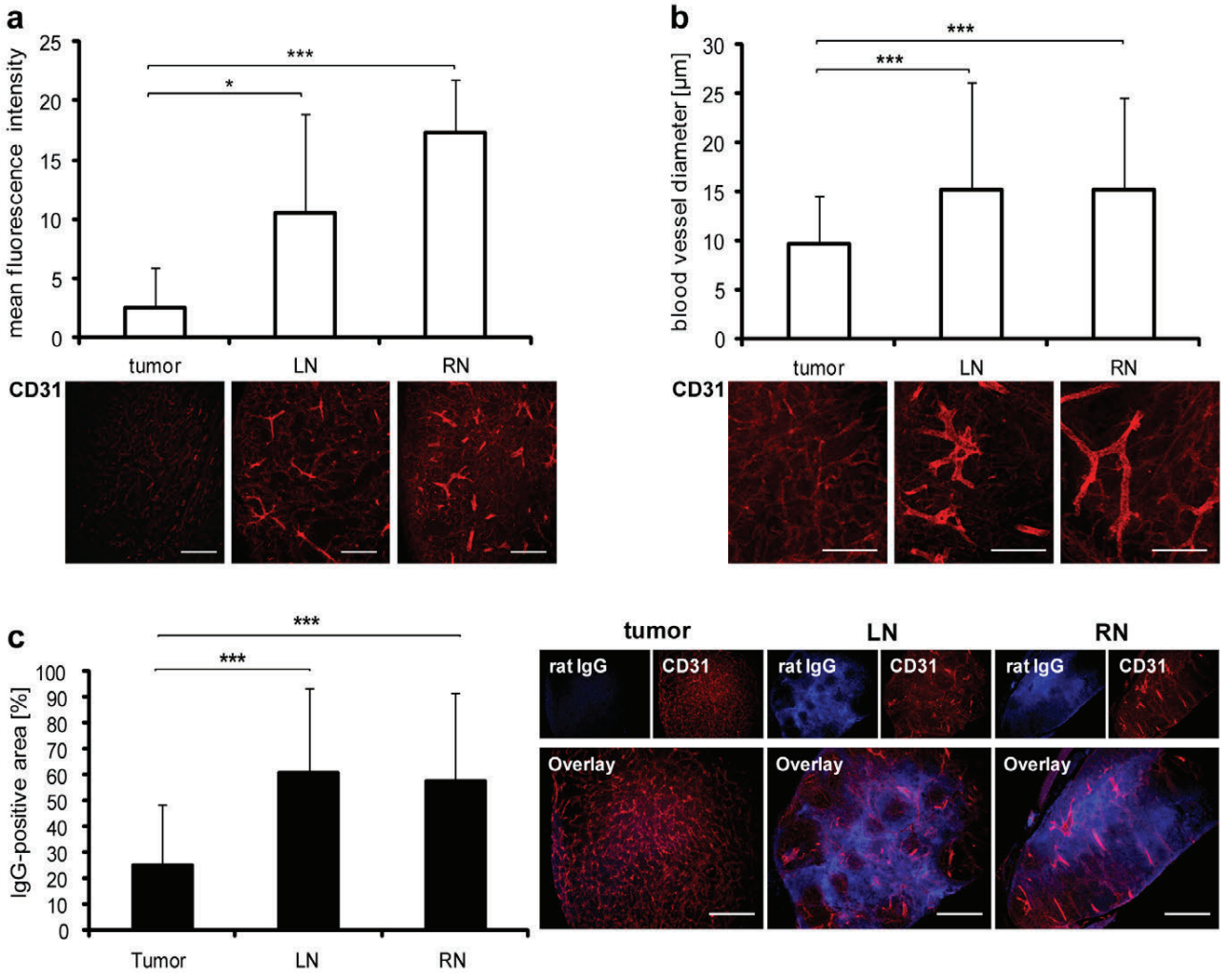

Figure 4. Blood vessels in PC-3-RFP tumors and lymph node metastases. PC-3-tumors, LNs and RNs were excised, cut in 100 µm sections and stained with anti-CD31 antibody. (a) Mean fluorescence intensity of CD31 staining in tumor, LN and RN sections of 5 mice 57 days post tumor cell implantation. The fluorescence signals of 4 images (×100 magnification) from each of 2 sections per sample were measured using ImageJ. (b) Diameter of blood vessels in PC-3 tumors, LNs and RNs of 6 mice 47 days post implantation. Measurement was performed in 2 images (×100 magnification) from each of 2 sections per sample using Leica IM1000 4.0 software. (c) Extravasation of unspecific rat IgGs in PC-3 tumors, LNs and RNs 47 days post implantation. 6 Mice were injected with 10 mg/kg rat IgGs 6 h before tumors, LNs and RNs were excised and histology performed. Extravasated IgG was visualized with Cy2-conjugated anti-rat antibody. Areas positive for IgG were measured in 8 images (×160 magnification) from each of 2 sections per sample using ImageJ. All images are representative examples. Scale bars represent 500 µm (a, c) and 250 µm (b).
doi:10.1371/journal.pone.0045942.g004

MDC, MCP-1 and MCP-3 were detected in metastases. Furthermore, chemokines secreted by macrophages, like GCP-2, MIP-1 beta, MIP-2 and MIP-3 beta and growth factors promoting macrophage proliferation, such as GM-CSF and M-CSF-1, were found to be up-regulated in metastases compared to primary tumors. These data indicate that macrophages might play an important role in infection and replication of the vaccinia virus GLV-1h68 in lymph node metastases. Thus, lymph node metastases are characterized by a pro-inflammatory microenvironment, which might promote tumor cell proliferation and virus replication due to increased secretion of cell growth stimulating cytokines.

Taken together, the presented data strengthened the following tendency: The further the distance of a lymph node metastasis to the solid tumor, the higher the tissue proliferation status and the higher the immune cell burden. Importantly, lymph node metastases showed significantly higher vascular permeability and pro-inflammatory signatures. All of the analyzed microenvironmental parameters positively correlate with increased viral titers and therefore may provide an explanation for the previously observed reduction of metastases in oncolytic vaccinia virus-treated tumor-bearing animals [11].

Discussion

Metastatic carcinomas represent a major health problem. Therefore, it is crucial to find effective strategies in treating metastases. We focused our study on the formation and microenvironment of lymph node metastases, especially the elucidation of conditions that might lead to efficient colonization with and subsequent eradication of metastases by the oncolytic vaccinia virus strain GLV-1h68.

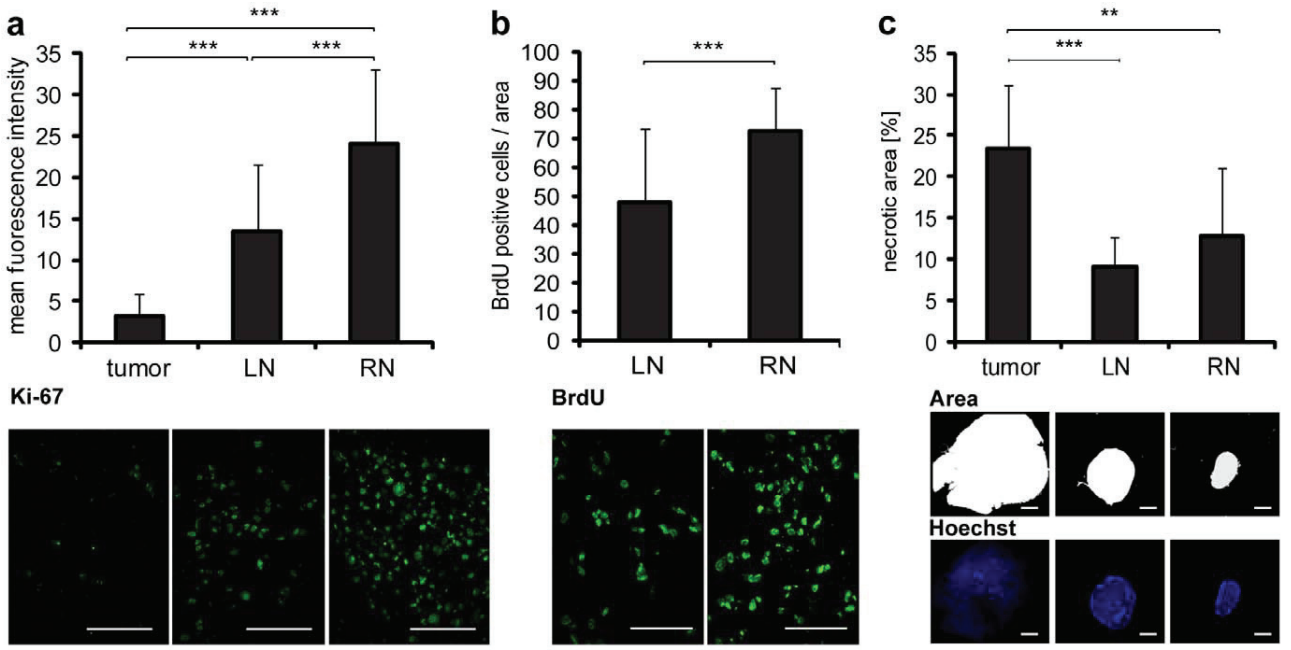

Figure 5. Proliferation status of cells in PC-3 tumors and lymph node metastases. (a, b) PC-3-RFP tumors, LNs and RNs were excised 50 days post tumor cell implantation. 10 μm cryosections were prepared and stained with anti-Ki-67 and anti-BrdU antibodies. (a) Mean fluorescence intensity of Ki-67 staining in tumor, LN and RN sections isolated from 8 mice. The fluorescence signals of 4 images (×400 magnification) from each of 2 sections per sample were measured using ImageJ. (b) Number of BrdU positive cells in LN and RN sections. 8 mice were intraperitoneally injected with 120 mg/kg BrdU 3 h before LNs and RNs were excised. BrdU positive cells were counted in 4 images (×400 magnification) from each of 2 sections per sample. (c) Amount of necrotic tissue in PC-3 tumors and metastases 57 days post implantation. 100 μm sections of tumors, LNs and RNs of 5 mice were stained with Hoechst to label the nuclei. The fluorescence signals in whole section images (×10 magnification) were analyzed. Two sections were measured per sample. The area of a section that was not stained by Hoechst, due to nuclei degradation, was defined as necrotic and measured using ImageJ. All images are representative examples. Scale bars represent 50 μm (a, b) and 2 mm (c).
doi:10.1371/journal.pone.0045942.g005

By inserting the cDNA encoding for *mRFP1* into the PC-3 genome, we generated a simple optical method to visualize metastatic spreading of tumor cells within the vasculature especially in the lymph system of mice. PC-3-RFP cells were detected in lymph nodes as well as in connecting lymph vessels. Although, we were not able to visualize PC-3 cells directly exiting primary tumors and subsequent their migration into lumbar lymph nodes, we hypothesize that this also takes place within lymph vessels. This notion was supported by the observed positive correlation between the lymph vessel density in primary PC-3 tumors and the formation of metastases in lymph nodes.

We described previously that GLV-1h68 showed a significant therapeutic effect on PC-3 lymph node metastases [11]. However, underlying mechanisms of the virus-mediated reduction of metastases are still unknown. Therefore, we set out to investigate microenvironmental parameters contributing to metastases eradication. Interestingly, the analyses of tumor-associated blood and lymph vessels, which are known to be crucial for tumor growth and metastases formation [13,14], revealed a drastic decrease in the density of both vessel types in PC-3-RFP tumors as well as in metastases upon virus treatment. The decrease of vessel density may eventually lead to a reduction of nutrient and oxygen supply, which in turn may have additive effects on the primary oncolytic tumor tissue destruction by GLV-1h68. Furthermore, migration of PC-3 cells may be limited due to the virus-dependent reduction of essential routes of the metastatic spreading finally leading to fewer metastases. The underlying mechanism of the virus-mediated vessel destruction is so far not resolved. A direct infection of endothelial cells of blood vessels by vaccinia virus leading to vascular collapse is described in the literature [21]. However, we were not able to visualize either infected blood vessels nor infected lymph vessels. It is further suggested that vaccinia virus infection causes massive neutrophil infiltration, resulting in intravascular thrombosis and vessel degradation [22]. We described previously that GLV-1h68 infection induces a strong pro-inflammatory response in tumorous tissues [11,23]. Furthermore, the strong oncolysis which results in massive tumor cell destruction in tumors and metastases [15] might lead to unfavorable conditions for endothelial cells of blood and lymph vessels, resulting in vessel destruction. In general, methods to inhibit angiogenesis as well as lymphangiogenesis and thereby reducing blood and lymph vessel density are frequently applied to cure cancer and metastases [24,25]. Data presented in this study suggest that GLV-1h68-treatment simultaneously fulfills both desired approaches in the PC-3 tumor model.

Since the virus-mediated reduction of blood and lymph vessel density was most efficient in renal lymph node metastases, we analyzed colonization patterns of GLV-1h68 in primary PC-3-RFP tumors and in lymph node metastases. Indeed we observed 10–70-fold higher viral titers per gram tissue in lymph node metastases compared to primary tumors at all time points analyzed. These findings might explain both: the stronger reduction of blood and lymph vessel density as well as the stronger oncolytic effect of GLV-1h68 in lymph node metastases. Since analysis was done in the advanced stage of PC-3 carcinoma, it was not possible to analyze time points exceeding 14 days post virus injection. In previous studies from Gentschev *et al.* low titers GLV-1h68 ($2.93\times10^3\pm1.9\times10^3$ pfu/gram) have been detected in

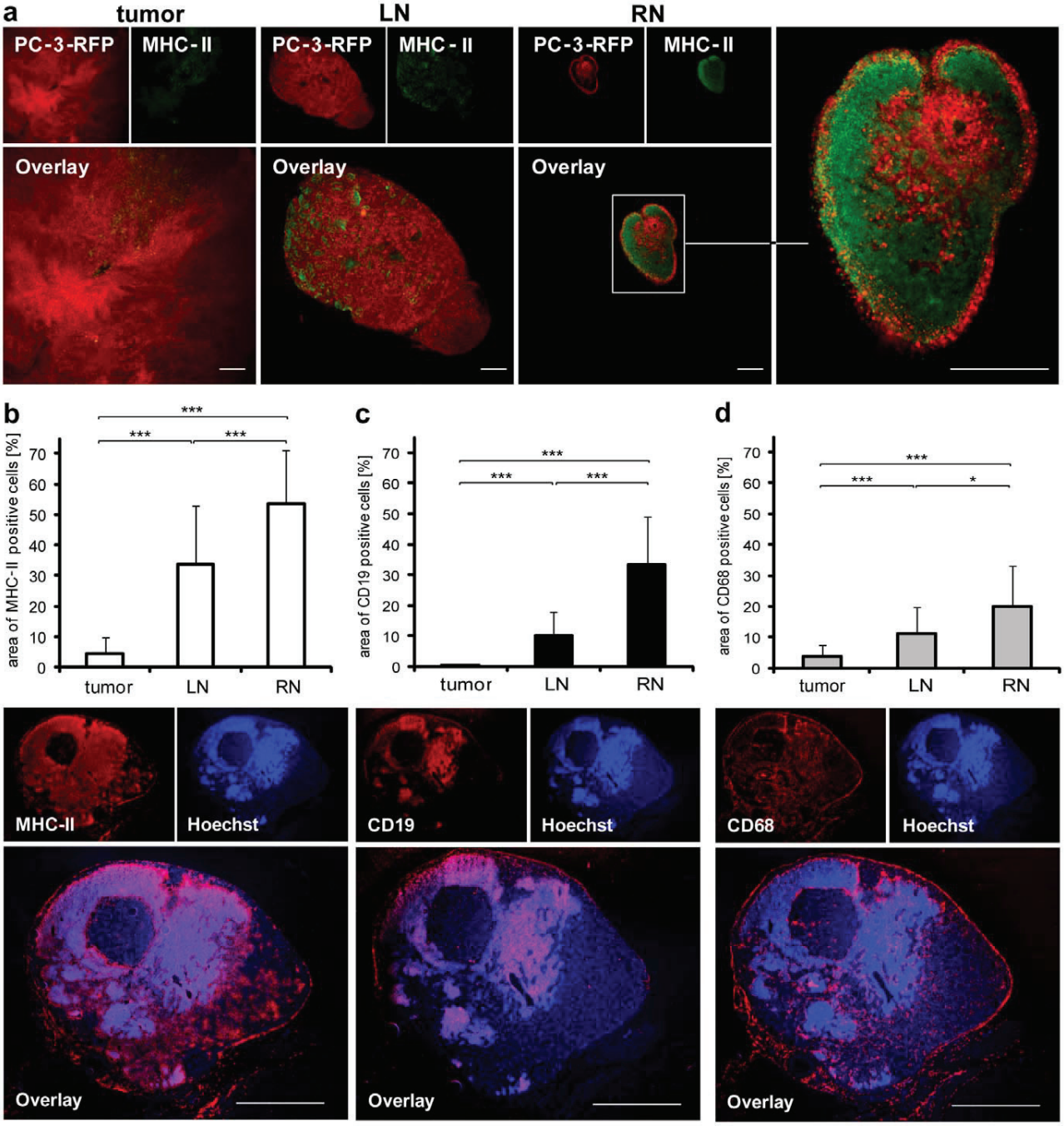

Figure 6. MHC-II-, CD19- and CD68-positive cells in PC-3 tumors and lymph node metastases. (a) Staining of 100 μm PC-3-RFP tumor, LN and RN sections with anti-MHC-II antibody 47 days post tumor cell implantation. (b, c, d) Amount of MHC-II-, CD19- and CD68-positive cells in PC-3-RFP tumors, LNs and RNs. 10 μm cryosections of tumors, LNs and RNs of 8 mice 50 days post implantation were stained with anti-MHC-II, anti-CD19 and anti-CD68 antibody, respectively. Images of whole sections were taken and the area of a section positive for MHC-II, CD19 or CD68 cells was measured using ImageJ. Two sections were analyzed per sample. Below the diagrams are representative images of cryosections of a renal lymph node metastasis stained for MHC-II, CD19 and CD68. Scale bars represent 500 μm (a) and 1 mm (b, c, d).
doi:10.1371/journal.pone.0045942.g006

lymph nodes of PC-3 tumor bearing mice 42 days after virus injection, which means that most of the cancer cells in the lymph nodes have probably been eradicated 6 weeks after virus injection [11].

Taken together, we observed a preferential colonization of metastases by GLV-1h68. Furthermore, based on the data in Figure 3b we found that the larger the distance of a lymph node metastasis from the solid tumor the higher the concentration of GLV-1h68 in the metastasis.

Consequently, we set out to analyze reasons for this metastatic tropism of GLV-1h68. We therefore studied different parameters such as vasculature, proliferative status of PC-3 cells as well as

Table 1. Biomarker patterns in PC-3 tumors and lymph node metastases.

Biomarker	Concentration +/− SD in tumors [pg/mg]	Concentration +/− SD in metastases [pg/mg]	p-value	Ratio: metastases/tumor	Classification
Granulocyte Chemotactic Protein-2 Mouse (GCP-2 Mouse)	89.63+/−15.06	564.15+/−240.26	0.0216	6.29	Proinflammatory cytokine
Granulocyte-Macrophage Colony-Stimulating Factor (GM-CSF)	1.23+/−0,38	2.34+/−0,69	0.0086	1.90	Proinflammatory cytokine
Interferon gamma-Induced Protein-10 (IP-10)	12.62+/−2.90	17.32+/−8.13	0.0209	1.37	Proinflammatory cytokine
Macrophage Colony-Stimulating Factor-1 (M-CSF-1)	231.57+/−41.87	360.61+/−9.53	0.0205	1.56	Proinflammatory cytokine
Macrophage Inflammatory Protein-1 beta (MIP-1 beta)	70.39+/−15.01	108.3+/−145.0	0.0399	1.54	Proinflammatory cytokine
Macrophage Inflammatory Protein-2 (MIP-2)	8.58+/−0.633	11.40+/−7.89	0.0351	1.33	Proinflammatory cytokine
Macrophage Inflammatory Protein-3 beta (MIP-3 beta)	138.81+/−36.63	1766.5+/−915.7	0.0430	12.73	Proinflammatory cytokine
Macrophage-Derived Chemokine (MDC)	11.27+/−2.651	63.60+/−32.83	0.0177	5.64	Proinflammatory cytokine
Monocyte Chemotactic Protein 1 (MCP-1)	61.37+/−13.53	78.43+/−27.53	0.0340	1.28	Proinflammatory cytokine
Monocyte Chemotactic Protein 3 (MCP-3)	55.44+/−13.67	67.96+/−39.30	0.0495	1.23	Proinflammatory cytokine

Biomarker expression in PC-3 tumors, LNs and RNs 49 days post tumor cell implantation. Samples of 3 mice were analyzed with a mouse immune-related protein antigen profiling. In the case of significant differences of the biomarker expression in tumors and metastases the ratio (metastases/tumor) was calculated and examples were listed.

doi:10.1371/journal.pone.0045942.t001

extent of necrosis, immune cell burden and cytokine expression in tumors and metastases before virus injection.

It is reported, that the tumor specifity of vaccinia virus is influenced by the enhanced permeability and retention (EPR) effect, due to size of virus particles [26]. Most solid tumors possess unique pathophysiological characteristics that are not observed in healthy tissues [27]. This includes hypervasculature and greatly increased permeability of blood vessels. To analyze whether there is a stronger EPR effect in metastases than in primary tumors, the vasculature of tumors and metastases was compared. Although no differences of the blood vessel density in tumors and metastases were observed, an up-regulation of CD31 marker protein was detectable in lymph node metastases when compared to solid tumors. CD31 is associated with a higher vascular permeability [17]. Accordingly, CD31 up-regulation in LNs and RNs indicated higher blood vessel permeability in metastases compared to solid tumors, which could alleviate the entrance of GLV-1h68 to metastases. Furthermore, an increased vessel diameter in LNs and RNs compared to solid tumors was observed, which also indicated a higher vascular permeability in metastases [28]. A subsequent extravasation assay with i.v. injected rat-IgG confirmed that the blood vessel permeability is, indeed, significantly increased in lymph node metastases when compared to solid tumors. Therefore, we suggest that a higher EPR effect, mainly characterized by the higher vessel permeability of metastases, may efficiently elevate the initial amount of GLV-1h68 particles in lymph node metastases. It is noteworthy that no major differences in the blood vessel permeability between LNs and RNs were detected. Although the data might explain why lymph node metastases are in general better colonized by GLV-1h68, it does not explain why there are significantly higher virus titers in RNs in comparison to LNs.

To explain this phenomenon, we analyzed the replication status of PC-3 cells in solid tumors and in metastases using Ki-67 and BrdU assays. Due to deletional mutation into the *J2R* gene encoding for thymidine kinase (TK) [10], replication of GLV-1h68 is directly dependent on cellular TK levels [19]. Highly proliferative cells exhibit higher TK levels [18], thus, providing more supportive conditions for virus replication. The Ki-67 assay showed higher amounts of proliferating PC-3-RFP cells in lymph node metastases than in solid tumors. Strikingly, PC-3-RFP cells in RNs proliferate more rapidly than in LNs. This observation was also confirmed by BrdU assays, which revealed significantly higher numbers of PC-3-RFP cells which were positive for incorporated BrdU in RNs than in LNs. In addition, we found that the area of necrotic tissues, which cannot be colonized by vaccinia virus, was significantly smaller in lymph node metastases than in solid tumors. We concluded therefore, that lymph node metastases contain on the one hand PC-3 cells with a higher proliferation status and on the other hand less necrotic regions than the corresponding primary tumors. The higher proliferation rates surely have consequences on the cellular level (such as architecture of the cytoskeleton, availability of nutrients, etc.) which probably facilitate better entry and/or replication of the virus in those cells. Taken together, the observed conditions seemed to be favorable for viral replication and dissemination.

Lymph nodes represent highly proliferative tissues and are essential organs of the immune system where antigen presentation as well as lymphocyte activation and proliferation takes place [20]. In this study, lymph nodes are target tissues for migrating and metastasizing PC-3 cells. Activated immune cells in lymph node metastases may influence viral replication and colonization due to production of cell growth-stimulating cytokines. Significantly higher amounts of MHC-II positive antigen presenting cells, B cells and macrophages were found in lymph node metastases than

in solid tumors. Additionally, we observed markedly higher amounts of all three immune cell populations in RNs when compared to LNs. Taken together, we discovered that the further the distance of a lymph node metastasis from the primary tumor, the larger the amount of immune cells and consequently the smaller the amount of metastasizing PC-3 cells (Figure 6a).

By further analyzing the immune cell enrichment in PC-3-RFP metastases, we observed that lymph node metastases exhibit a pro-inflammatory cytokine signature. In fact, significantly higher levels of several pro-inflammatory cytokines were found in LNs and RNs than in the primary tumors. Since most of the cytokines were related to the macrophage population, macrophages, well-known as a source of cytokines which are involved in immune response and inflammation [29], seem to orchestrate the effect of the local metastatic microenvironment more than the B cell population. We showed that growth-stimulating cytokines such as GM-CSF or M-CSF-1 are significantly up-regulated in metastases. These cytokines may be responsible for enhancing tumor cell proliferation which in return helps to accelerate virus replication leading to higher virus titers in metastases. Furthermore, it is conceivable that macrophages and B cells themselves may serve as hosts for vaccinia virus infection facilitating viral spreading and replication within metastases. Sanchez-Puig *et al.* described a high susceptibility of monocytes and B lymphocytes to vaccinia virus infection, these findings support this hypothesis [30]. However, in our laboratories we were not able to observe infected MHC-II positive cells in RNs and LNs upon i.v. administration of GLV-1h68 (Figure S4). Additionally, no vaccinia virus was detected in spleens of tumor-bearing virus-treated mice in previous experiments [10]. The spleen is known to serve as reservoir for monocytes and B cells [31]. Therefore, we propose that these immune cell populations may contribute to virus replication due to cytokine production and establishment of the pro-inflammatory microenvironment, rather than becoming host cells for GLV-1h68 infection. Whether the pro-inflammatory microenvironment will have effects on the adaptive immune system in metastasized lymph nodes in immunocompetent patients cannot be answered at this time as we do not have access to a comparable animal model in immunocompetent hosts. Activation of the adaptive immune system in those metastases could have both negative effects like eradication of the oncolytic virus as well as positive effects such as cross presentation of tumor antigens and therefore even faster eradication of even more tumor cells. Results from current clinical trials (http://clinicaltrials.gov/identifier numbers: NCT01443260 and NCT00794131) will likely answer this question and the effects on metastases should be analyzed in detail in these and similar trials. Even more, since the described pro-inflammatory status is not unique to metastases originating from human prostate carcinoma cell line PC-3, it has also been described in metastatic melanoma cell lines [32]. Therefore, the observed preferential colonization and eradication of metastases by oncolytic rVACVs may not be limited to PC-3 alone.

Taken together, all these findings indicate that the specific milieu of lymph node metastases might contribute to the preferential virus replication in metastases in comparison to primary tumors, finally leading to a more robust oncolytic effect. The elevated vascular permeability in metastases might lead to an increased release of the initial amount of GLV-1h68 particles. Furthermore, lymph node metastases might represent more attractive targets for virus infection compared to primary tumors due to the triggered PC-3 cell proliferation and the lack of necrotic tissues. Finally, the increased numbers of immune cells may also enhance virus replication in metastases by secreting cell growth-stimulating cytokines. The elevated permeability of the vessels of metastases can only enhance the initial viral load immediately after systemic virus injection. Replication differences of VACV in primary tumor cells and metastatic cells are attributable to inherent differences of the respective host cells. Therefore, the different immunological milieu and the proliferation index might be of higher importance for long term viral tumor and metastases colonization. Since metastatic carcinomas represent the major cause of cancer-related death, these findings may become very beneficial to the improvement of the therapy of metastases.

Conclusion

In this study, treatment of PC-3 tumor-bearing mice with the oncolytic vaccinia virus strain GLV-1h68 led to a distinctly higher infection and destruction of lymph node metastases compared to primary tumors. The virus infection resulted in a large reduction of blood and lymph vessels in tumor as well as metastatic tissues, explaining the recently shown metastases-reducing effect of the virus strain GLV-1h68. Moreover, we demonstrated that non-infected PC-3 lymph node metastases exhibited increased vascular permeability, higher proliferation of tumor cells, lower amounts of necrotic tissues, increased immune cell burden as well as up-regulation of pro-inflammatory cytokines compared to primary tumors. Each of these factors may have contributed to the preferential infection of metastases by vaccinia virus. Since metastatic carcinomas represent the major cause of cancer-related death, these findings may become very beneficial to the improvement of the therapy of metastases. In contrast to the treatment of primary tumors, which can be removed surgically in most cases, fighting metastases faces enormous difficulties, since metastases are often not amenable and surgery is rarely performed [1]. The patient's prognosis directly depends on the metastatic state of the disease. For this reason, combating metastasis formation represents the key to success in cancer treatment. Thus, combining surgical removal of primary tumors with oncolytic virotherapy using vaccinia virus strains, such as GLV-1h68, leading to an efficient destruction of metastases may become a very promising treatment strategy in fighting advanced prostate as well as other carcinomas in the clinic.

Supporting Information

Figure S1 Reduction of PC-3 lung metastases due to GLV-1h68 infection. Besides in lymph node PC-3-RFP cells could also be detected in lungs of PC-3-RFP tumor-bearing mice indicating the hematogenous route of migration. The RFP fluorescence signal was observed about 60–70 days post tumor cell implantation. Depicted are representative images of a lung 70 days after implantation (a). Furthermore the effect of GLV-1h68 on lung metastases was analyzed. Therefore 5×10^6 pfu GLV-1h68 was injected i.v. into PC-3 tumor-bearing mice 28 days post tumor cell implantation. At day 21 post virus injection lungs positive for human β-actin, the marker for the presence of PC-3 cells, were determined with an RT-PCR. 5 out of 6 lungs from the mice in the PBS group were tested positive for PC-3 cells. In contrast to this PC-3 cells could not be detected in any of the lungs of mice treated with GLV-1h68 (b). Scale bars represent 100 μm.
(TIF)

Figure S2 Colonization of inguinal and sciatic lymph node metastases by GLV-1h68. PC-3-RFP tumor-bearing mice were injected i.v. with 1×10^7 pfu GLV-1h68. (a) Titers of GLV-1h68 in tumors, inguinal (IN) and sciatic lymph node metastases (SN) per gram tissue 55 days post cell implantation, 14 days after virus injection. (b) Representative images of an inguinal

and a sciatic lymph node metastasis 69 days post tumor cell implantation and 7 days after virus injection. Scale bars represent 2 mm.
(TIF)

Figure S3 Colonization of PC-3 tumors LNs and RNs after i.t. injection of GLV-1h68. PC-3-RFP tumor-bearing mice were injected i.t. with 1×10^7 pfu GLV-1h68. (a) Titers of GLV-1h68 in tumors, LNs and RNs per gram tissue 7 days after i.t. (n = 6) and i.v. (n = 6) virus injection. I.v. injection was performed 48 days post cell implantation and i.t. injection 56 days post cell implantation. (b) Representative image of lumbar and renal lymph node metastases 14 days post i.t. virus injection and 64 days post tumor cell implantation. Scale bars represent 2 mm.
(TIF)

Figure S4 GLV-1h68 infection does not affect MHC-II-positive cells. Confocal images of RN sections 57 days after PC-3 cell implantation and 7 days after injection of 1×10^7 pfu GLV-1h68 showed that GLV-1h68 did not infect MHC-II positive cells. All images are representative examples. Scale bars represent 50 μm. Overlay shows GLV-1h68 dependent GFP and MHCII-staining.
(TIF)

Acknowledgments

The authors thank J. Langbein-Laugwitz, J. Aguilar and T. Trevino for excellent technical assistance and Drs. Q. Zang and Y.A. Yu for providing the rVACV GLV-1h68.

Author Contributions

Conceived and designed the experiments: UD AAS SW JS IG. Performed the experiments: UD MH JBS. Analyzed the data: UD SW. Contributed reagents/materials/analysis tools: NGC. Wrote the paper: UD SW MH AAS JS BH.

References

1. Sleeman J, Steeg PS (2010) Cancer metastasis as a therapeutic target. Eur J Cancer 46: 1177–1180.
2. Boyle P, Levin B (2008) The World Cancer Report - the major findings: World Health Organization, Press Release WHO/27/IARC/145.
3. Wynder EL, Mabuchi K, Whitmore WF Jr (1971) Epidemiology of cancer of the prostate. Cancer 28: 344–360.
4. Apple JS, Paulson DF, Baber C, Putman CE (1985) Advanced prostatic carcinoma: pulmonary manifestations. Radiology 154: 601–604.
5. Skvortsova I, Skvortsov S, Stasyk T, Raju U, Popper BA, et al. (2008) Intracellular signaling pathways regulating radioresistance of human prostate carcinoma cells. Proteomics 8: 4521–4533.
6. Fidler IJ (1990) Critical factors in the biology of human cancer metastasis: twenty-eighth G.H.A. Clowes memorial award lecture. Cancer Res 50: 6130–6138.
7. Suit HD (1992) Local control and patient survival. Int J Radiat Oncol Biol Phys 23: 653–660.
8. Vaha-Koskela MJ, Heikkila JE, Hinkkanen AE (2007) Oncolytic viruses in cancer therapy. Cancer Lett 254: 178–216.
9. Zhang Q, Liang C, Yu YA, Chen N, Dandekar T, et al. (2009) The highly attenuated oncolytic recombinant vaccinia virus GLV-1h68: comparative genomic features and the contribution of F14.5L inactivation. Mol Genet Genomics 282: 417–435.
10. Zhang Q, Yu YA, Wang E, Chen N, Danner RL, et al. (2007) Eradication of solid human breast tumors in nude mice with an intravenously injected light-emitting oncolytic vaccinia virus. Cancer Res 67: 10038–10046.
11. Gentschev I, Donat U, Hofmann E, Weibel S, Adelfinger M, et al. (2010) Regression of human prostate tumors and metastases in nude mice following treatment with the recombinant oncolytic vaccinia virus GLV-1h68. J Biomed Biotechnol 2010: 489759.
12. Yu YA, Galanis C, Woo Y, Chen N, Zhang Q, et al. (2009) Regression of human pancreatic tumor xenografts in mice after a single systemic injection of recombinant vaccinia virus GLV-1h68. Mol Cancer Ther 8: 141–151.
13. Burton JB, Priceman SJ, Sung JL, Brakenhielm E, An DS, et al. (2008) Suppression of prostate cancer nodal and systemic metastasis by blockade of the lymphangiogenic axis. Cancer Res 68: 7828–7837.
14. Hanahan D, Weinberg RA (2000) The hallmarks of cancer. Cell 100: 57–70.
15. Weibel S, Raab V, Yu YA, Worschech A, Wang E, et al. (2011) Viral-mediated oncolysis is the most critical factor in the late-phase of the tumor regression process upon vaccinia virus infection. BMC Cancer 11: 68.
16. Weibel S, Stritzker J, Eck M, Goebel W, Szalay AA (2008) Colonization of experimental murine breast tumours by Escherichia coli K-12 significantly alters the tumour microenvironment. Cell Microbiol 10: 1235–1248.
17. Vestweber D (2007) Adhesion and signaling molecules controlling the transmigration of leukocytes through endothelium. Immunol Rev 218: 178–196.
18. Lewenhaupt A, Ekman P, Eneroth P, Nilsson B (1990) Tumour markers as prognostic aids in prostatic carcinoma. Br J Urol 66: 182–187.
19. Parato KA, Breitbach CJ, Le Boeuf F, Wang J, Storbeck C, et al. (2011) The Oncolytic Poxvirus JX-594 Selectively Replicates in and Destroys Cancer Cells Driven by Genetic Pathways Commonly Activated in Cancers. Mol Ther.
20. Roger W, Williams PL (1973) Gray's anatomy: London: Longman. Angiology (Chapter 6), 588–785 p.
21. Kirn DH, Wang Y, Le Boeuf F, Bell J, Thorne SH (2007) Targeting of interferon-beta to produce a specific, multi-mechanistic oncolytic vaccinia virus. PLoS Med 4: e353.
22. Breitbach CJ, Paterson JM, Lemay CG, Falls TJ, McGuire A, et al. (2007) Targeted inflammation during oncolytic virus therapy severely compromises tumor blood flow. Mol Ther 15: 1686–1693.
23. Worschech A, Chen N, Yu YA, Zhang Q, Pos Z, et al. (2009) Systemic treatment of xenografts with vaccinia virus GLV-1h68 reveals the immunologic facet of oncolytic therapy. BMC Genomics 10: 301.
24. Folkman J (1971) Tumor angiogenesis: therapeutic implications. N Engl J Med 285: 1182–1186.
25. Chen Z, Varney ML, Backora MW, Cowan K, Solheim JC, et al. (2005) Down-regulation of vascular endothelial cell growth factor-C expression using small interfering RNA vectors in mammary tumors inhibits tumor lymphangiogenesis and spontaneous metastasis and enhances survival. Cancer Res 65: 9004–9011.
26. Shen Y, Nemunaitis J (2005) Fighting cancer with vaccinia virus: teaching new tricks to an old dog. Mol Ther 11: 180–195.
27. Maeda H, Wu J, Sawa T, Matsumura Y, Hori K (2000) Tumor vascular permeability and the EPR effect in macromolecular therapeutics: a review. J Control Release 65: 271–284.
28. Frantz S, Vincent KA, Feron O, Kelly RA (2005) Innate immunity and angiogenesis. Circ Res 96: 15–26.
29. Cavaillon JM (1994) Cytokines and macrophages. Biomed Pharmacother 48: 445–453.
30. Sanchez-Puig JM, Sanchez L, Roy G, Blasco R (2004) Susceptibility of different leukocyte cell types to Vaccinia virus infection. Virol J 1: 10.
31. Swirski FK, Nahrendorf M, Etzrodt M, Wildgruber M, Cortez-Retamozo V, et al. (2009) Identification of splenic reservoir monocytes and their deployment to inflammatory sites. Science 325: 612–616.
32. Ivanov VN, Partridge MA, Huang SX, Hei TK (2011) Suppression of the proinflammatory response of metastatic melanoma cells increases TRAIL-induced apoptosis. J Cell Biochem 112: 463–475.

Figure S1

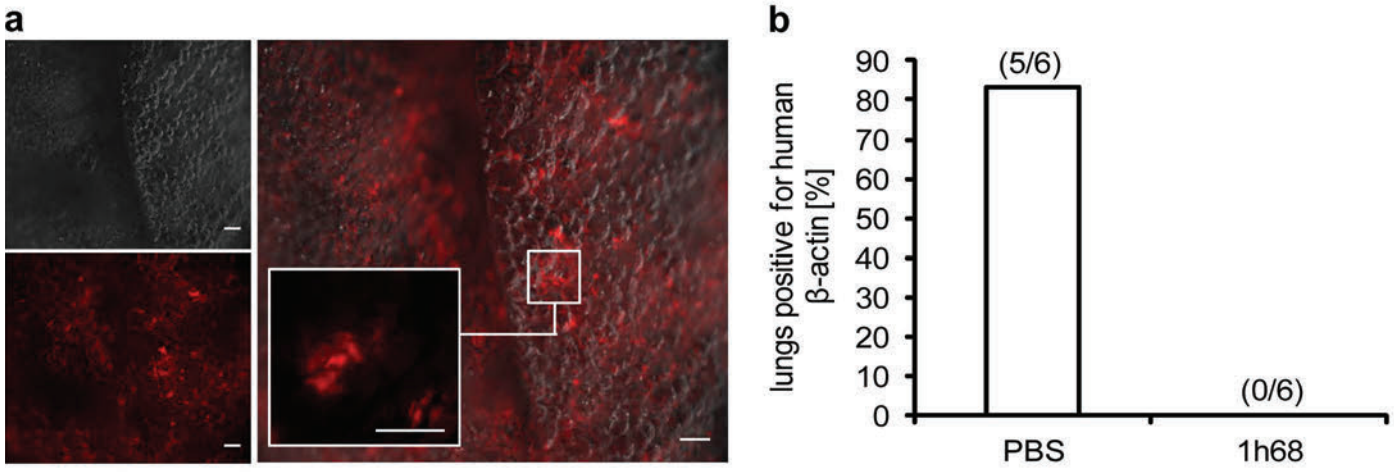
a
b
lungs positive for human β-actin [%]
90
80
70
60
50
40
30
20
10
0
(5/6)
(0/6)
PBS
1h68

Figure S2

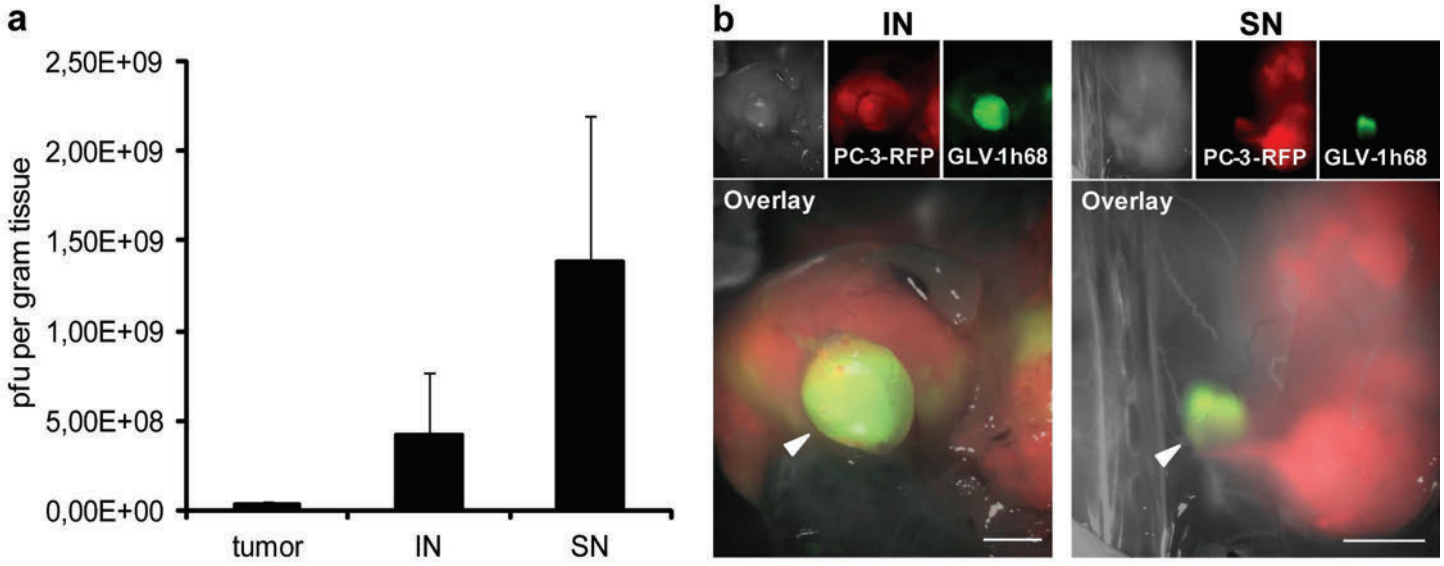
a
2,50E+09
2,00E+09
1,50E+09
1,00E+09
5,00E+08
0,00E+00
pfu per gram tissue
tumor
IN
SN
b
IN
SN
PC-3-RFP
GLV-1h68
Overlay
PC-3-RFP
GLV-1h68
Overlay

Figure S3

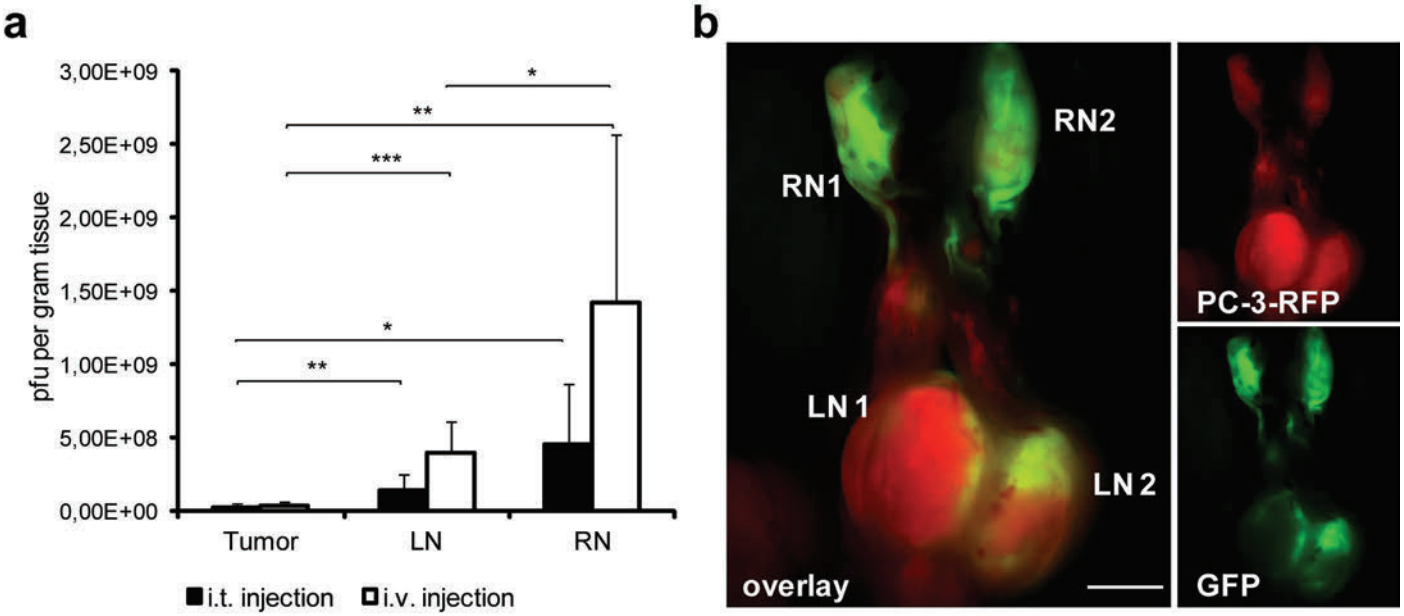
a
3,00E+09
2,50E+09
2,00E+09
1,50E+09
1,00E+09
5,00E+08
0,00E+00
pfu per gram tissue
*
**
***
*
**
Tumor
LN
RN
i.t. injection
i.v. injection
b
RN2
RN1
LN 1
LN 2
overlay
PC-3-RFP
GFP

Figure S4

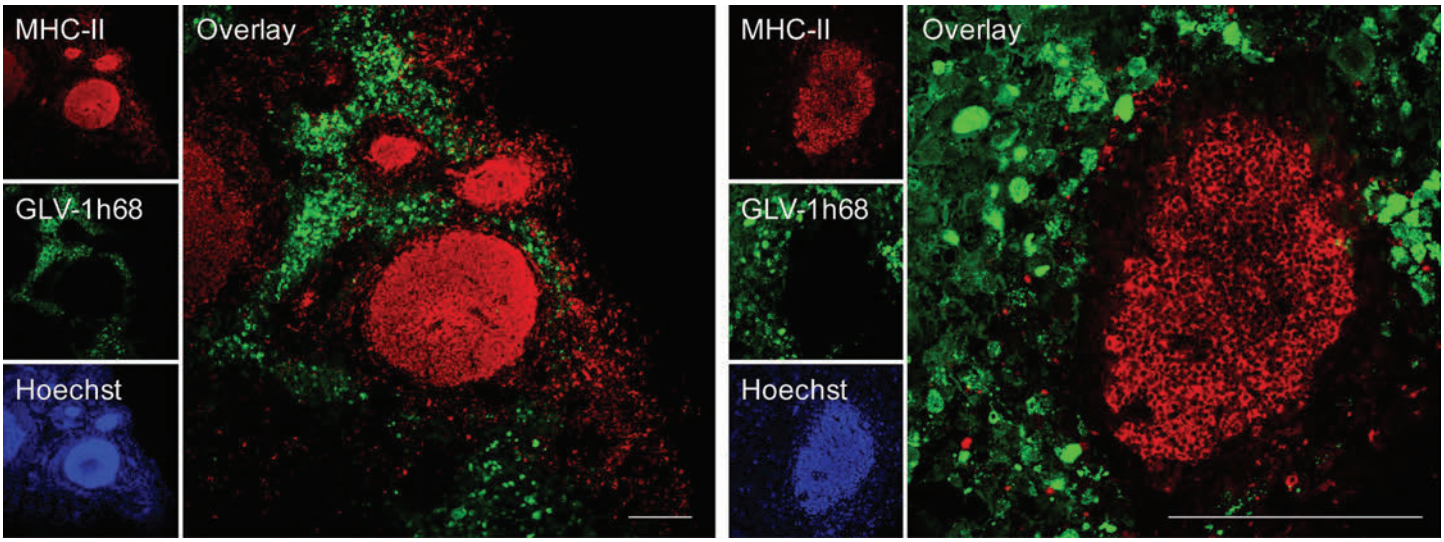
MHC-II
Overlay
GLV-1h68
Hoechst
MHC-II
Overlay
GLV-1h68
Hoechst

Publication (complete reference): Sturm JB, **Hess M**, Weibel S, Chen NG, Yu YA, Zhang Q, Donat U, Reiss C, Gambaryan S, Krohne G, Stritzker J, Szalay AA. Functional hyper-IL-6 from Vaccinia virus-colonized tumors triggers platelet formation and helps to alleviate toxicity of mitomycin C enhanced virus therapy. *J Transl Med*. 2012;10:9
Authors' contributions
JBS conceived the study, designed, performed and analyzed all experiments and wrote the manuscript. **MH** and UD participated in experimental design and performance. JS participated in conceiving the study, experiment analyzation and manuscript writing. SW, GK, CR and SG participated in conceiving the study. NGC, QZ and YAY participated in manuscript writing and provided essential material. AAS participated in conceiving the study and writing the manuscript. All authors read and approved the final version of the manuscript.

Julia B. Sturm	
Stephanie Weibel	
Nanhai G. Chen	
Yong A. Yu	
Qian Zhang	
Ulrike Donat	
Cora Reiss	
Stepan Gambaryan	
Georg Krohne	
Jochen Stritzker	
Aladar A. Szalay	

Sturm et al. Journal of Translational Medicine 2012, 10:9
http://www.translational-medicine.com/content/10/1/9

JOURNAL OF TRANSLATIONAL MEDICINE

RESEARCH Open Access

Functional hyper-IL-6 from vaccinia virus-colonized tumors triggers platelet formation and helps to alleviate toxicity of mitomycin C enhanced virus therapy

Julia B Sturm[1], Michael Hess[1], Stephanie Weibel[1], Nanhai G Chen[2,3], Yong A Yu[2,3], Qian Zhang[2,3], Ulrike Donat[1], Cora Reiss[4], Stepan Gambaryan[4], Georg Krohne[5], Jochen Stritzker[1,2] and Aladar A Szalay[1,2,3*]

Abstract

Background: Combination of oncolytic vaccinia virus therapy with conventional chemotherapy has shown promise for tumor therapy. However, side effects of chemotherapy including thrombocytopenia, still remain problematic.

Methods: Here, we describe a novel approach to optimize combination therapy of oncolytic virus and chemotherapy utilizing virus-encoding hyper-IL-6, GLV-1h90, to reduce chemotherapy-associated side effects.

Results: We showed that the hyper-IL-6 cytokine was successfully produced by GLV-1h90 and was functional both in cell culture as well as in tumor-bearing animals, in which the cytokine-producing vaccinia virus strain was well tolerated. When combined with the chemotherapeutic mitomycin C, the anti-tumor effect of the oncolytic virotherapy was significantly enhanced. Moreover, hyper-IL-6 expression greatly reduced the time interval during which the mice suffered from chemotherapy-induced thrombocytopenia.

Conclusion: Therefore, future clinical application would benefit from careful investigation of additional cytokine treatment to reduce chemotherapy-induced side effects.

Keywords: vaccinia virus, cancer, cytokine, hyper-IL-6, oncolysis, chemotherapy

Background

Interleukin-6 (IL-6) is one of the best characterized cytokines and much is known about its pleiotropic behavior. As described by many groups, IL-6 is produced by both lymphoid and nonlymphoid cells, such as T cells, B cells, monocytes, endothelial cells, fibroblasts and many tumor cell types [1]. It is also therefore involved in many biological processes including upregulation of acute phase proteins during inflammation [2], immune regulation and hematopoiesis [3] as well as hemostasis which includes platelet formation [4]. Furthermore, IL-6 has been shown to play a pathogenic role in the development and progression of several tumor types [5]. In contrast to this, IL-6 has been shown to possess anti-tumor effects as in the example of treatment of B16 melanoma [6] or small cell lung carcinoma [7]. In both cases, the growth or proliferation inhibition could only be detected after addition of soluble IL-6 receptor (sIL-6-R) in cell culture systems, indicating that the pleiotropic effects of IL-6 may be due to differing mechanisms in signal transduction. Two different forms of the IL-6 receptor have been characterized which orchestrate the signaling pathways of the cytokine. IL-6 binds to either a specific receptor on the cell surface (mIL-6-R) of hepatocytes, monocytes/macrophages and leukocytes [8] or to the soluble, circulating sIL-6-R version generated by alternative splicing or by shedding of the mIL-6-R. The latter kind of signal transduction is named IL-6 trans-signaling (IL-6TS) which can potentiate the signal transduced by mIL-6R and also extend the range of target cells [9]. In both cases, the IL-6/(s/m)IL-6-R

* Correspondence: aaszalay@genelux.com
[1]Department of Biochemistry, University of Würzburg, 97074 Würzburg, Germany
Full list of author information is available at the end of the article

complex binds to the glycoprotein gp130 which then forms homodimers [10], leading to activation of the Ras/MAPK- and the JAK/STAT pathway [11]. The JAK/STAT pathway in turn results in phosphorylation of STAT3, followed by dimerization and accumulation in the cell nucleus where phosphorylated STAT3 dimers act as transcription factors [12].

To further characterize the IL-6TS, Rose-John et al. (1996) constructed a fusion protein, named hyper-IL-6, in which human IL-6 is covalently linked to the human sIL-6R [13]. The hyper-IL-6 designer cytokine activates cells in the same way as the IL-6/sIL-6-R complex [14]. However, its activity is highly enhanced (100-1000 fold) and the time of action is extended, which is probably due to its prolonged half-life in blood plasma [15].

Recombinant vaccinia virus strains (rVACV) not only feature pronounced oncolytic activity, but also serve as efficient vehicles for delivery and expression of proteins *in vivo*. The vaccinia virus vector system has the ability to stably integrate over 25,000 base pairs of foreign DNA into the viral genome and is further characterized by its cytoplasm-restricted gene expression [16]. In rVACV mediated oncolytic therapy, this can be used to insert diagnostic or therapeutic genes, including fluorescent proteins and luciferases [17], anti-angiogenic agents [18], or immunostimulatory cytokines such as GM-CSF [19].

In this study, we constructed the hyper-IL-6-encoding VACV strain GLV-1h90, which was derived from the previously described strain GLV-1h68 [20]. After systemic delivery, GLV-1h90 was capable of infecting and replicating in established DU-145 prostate xenograft tumors, leading to overexpression of hyper-IL-6 which in turn is secreted into the blood circulation. We used this model to analyze the effects of IL-6 that are exclusively transduced via the IL-6 trans-signaling pathway in combination with the oncolytic activity of the vaccinia virus, which included gain in body weight, levels of thrombocytosis and accelerated epidermal barrier repair.

We further report on a possible medical application for GLV-1h90. Recently, our group demonstrated that the combination of viral- and chemotherapy with a number of different chemotherapeutic agents (e.g. cisplatin or gemcitabine) improved the oncolytic activity of the recombinant vaccinia virus GLV-1h68 [21]. Unfortunately, chemotherapies often implicate a wide range of side effects especially due to non-specific involvement of all rapidly proliferating cells. One of the most common side effects is myelosuppression, which includes a decreased production of thrombocytes [22]. Chemotherapy-induced thrombocytopenia is a significant safety concern due to the increased risk of bleeding and can delay scheduled treatment [23]. For this reason, we used the hyper-IL-6-encoding VACV strain GLV-1h90 in combination therapy with the chemotherapeutic agent mitomycin C. This approach improves therapeutic outcomes and reduces negative side effects such as thrombocytopenia.

Materials and methods

Virus and cell culture

Androgen-insensitive DU-145 human prostatic cancer cells (authenticated by nonaplex PCR in 2011 [24]) were cultured in MEM containing 1% glutamaxx, 1% NEAA, 1% sodium pyruvate, 1,5 g/L sodium bicarbonate, 1% 100 × penicillin (10000 units/ml)/streptomycin (10 mg/mL) solution and 10% fetal bovine serum (FBS) (Invitrogen GmbH, Karlsruhe, Germany).

African green monkey kidney fibroblasts (CV-1) (ATCC-No. CCL-70) were maintained in Dulbecco's modified Eagle's medium (DMEM) supplemented with 1% 100 × penicillin (10000 units/mL)/streptomycin (10 mg/mL) solution and 10% FBS at 37°C under 5% CO_2.

GLV-1h68 was derived from the vaccinia virus strain LIVP as described previously [20]. In GLV-1h90, the *gusA*-containing gene cassette was replaced by hyper-IL-6-encoding cDNA under control of a vaccinia virus synthetic early promoter (PE).

The plasmid DNA pCDM8-H-IL-6 for the construction of GLV-1h90 was kindly provided by Dr. Stefan Rose-John (University of Kiel, Germany), in which a fusion cDNA encoding a fusion protein of human IL-6 (corresponding to amino acid residues 29-212) fused to the C-terminus of human soluble receptor for IL-6 (sIL-6R, corresponding to amino acid residues 1-323) via a flexible peptide linker. This fusion cDNA was amplified with primers 5'-GTCGAC (*Sal I*) CCACCATGCTGGCCGTCGGC TGCGC-3' and 5'-GGTACC (*Kpn I*) CTAGAGTCGCG GCCGCGACC-3' in a PCR, and cloned into the pCR-Blunt II-TOPO vector (Invitrogen, Carlsbad, CA). The fusion cDNA was sequencing confirmed, released by *Sal I* and *Kpn I* digestion, and then subcloned into an intermediate vector, placing the cDNA under the control of a vaccinia synthetic early promoter (PsE). The vaccinia sIL-6R/IL-6 expression cassette was further subcloned into the vaccinia hemaglutinin (HA) transfer vector, yielding the final construct HA-SE-IL-6-1 that was used for recombination. GLV-1h90 was then generated by insertion of pSE-sIL-6R/IL-6 into the HA locus of parental strain GLV-1h68 via *in vivo* homologous recombination, interrupting the *gusA* expression cassette at the HA locus of GLV-1h68. For this, CV-1 cells were infected with GLV-1h68 at a multiplicity of infection (MOI) of 0.1 for 1 hour, then transfected with the hyper-IL-6 transfer vector HA-SE-IL-6-1 using Fugene (Roche, Indianapolis, IN, USA). Two days post infection (dpi), infected/transfected cells were harvested and the recombinant viruses were selected and plaque purified as described previously [25]. The genotype of hyper-IL-6 expressing GLV-1h90 was verified by PCR and sequencing. Also, the lack of expression of

β-glucuronidase was confirmed by staining with 5-bromo-4-chloro-3-indolyl-β-D-glucuronic acid (X-GlcA; Research Product International, Mt. Prospect, IL, USA).

Protein isolation and detection

At 2, 4, 8, 12, 24, 48, or 72 hours post-infection (hpi), DU-145 cells were harvested and lysed in RIPA buffer (25 mmol/L Tris-HCl pH 7.6, 150 mmol/L NaCl, 1% NP-40, 1% sodium deoxycholate, 0.1% SDS) supplemented with proteinase inhibitor cocktail (Roche, Penzberg, Germany). The cell lysates were separated on a 10% SDS-PAGE, and proteins were transferred onto a nitrocellulose membrane (Whatman GmbH, Dassel, Germany). The membrane was then incubated with anti-beta actin mouse monoclonal antibody (Abcam, Cambridge, UK), anti-beta galactosidase rabbit polyclonal antibody (Molecular Probes, Leiden, Netherlands), anti-GFP rabbit polyclonal antibody (Santa Cruz, Heidelberg, Germany), or anti-human IL-6 rat polyclonal antibody (BioLegend, San Diego, US) and detected using horseradish peroxidase (HRP) labeled secondary antibodies: anti-mouse (Abcam, Cambridge, UK), anti-rabbit (Abcam, Cambridge, UK) or anti-rat (Sigma-Aldrich, Taufkirchen, Germany), followed by enhanced chemiluminescence.

For the analysis of (Phospho-) STAT3 expression in DU-145 cells, the cells were incubated with sterile filtered (0.1 μm pore size) supernatants of mock-, GLV-1h68- or GLV-1h90-infected (MOI of 1.0 for 24 hours) DU-145 cells. Oncostatin M (Biomol GmbH, Hamburg, Germany), which also activates the JAK/STAT signaling cascade [26], was used as a positive control, while gp130/Fc chimera (R&D Systems, Minneapolis, MN, USA) were added into the supernatant of GLV-1h90-infected cells to prevent hyper-IL-6 from binding to the endogenous cellular gp130 receptors. Fifteen minutes later, cell lysates were prepared as described before, separated with a 10% SDS-PAGE and proteins were transferred onto a nitrocellulose transfer membrane. The membrane was then incubated with anti-STAT3 rabbit polyclonal antibody (Cell Signaling Technology, Danvers, MA) or anti-phospho-STAT3 rabbit polyclonal antibody (Cell Signaling Technology, Danvers, MA).

Quantitative IL-6 specific enzyme-linked immunosorbent assay (ELISA) was performed according to the manufacturer's protocols (R&D systems, Minneapolis, MN). DU-145 cell lysates and supernatants as well as tumor lysates and sera were analyzed at different time points. Absorbance was measured at 450 nm using a plate-reading spectrophotometer (SunriseTM, TECAN Group, Männedorf, Germany).

Histology and fluorescent microscopy

For the microscopic analysis of (Phospho-) STAT3 expression and distribution, DU-145 cells were seeded on coverslips and incubated with sterile filtered (0.1 μm pore size) supernatant of mock-, GLV-1h68- or GLV-1h90-infected (MOI of 1.0 for 24 hours) DU-145 cells. Fifteen minutes later cells were fixed using 4% paraformaldehyde, washed in PBS and stained using anti-STAT3 rabbit polyclonal antibody (Cell Signaling Technology, Danvers, MA) or anti-phospho-STAT3 rabbit polyclonal antibody (Cell Signaling Technology, Danvers, MA) and Hoechst 33342 (Sigma-Aldrich, Taufkirchen, Germany). Microscopy was performed using a fluorescence microscope (Axiovert 200 M, Zeiss, Oberkochen, Germany) equipped with an AxioCam MR camera and the Axiovision 4.5 aquisition software. Digital images (1388 × 1040 pixel 16-bit grayscale images) were processed with Photoshop 7.0 (Adobe Systems, USA) and merged to yield pseudo-coloured pictures.

Histology and fluorescence microscopy of tumor sections were performed as described previously [27]. Tissue sections were stained using anti-human IL-6 rabbit polyclonal antibody (BioLegend, San Diego, US) and Hoechst 33342 (Sigma-Aldrich, Taufkirchen, Germany), respectively. After several rinses in PBS, tissue sections were mounted in Mowiol 4-88 (Sigma-Aldrich, Taufkirchen, Germany).

Tumor specimens were examined with the stereo-fluorescence microscope (MZ16 FA, Leica, Heerbrugg, Switzerland) equipped with a digital CCD camera (DC500, Leica) and the Leica IM1000 4.0 acquisition software. Digital images (1300 × 1030 pixel color images) were processed with Photoshop 7.0 (Adobe Systems, USA) and merged to overlay pictures.

For analysis of megakarypoiesis, semi-thin sections of the bone marrow were prepared. First femurs of mice were cut in ~0.5 cm pieces and fixed overnight at 4°C with 0.1 M sodium cacodylate (pH 7.2) (Roth, Karlsruhe, Germany) containing 2.5% glutaraldehyde (AppliChem, Darmstadt, Germany) and 2% formaldehyde (Sigma-Aldrich, Taufkirchen, Germany). The bone was removed with forceps before the remaining bone marrow was washed with 50 mM sodium cacodylate (pH 7.2) and subsequently fixed for 2 hours at 4°C with 2% osmium tetroxide (Roth, Karlsruhe, Germany) in 50 mM sodium cacodylate (pH 7.2). Samples were washed with distilled water and stained overnight with 0.5% aqueous uranyl acetate (Merck, Darmstadt, Germany), dehydrated with ethanol, and embedded in Epon 812 (Serva, Heidelberg, Germany). Two-hundred nm semi-thin sections were stained using 1% methylene blue (Merck, Darmstadt, Germany) in 1% sodium borate (Sigma-Aldrich, Taufkirchen, Germany) containing 1% Azure II (Merck, Darmstadt, Germany). For quantification of megakaryocytes 5-8 bone marrow sections from different layers of each sample (n = 4) were examined with an Axiovert 200 M microscope (Zeiss, Oberkochen, Germany) equipped with an AxioCam MRc

5 camera and the Axiovision 4.5 aquisition software. Small (~ 30 μm diameter) and large (~ 60 μm diameter) megakaryocytes were counted in randomly selected areas.

Animal studies

DU-145 xenograft tumors were developed in 6-to-8-week-old female nude mice (NCI:Hsd:Athymic Nude-*Foxn1*^{nu}, Harlan, Borchem, Germany and Indianapolis, USA) by implanting 5×10^6 DU-145 cells subcutaneously in the right hind flank. Fourteen days after tumor cell implantation, groups of five mice were injected with a single intravenous (i.v.) dose of PBS, or 5×10^6 plaque forming units (pfu) of GLV-1h68 or GLV-1h90 in 100 μL of PBS. Weights of the mice, number of tail lesions as well as tumor growth, in two dimensions using a digital caliper, were recorded twice a week. Tumor volume was calculated as ([length × width^2] × 0.52) and reported in mm^3. Concentration of blood platelets was counted 0, 5, 8, 11, 14, 16, 18, 21 and 25 dpi. All animal experiments were carried out in accordance with protocols approved by the Institutional Animal Care and Use Committee (IACUC) of Explora Biolabs (San Diego, USA, protocol number EB08-003) or the government of Unterfranken (Würzburg, Germany, protocol number AZ 55.2-2531.01-17/08).

Tumor lysates

Tumors were collected 2, 5, 9 and 14 dpi, weighed, homogenized and added to 2x volume of lysis buffer (50 mM Tris-HCl with 2 mM EDTA, pH 7.4) supplemented with 2 mM phenylmethylsulfonyl fluoride and proteinase inhibitor cocktail (Roche Diagnostics GmbH, Penzberg, Germany). Samples were homogenized using a gentle MACS dissociator (Miltenyi Biotec) and centrifuged for 15 minutes (13000 g, 4°C).

Platelet counting

Peripheral blood samples were obtained by retro-orbital plexus puncture using 20 μl heparinized capillary tubes (Hecht assistent, Sondheim, Germany). Mean platelet numbers were measured in 50 μL whole blood diluted with 50 μL ACD buffer (12 mM citric acid, 15 mM sodium citrate, 25 mM D-glucose) with a Sysmex KX-21 automatic micro-cell counter (Sysmex GmbH, Norderstedt, Germany).

Combination therapy with mitomycin C

DU-145 tumor bearing mice with an average tumor volume of 250 mm^3 were divided into 3 groups (n = 10). One group was i.v. injected with a single dose of PBS, the second and third group with 5×10^6 pfu's of GLV-1h68 or GLV-1h90 in 100 μL of PBS. For combination therapy each group was subdivided into two groups which were injected with PBS or treated with i.v. injections of mitomycin C (Medac GmbH, Wedel, Germany) at 4 mg/kg/day on day 4 after PBS/virus injection and 3 mg/kg/day on day 5 after PBS/virus injection. Tumor volume, number of tail lesions as well as number of blood platelets was recorded over a time period of 25 dpi.

Statistical analysis

A two-tailed Student's *t* test was used for statistical analysis. *P* values of ≤ 0.05 were considered statistically significant

Results

Recombinant gene expression in GLV-1h68- or GLV-1h90-infected DU-145 tumor cells

Expression of the non-viral genes in the recombinant vaccinia virus strains used in this study was tested in the human prostatic cancer cell line DU-145. The cells were infected with the previously described GLV-1h68 [20] or the hyper-IL-6-encoding GLV-1h90 (Figure 1A).

Protein samples were obtained from infected DU-145 cells at different time points after infection with GLV-1h68 or GLV-1h90 at an MOI of 0.5. The expression of Ruc-GFP and beta-galactosidase was observed in cell lysates upon infection with either rVACV strains starting at 12 hpi. Concurrently, an increased amount of hyper-IL-6 was detectable in GLV-1h90-infected cells in contrast to GLV-1h68-infected cells, where only thin bands were observed indicating endogenously produced IL-6 (Figure 1B).

Since hyper-IL-6 must be secreted in order to bind the extracellular domain of gp130, the supernatant of infected cells was also analyzed for the presence of the fusion protein. Here, the secreted designer cytokine was detectable also at 12 hpi and the hyper-IL-6 concentration increased during the infection. This indicated active secretion of hyper-IL-6 by the infected tumor cells. At later stages, starting from 48 hpi, beta-actin was detectable in cell supernatants of GLV-1h68- or GLV-1h90-infected cells, indicating virus-mediated cell lysis (Figure 1B).

Increasing amounts of hyper-IL-6 in the supernatant of GLV-1h90-infected cells could also be confirmed using an IL-6-specific ELISA (Figure 1C) reaching a maximum of about 130 ng/mL at 72 hpi. On the other hand, no hyper-IL-6 was detectable in cell lysates or supernatants of GLV-1h68 or uninfected DU-145 cells (data not shown).

Vaccinia virus-mediated hyper-IL-6 expression activates the JAK/STAT signaling pathway

IL-6 activates the JAK/STAT signaling pathway and leads to phosphorylation of Tyr-705 of the STAT3 protein [15]. Upon phosphorylation, STAT3 translocates into the nucleus ultimately leading to the expression of target genes involved in differentiation, survival, apoptosis and proliferation (reviewed in [28]).

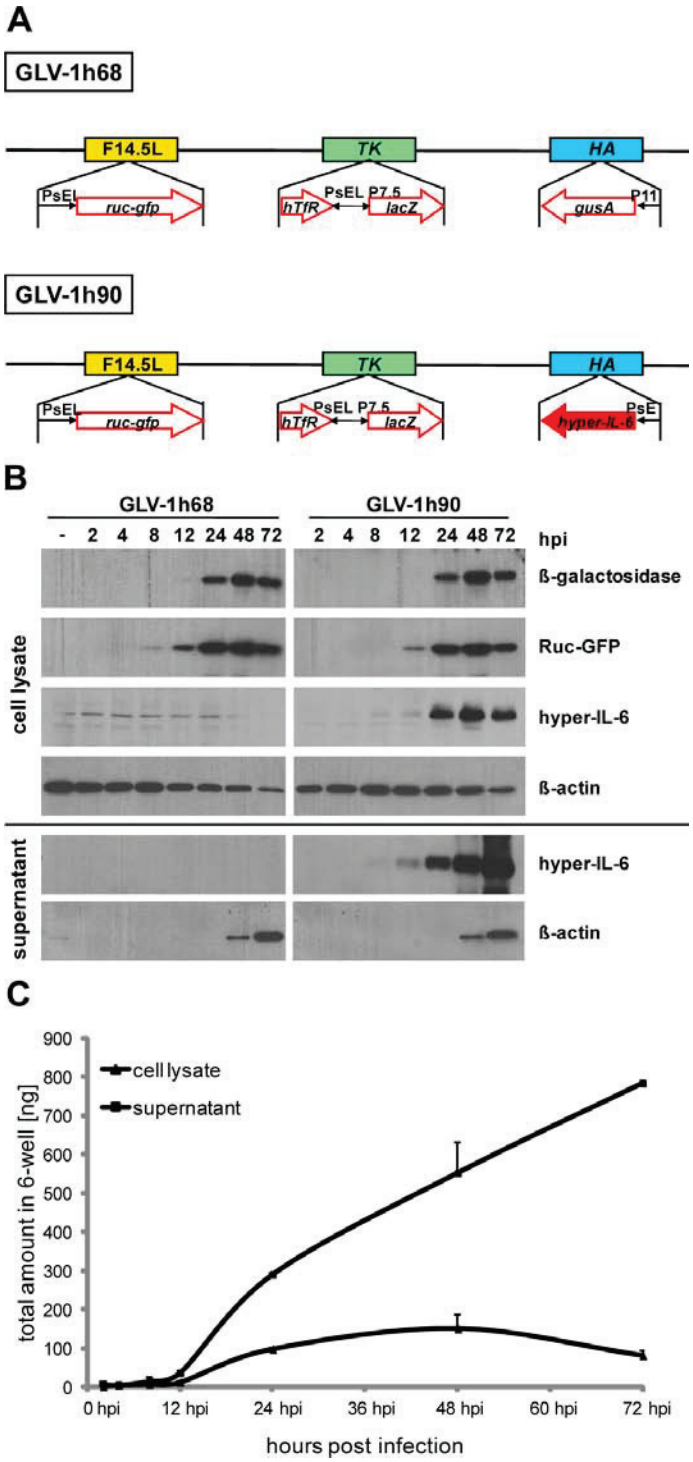

Figure 1 Vaccinia virus strains and recombinant protein expression. (A) Constructs of the recombinant vaccinia virus strains GLV-1h68 and GLV-1h90 which were derived from the wild-type Lister strain. The viral genes encoding for F14.5L, thymidine kinase (TK) and hemaglutinin (HA) were interrupted by the foreign gene expression cassettes encoding for a Renilla-luciferase-GFP (*Ruc-GFP*) fusion protein, beta-galactosidase (*lacZ*), beta-glucuronidase (*gusA*) and hyper-IL-6, respectively. (B) Infection of DU-145 cells led to expression of the marker genes as visualized by Western blot analysis of cell lysates and supernatants of infected cells at 2, 4, 8, 12, 24, 48, and 72 hpi. Mock-infected cells (-) served as negative control. (C) Quantitative (ELISA) measurements of (hyper-) IL-6 in cell lysates and supernatants of GLV-1h90-infected DU-145 cells.

To analyze the biological activity of GLV-1h90-encoded hyper-IL-6, the phosphorylation status of STAT3 and its translocation into the cell nucleus in DU-145 cells was determined after incubation with the supernatant of GLV-1h90-infected cells. DU-145 cells were treated with supernatants from mock-, GLV-1h68- and GLV-1h90-infected cells, respectively, and protein samples were harvested after 15 minutes. Oncostatin M, which also activates the JAK/STAT signal cascade [26], was used as a positive control, while gp130/Fc chimera was added in excess in supernatants of GLV-1h90-infected cells to prevent hyper-IL-6 from binding to the endogenous cellular gp130 receptors.

As shown in Figure 2A STAT3 was exclusively phosphorylated in DU-145 cells treated with oncostatin M and the supernatant of GLV-1h90-infected cells (hyper-IL-6). The STAT3 tyrosin 705 phosphorylation induced by hyper-IL-6 could be blocked by addition of the gp130/Fc chimera, showing the specificity of hyper-IL-6 to gp130. Total STAT3 expression was not altered (Figure 2A lower panels) and used as loading control.

Immunofluorescence analysis of STAT3 (Figure 2B) and Phospho-STAT3 (Figure 2C) confirmed these results and showed activation of the JAK/STAT pathway. The anti-STAT3 antibody detected STAT3 regardless of its phosphorylation state. Therefore, it was possible to directly track the translocation of (Phospho-) STAT3 into the cells' nucleus of DU-145 cells incubated with the conditioned media of GLV-1h90-infected cells or oncostatin M. The (Phospho-) STAT3 protein was detected exclusively in the nucleus in DU-145 cells treated with the supernatant of GLV-1h90-infected cells or oncostatin M, whereas in the remaining experimental groups the STAT3 protein could be detected both in the cytoplasm and in the nucleus. Staining for Phospho-STAT3 confirmed this observation as Phospho-STAT3 could only be detected in the GLV-1h90 and the oncostatin M groups and was exclusively located in the cell nucleus.

Taken together, virally encoded hyper-IL-6 was efficiently and functionally secreted from infected tumor cells. In addition, these results clearly showed specific activation of the JAK/STAT pathway by vaccinia virus-encoded hyper-IL-6 in human prostatic cancer cells.

Hyper-IL-6 expression could be detected both in tumors and in blood serum of GLV-1h90-injected mice

Similar to the observations made for GLV-1h68 [20], systemic administration of GLV-1h90 into tumor-bearing mice resulted in specific replication of vaccinia virus in tumor tissue (data not shown).

To demonstrate hyper-IL-6 expression in GLV-1h90-colonized tumors, tumors from PBS-, GLV-1h68-, or GLV-1h90-injected mice were isolated 2, 5, 9 and 14 dpi and tumor tissue homogenates were prepared. Quantitative protein analysis revealed high amounts of hyper-IL-6 in GLV-1h90-colonized tumors with a maximum concentration of about 7900 ng/g tissue at 9 dpi (Figure 3A). At this time point the concentration of IL-6 in control tumors of PBS- or GLV-1h68-injected mice was around 345-fold lower (on average 22,85 ng/g in PBS- and 23,45 ng/g in GLV-1h68-injected mice).

Of special interest was the presence of hyper-IL-6 in blood serum samples of GLV-1h90-injected mice (Figure 3B), which is essential for its ability to induce signal transduction pathways outside the tumor. Hyper-IL-6 was actively secreted into the blood circulation as indicated by the same detection pattern over infection time in both the tumor and the blood (Figure 3AB). The hyper-IL-6 concentration in the blood serum also reached its maximum 9 dpi and was ~ 800 pg/mL. In PBS-injected mice the IL-6 concentration was ~ 130-fold lower and ~ 65-fold lower in GLV-1h68-injected mice (on average 6 pg/mL and 12 pg/mL in PBS- and GLV-1h68-injected mice, respectively) (Figure 3B) compared to GLV-1h90-treated animals.

Also, fluorescence microscopy of tumor sections 11 dpi confirmed the expression of hyper-IL-6 (Figure 3C). While GFP could be observed in GLV-1h68- and GLV-1h90-infected tumors, high amounts of hyper-IL-6 could only be detected in GLV-1h90-colonized tumors. As expected, the distribution of the fusion protein correlated with the area of GFP expression, since both proteins were encoded by GLV-1h90.

Effects of GLV-1h90 in a DU-145 xenograft mouse model

For analysis of oncolytic effects in live animals, DU-145 tumor-bearing mice were injected i.v. with either PBS or 5×10^6 pfu of GLV-1h68 and the hyper-IL-6-encoding GLV-1h90, respectively. Systemic administration of either viral constructs led to significant tumor regression starting 18 dpi compared to PBS injection. The comparison of both viral constructs revealed no significant differences in the inhibition of tumor growth except 22 dpi when GLV-1h90-colonized tumors were significantly smaller compared to those colonized with GLV-1h68 (Figure 4A), while viral titers in tumor tissue showed no relevant difference between both constructs (data not shown).

Besides the slightly increased oncolytic activity, GLV-1h90 revealed important benefits over GLV-1h68 mediated by the overexpression of the encoded designer cytokine hyper-IL-6. One of those advantages compared to GLV-1h68 concerned the healthiness of the mice during viral therapy. The health status of the mice was determined by measurement of the net body weight (body weight without tumor weight). As shown in Figure 4B, GLV-1h90 injection led to a significant increase

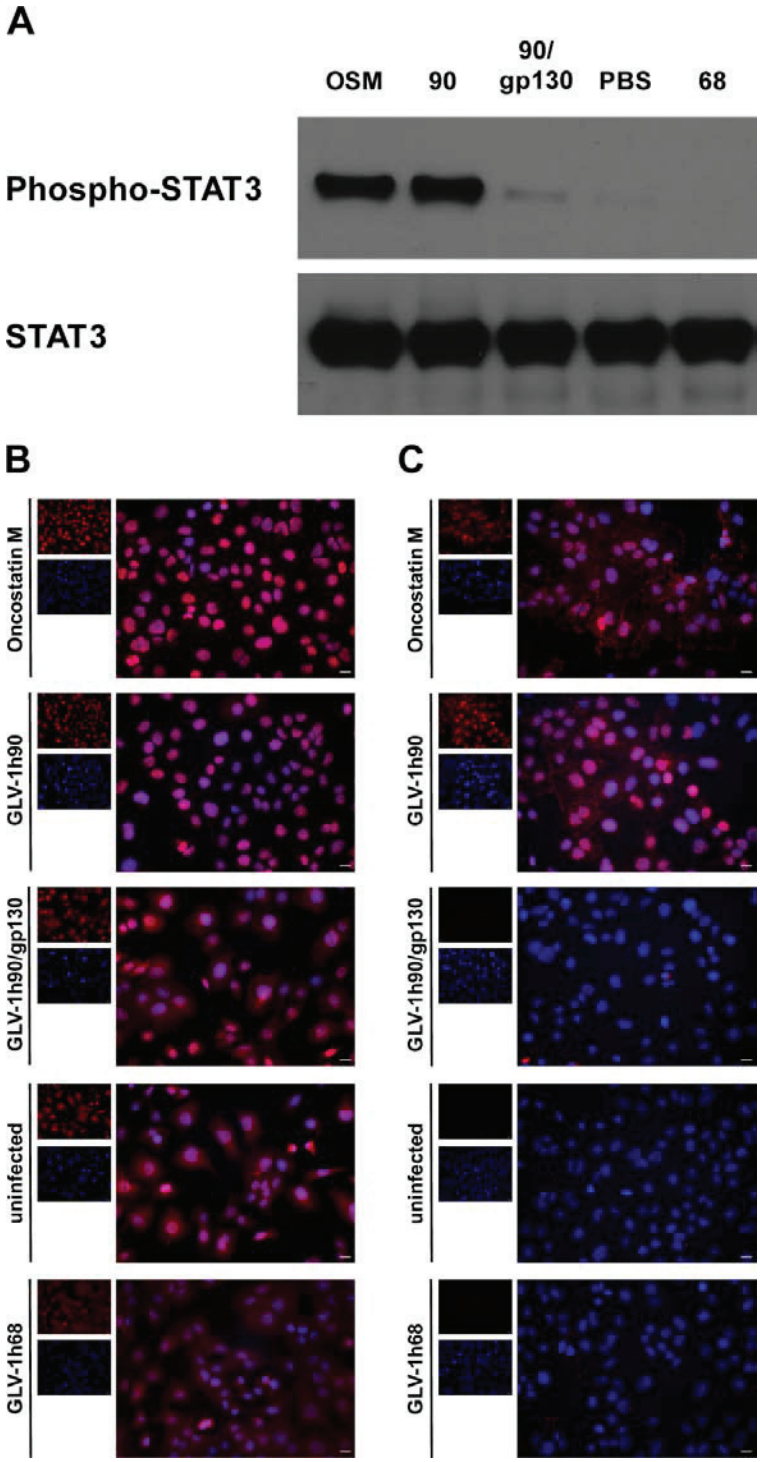

Figure 2 Hyper-IL-6 dependent activation of the JAK/STAT signaling pathway. (A) Western blot analysis of phosphorylated STAT3 (P-STAT3) and unphosphorylated STAT3 in DU-145 cells after co-incubation with sterile filtered supernatants of mock- (-), GLV-1h68- (68) or GLV-1h90- (90) infected cells. Oncostatin M (OSM) served as positive control and gp130/Fc chimera was added in excess to the supernatants of GLV-1h90-infected cells (90/gp130) to show specific activation via cellular gp130. Hyper-IL-6 and oncostatin M dependent migration of STAT3 into the nuclei (B) and phosphorylation (C) of STAT3 in DU-145 cells were proven by immunofluorescent microscopy. Overlay images (large picture) resulting from cells stained for (phosphorylated) STAT3 (red), and Hoechst 33342 stained nuclei (blue) were depicted. Scale bars indicate 8.6 μm.

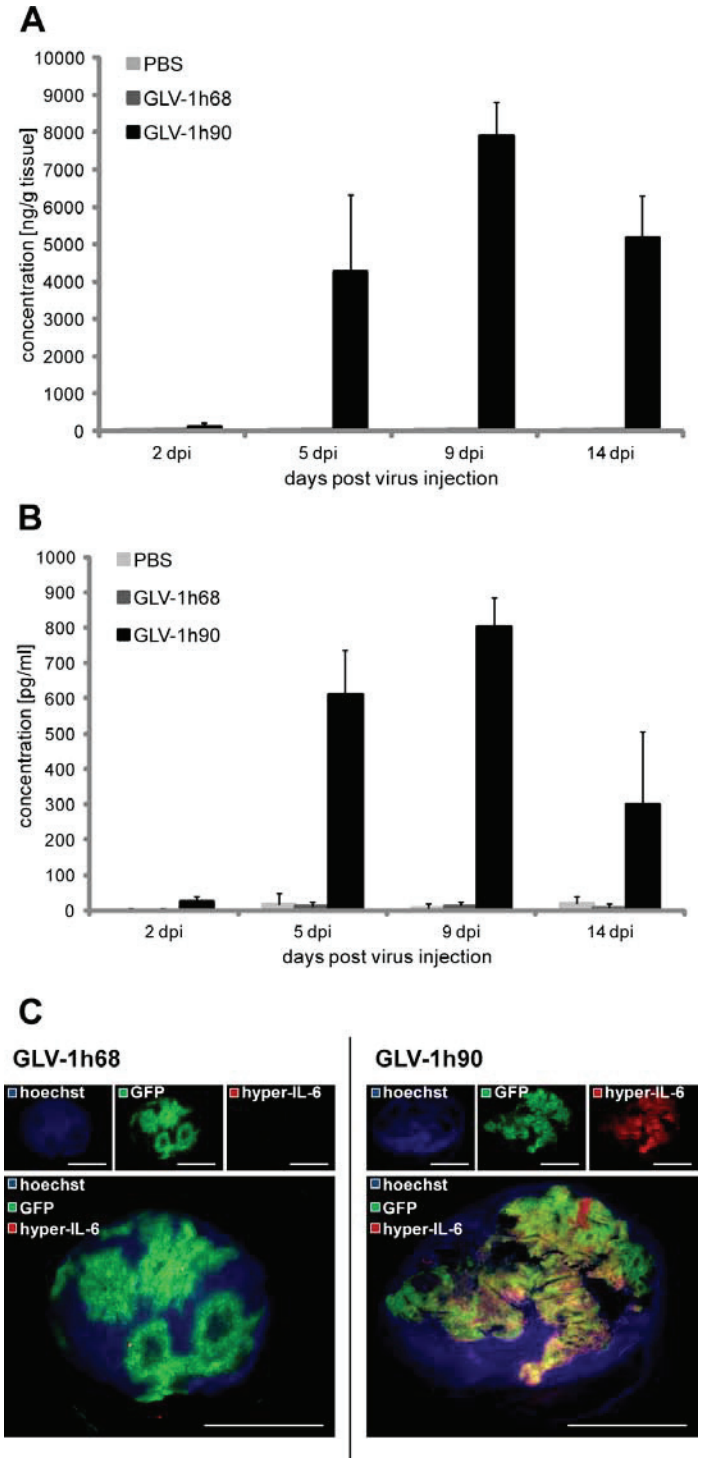

Figure 3 Detection of hyper-IL-6 in tumors and blood serum samples of GLV-1h90-injected mice. Quantification (ELISA) of hyper-IL-6 in tumor lysates (A) and blood serum samples (B) of mock-, 5×10^6 pfu GLV-1h68- or GLV-1h90-injected mice at 2, 5, 9 and 14 dpi. (C) Whole tumor cross sections (100 μm) 11 days post injection of 5×10^6 pfu GLV-1h68 or GLV-1h90 were stained with anti-IL-6 antibody (red) to confirm hyper-IL-6 expression only in GLV-1h90-infected tumors. Viral infection was indicated by GFP (green), and nuclei were stained with Hoechst 33342 (blue). Scale bars indicate 5 mm.

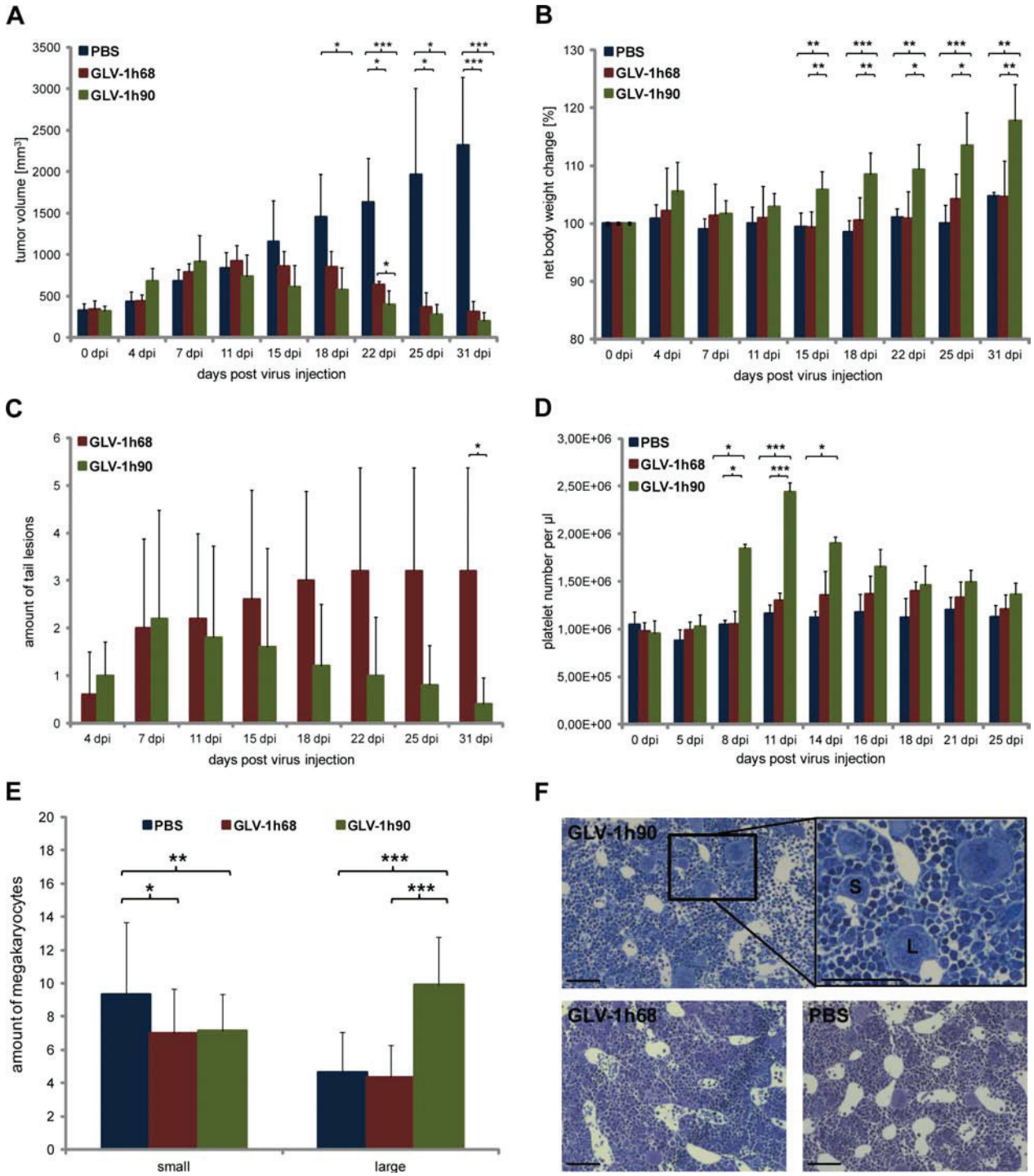

Figure 4 Effects of GLV-1h90 in a DU-145 xenograft mouse model. (A) Tumor measurements of DU-145 tumor bearing mice injected i.v. with PBS, 5×10^6 pfu GLV-1h68 or GLV-1h90 at 0, 4, 7, 11, 15, 18, 22, 25 and 31 dpi. (B) Net body weight change at the same time points. (C) Quantification of blood platelets in whole blood samples obtained by retro-orbital plexus puncture of PBS-, GLV-1h68- or GLV-1h90-injected mice. (D) Amount of tail lesions was counted over the whole experiment duration. Data represent average plus standard deviation for each group (n = 5). * indicates $p \leq 0.05$; ** indicates $p \leq 0.01$; *** indicates $p \leq 0.005$. (E) Quantification of megakaryocytes of different maturation stages 7 dpi in semi-this sections of the bone marrow. Data represent average of 2 analyzed areas (20 × 22 cm) per section with 5-8 sections per sample (n = 4) plus standard deviation. * indicates $p \leq 0.05$; ** indicates $p \leq 0.01$; *** indicates $p \leq 0.005$. (F) Examples for the analyzed bone marrow sections. S indicates small megakaryocytes; L indicates large megakaryocytes in advanced maturation phases; scale bars indicate 100 µm.

in the net body weight starting 15 dpi compared to GLV-1h68 or PBS injection. However, it was not investigated whether the increased weight could be attributed to tissue or fluid, althogh no obvious fluid retentions were detected. Furthermore, mice injected with the hyper-IL-6-encoding VACV seemed to be more active, which indicated (together with the increased weight) an improved health status of the mice.

Another indication for the health status of the mice was the number and fate of tail lesions. Mice injected with either viral construct developed tail lesions at the site of virus injection starting 4 dpi which began increasing over time. Seven dpi, the number of GLV-1h90-induced tail lesions were reduced markedly and by 31 dpi a significant difference was observed compared to mice injected with GLV-1h68 (on average 0.4 in GLV-1h90- and 3.2 tail lesions in GLV-1h68-injected mice) (Figure 4C and Additional File 1 Figure S1). The observed accelerated barrier repair of tail lesions can be the result of direct or indirect antiviral activity mediated by IL-6 [29], keeping in mind that tail lesions are not only wounds which occur after tissue injury, but rather are associated with viral infection.

Barrier repair is a tightly regulated process in which blood platelets play an important role. Based on this, we analyzed whether overexpression of hyper-IL-6 leads to elevated levels of blood platelets in GLV-1h90-injected mice. Figure 4D shows that, in contrast to PBS or GLV-1h68, GLV-1h90 injection into DU-145 tumor-bearing mice significantly increased the number of platelets in the blood first detected 8 dpi and reached its maximum around 11 dpi which was about 2-fold increased compared to the other experimental groups. Subsequently, platelet concentration decreased and was nearly at baseline at 25 dpi. The number of neutrophils, lymphocytes and monocytes and red blood cells as well as hemoglobin levels showed normal levels with no differences between GLV-1h90-injected mice and the control groups (data not shown).

To further characterize if the increased platelet production was due to a hyper-IL-6-dependent stimulation of megakaryopoiesis in the bone marrow, megakaryocytes of different maturation phases were quantified in semi-thin cuts of the bone marrow. After injection of GLV-1h90, significant higher numbers of megakaryocytes could be detected in an advanced maturation phase (indicated by bigger size due to polyploidy) compared to GLV-1h68- or PBS-injected mice. At the same time, significant lower numbers of megakaryocytes could be visualized in early stages of megakaryopoiesis with smaller size in GLV-1h90-treated when compared to PBS-treated mice. The GLV-1h68-group showed lower megakaryocyte numbers in both analyzed maturation phases (Figure 4EF).

Combination therapy with mitomycin C

Recently, we and others have demonstrated that the combination of oncolytic virotherapy with chemotherapy could lead to interactions that ultimately result in enhanced therapeutic effects [21,30]. On the other hand, chemotherapy is often associated with negative side effects, with thrombocytopenia one of the most frequently observed in cancer patients [31]. Consequently, we wanted to test the use of recombinant vaccinia virus-encoding hyper-IL-6 (GLV-1h90) instead of the parent virus GLV-1h68 in combination with the chemotherapeutic agent mitomycin C to improve not only the oncolytic effect but also the well being of the mice based on the observed effects of GLV-1h90. Mitomycin C is known to cause severe thrombocytopenia [32], which, as observed in first experiments, occurs around 7 days post chemotherapeutic treatment (data not shown). Therefore, as can be seen in the injection schedule (Figure 5A), we included mitomycin C injections at 4 and 5 days after initialization of virus treatment, assuming that GLV-1h90-induced production of thrombocytes could counteract chemotherapy-induced thrombocytopenia.

Combination therapy with mitomycin C and the oncolytic vaccinia virus strains led to a significantly improved DU-145 tumor regression compared to the respective monotherapies (Figure 5B). As early as 15 days post virus injection significant differences were observed between the groups injected with rVACV alone and those receiving the combination therapy regime. At that time, the tumor volume was already reduced to its initial dimension. In case of the rVACV monotherapy, it required ~ 22 days for the GLV-1h90- and 25 days for the GLV-1h68-injected group to reach the same tumor volume. Mitomycin C injection alone only led to tumor stagnation and therapeutic effects did not reach statistical significance when compared to PBS-treated controls.

As already observed in our previous experiment, tumor regression in GLV-1h90-injected animals was more pronounced compared to those injected with GLV-1h68, but again did not reach statistical significance. The same held true for the combination therapy with mitomycin C; although combination therapy was significantly better than the respective viral therapy alone, no significant differences in terms of tumor regression were observed between the GLV-1h68 and GLV-1h90 combination therapy groups.

However, analysis of the number of tail lesions revealed significant variations (Figure 5C and Additional File 2 Figure S2), indicating that combination of the viral constructs with the chemotherapeutic agent mitomycin C did not have any effects on wound healing. Approximately one week after virus injection the number of tail lesions decreased in GLV-1h90-injected mice

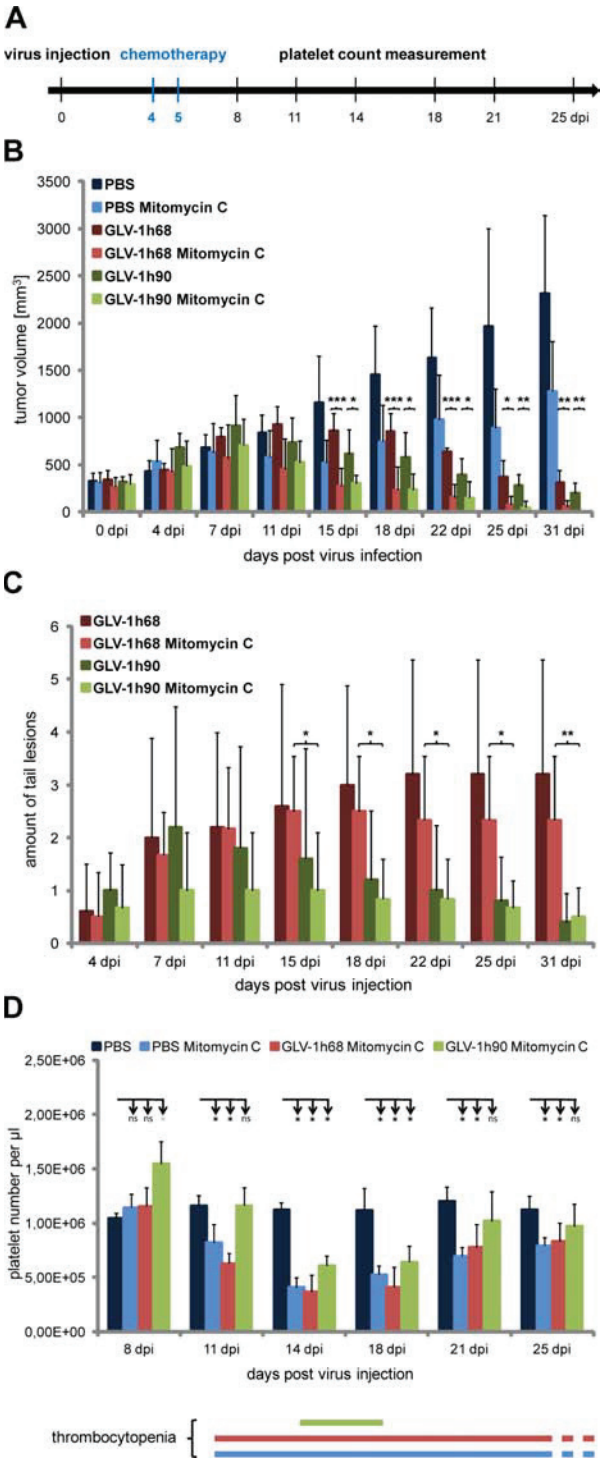

Figure 5 Combination therapy of GLV-1h90 with mitomycin C. (A) Injection schedule. (B) Tumor growth curve of DU-145 tumor bearing mice injected either with PBS, 5×10^6 pfu GLV-1h68 or GLV-1h90 alone or in combination with mitomycin C. Tumor volume was measured at 0, 4, 7, 11, 15, 18, 22 and 25 dpi. (C) Amount of tail lesions was counted starting 4 dpi, the time point when they occurred. (D) Quantification of blood platelets in whole blood samples of mice injected with PBS alone as well as of mice injected with PBS, GLV-1h68 or GLV-1h90 each in combination with mitomycin C at 8, 11, 14, 18, 21 and 25 dpi. The lower panel shows duration of thrombocytopenia in mice treated with mitomycin C. Thrombocytopenia is defined by a significantly decreased platelet number in relation to PBS-injected mice. Data in B, C and D represent average plus standard deviation for each group (n = 5). * indicates $p \leq 0.05$; ** indicates $p \leq 0.01$; *** indicates $p \leq 0.005$; ns not significant.

while remaining stable or slightly increased in the GLV-1h68-injected groups.

Noteable was the finding that GLV-1h90 significantly reduced the time interval during which the mice suffered from thrombocytopenia (Figure 5D). Compared to PBS-injected mice, the treatment with mitomycin C resulted in significantly reduced platelet numbers for at least two weeks (from day 11 to at least day 25) in the PBS plus mitomycin C as well as in the GLV-1h68 plus mitomycin C groups. In contrast, combination of GLV-1h90 and mitomycin C led to a delayed occurrence of thrombocytopenia, as well as acceleration of the recovery process. Consequently, reduced platelet numbers were detectable for less than one week in the GLV-1h90 plus mitomycin C-injected group (14 to 18 dpi).

Taken together, functionally expressed hyper-IL-6 through i.v. delivered vaccinia virus optimized the combination therapy of the oncolytic virus GLV-1h90 and the chemotherapeutic agent mitomycin C. Besides the improved oncolytic effect, which also occurred with the parental strain GLV-1h68, GLV-1h90 was further able to significantly reduce thrombocytopenia, a negative side effect caused by the chemotherapeutic agent.

Discussion

Among the currently investigated cancer therapies, the use of oncolytic vaccinia virus strains appear to be one of the most promising against a wide range of solid tumors [33]. While initial clinical trials using engineered oncolytic vaccinia virus strains have already been carried out [19,34], current research focuses on enhancing the already promising therapeutic effects of these viruses. This includes virus-mediated expression of immune-modulatory molecules [35,36], and combination with alternative therapies, such as prodrug therapy [37,38], radiation (Advani et al., submitted), or conventional chemotherapy [21,36]. The latter have been described to be very effective, but still suffer from the disadvantage of severe side effects.

Here, the hyper-IL-6-encoding rVACV strain GLV-1h90 was used to reduce the side effects resulting from the chemotherapeutic agent mitomycin C. This chemotherapeutic agent, as well as most other agents, is known to cause severe thrombocytopenia in mice as well as in human patients [32,39]. Interleukin-6 is a cytokine with multifunctional actions including regulation of immune responses [40,41], induction of acute-phase reactant release from hepatocytes [42] and enhancement of proliferation of hematopoietic progenitors [3]. In particular, the IL-6-promoted megakaryocyte maturation in the absence of other added growth factors, which leads to elevated platelet production [43,44] is an important focus when contemplating its implications on chemotherapy-induced thrombocytopenia.

Systemic administration of GLV-1h90 into DU-145 tumor-bearing mice led to significant tumor regression compared to mock-injected mice. This anti-tumor effect in this tumor model, as well as others, has been shown to be similar to that achieved by treatment with GLV-1h68 (data not shown). This result suggests that hyper-IL-6 itself has no significant direct anti-tumor activity or that virus-mediated oncolysis is, in the model systems tested, the most prominent factor responsible for tumor destruction, which may therefore mask potential cytokine effects.

However, our results clearly indicated that hyper-IL-6 maintained its biological activity when encoded by the oncolytic vaccinia virus strain. Large amounts of the cytokine were produced in and secreted from infected tumor cells in cell culture as well as in live animals. Secretion is crucial since the presence of hyper-IL-6 in blood is needed for the designer-cytokine to act outside the tumor tissue such as on megakaryocytes in the bone marrow [43,44] or on skin keratinocytes [45].

Hyper-IL-6-dependent activation of the JAK/STAT pathway was demonstrated on a molecular level by Western blot analysis and immunohistochemistry in cell culture. Furthermore, functionality of hyper-IL-6 in tumor-bearing mice resulted in elevated acute phase proteins (data not shown) as well as in accelerated epithelial barrier repair of tail lesions. IL-6 is known to affect multiple processes which are related to wound healing including attraction of neutrophils and their adhesion to dermal fibroblasts [46], recruitment of monocyte/macrophages responsible for clearance of debris and the provision of growth and angiogenic factors [47] and stimulation of keratinocyte proliferation which accelerates re-epithelialization after injury [45,48]. Furthermore, the observed accelerated barrier repair of tail lesions can be the result of direct or indirect antiviral activity mediated by IL-6 [29], keeping in mind that tail lesions are not only wounds which occur after tissue injury, but rather are associated with viral infection. Thus, future experiments are planned to investigate which processes are crucial in the here observed improved wound healing.

In addition, elevated platelet numbers in the blood circulation of mice injected with the hyper-IL-6 virus may also contribute to the accelerated healing of tail lesions [49]. In the blood of GLV-1h90-injected mice the platelet concentration increased after 5 dpi and reached its maximum around 11 dpi after which their concentration declined. A similar peak, about 2-3 days earlier, was also observed for the hyper-IL-6 concentration in the tumors as well as in the sera of GLV-1h90-injected mice. This suggests that, as a result of the intratumoral overexpression, hyper-IL-6 ends up in the blood circulation and can reach the bone marrow, where the designer cytokine can stimulate megakaryopoiesis. This process in turn leads to

increased production of platelets, which could then be found in the blood several days later [43]. This hypothesis could be proven by quantification of different maturation phases of megakaryocytes in semi-thin cuts of the bone marrow. Besides thrombopoietin (TPO), the main regulator of megakaryopoiesis, many pro-inflammatory cytokines are known to stimulate, either alone or in conjunction with TPO, platelet production during megakaryopoiesis. While interleukin-3 is essential in early steps of megakaryopoiesis, IL-6 is postulated to be mainly involved in a process called endomitosis, which include megakaryocyte proliferation, cell growth as well as formation of polyploidy at the latest phase of megakaryopoiesis. The observation that, compared to both control groups, 7 dpi significant higher numbers of megakaryocytes in advanced maturation phases could be detected in bone marrow sections of GLV-1h90-injected mice confirms the assumption that hyper-IL-6 was able to stimulate megakaryopoiesis which in turn leads to elevated platelet numbers 3-4 days later. The platelet decrease might reflect the therapeutic effects caused by the virus, reducing the amount of viable (hyper-IL-6 producing) tumor cells. The results also illustrate that possible complications associated with the overexpression of cytokines can be self-limiting due to the destruction of the virus replication site.

Here, we showed for the first time, that oncolytic tumor therapy could be optimized through reduction of therapeutic side effects associated with chemotherapy such as thrombocytopenia, in mice receiving combination therapy with mitomycin C by using a hyper-IL-6-encoding vaccinia virus. The time period that mice experienced thrombocytopenia was reduced by at least 50% (less than one week compared to at least 2 weeks). Moreover, the combination of mitomycin C with either of the oncolytic vaccinia virus strains GLV-1h68 or GLV-1h90 resulted in significantly enhanced therapeutic effects.

Taken together, GLV-1h90 resulted in the production of the functionally active designer-cytokine hyper-IL-6 thereby retaining the oncolytic effects of its parental strain GLV-1h68. Maybe even more importantly, GLV-1h90 significantly improved the wellbeing of mice during combination therapy with mitomycin C.

For translation into the clinic, future studies on a higher number of tumor models will have to show if this also holds true for combinations with other chemotherapeutic agents, and whether other cytokines such as IL-2 and IL-11 that are already applied for treatment of thrombocytopenia in cancer patients receiving chemotherapy, will be as efficacious or maybe even superior to hyper-IL-6 in reducing thrombocytopenia and improving overall wellbeing in combination with oncolytic viral therapy.

Conclusion

We have shown that the oncolytic vaccinia virus strain GLV-1h90 can be used to functionally express the designer cytokine hyper-IL-6 in human tumor xenografts of live mice. Hyper-IL-6 was secreted from the infected tumor tissue into the circulatory system enabling it to induce systemic effects. This was used, for the first time, to improve combination of oncolytic vaccinia virus therapy with conventional chemotherapy. Although this has previously been shown to have remarkable success in preclinical tumor models, the virus-mediated expression of the designer cytokine hyper-IL-6 offered a new approach to significantly reduce the duration of thrombocytopenia, a serious side effect of chemotherapy. Therefore, future pre-clinical studies investigating combination treatment with chemotherapy would benefit from careful investigation into the possibility of additional cytokine expression to reduce chemotherapy-induced side effects before progression to clinical trials.

Additional material

Additional file 1: Figure S1. Effect of hyper-IL-6 on epithelial barrier repair of tail lesions. Fluorescence microscopy of tail lesions of DU-145 tumor-bearing mice injected with 5×10^6 pfu GLV-1h68 (left panels) or GLV-1h90 (right panels), respectively. Viral infection was indicated by GFP (green). Images were taken at 25 dpi with a stereo-fluorescence microscope (MZ16 FA, Leica, Heerbrugg, Switzerland) equipped with a digital CCD camera (DC500, Leica) and the Leica IM1000 4.0 acquisition software. Digital images (1300 × 1030 pixel color images) were processed with Photoshop 7.0 (Adobe Systems, USA) and merged to overlay pictures. Scale bars in the upper panels indicate 5 mm; scale bars in the lower panels indicate 1 mm.

Additional file 2: Figure S2. Epithelial barrier repair of GLV-1h68- or GLV-1h90-induced tail lesions in combination therapy with mitomycin C. Fluorescence microscopy of tail lesions of DU-145 tumor bearing mice injected either with 5×10^6 pfu GLV-1h68 or GLV-1h90 alone or in each case in combination with mitomycin C at 25 dpi. Viral infection was indicated by GFP (green). Images were taken with a stereo-fluorescence microscope (MZ16 FA, Leica, Heerbrugg, Switzerland) equipped with a digital CCD camera (DC500, Leica) and the Leica IM1000 4.0 acquisition software. Digital images (1300 × 1030 pixel color images) were processed with Photoshop 7.0 (Adobe Systems, USA) and merged to overlay pictures. Scale bars indicate 5 mm.

List of abbreviations

dpi: days post infection; ELISA: enzyme-linked immunosorbent assay; FBS: fetal bovine serum; GFP: Green fluorescent protein; GM-CSF: *Granulocyte-macrophage colony-stimulating factor*, hpi: hours post-infection; HA: hemagluttinin; HRP: horseradish peroxidase; IL: interleukin; IL-6TS: IL-6 trans-signaling; i.v.: intravenous; mIL-6-R: membrane bound IL-6 receptor; rVACV: recombinant vaccinia virus strain; sIL-6-R: soluble IL-6 receptor; TK: thymidine kinase.

Acknowledgements

We would like to thank T. Trevino and J. Aguilar for assistance with GLV-1h90 production, A. Seidensal for help with cell culture and J. Langbein for excellent technical assistance. Furthermore, we would like to thank D. Haddad for her excellent editorial help. This publication was funded by the German Research Foundation (DFG) and the University of Würzburg in the

funding programme Open Access Publishing. This work was supported by Genelux Corporation (R&D facility in San Diego, CA, USA) and Genelux GmbH, a Service Grant to the University of Würzburg, Germany also funded by Genelux Corp., San Diego, USA.

Author details
[1]Department of Biochemistry, University of Würzburg, 97074 Würzburg, Germany. [2]Genelux Corporation, San Diego Science Center, San Diego, CA 92109, USA. [3]Department of Radiation Oncology, Rebecca & John Moores Comprehensive Cancer Center, University of California San Diego, La Jolla, CA 92093, USA. [4]Institute of Clinical Biochemistry and Pathobiochemistry, University of Würzburg, 97080 Würzburg, Germany. [5]Division of Electron Microscopy, University of Würzburg, 97074 Würzburg, Germany.

Authors' contributions
JBS conceived the study, designed, performed and analyzed all experiments and wrote the manuscript. MH and UD participated in experimental design and performance. JS participated in conceiving the study, experiment analyzation and manuscript writing. SW, GK, CR and SG participated in conceiving the study. NGC, QZ and YAY participated in manuscript writing and provided essential material. AAS participated in conceiving the study and writing the manuscript. All authors read and approved the final version of the manuscript.

Authors' information
JS, NGC, QZ and AAS are employees and shareholders of Genelux Corporation and Genelux GmbH respectively. SW, UD, GK, CR and SG are employees of the University of Würzburg. JBS and MH are supported by graduate stipends from Genelux Corporation. The funders had no role in study design, data collection and analysis or decision to publish.

Competing interests
The research was supported by the Research and Development Division of Genelux Corp., San Diego, USA, and a Service Grant to the University of Würzburg, Germany also funded by Genelux Corp., San Diego, USA. JS, NGC, QZ and AAS are employees and shareholders of Genelux Corporation and Genelux GmbH respectively. SW, UD, GK, CR and SG are employees of the University of Würzburg. JBS and MH are supported by graduate stipends from Genelux Corporation. The funders had no role in study design, data collection and analysis or decision to publish. No competing intersts exist for JBS, MH, SW, UD, GK, CR and SG.

Received: 4 November 2011 Accepted: 11 January 2012
Published: 11 January 2012

References

1. Kishimoto T, Akira S, Narazaki M, Taga T: **Interleukin-6 family of cytokines and gp130.** *Blood* 1995, **86**:1243-1254.
2. Kushner I: **Regulation of the acute phase response by cytokines.** *Perspect Biol Med* 1993, **36**:611-622.
3. Wong GG, Witek-Giannotti JS, Temple PA, Kriz R, Ferenz C, Hewick RM, Clark SC, Ikebuchi K, Ogawa M: **Stimulation of murine hemopoietic colony formation by human IL-6.** *J Immunol* 1988, **140**:3040-3044.
4. Kerr R, Stirling D, Ludlam CA: **Interleukin 6 and haemostasis.** *Br J Haematol* 2001, **115**:3-12.
5. Mumm JB, Oft M: **Cytokine-based transformation of immune surveillance into tumor-promoting inflammation.** *Oncogene* 2008, **27**:5913-5919.
6. Oh JW, Katz A, Harroch S, Eisenbach L, Revel M, Chebath J: **Unmasking by soluble IL-6 receptor of IL-6 effect on metastatic melanoma: growth inhibition and differentiation of B16-F10.9 tumor cells.** *Oncogene* 1997, **15**:569-577.
7. Ganapathi MK, Weizer AK, Borsellino S, Bukowski RM, Ganapathi R, Rice T, Casey G, Kawamura K: **Resistance to interleukin 6 in human non-small cell lung carcinoma cell lines: role of receptor components.** *Cell Growth Differ* 1996, **7**:923-929.
8. Hong DS, Angelo LS, Kurzrock R: **Interleukin-6 and its receptor in cancer: implications for translational therapeutics.** *Cancer* 2007, **110**:1911-1928.
9. Jones SA, Rose-John S: **The role of soluble receptors in cytokine biology: the agonistic properties of the sIL-6R/IL-6 complex.** *Biochim Biophys Acta* 2002, **1592**:251-263.
10. Scheller J, Ohnesorge N, Rose-John S: **Interleukin-6 trans-signalling in chronic inflammation and cancer.** *Scand J Immunol* 2006, **63**:321-329.
11. Ihara S, Nakajima K, Fukada T, Hibi M, Nagata S, Hirano T, Fukui Y: **Dual control of neurite outgrowth by STAT3 and MAP kinase in PC12 cells stimulated with interleukin-6.** *EMBO J* 1997, **16**:5345-5352.
12. Rawlings JS, Rosler KM, Harrison DA: **The JAK/STAT signaling pathway.** *J Cell Sci* 2004, **117**:1281-1283.
13. Fischer M, Goldschmitt J, Peschel C, Brakenhoff JP, Kallen KJ, Wollmer A, Grotzinger J, Rose-John S: **I. A bioactive designer cytokine for human hematopoietic progenitor cell expansion.** *Nat Biotechnol* 1997, **15**:142-145.
14. Chebath J, Fischer D, Kumar A, Oh JW, Kolett O, Lapidot T, Fischer M, Rose-John S, Nagler A, Slavin S, Revel M: **Interleukin-6 receptor-interleukin-6 fusion proteins with enhanced interleukin-6 type pleiotropic activities.** *Eur Cytokine Netw* 1997, **8**:359-365.
15. Peters M, Blinn G, Solem F, Fischer M, Meyer zum Buschenfelde KH, Rose-John S: **In vivo and in vitro activities of the gp130-stimulating designer cytokine Hyper-IL-6.** *J Immunol* 1998, **161**:3575-3581.
16. Carroll MW, Moss B: **Poxviruses as expression vectors.** *Curr Opin Biotechnol* 1997, **8**:573-577.
17. Yu YA, Shabahang S, Timiryasova TM, Zhang Q, Beltz R, Gentschev I, Goebel W, Szalay AA: **Visualization of tumors and metastases in live animals with bacteria and vaccinia virus encoding light-emitting proteins.** *Nat Biotechnol* 2004, **22**:313-320.
18. Frentzen A, Yu YA, Chen N, Zhang Q, Weibel S, Raab V, Szalay AA: **Anti-VEGF single-chain antibody GLAF-1 encoded by oncolytic vaccinia virus significantly enhances antitumor therapy.** *Proc Natl Acad Sci USA* 2009, **106**:12915-12920.
19. Liu TC, Hwang T, Park BH, Bell J, Kirn DH: **The targeted oncolytic poxvirus JX-594 demonstrates antitumoral, antivascular, and anti-HBV activities in patients with hepatocellular carcinoma.** *Mol Ther* 2008, **16**:1637-1642.
20. Zhang Q, Yu YA, Wang E, Chen N, Danner RL, Munson PJ, Marincola FM, Szalay AA: **Eradication of solid human breast tumors in nude mice with an intravenously injected light-emitting oncolytic vaccinia virus.** *Cancer Res* 2007, **67**:10038-10046.
21. Yu YA, Galanis C, Woo Y, Chen N, Zhang Q, Fong Y, Szalay AA: **Regression of human pancreatic tumor xenografts in mice after a single systemic injection of recombinant vaccinia virus GLV-1h68.** *Mol Cancer Ther* 2009, **8**:141-151.
22. Society AC: **Chemotherapy Principles: An In-depth Discussion.** 2010 [http://www.cancer.org/Treatment/TreatmentsandSideEffects].
23. Elting LS, Rubenstein EB, Martin CG, Kurtin D, Rodriguez S, Laiho E, Kanesan K, Cantor SB, Benjamin RS: **Incidence, cost, and outcomes of bleeding and chemotherapy dose modification among solid tumor patients with chemotherapy-induced thrombocytopenia.** *J Clin Oncol* 2001, **19**:1137-1146.
24. Dirks WG, Drexler HG: **Online verification of human cell line identity by STR DNA typing.** *Methods Mol Biol* 2011, **731**:45-55.
25. Falkner FG, Moss B: **Transient dominant selection of recombinant vaccinia viruses.** *J Virol* 1990, **64**:3108-3111.
26. Heinrich PC, Behrmann I, Muller-Newen G, Schaper F, Graeve L: **Interleukin-6-type cytokine signalling through the gp130/Jak/STAT pathway.** *Biochem J* 1998, **334(Pt 2)**:297-314.
27. Stritzker J, Weibel S, Hill PJ, Oelschlaeger TA, Goebel W, Szalay AA: **Tumor-specific colonization, tissue distribution, and gene induction by probiotic *Escherichia coli* Nissle 1917 in live mice.** *Int J Med Microbiol* 2007, **297**:151-162.
28. Heinrich PC, Behrmann I, Haan S, Hermanns HM, Muller-Newen G, Schaper F: **Principles of interleukin (IL)-6-type cytokine signalling and its regulation.** *Biochem J* 2003, **374**:1-20.
29. Kopf M, Baumann H, Freer G, Freudenberg M, Lamers M, Kishimoto T, Zinkernagel R, Bluethmann H, Kohler G: **Impaired immune and acute-phase responses in interleukin-6-deficient mice.** *Nature* 1994, **368**:339-342.
30. Mahoney DJ, Stojdl DF: **Potentiating oncolytic viruses by targeted drug intervention.** *Curr Opin Mol Ther* 2010, **12**:394-402.
31. Kaushansky K: **The thrombocytopenia of cancer. Prospects for effective cytokine therapy.** *Hematol Oncol Clin North Am* 1996, **10**:431-455.
32. Akahori H, Shibuya K, Ozai M, Ida M, Kabaya K, Kato T, Miyazaki H: **Effects of pegylated recombinant human megakaryocyte growth and development factor on thrombocytopenia induced by a new myelosuppressive chemotherapy regimen in mice.** *Stem Cells* 1996, **14**:678-689.

33. Kirn DH, Thorne SH: **Targeted and armed oncolytic poxviruses: a novel multi-mechanistic therapeutic class for cancer.** *Nat Rev Cancer* 2009, **9**:64-71.
34. Chen NG, Szalay AA: **Oncolytic vaccinia virus: a theranostic agent for cancer.** *Future Virology* 2010, **5**:763-784.
35. Kim JH, Oh JY, Park BH, Lee DE, Kim JS, Park HE, Roh MS, Je JE, Yoon JH, Thorne SH, *et al*: **Systemic armed oncolytic and immunologic therapy for cancer with JX-594, a targeted poxvirus expressing GM-CSF.** *Mol Ther* 2006, **14**:361-370.
36. Ziauddin MF, Guo ZS, O'Malley ME, Austin F, Popovic PJ, Kavanagh MA, Li J, Sathaiah M, Thirunavukarasu P, Fang B, *et al*: **TRAIL gene-armed oncolytic poxvirus and oxaliplatin can work synergistically against colorectal cancer.** *Gene Ther* 2010, **17**:550-559.
37. Foloppe J, Kintz J, Futin N, Findeli A, Cordier P, Schlesinger Y, Hoffmann C, Tosch C, Balloul JM, Erbs P: **Targeted delivery of a suicide gene to human colorectal tumors by a conditionally replicating vaccinia virus.** *Gene Ther* 2008, **15**:1361-1371.
38. Seubert CM, Stritzker J, Hess M, Donat U, Sturm JB, Chen N, von Hof JM, Krewer B, Tietze LF, Gentschev I, Szalay AA: **Enhanced tumor therapy using vaccinia virus strain GLV-1h68 in combination with a beta-galactosidase-activatable prodrug seco-analog of duocarmycin SA.** *Cancer Gene Ther* 2011, **18**:42-52.
39. Cantrell JE Jr, Phillips TM, Schein PS: **Carcinoma-associated hemolytic-uremic syndrome: a complication of mitomycin C chemotherapy.** *J Clin Oncol* 1985, **3**:723-734.
40. Cronstein BN: **Interleukin-6–a key mediator of systemic and local symptoms in rheumatoid arthritis.** *Bull NYU Hosp Jt Dis* 2007, **65(Suppl 1)**: S11-15.
41. Park JY, Pillinger MH: **Interleukin-6 in the pathogenesis of rheumatoid arthritis.** *Bull NYU Hosp Jt Dis* 2007, **65(Suppl 1)**:S4-10.
42. Gauldie J, Northemann W, Fey GH: **IL-6 functions as an exocrine hormone in inflammation. Hepatocytes undergoing acute phase responses require exogenous IL-6.** *J Immunol* 1990, **144**:3804-3808.
43. Ishibashi T, Kimura H, Shikama Y, Uchida T, Kariyone S, Hirano T, Kishimoto T, Takatsuki F, Akiyama Y: **Interleukin-6 is a potent thrombopoietic factor in vivo in mice.** *Blood* 1989, **74**:1241-1244.
44. Ishibashi T, Kimura H, Uchida T, Kariyone S, Friese P, Burstein SA: **Human interleukin 6 is a direct promoter of maturation of megakaryocytes in vitro.** *Proc Natl Acad Sci USA* 1989, **86**:5953-5957.
45. Grossman RM, Krueger J, Yourish D, Granelli-Piperno A, Murphy DP, May LT, Kupper TS, Sehgal PB, Gottlieb AB: **Interleukin 6 is expressed in high levels in psoriatic skin and stimulates proliferation of cultured human keratinocytes.** *Proc Natl Acad Sci USA* 1989, **86**:6367-6371.
46. Giuliani AL, Spisani S, Cavalletti T, Reali E, Melchiorri L, Ferrari L, Lanza F, Traniello S: **Fibroblasts increase adhesion to neutrophils after stimulation with phorbol ester and cytokines.** *Cell Immunol* 1993, **149**:208-222.
47. Leibovich SJ, Ross R: **The role of the macrophage in wound repair. A study with hydrocortisone and antimacrophage serum.** *Am J Pathol* 1975, **78**:71-100.
48. Sato M, Sawamura D, Ina S, Yaguchi T, Hanada K, Hashimoto I: **In vivo introduction of the interleukin 6 gene into human keratinocytes: induction of epidermal proliferation by the fully spliced form of interleukin 6, but not by the alternatively spliced form.** *Arch Dermatol Res* 1999, **291**:400-404.
49. Martin P, Leibovich SJ: **Inflammatory cells during wound repair: the good, the bad and the ugly.** *Trends Cell Biol* 2005, **15**:599-607.

doi:10.1186/1479-5876-10-9
Cite this article as: Sturm *et al.*: Functional hyper-IL-6 from vaccinia virus-colonized tumors triggers platelet formation and helps to alleviate toxicity of mitomycin C enhanced virus therapy. *Journal of Translational Medicine* 2012 **10**:9.

Figure S1

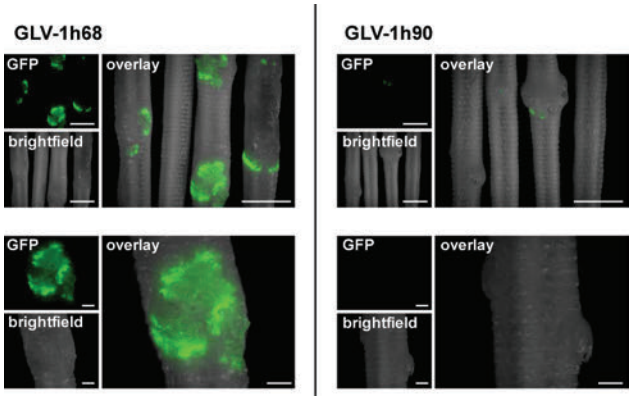
GLV-1h68
GFP
overlay
brightfield
GFP
overlay
brightfield
GLV-1h90
GFP
overlay
brightfield
GFP
overlay
brightfield

Figure S2

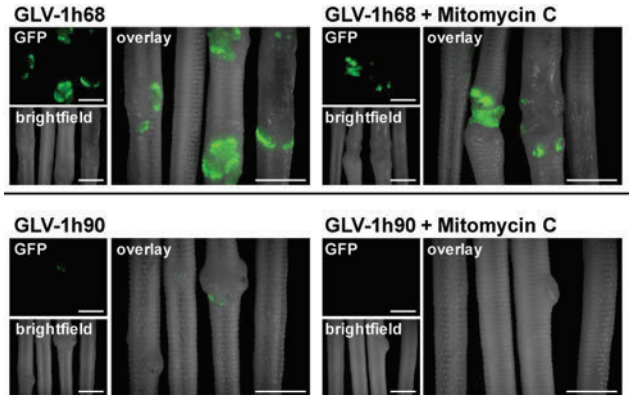
GLV-1h68
GFP
overlay
brightfield
GLV-1h68 + Mitomycin C
GFP
overlay
brightfield
GLV-1h90
GFP
overlay
brightfield
GLV-1h90 + Mitomycin C
GFP
overlay
brightfield

Publication (complete reference): Gentschev I, Ehrig K, Donat U, **Hess M**, Rudolph S, Chen N, Yu YA, Zhang Q, Bullerdiek J, Nolte I, Stritzker J, Szalay AA. Significant growth inhibition of canine mammary carcinoma xenografts following treatment with oncolytic Vaccinia virus GLV-1h68. *J Oncol*. 2010;2010:736907
Authors' contributions
Conceived and designed the experiments: IG, KE, UD, **MH**, JS, AAS. Performed the experiments: IG, KE, UD, **MH**, SR, JS. Analyzed the data:. IG, KE, UD, **MH**, SR, JS. Contributed reagents/materials/analysis tools: NC, YAY, QZ, JB, IN. Wrote the paper: IG, AAS.

Ivaylo Gentschev	
Klaas Ehrig	
Ulrike Donat	
Stephan Rudolph	
Nanhai G. Chen	
Yong A. Yu	
Qian Zhang	
Jörn Bullerdiek	
Ingo Nolte	
Jochen Stritzker	
Aladar A. Szalay	

Hindawi Publishing Corporation
Journal of Oncology
Volume 2010, Article ID 736907, 10 pages
doi:10.1155/2010/736907

Research Article

Significant Growth Inhibition of Canine Mammary Carcinoma Xenografts following Treatment with Oncolytic Vaccinia Virus GLV-1h68

Ivaylo Gentschev,[1,2] Klaas Ehrig,[2] Ulrike Donat,[2] Michael Hess,[2] Stephan Rudolph,[2] Nanhai Chen,[1] Yong A. Yu,[1] Qian Zhang,[1] Jörn Bullerdiek,[3,4] Ingo Nolte,[4] Jochen Stritzker,[1,2] and Aladar A. Szalay[1,2,5,6,7]

[1] *Genelux Corporation, San Diego Science Center, San Diego, CA 92109, USA*
[2] *Department of Biochemistry, University of Wuerzburg, 97074 Wuerzburg, Germany*
[3] *Center for Human Genetics, University of Bremen, 28359 Bremen, Germany*
[4] *Small Animal Clinic, University of Veterinary Medicine, Bischofsholer Damm 15, 30173 Hannover, Germany*
[5] *Rudolf Virchow Center for Experimental Biomedicine, University of Wuerzburg, 97078 Wuerzburg, Germany*
[6] *Institute for Molecular Infection Biology, University of Wuerzburg, 97078 Wuerzburg, Germany*
[7] *Department of Radiation Oncology, Moores Cancer Center, University of California, San Diego, 3855 Health Sciences Drive 0843, La Jolla, CA 92093-0843, USA*

Correspondence should be addressed to Aladar A. Szalay, aaszalay@genelux.com

Received 28 August 2009; Revised 18 February 2010; Accepted 11 May 2010

Academic Editor: Dominic Fan

Canine mammary carcinoma is a highly metastatic tumor that is poorly responsive to available treatment. Therefore, there is an urgent need to identify novel agents for therapy of this disease. Recently, we reported that the oncolytic vaccinia virus GLV-1h68 could be a useful tool for therapy of canine mammary adenoma *in vivo*. In this study we analyzed the therapeutic effect of GLV-1h68 against canine mammary carcinoma. Cell culture data demonstrated that GLV-1h68 efficiently infected and destroyed cells of the mammary carcinoma cell line MTH52c. Furthermore, after systemic administration, this attenuated vaccinia virus strain primarily replicated in canine tumor xenografts in nude mice. Finally, infection with GLV-1h68 led to strong inflammatory and oncolytic effects resulting in significant growth inhibition of the tumors. In summary, the data showed that the GLV-1h68 virus strain has promising potential for effective treatment of canine mammary carcinoma.

1. Introduction

Malignant tumors of the mammary glands are among the most frequently observed tumors in female dogs [1–3]. Despite the success in diagnosis and treatment of mammary cancer, this disease entity remains one of the leading causes of cancer-related death in female dogs. Therefore, there is an urgent need to identify novel agents for therapy and diagnosis of mammary cancer. Among the most promising new therapeutic candidates are oncolytic viruses, which can target tumor tissue and specifically eradicate the cancer cells. This concept was already confirmed in human tumor xenograft treatment by the use of several viruses [4–9].

In the present study, we tested the recombinant oncolytic vaccinia virus GLV-1h68 as a therapeutic agent against canine mammary carcinoma. The GLV-1h68 virus strain was engineered by inserting expression cassettes encoding a *Renilla* luciferase-green fluorescent protein (GFP) fusion protein, β-galactosidase, and β-glucuronidase into the genome of the wild-type strain LIVP [10]. In nude mouse models, GLV-1h68 is highly attenuated compared to the wild-type strain [10]. We have already demonstrated that the injection of

GLV-1h68 leads to regression and elimination of different tumor xenografts in nude mice [10–15]. More recently, we reported that GLV-1h68 could be a useful tool for therapy of canine mammary adenoma [12].

Here we describe that the GLV-1h68 virus successfully infected, replicated, and lysed canine mammary carcinoma MTH52c cells in cell culture. In addition, GLV-1h68 can efficiently prevent cancer growth in female nude mice with tumors derived from MTH52c cells. Finally, the localization and effects of GLV-1h68 in the primary tumor were analyzed by immunohistochemical studies and by mouse Immune-Related Protein Antigen Profiling.

2. Materials and Methods

2.1. Cell Culture. African green monkey kidney fibroblasts (CV-1) were obtained from the American Type Culture Collection (ATCC). MTH52c is derived from a malignant small-cell canine carcinoma [16].

Cells were cultured in DMEM supplemented with antibiotic solution (100 U/ml penicillin G, 100 units/ml streptomycin) and 10% fetal bovine serum (FBS; Invitrogen GmbH, Karlsruhe, Germany) for CV-1 and 20% FBS for MTH52c at 37°C under 5% CO_2.

2.2. Virus Strain. GLV-1h68 is a genetically stable oncolytic virus strain designed to locate, enter, colonize, and destroy cancer cells without harming healthy tissues or organs [10].

2.3. Cell Viability Assay with GLV-1h68. MTH52c cells were seeded in 24-well plates (Nunc, Wiesbaden, Germany). After 24 hours in culture, cells were infected with GLV-1h68 using multiplicities of infection (MOI) of 0.1 and 1.0. Cells were incubated at 37°C for 1 hour, after which the infection medium was removed, and cells were subsequently incubated in fresh growth medium. The amount of viable cells after infection with GLV-1h68 was measured as described previously [12].

2.4. Viral Replication. For the viral replication assay, MTH52c cells grown in 24-well plates were infected with GLV-1h68 at an MOI of 0.1. After one hour of incubation at 37°C with gentle agitation every 20 minutes, the infection medium was removed and replaced by a fresh growth medium. After 1, 6, 12, 24, 48, 72, and 96 hours, the cells and supernatants were harvested. Following three freeze-thaw cycles, serial dilutions of the lysates were titered by standard plaque assays on CV-1 cells. All samples were measured in triplicate.

2.5. Western Blot Analysis of Virus-Mediated Marker Proteins. Three days prior to infection, MTH52c cells were seeded in 24-well plates (Nunc, Wiesbaden, Germany). If not otherwise indicated, the 90% confluent cell layer was mock-infected or infected with GLV-1h68 at MOIs of 0.1 and 1.0 for 1 hour at 37°C. The virus-containing medium was aspirated and replaced by fresh medium containing 20% FBS. For protein isolation and detection, cells were harvested and resuspended in sodium dodecyl sulfate (SDS) sample buffer at one, 12, 24, 48, 72, and 96 hours post infection (hpi). The protein samples were separated by 10% SDS polyacrylamide gel electrophoresis (PAGE) and subsequently blotted onto a nitrocellulose membrane (Whatman GmbH, Dassel, Germany). The membrane was then incubated with anti-beta-actin mouse monoclonal antibodies (ab6276, Abcam, Cambridge, UK), anti-beta-galactosidase rabbit polyclonal antibodies (A-11132, Molecular Probes, Leiden, Netherlands), or anti-GFP rabbit polyclonal antibodies (sc-8334, Santa Cruz, Heidelberg, Germany), and detection was obtained using horseradish peroxidise-labeled secondary antibodies against mice (ab6728, Abcam, Cambridge, UK) or rabbits (ab6721, Abcam, Cambridge, UK) followed by enhanced chemiluminescence.

2.6. Fluorescence Imaging. The GFP signals of virus-infected cells and animals were analyzed with a fluorescence microscope (Leica DM IRB; Wetzlar, Germany) and a fluorescence stereomicroscope (Leica MZ 16 FA; Wetzlar, Germany), respectively. Images were captured with an electronic camera and were processed using META-MORPH (Universal Imaging; Downingtown, PA, USA) and Photoshop 7.0 (Adobe Systems, Mountain View, CA, USA).

2.7. Flow Cytometry (FACS) Analysis. MTH52c cells were grown on 24-well plates (Nunc, Wiesbaden, Germany) and infected by GLV-1h68 at an MOI of 0.1 or 1.0, respectively. At various time points, infected and noninfected MTH52c cells were harvested by Trypsin-EDTA treatment (PAA Laboratories GmbH, Pasching, Austria) and resuspended in PBS. For discrimination between viable and dead, MTH52c cells were stained using 2 μl propidium iodide (1mg/ml; Sigma, Taufkirchen, Germany) per 1 ml cell suspension for 5 min at room temperature. A minimum of 2×10^5 cells were then measured using an Epics XL flow cytometer (Beckman Coulter GmbH Krefeld, Germany).

2.8. Bioluminescence Imaging. For monitoring studies of the distribution of the GLV-1h68 virus in tumor-bearing mice, animals were analyzed for the presence of virus-dependent luciferase activity. For this purpose, mice were injected intravenously with a mixture of 5 μl of coelenterazine (Sigma, Taufkirchen, Germany; 0.5 μg/μl diluted ethanol solution) and 95 μl of luciferase assay buffer (0.5 M NaCl; 1 mM EDTA; 0.1 M potassium phosphate, pH 7.4). The animals were then anaesthetized with 2.5% Isoflurane (Forene, Abbott, Ludwigshafen, Germany) in a knockout box and were maintained in an anaesthesia module aerated with 1.5% Isoflurane/oxygen. The mice were imaged using the CCD-Camera-based NightOWL LB 981 Imaging System (Berthold Technologies, Bad Wildbad, Germany). Photons were collected for 5 minutes from dorsal views of the animals, and the images were recorded using Image WinLight 32 software (Berthold Technologies, Bad Wildbad, Germany).

2.9. GLV-1h68-Mediated Therapy of MTH52c Xenografts. Tumors were generated by 5×10^6 implanting cells in 100 μl

PBS subcutaneously into the right hind leg of 6- to 8-week-old female nude mice (NCI/Hsd/Athymic Nude-*Foxn*1^{nu}, Harlan Winkelmann GmbH, Borchen, Germany). Tumor growth was monitored 3 times weekly in two dimensions using a digital caliper. Tumor volume was calculated as [(length $\times$ width^2)/2]. On day 12, a single dose of GLV-1h68 virus (5×10^6 plaque forming units [pfu] in 100 μl PBS) was injected into the tail vein (i.v.). The control animals were injected i.v. with PBS only.

The significance of the results was calculated by two-way analysis of variance (ANOVA) using the GraphPad Prism software (San Diego, USA). Results are displayed as means $\pm$ s.d. (standard deviation). *P*-values of <.05 were considered significant.

The animals were euthanized by cervical dislocation. All animal experiments were approved by the government of Unterfranken and conducted according to the German animal protection guidelines.

2.10. Toxicity Studies. Mice with MTH52c xenograft tumors were developed to assess the biodistribution and toxicity of the GLV-1h68 virus. After virus infection, animals were observed daily for any sign of toxicity, and body weight was checked twice weekly. At day 21 and 42 after injection, viral distribution in animals from each group was analyzed. The tumors and organs were excised, inspected, and homogenized using FastPrep FP120 Cell Disruptor (BIO 101, Qbiogene, Germany) at a speed of 6 for 20 s (three times). After three freeze-thaw cycles, the supernatants were collected by centrifugation at 1000$\times$g for 5 minutes. The viral titers were then determined in duplicate by standard plaque assays using CV-1 cells.

2.11. Histological Analysis of Tumors. For histological studies, tumors were excised and snap-frozen in liquid N_2, followed by fixation in 4% paraformaldehyde/PBS at pH 7.4 for 16 h at 4°C. Tissue sectioning was performed as described by Weibel et al. [17]. GLV-1h68 was labeled using polyclonal rabbit antivaccinia virus (anti-VACV) antibody (Abcam, Cambridge, UK), which was stained using Cy3-conjugated donkey antirabbit secondary antibodies obtained from Jackson ImmunoResearch (West Grove, PA, USA). Phalloidin-TRITC (Sigma, Taufkirchen, Germany) was used to label actin.

The fluorescent-labeled preparations were examined using the Leica MZ 16 FA Stereo-Fluorescence microscope equipped with a Leica DC500 Digital Camera. Digital images were processed with Photoshop 7.0 (Adobe Systems, Mountain View, CA, USA) and merged to yield pseudocolored images.

2.12. Preparation of Tumor Lysates for Mouse Immune-Related Protein Antigen Profiling. GLV-1h68-infected and noninfected tumors of MTH52c or ZMTH3 xenografted nude mice were used for preparation of tumor lysates at 42 days after virus infection. Tumors were resuspended in 9 volumes (W/V) lysis buffer [50 mM Tris-HCl (pH 7.4), 2 mM EDTA (pH 7.4), 2 mM PMSF and Complete Mini protease inhibitors (Roche, Mannheim, Germany)] and lysed using a FastPrep FP120 Cell Disruptor (BIO 101, Qbiogene, Germany) at a speed of 6.0 for 20 s (three times). Samples were centrifuged at 20,000 g at 4°C for 5 minutes, and supernatants were then analyzed for mouse immune-related protein antigen profiling by Multianalyte Profiles (mouse MAPs; Rules-Based Medicine, Austin, USA) using antibody-linked beads. Results were normalized based on total protein concentration.

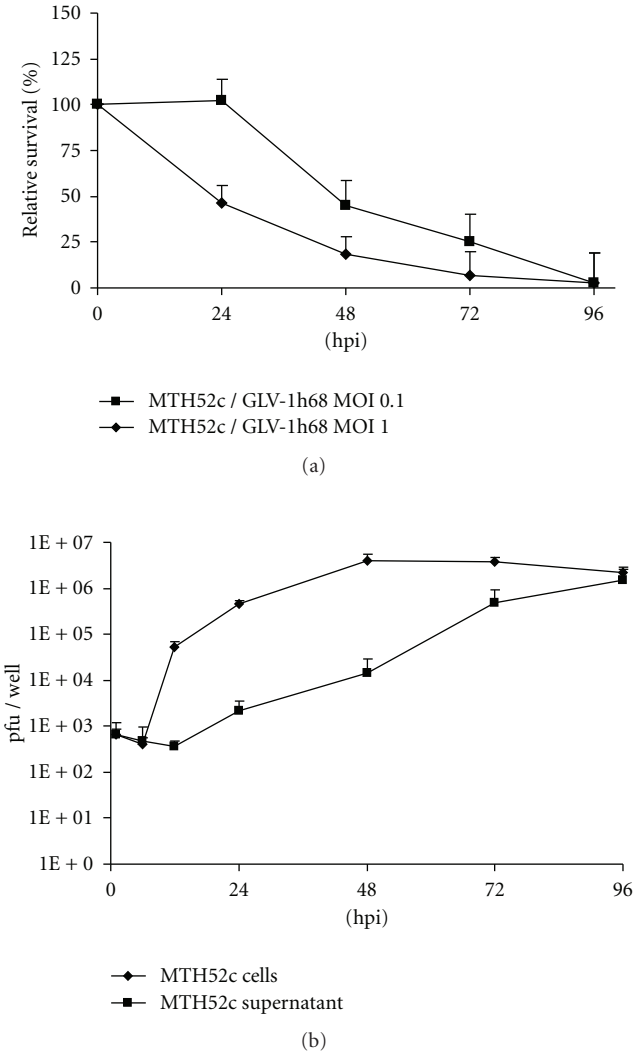

FIGURE 1: Cytotoxicity (a) and replication (b) of the GLV-1h68 virus in canine mammary MTH52c cells. (a) Viability of MTH52c cells after GLV-1h68 infection using MOIs of 0.1 and 1 was monitored over 96 hours. The amount of viable cells after infection with GLV-1h68 was measured in triplicate. Values are shown as percentages of respective uninfected controls. (b) Viral titer analysis in MTH52c cell culture after infection with GLV-1h68 at an MOI of 0.1. Cells and supernatant of virally treated cells were collected at various times post infection. Viral titers were determined as pfu per well in triplicate by plaque assay in CV-1 cell monolayers. Average plus standard deviations plotted.

Table 1: Viral titer in tissue samples (pfu/organ or tumor).

Animal no./dpi	1/21 dpi	2/21 dpi	3/21 dpi	4/42 dpi	5/42 dpi
Liver	120	1716	840	n.d	n.d
Lungs	1520	480	n.d.	56	324
Kidneys	n.d.	n.d.	n.d.	NT	NT
Spleen	150	n.d	n.d	n.d	n.d
Ovaries	n.d.	n.d	30	NT	NT
Tumor	2×10^7	1×10^7	2.1×10^7	7.3×10^5	7.3×10^5

Tumor-bearing mice were injected with 5×10^6 pfu of GLV-1h68. Mice were sacrificed at day 21 or 42 after virus injection (dpi). The data were determined by standard plaque assays on CV-1 cells using aliquots of the homogenized organs and were displayed as mean pfu/organ or tissue. For each organ, two aliquots of 0.1 ml were measured in triplicates.
n.d.: not detected (detection LIMIT<10 pfu/organ).
NT: not tested.

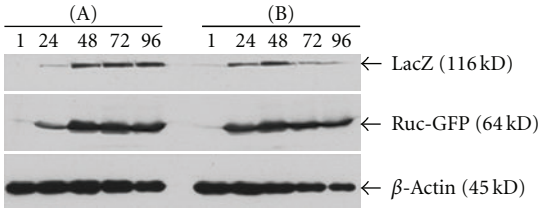

Figure 2: Western blot analysis of virus-mediated expression of Renilla luciferase-GFP fusion protein and β-galactosidase. MTH52c cells infected with GLV-1h68 at MOIs of 0.1 (a) and 1.0 (b) were used for protein isolation at 1, 12, 24, 48, 72, and 96 hours post infection (hpi). The time-dependent expression of Renilla luciferase-GFP fusion protein (Ruc-GFP), β-galactosidase (LacZ), and beta-actin as a control was analyzed as described in Materials and Methods.

3. Results

3.1. Infection and Replication of GLV-1h68 in the Canine Mammary Cell Line MTH52c. In order to test the ability of the GLV-1h68 virus to infect and lyse MTH52c cells in cell culture, we first performed a cell viability assay, as described in Materials and Methods. Ninety-six hours after GLV-1h68 infection at an MOI of 0.1 and 1.0, the MTH52c cells were eradicated, with only 2.4 ± 1.04% and 206 ± 0.68%surviving the treatment, respectively (Figure 1(a)). These results indicate that GLV-1h68 virus infection leads to an efficient eradication of the carcinoma MTH52c cells in culture.

To determine the replication efficacy of GLV-1h68 in MTH52c cells, we analyzed both the supernatant and the cell-associated virus titers at different times post infection (Figure 1(b)). Whereas the cell-associated virus titer in MTH52c peaked at 48 hours p.i. (3.94×10^6 pfu/well), the maximum yield in the supernatant was observed at 96 hours p.i. (1.54×10^6 pfu/well). These data correlated very well with cell death and demonstrated that GLV-1h68 can efficiently replicate in MTH52c cells.

In addition, the infectivity of GLV-1h68 was assessed and compared by virus titration in two pairs of cell lines (see in Supplementary Material available online at doi 10.1155/2010/736907). In both cases, GLV-1h68 formed plaques 70–200 times more efficiently in cancer cells than in normal cells, indicating that GLV-1h68 preferentially replicates in tumor cells.

3.2. Confirmation of Infection and Replication of GLV-1h68 in MTH52c Cells in Cell Culture and In Vivo through Virus-Mediated Protein Expression. To verify the infection and replication of GLV-1h68 in canine carcinoma cells, we followed the expression of the virus-mediated *Renilla* luciferase—green fluorescent protein—fusion protein (Ruc-GFP) and β-galactosidase (LacZ) in cell culture (Figure 2). Our Western blot analysis revealed that both marker proteins were efficiently expressed over a period of four days (Figure 2). The expression of Ruc-GFP and LacZ in cells infected at MOI of 0.1 peaked between 48 and 96 hpi, whereas maximum expression with an MOI of 1.0 was around 48 hpi.

Similar data were obtained by fluorescence microscopy (Figure 3). In these experimental settings we found that MTH52c cells infected with GLV-1h68 at MOI of 0.1 and 1.0 exhibited the strongest GFP expression at 72 and 96 hours, respectively, (supplementary Figure 1 and Figure 3). These data were also confirmed by flow cytometry (Figure 4) showing that the amount of infected cells increased over time and that those cells infected with vaccinia virus (detectable by GFP expression) were those cells that exhibited the major population of dead/dying cells (detectable by positive propidium iodide staining). In fluorescence microscopy, we used the same dye to demonstrate that most of the infected cells were dead/dying at 96h p.i. (Figure 3). These results indicate that GLV-1h68 was able to efficiently infect, replicate, and kill the MTH52c cells in cell culture.

Next, we examined the efficacy of GLV-1h68 to target MTH52c tumors *in vivo*. For this purpose, at different days postinjection, the mice of each group were observed either under a fluorescence stereomicroscope (Leica MZ 16 FA; Wetzlar, Germany) to detect GFP-dependent fluorescence or using the low-light Imager (NightOWL LB 981, Berthold Technologies, Bad Wildbad, Germany) to detect luciferase-catalyzed light emission in the presence of intravenously injected coelenterazine (Sigma, Taufkirchen, Germany). The GFP and luciferase expressions are dependent on vaccinia

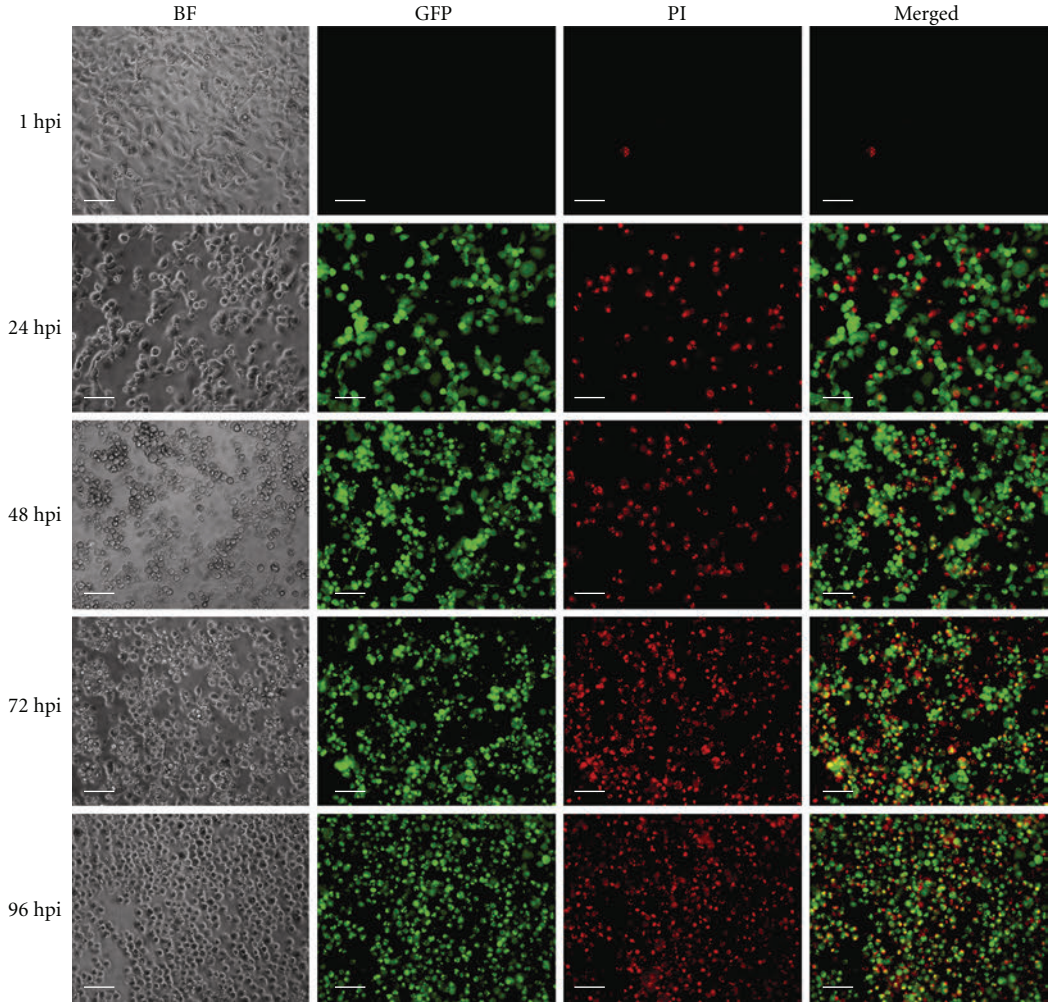

Figure 3: Time-dependent effects of infection of MTH52c with GLV-1h68 at an MOI of 1.0. (BF) Transmitted light view of virus-infected MTH52c cells; (GFP) expression of GFP in infected cells detected by direct fluorescence; (PI) propidium iodide staining of dead cells; (Merged) colocalization of GFP with the dead cells is shown in the merged imaged. All pictures in this set were taken at the same magnification. Scale bars represent 0.1 mm.

virus replication *in vivo*. As demonstrated, GFP fluorescence and luminescence were detected only within tumors of GLV-1h68-injected mice (Figure 5). The imaging data indicated the preferential accumulation of GLV-1h68 in MTH52c tumors.

3.3. A Single Systemic Application of GLV-1h68 Causes Significant Inhibition of Tumor Growth in MTH52c Xenografts. The therapeutic capacity of GLV-1h68 against an induced canine mammary cancer was tested in 10 female nude mice implanted with MTH52c cells at the age of 6–8 weeks. Twelve days postimplantation, all nude mice developed tumors with sizes between 400 and 500 mm^3. Then groups of five tumor-bearing mice were injected with either 5×10^6 pfu of GLV-1h68 or PBS (control). The tumor size of all animals was measured thrice weekly for six weeks. The single vaccinia virus injection caused an efficient inhibition of tumor growth in all GLV-1h68-treated tumor-bearing mice compared to control mice (Figure 6(a)). In addition, no reduction of net body weight of the animals was observed (Figure 6(b)).

The data revealed that GLV-1h68 could be an effective tool for the therapy of canine mammary carcinoma.

3.4. Viral Localization in GLV-1h68-Treated Mice after Inhibition of Tumor Growth. We analyzed the viral distribution in GLV-1h68-treated tumor-bearing mice by standard plaque assay and immunohistochemical staining. The plaque assay analysis revealed that viral titers in tumors were 10^4 to 10^7 and 10^3 to 10^5 times higher than the titers found in all the other organs combined at day 21 and 42, respectively (Table 1). These results show that GLV-1h68 can specifically infect and replicate in canine cancer cells.

To further examine the tumor tissues, we analyzed the tissue sections of the primary tumors at 42 days after virus injection by immunohistology. Microscopic analysis of viral distribution demonstrated that GLV-1h68 was present

Table 2: Comparison of mouse immune-related protein antigen profiling in primary ZMTH3 and MTH52c tumors with or without GLV-1h68 at day 42 after virus infection ($n = 2$). Folds of enhancement (a) or suppression (b) of mouse protein expression after virus injection are shown.

(a) Protein expression level: upregulated (day 42 after virus infection).

Antigen	GLV-1h68/untreated ratio (MTH52c)	GLV-1h68/untreated ratio (ZMTH3)	Classification
Apo A1	7.56	1.21	Anti-inflammatory protein
IFN-gamma	4.00	1.8	Proinflammatory cytokine
IL-6	7.04	5.52	Proinflammatory cytokine
IL-11	6.59	1.6	Pleiotropic cytokine
IL-18	8.00	3.21	Proinflammatory cytokine
IP-10 (CXCL10)	29.47	11.21	Interferon-gamma-induced protein
MCP-1 (CCL2)	18.36	4,99	Proinflammatory cytokine
MCP-3 (CCL7)	13.26	2.36	Proinflammatory cytokine
MCP-5 (CCL12)	3.84	7.13	Proinflammatory cytokine
M-CSF (KC/GROα)	8.28	3.51	Proinflammatory cytokine
MDC (CCL22)	4.02	1.97	chemokine
MIP-1beta	9.34	1.66	Proinflammatory cytokine
MIP-2 (CXCL2)	6.91	11.93	Proinflammatory chemokine
MMP-9	12.68	26.31	Matrix Metalloproteinase-9
TIMP-1	5.05	2.91	Tissue inhibitor of metalloproteinase type-1
TNF-alpha	6.47	1.5	Proinflammatory cytokine

(b) Protein expression level: downregulated (day 42 after virus infection).

Antigen	untreated/GLV-1h68ratio (MTH52c)	untreated/GLV-1h68ratio (ZMTH3)	Classification
VWF	1.33	1.01	von Willebrand factor
MIP-1gamma (CCL9)	2.71	1.96	Macrophage inflammatory protein

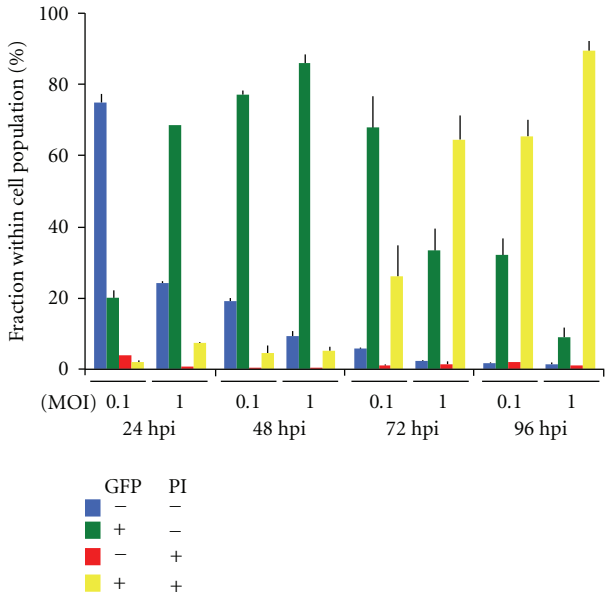

Figure 4: FACS analysis of MTH52c after infection with GLV-1h68 at MOIs of 0.1 and 1.0. Flow cytometry data indicate percentage of GFP and propidium iodide (PI) positive or negative cells.

throughout the tumor tissue of virus-infected mice but not in control mice (Figure 7). As expected, both the virus and the GFP distribution were similar in the whole tumor tissue, indicating that in this case GFP expression is an optimal tool for the monitoring of the GLV-1h68 infection *in vivo* (Figure 7AB). In addition, the histological data revealed that vaccinia virus infection led to oncolysis and damage of tumor tissue (Figure 7AI).

3.5. Analysis of Host Immune Response in GLV-1h68-Infected and Noninfected Primary Tumors. In order to analyze the effects of virus infection *in vivo*, we determined the mouse antigen profiling of GLV-1h68-infected and noninfected tumors of MTH52c or ZMTH3 xenografted nude mice. Canine mammary ZMTH3 adenoma tumors are susceptible to GLV-1h68 treatment *in vivo* [12] and therefore were used as an additional control.

At 42 days after virus injection, MTH52c and ZMTH3 tumors of nude mice with or without GLV-1h68 treatment were removed and used for generation of tumor tissue lysates as described in Material and Methods.

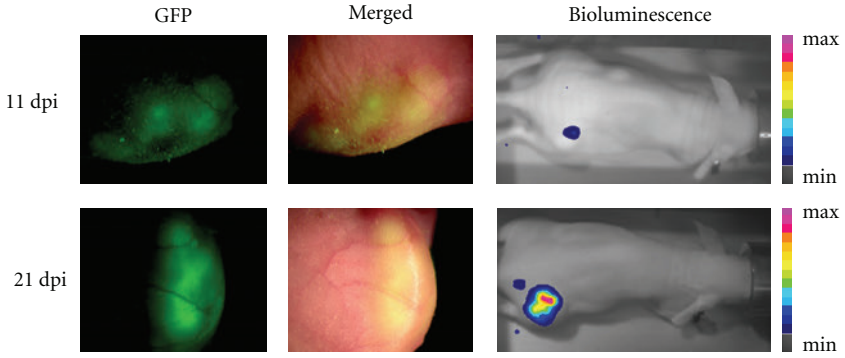

Figure 5: Fluorescence and luminescence imaging of MTH52c tumor-bearing mice after virus treatment. Fluorescence (GFP and Merged) imaging from the local tumor site and luminescence imaging of one representative mouse were taken 11 and 21 days post injection. Min: minimum; max: maximum.

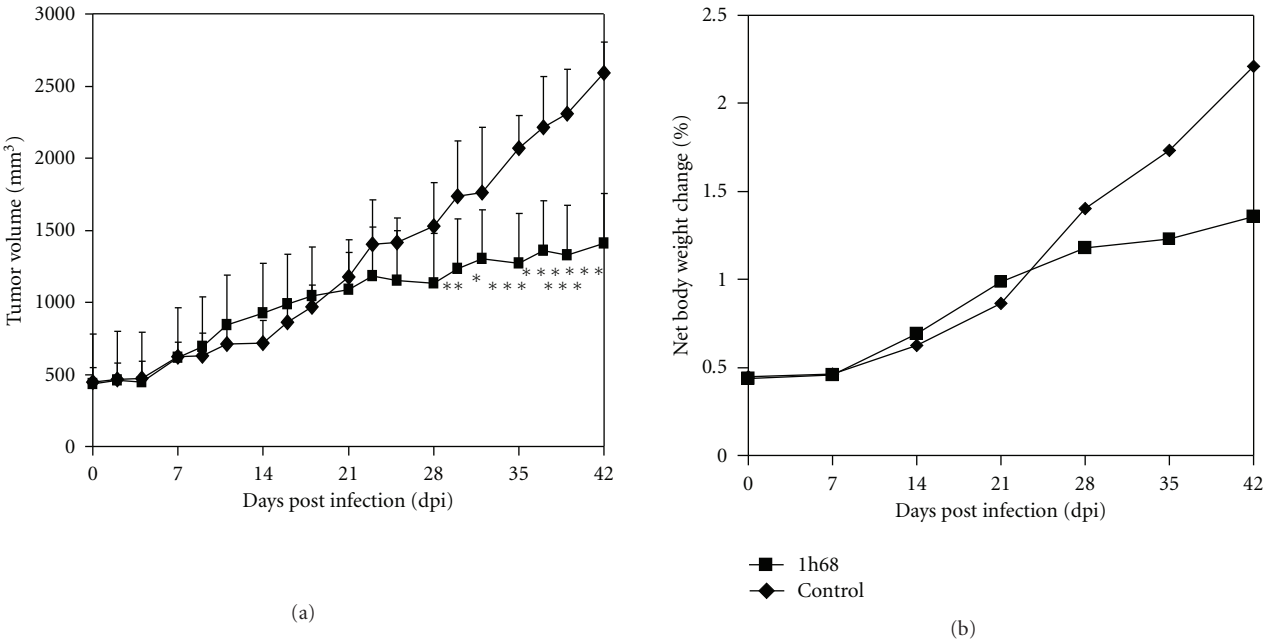

Figure 6: Effect of GLV-1h68 on MTH52c tumor growth in nude mice. (a) MTH52c tumor development in mice after GLV-1h68-treatment versus PBS treatment. Two-way analysis of variance (ANOVA) was used to compare the two corresponding data points of the two groups. $P < .05$ was considered as statistically significant $^{*}P < .05$; $^{**}P < .01$; $^{***}P < .001$. (b) Body weights of MTH52c cell xenografted mice after virus treatment.

The data in both xenograft models revealed that GLV-1h68 injection led to increased production of most of the tested proinflammatory cytokines and chemokines, such as MCP-1, MCP-3, MCP-5, M-CSF, IP-10, and IL-18 whereas only the cytokine MIP-1-gamma (CCL9) and the von Willebrand factor were downregulated (Table 2).

4. Discussion

Despite advances in surgery, radiation, and chemotherapy, the available treatment options for mammary carcinoma in dogs are limited and the prognosis for patients with advanced-stage disease is very poor. Therefore, the development of novel agents for therapy and diagnosis of canine mammary carcinoma is essential.

In this study, we showed for the first time that the recombinant vaccinia virus GLV-1h68 was able to effectively infect, replicate in, and lyse canine carcinoma cells in culture. The viral replication correlated well with cell lysis and with expression of the marker GLV-1h68 genes encoding β-galactosidase and *Renilla* luciferase-green fluorescent protein (GFP) fusion protein, respectively. In addition, flow cytometry data (Figure 4) confirmed that the virus-infected cells, detectable by GFP expression, were those cells that exhibited the major population of dead/dying cells (detectable by positive propidium iodide staining).

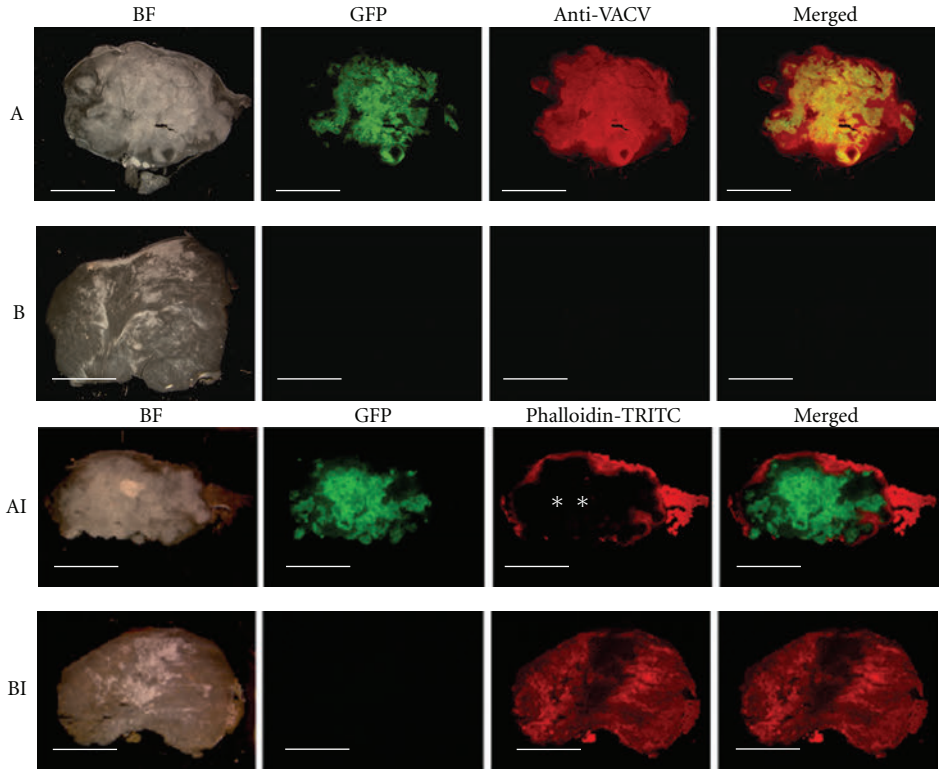

Figure 7: Immunohistochemical staining of MTH52c tumors. Tumor-bearing mice were i.v. injected either with $5 \times 10_6$ pfu of At day 42 after injection, GLV-1h68 (A and AI) or PBS (B and BI). whole tumor cross-sections (100 μm) were labeled either with antivaccinia virus or Phalloidin-TRITC (I) antibodies (both red) and analyzed by fluorescence microscopy to detect GFP (green) and actin or vaccinia virus-dependent (red) fluorescence. Scale bars represent 5 mm. *Large areas lacking actin staining indicate dead tumor tissue damaged by GLV-1h68.

Taken together, we did not find any evidence of possible resistance of canine carcinoma cancer MTH52c cells to infection with vaccinia virus in cell culture.

The current study also demonstrated the ability of GLV-1h68 to provide highly effective therapy *in vivo*. We observed a significant inhibition of tumor growth and damage of tumor tissue in the GLV-1h68-treated tumor-bearing mice compared to control mice. Most importantly, the treated animals appeared in good health without signs of toxicity, and no reduction of net body weight of virus-infected mice was observed (Figure 6(b)). In addition, experiments analyzing viral biodistribution in different organs (Table 1), as well as GFP fluorescence and luminescence studies on the living mice (Figure 5), confirmed the fact that the GLV-1h68 virus has an outstanding infection and replication capability and specificity in tumors [10, 13].

In order to analyze the possible mechanism of tumor elimination by GLV-1h68 in our MTH52c tumor xenograft model, we investigated the mouse immune-related protein antigen profiling in the primary tumors with or without virus injection. In these experimental settings we also used GLV-1h68-infected tumors of ZMTH3 xenografted nude mice as an additional control. The data revealed that in both the MTH52c and the ZMTH3 virus-infected tumors, the protein expression levels of most of the tested pro-inflammatory cytokines and chemokines were significantly upregulated compared to the corresponding noninfected tumors (Table 2).

Many of the upregulated proteins, such as MCP-1, MCP-3, MCP-5, M-CSF, IP-10, and IL-18, augment innate immunity mediated by dendritic cells, neutrophils, macrophages, and NK cells. Interestingly, similar mouse immune-related protein antigen profilings were also determinated in other xenograft models after a single GLV-1h68 injection [13, 18]. Therefore, GLV-1h68 may induce upregulation of the innate immune system, leading to increasing levels of pro-inflammatory cytokines. This notion is also supported by recent immunohistological studies demonstrating specific peri- and intratumoral infiltration of MHC class II-expressing host cells (like e.g., macrophages, and dendritic cells) surrounding virus-infected cancer cells [18, 19]. The presence of activated macrophages or dendritic cells in virus-infected xenografts only could serve as an evidence for the association between xenograft eradication and activation of the innate immune system. These findings suggest that activation of the innate immune system may act together with viral oncolysis to induce inhibition of tumor growth and tumor eradication in this model. However, which components of the innate immune system are involved in the elimination of tumor cells remains unknown.

We have reported previously that the GLV-1h68 virus can be successfully used for the treatment of canine mammary

ZMTH3 adenoma *in vivo* [12]. The comparison of the antitumor effects of GLV-1h68 with that of the present study showed that, in the adenoma xenograft ZMTH3 model, GLV-1h68 injection led to a faster and more efficient tumor inhibition and regression than in mice bearing MTH52c carcinoma tumors. One possible explanation could be the better replication efficacy of GLV-1h68 in the ZMTH3 tumors compared to that of MTH52c tumors *in vivo* [12]. However, a significant inhibition of the tumor growth was found in both ZMTH3 and MTH52c xenografts at day 30 after virus injection.

Therefore, GLV-1h68 could be a useful tool for treatment of both mammary cancer types in canine patients.

5. Conclusion

Our study demonstrates that the attenuated vaccinia virus strain GLV-1h68 can efficiently infect and destroy the canine mammary carcinoma MTH52c cells in cell culture and *in vivo*. In addition, a single systemic administration of GLV-1h68 causes a significant inhibition of tumor growth in MTH52c xenografts and damage of tumor tissue without detectable effects on the health status of the treated animals.

In summary, these data indicate that GLV-1h68 is a promising candidate virus in the treatment of breast carcinomas in canine patients.

Abbreviations

ApoA1:	Apolipoprotein A1
IL-6:	Interleukin-6
IP-10:	Interferon-inducible protein
MCP-1:	Monocyte chemoattractant protein-1
M-CSF:	Macrophage colony-stimulating factor
MIP:	Macrophage inflammatory protein
MMP-9:	Matrix metalloproteinase 9
MOI:	Multiplicities of infection
TIMP-1:	Metallopeptidase inhibitor 1
TNF-alpha:	Tumor necrosis factor-alpha
VWF:	Von Willebrand factor.

Acknowledgments

The authors declare that they have competing interests. I. Gentschev, N. Chen, Y. A. Yu, Q. Zhang, J. Stritzker, and A. A. Szalay have financial interests in Genelux Corporation. K. Ehrig, M. Hess, S. Rudolph, and U. Donat were supported by grants of Genelux Corporation. The costs of publication of this paper were defrayed in part by the payment of page charges. This paper must therefore be hereby marked *advertisement* in accordance with 18 U.S.C. Section 1734 solely to indicate this fact. The authors thank Ms. J. Langbein for excellent technical support and Dr. D. Haddad and Dr. Z. Sokolovic for critical reading of the paper. I. Gentschev and K. Ehrig contributed equally to this paper.

References

[1] M. Mottolese, L. Morelli, U. Agrimi et al., "Spontaneous canine mammary tumors: a model for monoclonal antibody diagnosis and treatment of human breast cancer," *Laboratory Investigation*, vol. 71, no. 2, pp. 182–187, 1994.

[2] E. Hellmén, "Complex mammary tumours in the female dog: a review," *Journal of Dairy Research*, vol. 72, pp. 90–97, 2005.

[3] K. Sorenmo, "Canine mammary gland tumors," *Veterinary Clinics of North America—Small Animal Practice*, vol. 33, no. 3, pp. 573–596, 2003.

[4] M. J. V. Vähä-Koskela, J. E. Heikkilä, and A. E. Hinkkanen, "Oncolytic viruses in cancer therapy," *Cancer Letters*, vol. 254, no. 2, pp. 178–216, 2007.

[5] A. M. Crompton and D. H. Kirn, "From ONYX-015 to armed vaccinia viruses: the education and evolution of oncolytic virus development," *Current Cancer Drug Targets*, vol. 7, no. 2, pp. 133–139, 2007.

[6] T.-C. Liu, E. Galanis, and D. Kirn, "Clinical trial results with oncolytic virotherapy: a century of promise, a decade of progress," *Nature Clinical Practice Oncology*, vol. 4, no. 2, pp. 101–117, 2007.

[7] R. Cattaneo, T. Miest, E. V. Shashkova, and M. A. Barry, "Reprogrammed viruses as cancer therapeutics: targeted, armed and shielded," *Nature Reviews Microbiology*, vol. 6, no. 7, pp. 529–540, 2008.

[8] D. H. Kirn and S. H. Thorne, "Targeted and armed oncolytic poxviruses: a novel multi-mechanistic therapeutic class for cancer," *Nature Reviews Cancer*, vol. 9, no. 1, pp. 64–71, 2009.

[9] A. Worschech, D. Haddad, D. F. Stroncek, E. Wang, F. M. Marincola, and A. A. Szalay, "The immunologic aspects of poxvirus oncolytic therapy," *Cancer Immunology, Immunotherapy*, vol. 58, no. 9, pp. 1355–1362, 2009.

[10] Q. Zhang, Y. A. Yu, E. Wang et al., "Eradication of solid human breast tumors in nude mice with an intravenously injected light-emitting oncolytic vaccinia virus," *Cancer Research*, vol. 67, no. 20, pp. 10038–10046, 2007.

[11] K. J. Kelly, Y. Woo, P. Brader et al., "Novel oncolytic agent GLV-1h68 is effective against malignant pleural mesothelioma," *Human Gene Therapy*, vol. 19, no. 8, pp. 774–782, 2008.

[12] I. Gentschev, J. Stritzker, E. Hofmann et al., "Use of an oncolytic vaccinia virus for the treatment of canine breast cancer in nude mice: preclinical development of a therapeutic agent," *Cancer Gene Therapy*, vol. 16, no. 4, pp. 320–328, 2009.

[13] Y. A. Yu, C. Galanis, Y. Woo et al., "Regression of human pancreatic tumor xenografts in mice after a single systemic injection of recombinant vaccinia virus GLV-1h68," *Molecular Cancer Therapeutics*, vol. 8, no. 1, pp. 141–151, 2009.

[14] S.-F. Lin, D. L. Price, C.-H. Chen et al., "Oncolytic vaccinia virotherapy of anaplastic thyroid cancer in vivo," *Journal of Clinical Endocrinology and Metabolism*, vol. 93, no. 11, pp. 4403–4407, 2008.

[15] S.-F. Lin, Z. Yu, C. Riedl et al., "Treatment of anaplastic thyroid carcinoma in vitro with a mutant vaccinia virus," *Surgery*, vol. 142, no. 6, pp. 976–983, 2007.

[16] K. A. Sterenczak, S. Willenbrock, M. Barann et al., "Cloning, characterisation, and comparative quantitative expression analyses of receptor for advanced glycation end products (RAGE) transcript forms," *Gene*, vol. 434, no. 1-2, pp. 35–42, 2009.

[17] S. Weibel, J. Stritzker, M. Eck, W. Goebel, and A. A. Szalay, "Colonization of experimental murine breast tumours by

Escherichia coli K-12 significantly alters the tumour microenvironment," *Cellular Microbiology*, vol. 10, no. 6, pp. 1235–1248, 2008.

[18] I. Gentschev, U. Donat, E. Homann, et al., "Regression of human prostate tumors and metastases in nude mice following treatment with the recombinant oncolytic vaccinia virus GLV-1h68," *Journal of Biomedicine and Biotechnology*, vol. 2010, Article ID 489759, 11 pages, 2010.

[19] A. Worschech, N. Chen, Y. A. Yu et al., "Systemic treatment of xenografts with vaccinia virus GLV-1h68 reveals the immunologic facet of oncolytic therapy," *BMC Genomics*, vol. 10, article 301, 2009.

Supplementary Material

Supplementary Table 1. Comparison of the replication efficacy of vaccinia virus strains in cancer and in normal cell lines.

The cell lines were treated with serial dilutions of viruses in duplicates. Two days post infection the cells were stained with 0.13% crystal violet. The viral titers in each cell line were calculated.

Tab.1A.: Virus infectivity in Hs578T vs. Hs578 Bst cells

Virus	**Titer (pfu/ml)**		
	human breast carcinoma cell line Hs578T [1]	human normal breast epithelial cell line Hs578 Bst [1] (from the same patient)	Hs578T versus Hs578 Bst
GLV-1h68	7.5×10^8	1.1×10^7	68.18
Lister strain (wild-type)	2.1×10^9	7.5×10^8	2.80
Western Reserve (wild-type)	2.1×10^9	2.1×10^9	1.00

Tab1B.: Infectivity of GLV-1h68 in hDF and HT-1080(pLEIN) cells [2]

Cell line	**Titer (pfu/ml)**
primary human dermal fibroblast (hDF) [2]	8.5×10^6 +/- 1.4×10^6
human fibrosarcoma HT-1080 (pLEIN) [2]	1.7×10^9+/- 3.5×10^6

In both cases, GLV-1h68 formed plaques more efficiently in cancer cells than in normal cells, indicating GLV-1h68 preferentially replicates in tumor cells.

Literature:

1. Hackett AJ, Smith HS, Springer EL, et al. Two syngeneic cell lines from human breast tissue: the aneuploid mammary epithelial (Hs 578T) and the diploid myoepithelial (Hs 578Bst) cell lines. *J. Natl. Cancer Inst.* 1977; **58**: 1795-1806.

2. Patent application (WO/2008/100292) MODIFIED VACCINIA VIRUS STRAINS FOR USE IN DIAGNOSTIC AND THERAPEUTIC METHODS, Table 52, Example 33

Supplementary figure 1. Time-dependent effects of infection of MTH52c with GLV-1h68 at an MOI of 0.1

(**BF**) Transmitted light view of virus-infected MTH52c cells; (**GFP**) Expression of GFP in infected cells detected by direct fluorescence; (**PI**) Propidium iodide staining of dead cells and (**Merged**) co-localization of GFP with the dead cells is shown in the merged imaged. All pictures in this set were taken at the same magnification. Scale bars represent 0.1 mm.

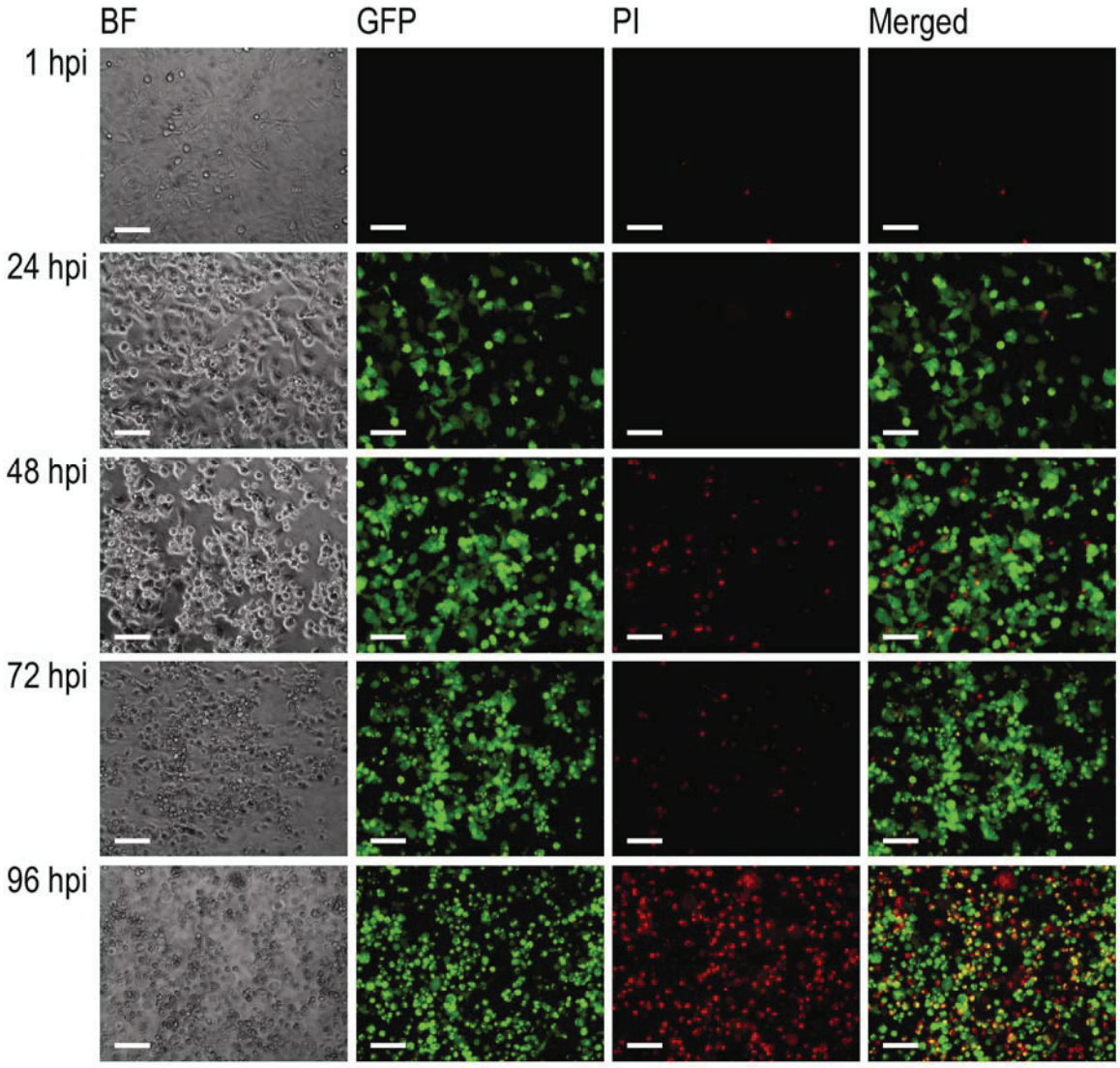
BF
GFP
PI
Merged
1 hpi
24 hpi
48 hpi
72 hpi
96 hpi

6. Discussion

Oncolytic virotherapy is evolving to become one of the hot-topics in oncology research in the near future. Advanced preclinical and early clinical results suggest the potential of especially oncolytic vaccinia viruses to revolutionize cancer treatment [42]. As therapy monitoring is one of the most critical points to prove the continuous efficacy of oncolytic viruses, groundbreaking diagnosis and therapy techniques have to be evaluated for this new era of cancer therapeutics.

In this thesis, the elaboration, establishment and validation of a body fluid-based biomarker test, that allows a statement about the oncolytic activity of recombinant vaccinia viruses in animal models and patients, was shown. An exogenous marker was used in this study to minimize the endogenous background signals in patients. GLV-1h68 expresses beta-galactosidase as well as beta-glucuronidase (GusA), whereby the latter was chosen as marker enzyme in our studies. Beta-galactosidase was not suitable because of systemic galactosidase activity, occurring due to the endogenous presence of beta-galactosidase in mammals and resulting in background signals. Beta-glucuronidase can also be found in mammals, but background signals in biomarker tests are almost lacking because of humans' glucuronidase specific features. Whereas the bacterial glucuronidase encoded by GLV-1h68 obtains its maximum activity at pH 6.8 to 7.7 [43], the human equivalent shows its activity peak at pH 4 to 5 due to its natural localization in acidic lysosomes. The activity of human glucuronidase reduces to zero in a neutral environment allowing the use of bacterial GusA as a blood biomarker without any detectable background signals. The lack of a glucuronidase secretion signal allows an assumption of the progression of cell lysis induced by GLV-1h68: As no glucuronidase should be present in the serum when cells are intact, the amount of detectable enzyme increases with progressive cell destruction and the accompanying release of bacterial GusA. This theory was proven within the experiments shown in chapter one of the results section.

Data verified the expression of glucuronidase in vaccinia-infected malignant cells in cell culture as well as in xenografts. The high expression of GusA by GLV-1h68 facilitated low detection limits resulting in the possibility to identify one single infected cell in culture experiments. In addition, it was possible to draw a distinction between tumor-bearing and non tumor-bearing mice as early as nine days after viral injection. Low background signals in animal experiments preventing an even earlier detection of tumors using this assay could be explained by circulating viral particles after systemic injection and unwanted viral replication in paws as well as ovaries of female non-tumor-bearing mice [44]. These background signals

prevented an even better outcome of the assay in this setting. But the fact that tumor-bearing mice showed no replication in other organs than the tumor, led us to the assumption that the GusA-based biomarkertest is able to serve as an almost background-free viral replication assay in a preclinical setup with tumor-bearing animals and finally in human patients.

The general need for biomarkers in context with virotherapies is evident by a closer examination of the present literature. Only few other serum biomarkers facilitating the monitoring of the performance of oncolytic viruses are described. For immunohistochemical investigations of biopsy material, commonly available anti-vaccinia antibodies are a simple tool to point out the presence of vaccinia virus in histological samples. Additionally, beta-galactosidase as a reporter system is used for histological studies by other groups even in clinical settings [42]. However, both approaches are not suitable for tests in body fluids, as commonly used antibodies are directed against surface molecules of vaccinia virus. But these molecules are potentially reorganized or destroyed during oncolysis limiting the use of these antibodies up to now. Beta-galactosidase on the other hand shows a disadvantage as mentioned before: Endogenous background signals in serum do not allow a sensitive detection because the distinction between human and virus-encoded beta-galactosidase is not possible in this setting.

A remarkable alternative to the glucuronidase system presented in this thesis is a secreted version of *Gaussia* luciferase. Browne et al. used a luciferase-expressing, tumor-selective herpes simplex virus to show the feasibility of this enzyme serving as a biomarker [45]. Virus replication and luciferase expression could be determined in different cancer cell lines as well in mouse models after intratumoral or systemic administration of the virus. The sensitivity of this system was demonstrated down to 1.000 infected cells in cell culture experiments and tumors consisting of 1.000.000 cells in xenografts. However, glucuronidase and luciferase approaches have to be compared critically in connection with theranostic virotherapies.

In this context, a major disadvantage is the secretion feature of *Gaussia* luciferase: In contrast to virally expressed glucuronidase, *Gaussia* luciferase can be detected in blood serum as early as viral replication happens due to its characteristic secretion. Nevertheless, viral replication does not necessarily result in tumor cell lysis, thus the luciferase system can only serve as a replication assay instead of being a combined replication and cell death assay like it is the case for the GusA procedure. Furthermore, the detection of the glucuronidase system is based on stable fluorogenic compounds while the luciferase approach uses a coelenterazine-based detection signal with unfavorable flash kinetics. Another argument to favor a GusA-dependent assay could be the long half-life of glucuronidase in blood. While luciferase gets renally cleared within minutes [46], GusA activity was not detectable in urine making this test more sensitive, as more glucuronidase can accumulate in the blood. Therefore glucuronidase in combination with fluorogenic compounds seems to be an excellent reporter system to monitor the therapy performance of

oncolytic viruses. On this basis, serum samples of patients participating in GL-ONC1 (clinical grade GLV-1h68) clinical trials were evaluated using the GusA assay (Yu et al., personal communication). These results show a strong correlation between the commonly used gold standard technology quantitative PCR and the newly developed beta-glucuronidase-based assay indicating the benefit of our system. Therefore the GusA-assay is currently applied in different GL-ONC1 trials to gain reliable data on the applicability in humans.

In addition to virotherapy, other areas of application for glucuronidase-based serum tests are conceivable. The success of stem cell therapies for example is strongly dependent on nidation and proliferation of exogenous administered stem cells [47]. GusA could therefore serve as a biomarker in stem cell therapies. However, due to the fact that cell lysis does not take place in stem cell therapies, a secreted form of glucuronidase would be necessary to serve as a cell survival marker measurable in blood. Basic approaches with membrane-anchored, humanized or secreted forms of glucuronidase are currently under investigation [48, 49] and provide evidence for an expansion of the application fields for bacterial glucuronidase as a biomarker.

Beta-glucuronidase could therefore be presented as a promising diagnostic tool for oncolytic virotherapy. However, this approach is only one of many possible starting points to gain an improved success in fighting cancer with oncolytic viruses. The application of different innovative diagnostic methods could also provide valuable insights in cancer treatment with virotherapeutica.

In this context, it could be shown that virally expressed beta-glucuronidase was able to serve as a diagnostic tool for preclinical imaging. The local conversion of FDGlcU to fluorescein by virus-encoded beta-glucuronidase led to a significant fluorescent signal in GLV-1h68 infected cells and tissues. With the help of an *in vivo* imaging system, it was possible to visualize vaccinia virus-infected tumors in mice. This method, based on enzymes and fluorescent substrates, is a direct competitor to the visualization of oncolytic viruses with fluorescent proteins like green fluorescent protein (GFP). Since GFP is encoded by GLV-1h68, it is possible to directly compare both light emitting systems. We could show that the fluorescent signal of fluorescein exceeded the intensity of the GFP signal by a factor of 40 in GLV-1h68 colonized tumors. This could enable a detection of early viral replication *in vivo*, when GFP-fluorescence is too weak to penetrate the outer skin. Additionally, tumors which are low permissive to viral replication could be imaged and even comparative studies with viruses expressing for example red-fluorescent proteins in contrast to GFP are conceivable.

But not only beta-glucuronidase is able to serve as a tool for the detection of tumors colonized with oncolytic viruses. Consequently, other partial aspects of this thesis dealt with the elaboration of innovative detection and imaging methods to improve the diagnostic feature of oncolytic viruses and the implementation of the GusA-based biomarker assay in these studies. We could demonstrate the feasibility of melanin producing vaccinia viruses to

serve as an innovative diagnostic tool as well as a therapy enhancing agent. The expression of melanogenic enzymes by engineered vaccinia strains finally led to dark-colored malignant cells opening new possibilities in second line therapies and imaging. The exposure of high-energy light to tumors treated with those viruses enhanced the oncolytic effect and promoted tumor regression by so-called heat therapy. Beside the therapeutic aspects, we could also show diagnostic features of these virus strains. The expression of beta-glucuronidase for example could be used to display viral replication in urine samples with the previously mentioned GusA-based fluorescence-assay. Additionally, the generation of melanin in malignant cells opens up new possibilities for diagnostic methods. An innovative preclinical modality like optoacoustic imaging [50] could be applied in this manner and showed great feasibility. However, to transfer those cutting-edge theranostics to patients, established imaging modalities have to be involved. This aim was fulfilled with the melanin expressing viruses by exhibiting their ability to lead to shortened T1 relaxation times in magnet resonance imaging in preclinical as well as clinical scanners. Whether those outcomes warrant a clinical testing of melanin-expressing biologicals for cancer treatment has to be evaluated. Innovative techniques for tumor diagnosis in early stages of cancer progression are urgently needed, thus optoacoustic imaging is on a good way into the clinics [51]. Magnetic resonance imaging is well established and routinely used in cancer diagnostics. However, the question remains, if melanin-expressing viruses are obligatory needed to detect a malignancy. MRI diagnoses are often possible without any tracer or reporter gene, making exogenous reporters redundant. The key to a clinical application of melanin-expressing viruses could be the combination of diagnosis-improving attributes together with the possibility of heat therapy.

Beside diagnostic successes, virally expressed enzymes could also be used to gain therapeutic improvements of oncolytic virotherapy. The combination of apoptosis-inducing prodrugs and enzyme-expressing oncolytic viruses which are able to activate these prodrugs showed significant enhanced tumor reduction in comparison to monotherapies. In particular, these observations became of special interest because of the ability of vaccinia viruses to initiate anti-apoptotic mechanisms to avoid their clearance by the host immune system. Although our experiments showed promising results, the oncolytic effect of vaccinia viruses could be further improved by trying to find new compounds that exhibit even stronger apoptosis-inducing effects while not hindering viral replication. Since the synthesis of such molecules is as difficult as their clinical validation and approval, it could be even more realistic to focus on already approved chemotherapeutics showing prodrug-features. This strategy is currently pursued in a phase I clinical trial combining an oncolytic vaccinia virus with irinotecan (ClinicalTrials.gov Identifier: NCT01394939). Since SN-38, the activated form of irinotecan, acts as an apoptosis-inducing topoisomerase I inhibitor, the outcomes of this clinical trial could be analogous to our preclinical findings.

In addition to the work with virally expressed enzymes like beta-glucuronidase, supportive imaging modalities were used to investigate viral replication in tumors together with the host immune response. Perfluorocarbons (PFCs) can be applied as blood substitute substances as well as contrast agents for magnet resonance imaging. PFCs are phagocytized by immune cells like monocytes and macrophages and hence enable a visualization of inflammatory processes [52]. We could reveal the immune reaction taking place in context of vaccinia virus replication in tumor tissue by using 19F MRI in combination with perfluorocarbon nanoemulsions. These results gave insights into the complex virus-tumor-immune system coherence in context of oncolytic virotherapy. The influence of innate and adaptive immune reactions on viral replication, oncolysis and tumor regression is yet unclear. Microarray studies of Worschech et al. gave a first insight into the complex interplay between the immune system and oncolytic viruses [53, 54], but the chronological order of immune processes is still unknown. The visualization of different components of the immune system via magnet resonance imaging could open up an opportunity to get further knowledge about the influence of immune cells on oncolytic virotherapy. Again, beta-glucuronidase, especially when used as a marker for early viral replication in tumors, could help to reveal a possible interplay between viral replication, oncolysis and immune response.

Beside fundamental studies of mechanistic details of oncolytic viruses, a continuous development of improved virus strains has to be addressed. Different approaches in this direction were implemented in this work. Many state-of-the-art therapies were combined with oncolytic vectors to underline the variety of possibilities obtained by genetically engineering oncolytic viruses. Anti-angiogenic agents are one of the most promising innovative therapy forms of cancer treatment. Achievements like the FDA approval of bevacizumab [55] led to intense research efforts in expanding this field of treatment modalities. We could show that a vaccinia virus strain expressing an anti-VEGF single-chain antibody could enhance the tumor regression significantly. In this context, the GusA-based fluorescence assay could serve as a comparative test to investigate a possible secretion of the virus-encoded antibody. Positive therapeutic results could also be demonstrated with an approach using an interleukin 6-expressing vaccinia virus strain that showed improved alleviation of chemotherapy-induced toxicity.

In conclusion, the data of this thesis showed first and foremost the enormous potential of beta-glucuronidase to serve as a diagnostic tool for oncolytic virotherapy. The expression of bacterial beta-glucuronidase by oncolytic viruses in combination with specific fluorogenic substrates enabled an *ex vivo* detection of viral replication in serum samples as well as optical imaging of weakly infected tumors in mice. Additionally, other aspects of oncolytic virotherapy could be evaluated in the framework of this thesis, including therapy

improvement by enzyme-activated prodrugs, the establishment of innovative imaging modalities and the investigation of groundbreaking virus strains.

Our preclinical results give indication in how a beta-glucuronidase-based biomarker assay can be implemented into clinical studies of oncolytic vaccinia viruses to improve the therapy-accompanying diagnostic analyses.

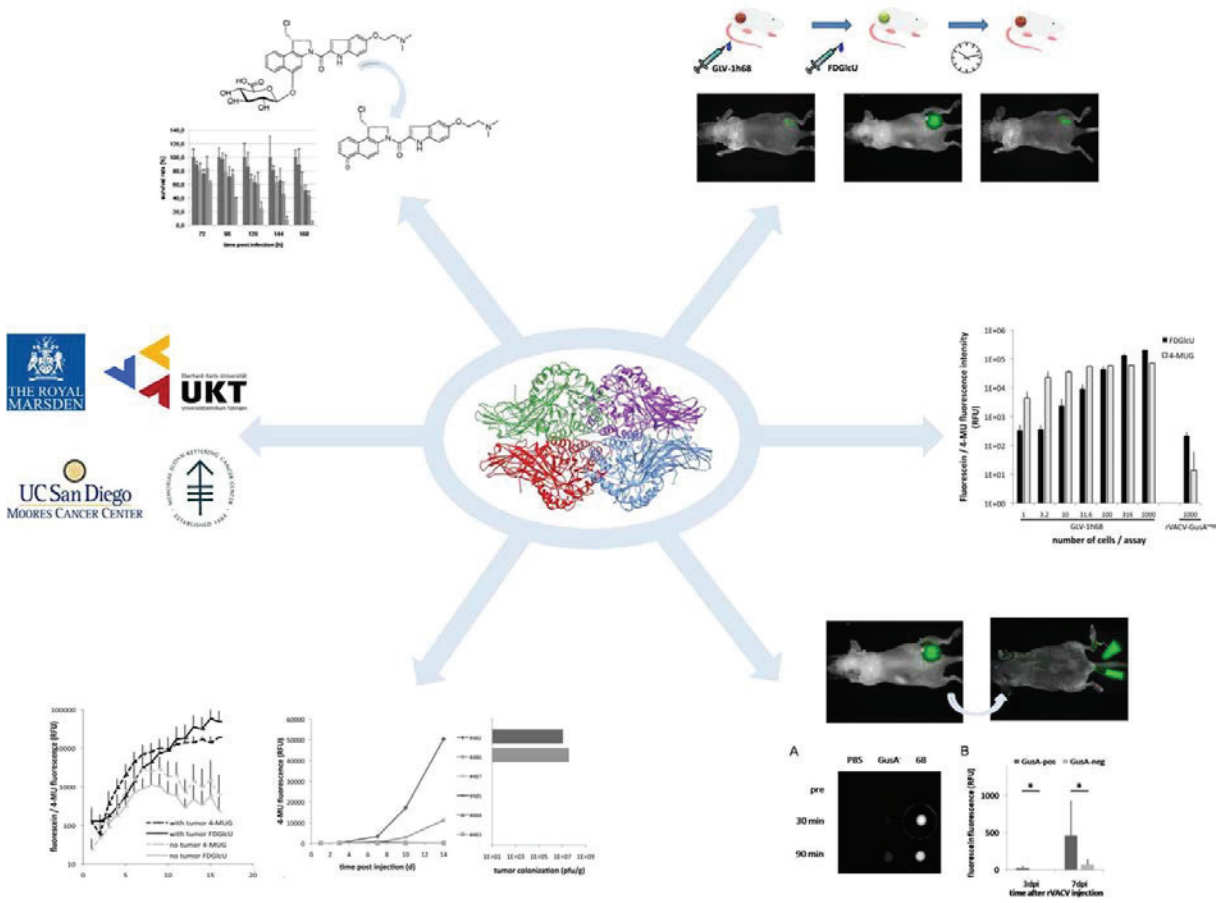

Fig. 4 **Schematic overview about the various possibilities of using virus-encoded beta-glucuronidase in combination with oncolytic virotherapy**

6.1 References

42. Breitbach, C.J., et al., *Intravenous delivery of a multi-mechanistic cancer-targeted oncolytic poxvirus in humans.* Nature, 2011. 477(7362): p. 99-102.
43. Fang, W., M. Vikerpuur, and M. Sandholm, *A fluorometric beta-glucuronidase assay for analysis of bacterial growth in milk.* Vet Microbiol, 1995. 46(4): p. 361-7.
44. Karupiah, G., et al., *Vaccinia virus-mediated damage of murine ovaries and protection by virus-expressed interleukin-2.* Immunol Cell Biol, 1990. 68 (Pt 5): p. 325-33.
45. Browne, A.W., et al., *Cancer screening by systemic administration of a gene delivery vector encoding tumor-selective secretable biomarker expression.* PLoS One, 2011. 6(5): p. e19530.
46. Tannous, B.A., *Gaussia luciferase reporter assay for monitoring biological processes in culture and in vivo.* Nat Protoc, 2009. 4(4): p. 582-91.
47. Chidgey, A.P., et al., *Tolerance strategies for stem-cell-based therapies.* Nature, 2008. 453(7193): p. 330-7.
48. Weyel, D., et al., *Secreted human beta-glucuronidase: a novel tool for gene-directed enzyme prodrug therapy.* Gene Ther, 2000. 7(3): p. 224-31.
49. Chen, K.C., et al., *A humanized immunoenzyme with enhanced activity for glucuronide prodrug activation in the tumor microenvironment.* Bioconjug Chem, 2011. 22(5): p. 938-48.
50. Bednar, B. and V. Ntziachristos, *Opto-acoustic imaging of drug discovery biomarkers.* Curr Pharm Biotechnol, 2012. 13(11): p. 2117-27.
51. Valluru, K.S., B.K. Chinni, and N.A. Rao, *Photoacoustic imaging: opening new frontiers in medical imaging.* J Clin Imaging Sci, 2011. 1: p. 24.
52. Flogel, U., et al., *In vivo monitoring of inflammation after cardiac and cerebral ischemia by fluorine magnetic resonance imaging.* Circulation, 2008. 118(2): p. 140-8.
53. Worschech, A., et al., *Systemic treatment of xenografts with vaccinia virus GLV-1h68 reveals the immunologic facet of oncolytic therapy.* BMC Genomics, 2009. 10: p. 301.
54. Worschech, A., et al., *The immunologic aspects of poxvirus oncolytic therapy.* Cancer Immunol Immunother, 2009. 58(9): p. 1355-62.
55. *The FDA approves drugs for colorectal cancer, lung cancer.* FDA Consum, 2007. 41(1): p. 5.

7. Appendix

7.1 Acknowledgement

An erster Stelle möchte ich mich bei Herrn Prof. Dr. A. A. Szalay bedanken: Für die Möglichkeit meine Dissertation in seiner Arbeitsgruppe anzufertigen, für die Überlassung des ebenso faszinierenden wie herausfordernden Themas sowie für die Unterstützung während der gesamten Zeit meiner Doktorarbeit.

Herzlich möchte ich mich zudem bei Prof. Dr. G. Krohne für die freundliche Übernahme des Zweitgutachtens dieser Arbeit bedanken.

Zudem gilt mein Dank Herrn Prof. Dr. F. Grummt, der mir vor allem beim endgültigen Verfassen dieser Dissertation stets mit Rat und Tat zur Seite stand.

Einen großen Anteil am Gelingen dieser Arbeit hatte Priv. Doz. Dr. J. Stritzker, der mir über weite Strecken meiner Doktorarbeit als Betreuer zur Seite stand und dem dabei die Gratwanderung gelang, mir genügend wissenschaftlichen Freiraum zu lassen ohne mir das Gefühl zu geben verloren zu sein.

Ein Dank gebührt auch allen Kollaborateuren, die es mir ermöglicht haben, an den verschiedensten Projekten teil zu haben und dadurch Einblicke in unglaublich viele Forschungsgebiete abseits meines Hauptprojektes zu erhalten.

Herzlichen Dank an die gesamte Arbeitsgruppe Szalay / Genelux. Egal ob in Würzburg oder San Diego: Die gute Arbeitsatmosphäre hat diese Doktorarbeit zu einer sehr angenehmen Zeit gemacht. Neben der wissenschaftlichen Unterstützung, die ich von allen Mitarbeitern erfahren durfte, möchte ich mich im Besonderen bei Johanna, Rike, Julie, Caro und Lorenz für Freundschaften bedanken, die weit über den Laboralltag hinaus gingen. Vielen Dank auch an Stefi, Ivo, Barbara, Thomas, Simon, Sandeep, Klaas, Lisa und all den anderen, deren Namen diesen Rahmen hier sprengen würden. Jeder in dieser Arbeitsgruppe hat seinen Teil zu dieser Arbeit beigetragen und verzeiht mir hoffentlich, falls er an dieser Stelle nicht explizit genannt wird.

Der abschließende Dank gilt meinen Eltern Bärbel und Heinz sowie meiner Freundin Melanie, die mich in allen Lebenslagen unterstützt haben und vor allem dadurch großen Anteil am Gelingen dieser Arbeit hatten.

7.3 Publications

7.3.1 Peer-reviewed publications

Vaccinia virus mediated melanin production allows MR and optoacoustic deep tissue imaging and laser induced thermotherapy of cancer

Stritzker J, Kirscher L, Scadeng M, Deliolanis NC, Morscher S, Symvoulidis P, Schaefer K, Zhang Q, Buckel L, Hess M, Donat U, Bradley WG, Ntziachristos V, Szalay AA

Proc Natl Acad Sci U S A. 2013

Imaging of intratumoral inflammation during oncolytic virotherapy of tumors by 19F-magnetic resonance imaging (MRI)

Weibel S, Basse-Luesebrink TC, Hess M, Hofmann E, Seubert CM, Langbein- Laugwitz J, Gentschev I, Sturm VJF, Ye Y, Kampf T, Jakob PM, Szalay AA

PLoS One. 2013;10.1371/journal.pone.0056317

Preferential colonization of metastases by oncolytic Vaccinia virus strain GLV-1h68 in a human PC-3 prostate cancer model in nude mice

Donat U, Weibel S, Hess M, Stritzker J, Härtl B, Sturm JB, Chen NG, Gentschev I, Szalay AA

PLoS One. 2012;7:e45942

Virotherapy of canine tumors with oncolytic Vaccinia virus GLV-1h109 expressing an anti-VEGF single-chain antibody

Patil SS, Gentschev I, Adelfinger M, Donat U, Hess M, Weibel S, Nolte I, Frentzen A, Szalay AA

PLoS One. 2012;7:e474726

Functional hyper-IL-6 from Vaccinia virus-colonized tumors triggers platelet formation and helps to alleviate toxicity of mitomycin C enhanced virus therapy

Sturm JB, Hess M, Weibel S, Chen NG, Yu YA, Zhang Q, Donat U, Reiss C, Gambaryan S, Krohne G, Stritzker J, Szalay AA

J Transl Med. 2012;10:9

Bacterial glucuronidase as general marker for oncolytic virotherapy or other biological therapies

Hess M, Stritzker J, Härtl B, Sturm JB, Gentschev I, Szalay AA

J Transl Med. 2011;9:172

Enhanced tumor therapy using Vaccinia virus strain GLV-1h68 in combination with a beta-galactosidase-activatable prodrug seco-analog of duocarmycin SA

Seubert CM, Stritzker J, Hess M, Donat U, Sturm JB, Chen N, von Hof JM, Krewer B, Tietze LF, Gentschev I, Szalay AA

Cancer Gene Ther. 2011;18:42-52

Significant growth inhibition of canine mammary carcinoma xenografts following treatment with oncolytic Vaccinia virus GLV-1h68

Gentschev I, Ehrig K, Donat U, Hess M, Rudolph S, Chen N, Yu YA, Zhang Q, Bullerdiek J, Nolte I, Stritzker J, Szalay AA

J Oncol. 2010;2010:736907

7.3.2 Reviews

Imaging cancer with oncolytic viruses

Hess M, Donat U, Stritzker J, Szalay AA

in preparation

7.3.3 Non peer-reviewed publications

Long-term tumor visualization by NiraWave M

Hess M, Stritzker J, Szalay AA

Miltenyi Biotech customer report, printed 2012

7.3.4 Patent applications

Method for detecting replication or colonization of a biological therapeutic

Szalay AA, Stritzker J, Hess M

US patent Application No.: 13/573,845. Filling date: Oct.5, 2012